High-Throughput Development of Solid Electrolytes and High Potential Cathodes for All-Solid Lithium Secondary Batteries

Antranik Jonderian

A thesis submitted to McGill University
in partial fulfillment of the requirements of the degree of
Doctor of Philosophy
at

Department of Chemistry, McGill University
Montreal, Quebec, Canada
March 2023

“The important thing is not to stop questioning.

Curiosity has its own reason for existing.”

-Albert Einstein

I dedicate this thesis to my wife, mom, dad, and brother.

Table of contents

Abstract viii
Résumé x
Acknowledgments xii
Author contributions xiv
Contribution to original knowledge xvi
List of figures xviii
List of tables xxiii
List of abbreviations xxiv
List of Symbols xxvi
Chapter 1 Introduction 1
  1.1 Evolution of battery technology 2
  1.2 Principles of lithium-ion batteries 3
  1.3 Liquid electrolytes 4
  1.4 Solid electrolytes 6
    1.4.1 Inorganic solid electrolytes 9
    1.4.2 Sulfide solid electrolytes 15
    1.4.3 Halide solid electrolytes 16
    1.4.4 Phosphide and hydride solid electrolytes 17
    1.4.5 Oxide solid electrolytes 17
    1.4.6 Synthesis and sintering techniques 20
  1.5 Characterization techniques for solid electrolytes 21
    1.5.1 Electrical conductivity 21

1.5.2 Electronic conductivity 23

1.5.3 Electrochemical stability window 24

1.5.4 Stability against lithium metal 25

1.6 Intercalation cathodes 26

1.6.1 Olivine cathodes 27

1.6.2 Characterization techniques for cathodes 28

1.7 High-throughput experimentation 28

1.8 Context and scope of this thesis 30

1.9 References 32

Chapter 2 Suite of High-Throughput Experiments for Screening Solid Electrolytes for Li Batteries 39

2.1 Abstract 39

2.2 Introduction 40

2.3 Experimental methods 43

2.4 Results & discussion 47

2.4.1 Ionic conductivity 47

2.4.2 Electronic conductivity 50

2.4.3 Electrochemical stability window 52

2.4.4 Chemical compatibility with lithium 55

2.5 Conclusion 56

2.6 Acknowledgments 57

2.7 Supporting information 57

2.8 References 60

Chapter 3 Metastability in Li–La–Ti–O Perovskite Materials and Its Impact on Ionic Conductivity 62

3.1 Abstract 62

3.2 Introduction 63

3.3 Experimental methods.. 69

3.4 Results and discussion.. 72

3.4.1 Li-La-Ti-O pseudoternary phase diagram 72

3.4.2 Lithium conductivity 84

3.5 Conclusions 91

3.6 Acknowledgments... 92

3.7 Supporting information 92

3.8 References 109

Chapter 4 226 Substitutions Into Li-La-Ti-O Perovskites: Benefits and Limitations 113

4.1 Abstract 113

4.2 Introduction 114

4.3 Experimental 116

4.4 Results and discussions 118

4.4.1 Structure.. 118

4.4.2 Transport properties.. 122

4.4.3 Electrochemical stability window 127

4.5 Conclusion.. 129

4.6 Acknowledgments.. 131

4.7 Supporting information 132

4.8 References 141

Chapter 5 Accelerated Development of High Voltage Li-Ion Cathodes............................ 144

5.1 Abstract 144

5.2 Introduction 145

5.3 Experimental section.. 146

5.4 Results and discussion.. 150

5.5 Conclusions 162

5.6 Acknowledgments.. 163

5.7 Supporting information 164

5.8 References 186

Chapter 6 Discussion 189

6.1 Charge transport properties in solid electrolytes and cathode materials 189

6.2 ESW of solid electrolytes.. 193

6.3 Stability of SEs against lithium metal anode 195

6.4 Composition-structure relationships in LLTO and effect of substitutions....................... 196

6.5 Improvement of $LiCoPO_4$ performance by substitutions... 198

6.6 References 201

Chapter 7 Conclusions and Future Work 202
7.1 Conclusions 202

7.2 Future work by chapter 205

  7.2.1 Chapter 2 205

  7.2.2 Chapter 3 206

  7.2.3 Chapter 4 206

  7.2.4 Chapter 5 207

7.3 References 209

Abstract

There is a massive global demand for lithium-ion batteries that offer greater safety and energy density for electric vehicles and renewable energy storage systems. This demand can be fulfilled by replacing the liquid electrolyte with an inorganic solid electrolyte that is non-flammable and compatible with low/high potential electrodes. Although much research is conducted to optimize already known inorganic solid electrolytes and discover novel ones, it is slowed by conventional experimentation, which involves testing one composition at a time. Therefore, we developed high-throughput tools for synthesizing and screening ceramic inorganic Li-ion conductors. This high-throughput suite generates highly reproducible 30mg scale samples. It also permits the reliable screening of their essential properties for battery applications: structure, ionic conductivity, activation energy of Li-ion diffusion, electronic conductivity, electrochemical stability window, and stability against lithium metal.

The first materials studied with the new methodology were lithium lanthanum titanate electrolytes with perovskite structure. These have promising high bulk ionic conductivity and good stability at high potentials but are unstable at low potentials, and their grain boundaries limit the total conductivity. To investigate the origin of the low grain boundary conductivity, we explored the composition-structure-conductivity relationship of Li-La-Ti-O pseudoternary phase stability diagram. We discovered that the perovskite phase is, in fact, metastable and secondary phases play an important role in lowering the grain boundary resistance. The low potential stability was also altered by a systematic substitution study wherein 50 different elements were tested at 5 different substitution levels. We discovered that specific substitutions stabilize the lanthanum titanate phase. We also observed a minor improvement in conductivity, as well as a shift in low potential stability with various substitutions.

The electrolytes explored in this study can facilitate the use of high-potential cathodes such as $LiCoPO_4$ (LCP), which has a high theoretical specific capacity; however, its practical capacity is hindered by its low intrinsic ionic and electronic conductivity. The final accomplishment of this thesis is to develop a doped LCP material that achieved near theoretical specific capacity and had dramatically improved capacity retention compared to the pristine $LiCoPO_4$ by enhancing the electronic conductivity, tuning the morphology and suppressing antisite defects through conducting combinatorial screening.

Not including materials made for the methodology development, a total of ~2000 samples were synthesized and characterized thoroughly in this thesis. The outcomes are not only improved battery materials but also a deepened understanding of the composition-structure-property relationships in these important materials. Additionally, this research highlights the role small amounts of substitutions play in stabilizing phases, enhancing their properties, and tuning morphology.

Résumé

Il existe une demande croissante mondiale au niveau de batterie au lithium qui sont moins dangereuses et offrent une meilleure densité énergétique, qui peuvent être utilisé pour des voitures électriques et des moyens de stockage d’énergie renouvelable et éco-responsable. Cette demande peut être satisfaite en remplaçant les électrolyte liquide par des électrolytes solides inorganiques qui sont non-inflammables et compatibles avec des bas ou des hauts potentiels d’électrode. Malgré le fait que de multiples projets de recherche visent à optimiser des électrolytes solides déjà connus, ces projets sont freinés par les moyens d’expérimentation conventionnels qui ne testent qu’une composition à la fois. Ainsi, nous avons développé une méthode à haut rendement (« High-Throughput ») pour synthétiser et étudier la conductivité des ions de lithium. Cette méthode génère de manière reproductible des échantillons de 30 mg. De plus, elle permet un dépistage fiable afin d’étudier les propriétés essentielles des batteries : structure, conductivité ionique, énergie d’activation des ions de lithium, conductivité électronique, plages de stabilité électrochimique, stabilité en présence de lithium métallique.

Les premiers matériaux étudiés avec cette nouvelle méthodologie sont les électrolytes de titanate de lithium et de lanthane ayant la structure pérovskite. Ces matériaux ont démontré une bonne conductivité ionique et une stabilité à haut potentiel prometteuse. À bas potentiel une instabilité existe, causée par la taille des grains qui limite la conductivité. Afin d’investiguer l'origine de la faible conductivité à la limite du grain, nous avons exploré la relation composition-structure-conductivité du diagramme de stabilité de la phase pseudo ternaire Li-La-Ti-O.

Nous avons découvert que la phase pérovskite est métastable et la phase secondaire joue un rôle majeur dans la réduction de la résistance à la frontière des grains. Le bas potentiel de stabilité a été altéré due à une substitution systématique où 50 éléments ont été testés à 5 niveaux

de substitution différents. Nous avons découvert que des substitutions spécifiques stabilisent la phase de titanate de lanthane. Nous avons également observé une légère amélioration de la conductivité, ainsi qu'un changement dans la stabilité à faible potentiel avec diverses substitutions.

L'électrolyte étudié permet de faciliter l'usage de cathode a haut potentiel tel que $LiCoPO_4$ (LCP) qui a une capacité théorique élevée. Cependant, sa capacité pratique est restreinte par sa faible conductivité ionique et électronique intrinsèque.

L'accomplissement final de cette thèse a été de développer un matériau LCP dopé offrant une capacité si avoisinante de la valeur théorique ainsi qu'une amélioration drastique de la capacité de rétention comparé au $LiCoPO_4$ non-dopé par une amélioration de la conductivité électronique. L'ajustement de la morphologie et la suppression des défauts antisites via un criblage combinatoire.

Sans compter les matériaux fabriqués pour le développement de la méthodologie, un total de ~2000 échantillons ont été synthétisés et caractérisés en profondeur pour cette thèse. Les résultats ne sont pas seulement des matériaux de batterie améliorés, mais aussi une compréhension approfondie des relations composition-structure-propriété de ces matériaux importants. De plus, cette recherche met en évidence le rôle que jouent de petites quantités de substitutions dans la stabilisation des phases, l'amélioration de leurs propriétés et l'ajustement de la morphologie.

Acknowledgments

I am deeply grateful to the many people who have touched my life during this journey and made it possible for me to complete my thesis. Without their support and encouragement, I would not have been able to achieve this significant milestone. First and foremost, I want to express my sincere appreciation to my supervisor, Prof. Eric McCalla, for his unwavering mentorship, guidance, support, and patience throughout my Ph.D. Under his leadership, I developed versatile chemistry and engineering skills and received the best tools to prepare for my next chapter of life. His constant encouragement and support made it possible for me to enjoy this journey by learning new things every day. Thank you for equipping me with all the necessary skills to find my dream industrial job. Thank you for always being there for me.

My heartfelt appreciation also goes to Professors Janine Mauzeroll and Mark Andrews, who kindly agreed to be part of my review committee and provided me with invaluable constructive criticism and input that helped me refine and advance my projects. I am also grateful to Professors Michael Dolle and Dima Perepichka for generously allowing me to use their lab instruments at the start of my project. I would like to thank Afshin Dadvand for his valuable input and for training me on their lab instruments.

I would like to express my gratitude to Ehsan, Chris, and Shoronia for giving me the opportunity to contribute to their wonderful work and learn from their expertise. I am deeply indebted to the current and past members of the McCalla lab, including Karlie, Michelle, Alex, Ethan, Sarish, Tham, Shipeng, Sofina, Michel, Rui, Elissa, Michael, Nooshin, Marzieh, Mohammad, Marc, and Jean-Danick who have made invaluable contributions to my research. They have not only been great colleagues but have also made the lab feel like a second home, and they are my second family. Thank you all for the valuable science discussion and advice and for making the lab a fun place to work and exchange ideas.

I am also grateful to Sang Bok for his valuable questions that have improved my research. I would like to thank my previous advisors, Professors Kamal Bouhadir and Mazen Al-Ghoul, for equipping me with the necessary tools for the Ph.D. program. The collaboration opportunities within our lab have been significant, and I am grateful for that. Thanks to Rui, Shipeng, and Sarish, who have helped to make our projects run smoothly with their valuable input and dedication. I would like to thank the undergrads who assisted me during the summer, including Victor, Daniel, and Malcolm.

I extend my deepest gratitude to Mostafa and Dani for their friendship and for making me feel at home when I first arrived in Canada. I would like to thank the chemistry staff, including Chantal for her support and swift replies, Hatem for his friendship and training on XRD, Petr for transferring his expertise on using many instruments, and Jean-Marc for providing our lab with everything we need to do good science. Finally, thank you Richard, Weihua, and Jean-Philippe, for your expertise in electronics and machining, which was instrumental in creating the custom components required for my experiments.

The list of people who have contributed to helping me overcome all the obstacles in my Ph.D. research is long, and I am grateful to every one of you. Finally, I want to thank my wife Tamar Amoghlian for her unwavering emotional support, encouragement, and for providing a peaceful and loving environment to complete my Ph.D. Her patience and constant advice have helped me to stay focused and not forget my priorities. I also want to thank my parents, although distant, their love has always been with me. Their support has been unwavering, and their hearts have always been with me, standing by me through all my decisions.

Author contributions

All projects presented in this thesis were performed under the supervision of **Professor Eric McCalla** who provided guidance and helped design the experiments. He assisted in writing the manuscripts and provided corrections.

Chapter 2

Data treatment, figure preparation and writing were done by **Antranik Jonderian. Ethan Anderson** synthesized the tetragonal lithium lanthanum zirconate. **Shipeng Jia** and **Victor Teodor Cozea** prepared the combinatorial cell for the electrochemical stability window experiment.

Chapter 3

Data treatment, figure preparation and writing were done by **Antranik Jonderian. Michelle Ting** performed the X-ray photoelectron spectroscopy (XPS) measurements and analysis.

Chapter 4

Data treatment, and figure preparation were done by **Rui and Antranik Jonderian**

Antranik Jonderian wrote the manuscript**. Rui Peng** and I equally contributed to the synthesis, characterization, and data analysis. **Danielle Davies** prepared the cations solutions for the substitution experiments**.**

Chapter 5

Data treatment and figure were prepared by **Shipeng Jia, and Antranik Jonderian. Dr. Eric McCalla, Shipeng Jia and Antranik Jonderian** contributed to the writing. **Shipeng Jia** prepared the combinatorial cells and performed the electrochemical analysis. He and I contributed equally to this project. **Victor Teodor Cozea** assisted in the experimentation and data analysis. **Gabin Yoon** performed the DFT calculations. **Sang Bok Ma** provided guidance.

Contribution to original knowledge

In this thesis, we have developed a suite of tools that allows for the high-throughput synthesis and screening of bulk-type solid electrolytes for all-solid-state batteries. While previous tools have been developed for screening solid electrolytes, they are limited to thin films and only screen for room temperature conductivity. This is insufficient for predicting the final performance of solid electrolytes in all-solid-state batteries. Our suite is the first report of a complete set of high throughput tools for screening all the essential properties of bulk-type solid electrolytes, which includes charge transport properties (electronic and ionic conductivity and activation energy of lithium diffusion), as well as the electrochemical stability window.

The lithium lanthanum titanate (LLTO) solid electrolyte with perovskite structure has been studied for many years, but there is still much to be explored and understood about its composition-structure-property relationship. While it shows promising bulk ionic conductivity, its total conductivity is constrained by grain boundary conductivity and it is also unstable at low potentials. Our developed high-throughput method allowed us to comprehensively study the composition-structure-property relationship of the LLTO system across a broad range of compositions. Unlike previous studies that only examined single compositions along the LLTO composition line, our suite enabled us to thoroughly map the compositions around this line. Our findings using this methodology revealed that LLTO is in fact a metastable state, which was previously unknown due to the neglect of trace amounts of secondary phases

Researchers have attempted to enhance the conductivity of LLTO through substitutions. However, comparing the results of these independent investigations has proven difficult, as each study employed different substitution levels, synthesis methods, and testing conditions. This makes it challenging to systematically identify the role of each substitution and there may be missed substitutions/levels that were never tried. Moreover, not all properties are measured in these studies; mostly only the ionic conductivity is measured. It is important to note that assessing the performance of these substituted LLTOs based only on one property is not enough. We performed a systematic investigation to assess the impact of 50 different substitutions at varying levels on ionic and electronic conductivities, the activation energy for ionic conduction, and the electrochemical stability window using our high-throughput suite. By conducting our investigation under identical synthesis and testing conditions, we were able to make valid comparisons and draw robust conclusions.

The LLTO that we developed enables the use of $LiCoPO_4$, a high-voltage cathode with an olivine structure that is incompatible with current carbonate-based liquid electrolytes. $LiCoPO_4$ suffers from low ionic and electronic conductivities, which have prompted numerous investigations aimed at improving its performance. However, despite these efforts, the performance of LCP has remained suboptimal. To address this, we systematically screened 46 single and co-substitutions to enhance $LiCoPO_4$ performance. We achieved state-of-the-art material through co-substitution by utilizing a high-throughput approach. Furthermore, we conducted complementary experiments and computational studies, which provided valuable insights into the mechanisms responsible for the improved performance.

In light of the fact that all the synthesis and testing were carried out under identical conditions, the extensive data gathered from our study (>2000) is suitable for utilization in machine learning to steer forthcoming research endeavors. This would enable us to expand our understanding and improve our predictions in the field.

List of figures

Figure 1.1 Forecasted global battery usage by application between 2020 and 2030. Reproduced with permission from ref. [4]. 1
Figure 1.2 Timeline of batteries development. Reproduced with permission from ref. [7]. 2
Figure 1.3 (a) Schematic diagram of conventional lithium-ion battery with intercalation/de-intercalation electrodes and a liquid electrolyte. Reproduced with permission from ref.[10]. (b) The electrode potential is composed of both ionic and electronic contributions. Reproduced with permission from ref. [8]. 4
Figure 1.4 Potential vs. specific capacity of various positive electrodes. The dashed line corresponds to the oxidative potential limit of 1 M $LiPF_6$ in EC/DEC (1:1) electrolyte. Reproduced with permission from ref. [19]. 5
Figure 1.5 Radar plots showing the properties of different types of electrolytes for lithium battery: (a) liquid electrolytes, (b) polymer electrolytes, (c) oxide electrolytes, (d) sulfide electrolytes, and (e) ideal electrolytes. Reproduced with permission from ref. [26]. 8
Figure 1.6 Mechanisms of lithium diffusion in solid electrolytes. Reproduced with permission from ref.[27]. 9
Figure 1.7 Structure of LLTO and the energy barrier window made of 4 oxygens. Reproduced with permission from ref. [59]. 19
Figure 1.8 (a) Nyquist plot for EIS spectrum of solid electrolyte shown with the equivalent circuit. The dots are the EIS data, and the red line is the fit. (b) Current vs time plot under applied constant voltage for electronic conductivity measurement. The electronic resistance is calculated by Ohm's law from the steady state current. Reproduced with permission from ref. [77]. 23
Figure 1.9 Electrochemical stability window CV tests in Li/LGPS/Au configuration (a) and by preparing electrode in Li/LGPS/LGPS-Pt/Pt configuration (b). Due to sluggish ionic and electronic kinetics the stability window is overestimated in Li/LGPS/Au configuration. Reproduced with permission from ref. [78, 79]. 24
Figure 1.10 EIS spectra of a symmetric Li/Nb-LLZO/Li cell demonstrate the variation of impedance over 72 hours as a result of the electrolyte and Li metal interaction. The inset shows the assignment of the different features of the EIS spectrum. Reproduced with permission from ref.[80]. 25
Figure 1.11 Classification of intercalation-deintercalation cathodes for lithium-ion batteries and the lithium motion dimensionality in each. Reproduced with permission from ref. [82]. 26
Figure 1.12 (a) Various possible configurations of antisite exchange pairs in $LiFePO_4$. Reproduced with permission from ref. [83]. (b) 1st discharge capacity of different sized $LiFePO_4$ particles. Reproduced with permission from ref. [84]. (c) Discharge capacity of bare $LiFePO_4$ and carbon coated by various organic reagents. Reproduced with permission from ref. [85]. 27
Figure 1.13 (a) Combinatorial cell for screening battery materials 64 samples at a time. (b) CV data from 64 samples checkerboard made of two cathode materials showing reproducibility. Reproduced with permission from ref. [92]. 30

Figure 2.1 High-throughput structural and electrochemical characterization tools for solid electrolyte discovery and screening. All measurements are performed on 64 samples at once and result in the properties shown in the radar plot: room temperature ionic conductivity (σ_{ionic}), activation energy (E_a), electronic conductivity ($\sigma_{electronic}$), stability at low voltage (LV) and high voltage (HV). Each measurement is shown in greater detail throughout this manuscript. 43

Figure 2.2 The scheme of the high-throughput synthesis and structural/chemical/electrochemical characterization of solid electrolytes. Precursors are first dispensed into 64 alumina cups, then preheated with an aluminum plate to prevent mixing, samples are then pelletized in high-throughput, sintered to high temperature on alumina plates. Prior to conductivity tests, pellets are coated with gold, then assembled in the house-made cell with spring mounted contacts. After conductivity measurements, samples are crushed into powders and XRD is performed. Finally, the powders are mixed into slurries to make electrodes for the electrochemical stability tests on aluminum for HV, and on gold for LV. 44

Figure 2.3 Nyquist plots of identical LLTO samples measured on Au/LLTO/Au cell using EIS at (a) 22 °C, and (b) 50 °C. The red lines are the fits to the equivalent circuit. From the fits, ionic conductivity and activation energy are extracted and presented in **Table 2.1**. 48

Figure 2.4 (a) DC polarization curves for 64 identical LLTO samples and a single LLZO sample (inset) measured in Au/SE/Au cell configuration. (b) The average steady state current (I_e) for the LLTO samples vs the applied DC voltage. The inset is a zoom-in on the Ohmic region. 51

Figure 2.5 (a) CV profiles of identical LLTO samples (blue), LLZO samples (red) and blank (carbon black and PVDF only, black) swept from 3 V down to 0.1 V at 0.1 V/h scan rate. The solid electrolytes were made into electrodes as described in the text for this electrochemical stability window test. (b) CV profiles from 3-5.5 V at 0.1 V/h scan rate in a half cell configuration with the solid electrolytes made into electrodes for electrochemical stability window test. Both sets of CVs were run for 1.5 cycles. 53

Figure 2.6 Electrochemical stability of LLTO and LLZO at low and high voltage from Figure **2.5**, overlayed for comparison. The CVs of same composition LLTO, LLZO, and blank cycled as cathodes shows the accuracy of the tool. The arrow indicates the feature that appeared on the first cycle. The stability windows in Table **2.1** were extracted from this data. 54

Figure 2.7 The EIS spectra evolution as a function of time after contact with lithium. The Nyquist plots are shown for LLTO (the inset is an expanded view of the high frequency region) (a) and LLZO (b) in the asymmetric configuration Li/SE/Au. 55

Figure 3.1 (a) The structure of perovskite LLTO, with the oxygen window representing the barrier to Li diffusion indicated in yellow and the path followed by lithium as a black arrow. (b) The Li-La-Ti-O pseudo-ternary phase diagram with the previously studied compositions by both computational means (the materials project, MP) and experiment. (c) The compositions studied during this study. The axes are Li, La, and Ti metal molar fractions. The triangle defined by the three points T_1, T_2 and T_3 represents the triplicate region (all three of the Li, Ti and La corner plates contain these triplicates) and serves as verification that the synthesis is consistent between plates. 65

Figure 3.2 The complete phase stabilities obtained by quenching from 1200 °C. The red dashed lines are tie-lines, the black line represents the $Li_{3x}La_{(2/3)-x}TiO_3$ composition line (note that this is not a solid solution), and the blue oval shows the region of stabilization of the LLTO-TiO_2 composites discussed throughout the text. (b) The corresponding complete phase stabilities for samples obtained by slow cooling from 1200 °C. (c) The compositions obtained for slow cooling: the black points are the as-dispensed compositions while the red symbols are the compositions after synthesis as measured by ICP-OES. The lines shown that extrapolates back to the Li corner indicates Li loss during synthesis, and the gray region represents the part of the composition space showing extreme Li loss. 73

Figure 3.3 Molar phase fractions obtained with Rietveld refinement for samples made by heating at 1200 °C for 6 h and slow cooling. Includes results for all samples except those made in the zoomed-in region. The red stars indicate the single-phase compositions in each contour. The white lines correspond to the two-phase regions and are corrected for the lithium loss (from ICP-OES). 74

Figure 3.4 Molar phase fractions obtained with Rietveld refinement for samples made by heating at 1200 °C for 6 h and quenching. Includes results for the $TiT_1T_2T_3$ plate only. This serves to better understand how the LLTO phases are stabilized at high temperature. The red stars indicate the single-phase compositions in each contour. The white lines correspond to the two-phase regions and corrected for the lithium loss (from ICP-OES). 75

Figure 3.5 Powder XRD patterns of samples along the composition line with various fractions of LLTO. The compositions are shown as metal molar fractions: (Li,La), where the titanium fraction is Ti = 1-Li-La. The legend shows contaminant peaks present, all other peaks index well to the perovskite LLTO phases. The compositions A,B,C, and D have increasing lithium content as shown in Figure **3.8** and the fits for these patterns are included in Figures **S3.2** and **S3.3**. 77

Figure 3.6 Phase maps for the TiO_2 molar fraction obtained by heating at 1200 °C for 6 h and then quenching (a) or slow cooling (b). The red points represent the result of using the lever rule on all samples that showed co-existence between TiO_2 and LLTO (each sample yields 1 red point). The labels E, F and G correspond to the points with highest LLTO content in Figures **3.3** and **3.4** and are used in the main text to discuss the significance of these results. 78

Figure 3.7 Phase maps obtained in the zoomed-in LLTO region of the phase diagram after heating at 1200 °C for 6 h and then either quenching (a) or slow cooling (b). The black line represents the $Li_{3x}La_{(2/3)-x}TiO_3$ composition line. The highest LLTO content in quenched samples is 93% while 96% in the slow cooled. 79

Figure 3.8 The contour map of the a, b and c lattice parameters as a function of composition in the zoomed-in plates discussed in Figure **3.7** Phase maps obtained in the zoomed-in LLTO region of the phase diagram after heating at 1200 °C for 6 h and then either quenching (a) or slow cooling (b). The black line represents the Li3xLa$_{(2/3)\text{-xTiO3}}$ composition line. The lattice parameters are reported as pseudo cubic (conversions shown in Table **S3.1**). 82

Figure 3.9 EIS spectra obtained in the zoomed-in LLTO region for samples heated at 1200 °C for 6 h and then slow cooled to room temperature. The four corners are labeled by compositions using molar metal fractions: (Li, La) where Ti = 1 – Li – La. The red lines are the results of fitting as described in the main text and the dots are the EIS data. 84

Figure 3.10 EIS spectra obtained in the zoomed-in LLTO region for samples heated at 1200 °C for 6 h and then slow cooled to room temperature. The spectra are zoomed-in (high frequency region) in order to show the bulk contributions to the EIS data. The dots are the EIS data, and the red lines are the fits. 85

Figure 3.11 The contour map of bulk and total ionic conductivities of quenched (a) and slow cooled (b) samples after heating to 1200 °C for 6 h extracted by fitting the EIS spectra. The line indicates $Li_{3x}La_{2/3-x}TiO_3$ composition line. 86

Figure 3.12 SEM images of 6 pellets made at each of compositions H, I and J from Figure **3.11**, and either synthesized at 1200 °C in either air or oxygen. Below each image, we include the average total conductivity values obtained by making 8 replicates, as well as the average relative densities. 87

Figure 4.1 XRD patterns of undoped, 10% Al, 6%Mn and 3%Ni with reference patterns at the bottom of LLTO and TiO_2. Inset: zoomed-in region at the low angles where only LLTO peaks and a TiO_2 peak near 27.5° are seen. The red asterisk indicates the TiO_2 Phase. The goodness of fit $\chi^2$is reported at the center. 118

Figure 4.2 Perovskite phase fraction in 3% (a) and 6% (b) substitutions. The red dashed line indicates the perovskite content in unsubstituted samples. A lot of substitutions show improved perovskite stabilization. Red asterisks indicate samples that were not made. The samples with 3%Si and 3%W substitution were stuck on the alumina plate. 1-c/a indicating how much close to perfect cubic the perovskite is (c). The red dashed line indicates the 1-c/a of substituted LLTO. 120

Figure 4.3 Perovskite weight fraction at 3%, 6%, 15%, and 20% substitution levels vs. BVM on the Ti-site. Some substituents with large BVM still manage to incorporate into the structure. The BVM on the La-site is depicted in Figure **S4.3a**. 122

Figure 4.4 Transport properties: bulk conductivity (a), grain boundary conductivity (b) and electronic conductivity (c) for 5 substitution levels. The red dashed line corresponds to the unsubstituted sample. 123

Figure 4.5 Grain boundary conductivity changes by the fraction of substituted perovskite. Substitutions affected the grain boundary conductivity in pure perovskite and by introducing secondary phases. 125

Figure 4.6 Electrochemical stability at the low potential limit for unsubstituted, 6% Fe and 20% Mg substitutions (a) at the high potential for unsubstituted, and 20% Cr substituted sample (b). (c)The low stability limit potential (extracted from CVs) of 50 substituents at 5 different substitution levels in LLTO with the dashed line corresponding to the unsubstituted sample... 127

Figure 5.1 (a) Workflow for the current study where high-throughput (HT) synthesis/characterization is used to screen cathode materials, followed by traditional experiments/computations to motivate further HT tests. (b) XRD (the fits in red and the difference plots in blue), (c) CV, and (d) corresponding voltage curve of the undoped sample made at 850 °C show limited capacity and high overpotentials, while the Li diffusion path in the undoped is shown in (d). (e) Pictures of the $Li_yCo_{0.9}M_{0.1}PO_4$ samples after heating in air to 750 °C (prior to carbon coating). 150

Figure 5.2 SEM images of unsubstituted LCP along with 10% In-doped, as well as In/Mo and In/Nb co-doped samples. In all cases the images are representative. The scale bar applies to all four SEM images. The zoomed-out SEM image of the In/Mo substituted LCP is depitcted in Figure **S5.11**. 151

Figure 5.3 XRD results for single dopant samples heated at 850 °C and carbon coated. Top: two representative XRD patterns along with the fits in red and the difference plots in blue. The * indicates small peaks corresponding to the unidentified phase in the In-doped sample. Lower: extracted values for molar phase % of the olivine LCP phase, * indicates the presence of an unidentified phase, x (the calculated x-value in $Li_yCo_{1-x}M_xPO_4$ as detailed in Table **S5.2**), and the shift in lattice parameters with respect to the undoped samples (standard deviations in undoped duplicates were less than 0.0002 Å)**.** 153

Figure 5.4 Results of the high-throughput electrochemical testing on the $Li_yCo_{0.9}M_{0.1}PO_4$ samples prepared at 850 °C in air prior to carbon coating. Representative CVs (a-d) and corresponding voltage curves (e-h) are shown. The properties extracted for the first cycle are shown in (i,j) while (k) shows the retention after 10 cycles. The grey dashed line in (j) indicates the discharge capacity of the undoped sample as a reference. While a number of samples show significantly improved capacities, the retention continues to be poor. 154

Figure 5.5 Results for In-doped samples with varying In content. The XRD results in (a) yield the shifts in lattice parameters shown in (b). Phase pure materials are obtained below 10% In substitution. The resulting electrochemical data is shown in (c) along with the theoretical capacities assuming electrochemically inactive In. The blue and orange bars correspond to the 1st and 10th discharge specific capacities, respectively. The yellow dots correspond to the capacity retentions after 10 cycles. (d) Results of DFT calculations for the energy barriers of Li diffusion along the paths indicated in the structure, the position of the In atom and Li vacancy are also shown. 156

Figure 5.6 Battery properties extracted for the $Li_yCo_{0.9}In_{0.05}M_{0.05}PO_4$ samples. The first cycle average voltages and capacities are shown in (a), (b), respectively. (c) shows capacity retention after 9 cycles, while (d-e) show the capacities and average voltages vs. cycle number for a selection of samples with a particularly high capacity retention. The blue and orange bars in (c) correspond to the 1st and 9th discharge specific capacities, respectively. 159

Figure 5.7 Results of optimization of co-doping with indium. Results of DFT calculations (a) show which dopants are most effective in suppressing Li/Co antisite defects. The first cycles of CVs for various co-doping with either Mo (b) or Nb (c) are shown, while (d,e) show the corresponding capacity retentions after 10 cycles as dots. The dark blue and brown bars are the 1st discharge specific capacity while the light blue and brown bars are the 10th cycle discharge specific capacity. 160

List of tables

Table 1.1 Substitutions in LLTO. Reproduced with permission from ref. [60]........................... 20

Table 2.1 Ionic conductivity, activation energy, electronic conductivity, and electrochemical stability window of LLTO and LLZO, all obtained using our high-throughput methods in this study and compared to results from traditional studies in the literature. The uncertainties on all values from this study are the standard deviations on the measurements and therefore represent the precisions of the high-throughput techniques developed here... 49

Table 4.1 Stoichiometry of 3% and 6% Ti-site substituted samples. Empty cells indicate samples that were not made.. 121

Table 5.1 Ionic and electronic conductivities measured on cold pressed pellets of various LCP samples. The electronic conductivity was determined using DC measurements in a Au/LCP/Au configuration as per ref. [37]. The ionic conductivities were extracted by fitting the EIS spectra with an equivalent circuit for a mixed conductor (the second conductor corresponding to the electronic conductivity, the extracted value from EIS matched that from DC measurements as expected). Typical patterns of each are shown in Figure **S5.8**. Carbon coated samples are denoted with @C.. 157

List of abbreviations

BVM	bond valence mismatch
CB	carbon black
CV	cyclic voltammetry
COD	crystallography open database
DFT	density functional theory
DMC	dimethyl carbonate
EBSD	electron backscatter diffraction
EC	ethylene carbonate
EDS	energy-dispersive X-ray spectroscopy
EELS	electron energy loss spectroscopy
EIS	electrochemical impedance spectroscopy
ESW	electrochemical stability window
EV	electric vehicle
FWHM	full width half maximum
HAADF-STEM	high-angle annular dark-field scanning transmission electron microscopy
HOMO	highest occupied molecular orbital
ICP-OES	inductively coupled plasma optical emission spectroscopy
ICSD	inorganic crystal structure database
LCP	$LiCoPO_4$
LE	liquid electrolyte
LFP	$LiFePO_4$
LiPON	lithium phosphorus oxynitride ceramic solid electrolyte
LISICON	lithium superionic conductors
LLTO	lithium lanthanum titanate
LLZO	lithium lanthanum zirconate
LUMO	lowest unoccupied molecular orbital
M	metal cation
NASICON	sodium superionic conductors
NMP	N-Methyl-2-pyrrolidon

PC	propylene carbonate
PE	polyethylene
PP	polypropylene
PVDF	polyvinylidene fluoride
SE	solid electrolyte
SEI	solid electrolyte interphase
SEM	scanning electron microscope
TEM	transmission electron microscopy
TM	transition metal
XAS	X-ray absorption spectroscopy
XPS	X-ray photoelectron spectroscopy
XRD	X-ray diffraction

List of Symbols

Symbol	Unit	Meaning
σ	S cm^{-1}	conductivity
σ_e	S cm^{-1}	electronic conductivity
σ_b	S cm^{-1}	bulk ionic conductivity
σ_{gb}	S cm^{-1}	grain boundary ionic conductivity
A	cm^2	area of gold contact
l	cm	thickness of pellet
E_a	eV	activation energy
$E_{a, b}$	eV	activation energy for bulk conduction
$E_{a, gb}$	eV	activation energy for grain boundary conduction
σ_0	S cm^{-1} K^{-1}	pre-exponential factor
k	eV K^{-1}	Boltzmann constant
ρ	Kg m^{-3}	density

Chapter 1

Introduction

Lithium-ion batteries have become essential in our daily lives, powering many of our portable electronics. They are considered one of the best options for efficiently storing electrical energy (97% energy efficiency at 2 hours charge/discharge rate compared to 40% - 60% for current fuel cells[1]) by directly converting electrical energy into chemical energy and back again. As we increasingly rely on intermittent renewable energy sources like solar and wind, energy storage devices are necessary for storing excess energy and releasing it when needed. Lithium-ion batteries have emerged as a promising candidate for grid stationary storage.[2] They have recently been used more extensively in electrifying transportation to reduce our dependence on fossil fuels. However, current electric vehicles (EVs) require lithium-ion batteries with higher energy density, improved safety, and lower costs to compete with internal combustion automobiles.[3] The demand for such batteries is growing exponentially (Figure **1.1**),[4] reflecting our continued commitment to reducing our reliance on fossil fuels and transitioning towards a more sustainable energy future.[5]

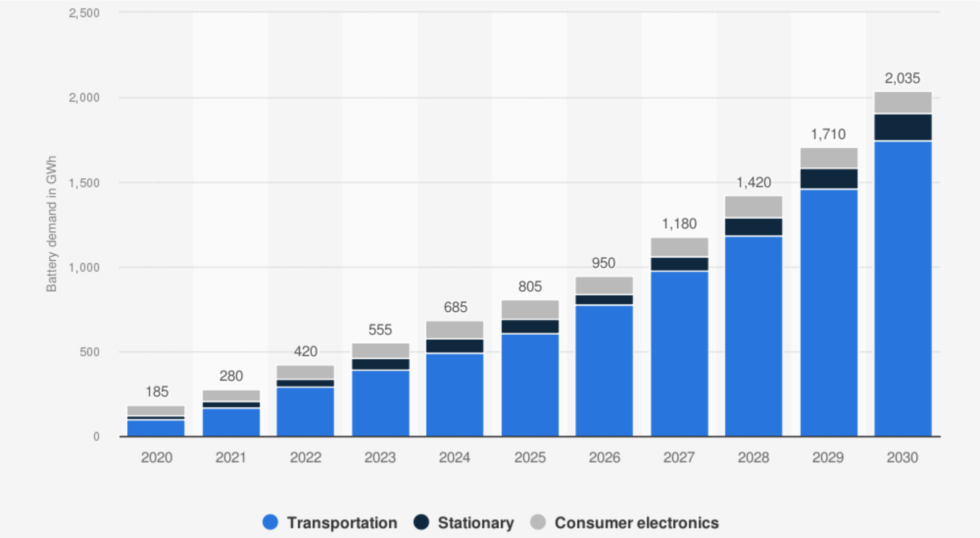

Figure 1.1 *Forecasted global battery usage by application between 2020 and 2030. Reproduced with permission from ref. [4].*

1.1 Evolution of battery technology

The timeline of batteries development *Figure **1.1*** can be traced back to 1800 A.D. when Alessandro Volta discovered the first primary battery that could be discharged but not recharged due to the irreversible electrochemical reactions that occurred within it. However, in 1859, French physician Gaston Planté invented the first rechargeable battery based on lead acid.[6] This breakthrough paved the way for developing secondary batteries, which could be recharged and used multiple times. It was not until the groundbreaking work of John Goodenough, Stanley Whittingham, and Akira Yoshino that the modern lithium-ion battery was developed, leading to its commercialization by Sony in 1991. These three inventors were awarded the Nobel Prize in Chemistry in 2019 for their contributions to developing this revolutionary technology. The lithium-ion battery has a significantly higher energy density than earlier rechargeable batteries due to its low mass and low redox potential (high cell voltage). This has made it a preferred choice for various applications, from portable electronics to electric vehicles and stationary energy storage

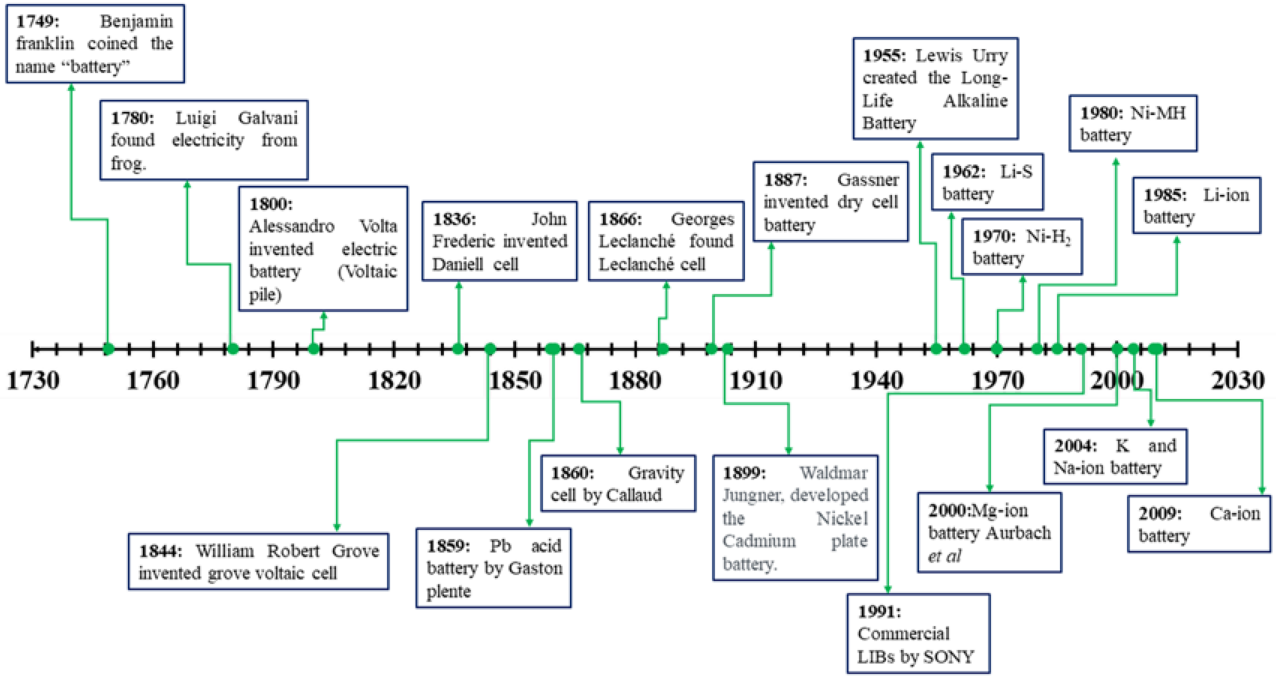

Figure 1.2 *Timeline of batteries development. Reproduced with permission from ref. [7].*

systems. As research into battery technology continues, it is expected that even more advanced and efficient batteries will be developed, further revolutionizing how we store and use energy.

1.2 Principles of lithium-ion batteries

A lithium-ion battery consists of a cathode and anode separated by a polyolefin membrane such as polypropylene (PP) and polyethylene (PE) containing a liquid electrolyte as shown in Figure **1.3**a. During charging, the redox-active metal in the cathode undergoes oxidation by sending electrons to the anode via the external circuit and lithium ions through the electrolyte. Simultaneously, the anode undergoes reduction by incorporating lithium ions from the electrolyte. The reverse processes occur during discharge, where the cathode undergoes reduction and the anode undergoes oxidation, resulting in lithium ions from the electrolyte and electrons from the external circuit returning to the cathode. The voltage in a lithium cell is due to the difference in lithium electrochemical potential between the two electrodes. The electrochemical potential of a lithium-ion is made up of both ionic and electronic contributions. The electronic contribution is mainly determined by the Fermi energy of the host structure, while the ionic contribution depends on the occupancy of lithium-ion sites as illustrated in Figure **1.3**b.[8] The energy density of a lithium-ion battery is determined by multiplying the charge of lithium ions that can be stored in the electrodes (capacity) by the potential difference between the cathode and anode.

The most common current generation of lithium-ion batteries uses graphite as the anode and a layered metal oxide as the cathode. The liquid electrolyte facilitates the movement of lithium ions between the anode and cathode while preventing the flow of electrons. The liquid electrolyte consists of a lithium salt, such as $LiPF_6$ or $LiClO_4$, dissolved in an organic solvent, such as ethylene carbonate (EC), dimethyl carbonate (DMC) or propylene carbonate (PC). [9] The movement of lithium ions in the electrolyte is driven by the concentration gradient and electric field between the electrodes through diffusion and migration, respectively.

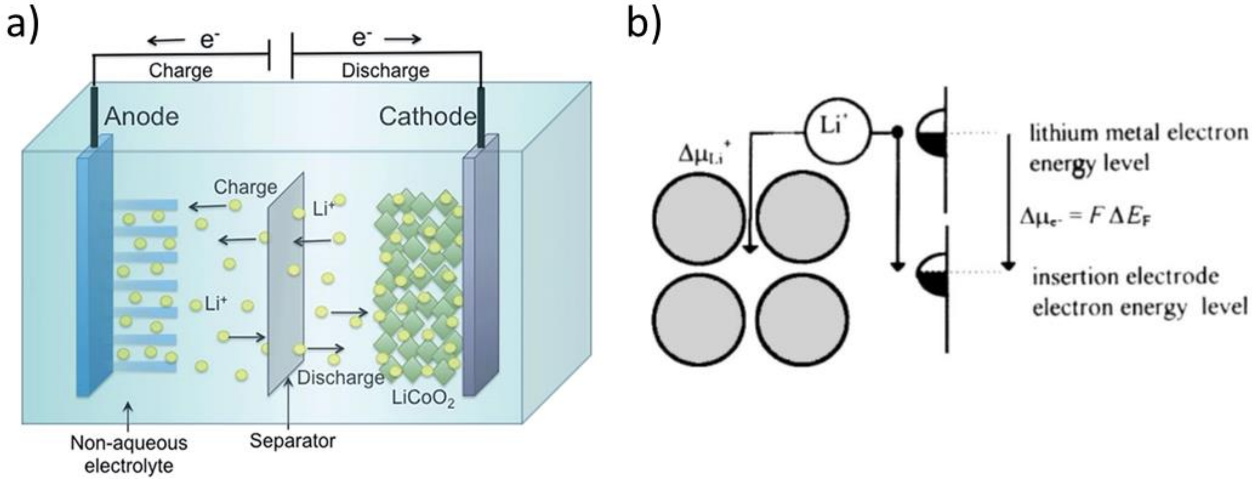

Figure 1.3 *(a) Schematic diagram of conventional lithium-ion battery with intercalation/de-intercalation electrodes and a liquid electrolyte. Reproduced with permission from ref.[10]. (b) The electrode potential is composed of both ionic and electronic contributions. Reproduced with permission from ref. [8].*

1.3 Liquid electrolytes

The electrochemical stability window (ESW) is the range of potentials where the electrolyte can operate without decomposing. The lower and upper limits of the ESW are determined by the HOMO (highest occupied molecular orbital) and LUMO (lowest unoccupied molecular orbital) energy levels of the salt and solvent in the liquid electrolyte. A conventional liquid electrolyte has high ionic conductivity, around 11.5 mS cm^{-1} for 1M LiPF$_6$ in a 1:1 EC:DMC mixture,[11] and wets the electrodes well, but it has a limited ESW (1V[12] - 4.2V[13]) that restricts the types of electrodes that can be used as shown in Figure **1.4**. This intrinsic thermodynamic ESW can be extended by the formation of a solid electrolyte interphase (SEI), an electronic insulator, on both electrodes when the electrolyte is exposed to potentials outside the ESW. The SEI layer acts as a barrier between the electrode and electrolyte, slowing down the reaction rate. The properties of the SEI layer can affect the performance of the lithium battery. The performance of a lithium-ion battery can be improved by additives that can help engineer the nature SEI. Additionally, liquid electrolytes can leak, are flammable, and do not prevent dendrites growth across the separator when used with lithium metal or at high charging rates which can cause internal short circuits. Furthermore, liquid electrolytes contribute indirectly (solid electrolyte interphase can decompose at temperatures as low as 57°C) to the start of thermal runaway[14] where a sequence of exothermic reactions causes an exponential temperature increase and ultimately ignites the electrolyte. Therefore, current batteries require cooling and a thermal management system to keep them below 50°C to prevent thermal runaway[15] and capacity loss[16] caused by SEI decomposition at elevated temperatures. Besides, liquid electrolytes can facilitate the dissolution of transition-metal (TM) cations[17] and polysulfides[18] from the cathode material into the liquid electrolyte, which can then deposit onto the anode impeding the performance of the battery. Replacing the liquid electrolyte with a solid electrolyte can solve some of these problems but also brings challenges.

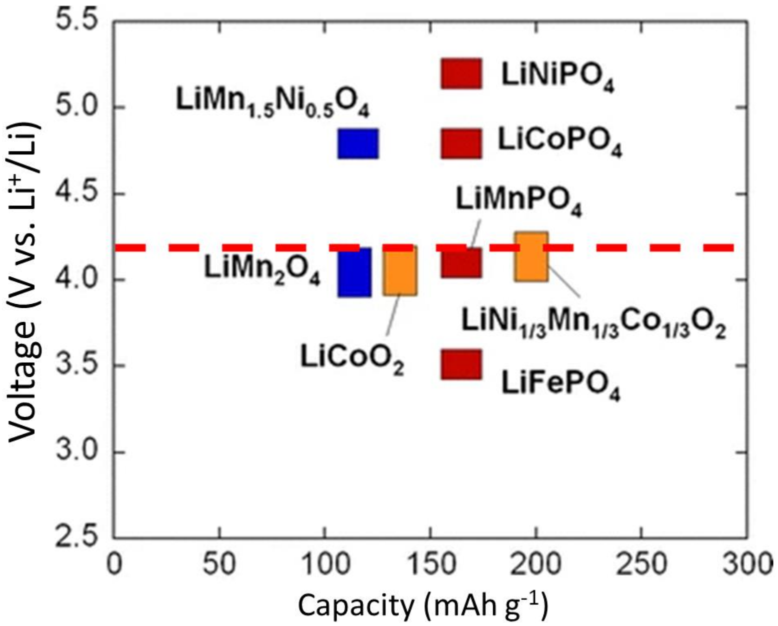

Figure 1.4 *Potential vs. specific capacity of various positive electrodes. The dashed line corresponds to the oxidative potential limit of 1 M* $LiPF_6$ *in EC/DEC (1:1) electrolyte. Reproduced with permission from ref. [19].*

1.4 Solid electrolytes

Solid electrolytes have emerged as a promising alternative to liquid electrolytes in lithium batteries, mainly due to their potential to enhance safety and increase energy density. To effectively integrate solid electrolytes into all-solid-state batteries, they must possess certain characteristics presented in Figure **1.5**. First, the ionic conductivity of the electrolyte must be high, ensuring low internal resistance and facilitating fast charge and discharge rates. Ideally, the ionic conductivity should be above 10^{-4} mS cm^{-1}.[20] Additionally, the electronic conductivity of the electrolyte should be low to prevent self-discharge of the battery and dendrite growth from the bulk of the electrolyte. Dendrite growth was observed nucleating from the bulk of the electrolyte at electronic conductivities as low as 2.2×10^{-9} S cm^{-1} at room temperature.[21]

Furthermore, the electrolyte must possess a wide electrochemical stability window (cathodic and anodic stability shown in Figure **1.5**) to prevent electrolyte decomposition and ensure long-term battery stability, especially when used with low-potential anodes and high-potential cathodes to maximize energy density. It is preferable for the electrolyte to be stable against lithium metal, which has the highest specific capacity and lowest potential among anodes. The use of metallic lithium as an anode can significantly increase the energy density of the battery. Moreover, the electrolyte should have good mechanical properties, such as high stiffness, to withstand the stresses applied by the volume expansion of the electrodes and prevent the formation of cracks. Finally, the solid electrolyte must be compatible with the electrodes to prevent unwanted side reactions and effectively wets them to promote good electrolyte/electrode interfacial contact and reduce interfacial resistance. Maintaining a stable and low-resistance interface between the solid electrolyte and electrodes is crucial for efficient ion transport and long-term stability. In addition to having a good compatibility with electrodes, solid electrolytes must also have high thermal stability to prevent thermal runaway and ensure the safe operation of batteries, as well as to improve the performance and reliability of batteries in high-temperature environments. Aside from the technical characteristics, the final commercial viability of solid-state batteries will also depend on other factors such as ease of processability and cost-effectiveness of the solid electrolyte material. The development of solid electrolytes with the properties mentioned above is crucial for the advancement of high-performance and safe all-solid-state batteries.

Solid electrolytes are categorized into inorganic and organic. Figure **1.5** displays performance radar plots of different families of electrolytes, highlighting their strengths and limitations. Organic solid electrolytes include polymers with salts,[22] single-ion conducting polymers (anionic polymer),[23] and organic ionic plastic crystals.[24] Polymer electrolytes, as shown in Figure **1.5**b, form better interfacial contact with electrodes and are easier to process (e.g. extrusion) than inorganic solid electrolytes due to higher deformability. Furthermore, polymers are more stable than liquid electrolytes at low potentials, allowing for the use of lithium metal. However, they suffer from low ionic conductivity and high potential instability. Polymer electrolytes have been commercialized and are used in some EVs, such as in the Bluecar manufactured by Bolloré, where the battery operates at temperatures between 50-80 °C and uses a lithium metal anode and a vanadium oxide cathode. One drawback of polymer electrolytes is their low room-temperature conductivity, such that heating is required.

Inorganic solid electrolytes can be classified as either ceramic or glassy. Solid-state batteries with lithium phosphorus oxynitride ceramic solid electrolyte (LiPON) are commercially available. Due to the low ionic conductivity of LiPON, it is used only as thin films in microbatteries. STMicroelectronics produces commercial microbatteries using LiPON with a lithium metal anode and $LiCoO_2$ cathode. There are currently no commercially available bulk solid-state batteries with inorganic solid electrolytes. Other hybrid concepts, such as ceramic-polymer and gel (polymer with Liquid) electrolytes, are also being investigated.[25]

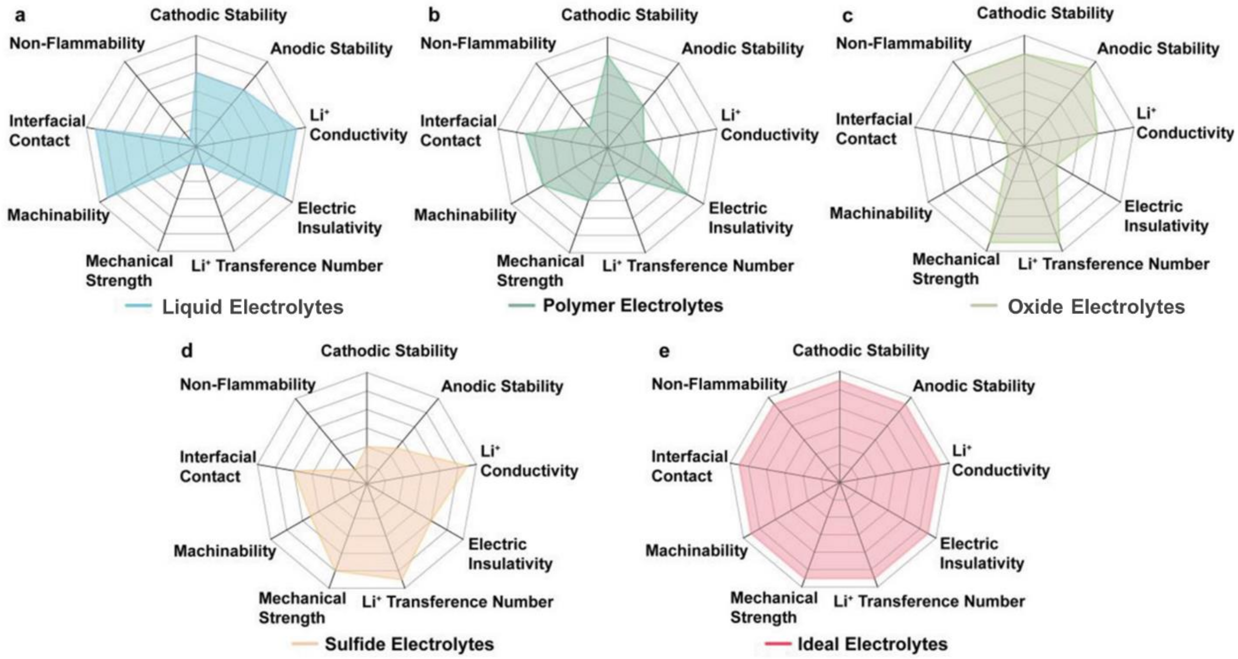

Figure 1.5 *Radar plots showing the properties of different types of electrolytes for lithium battery: (a) liquid electrolytes, (b) polymer electrolytes, (c) oxide electrolytes, (d) sulfide electrolytes, and (e) ideal electrolytes. Reproduced with permission from ref. [26].*

Lithium migration in ceramic solid electrolytes has three main mechanisms shown in Figure **1.6**: vacancy diffusion, direct interstitial mechanism, and concerted or correlated interstitial (knock-on) mechanism. In the latter mechanism, the migrating interstitial ion displaces a neighboring lattice ion into the adjacent site. The ionic conductivity (σ) of the electrolyte is proportional to the concentration of the charge carrier (n) and lithium mobility (μ) described by the following equation:

$$\sigma = n\mu e \tag{1}$$

where e is the charge of an electron.

Mobility determines the ability of the Li ion to move within the solid electrolyte, which correlates to the activation energy (the highest energy along the lithium path) required for lithium movement. The lithium mobility in certain solid electrolytes containing polyanionic moieties (e.g. SO_4^{2-} and PO_4^{3-}) is assisted (activation energy of lithium conduction lowered) by the rotations of these groups, referred to as the paddle-wheel effect.

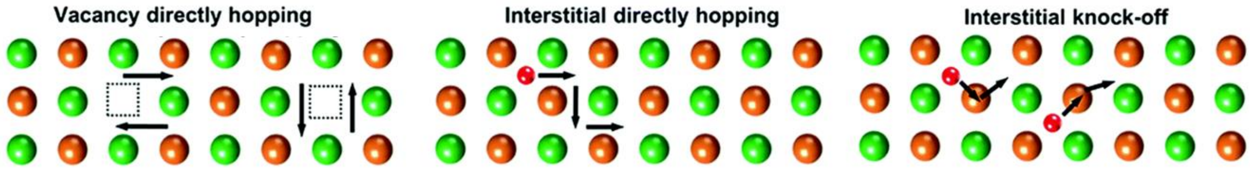

Figure 1.6 *Mechanisms of lithium diffusion in solid electrolytes. Reproduced with permission from ref. [27].*

1.4.1 Inorganic solid electrolytes

Inorganic solid electrolytes have enormous potential to revolutionize energy storage technology by providing a high electrochemical stability window. This allows the use of low and high potential cathodes, resulting in energy densities that cannot be achieved using current liquid electrolytes. The shear modulus is defined as the ratio of shear stress to shear strain. The bulk shear modulus of a polycrystalline solid electrolyte can be measured using acoustic impulse excitation, while the grain shear modulus can be determined through nanoindentation. Ceramic solid electrolytes, owing to their high shear modulus, can effectively inhibit dendrite formation, making them suitable for use with lithium metal as the anode.[28] Most importantly, their non-flammable nature can prevent thermal runaway, significantly enhancing safety. Inorganic solid electrolytes may allow the usage of certain cathode chemistries (such as $LiNi_{0.5}Mn_{1.5}O_4$,[29] or sulfur[30]) that are not compatible with current liquid electrolytes because it can prevent transition metal and polysulfide dissolution.

Inorganic solid electrolytes can be divided into various families, including oxides,[31] sulfides,[32] halides,[33] phosphides,[34] and hydrides,[35] with new structures continuously emerging.

1.4.1.1 Crystal Structure

The properties of solid electrolytes, including electronic and ionic conductivity, as well as their electrochemical stability window, are greatly influenced by the crystalline structure. Therefore, understanding the relationship between the crystal structure and these properties is crucial for the development and design of solid electrolytes.

The concept of a space group is used to describe the arrangement of atoms or ions in a crystal lattice. A space group represents the symmetry elements present in a crystal lattice, such as translations, rotations, reflections, and inversions. When combined, these elements generate the complete crystal structure. The International Tables for Crystallography (ITC) provides a systematic method for categorizing and describing space groups, assigning them unique symbols like Pm-3m or Fd-3m, which indicate the symmetry elements and arrangement of atoms or ions in the lattice.

Experimental techniques such as X-ray crystallography or neutron diffraction are used to determine the crystal structure. By determining the positions of atoms or ions within the lattice, the symmetry elements can be deduced, and the corresponding space group can be derived. This knowledge provides valuable insights into the pathways available for ionic movement in the crystal lattice. A crystal structure with suitable interstitial sites and open channels enables enhanced ionic conductivity due to facilitated ion migration. Additionally, the crystal structure influences the electronic band structure of the material, impacting its electronic conductivity. Moreover, the arrangement of atoms or ions and their bonding environment in the crystal lattice is critical in determining the electrochemical stability window of the material.

It is possible to optimize the properties of solid electrolytes, including electronic and ionic conductivity, as well as their electrochemical stability window by carefully selecting and designing crystal structures. Understanding the interplay between crystal structure and properties is fundamental in the pursuit of effective solid electrolyte materials.

Powder X-ray diffraction (XRD) is a technique used to measure the crystal structure of polycrystalline samples. The collected diffraction pattern is compared with database patterns to identify the phases present based on the 2theta diffraction peak positions and their relative intensities. Various parameters can be extracted from the diffraction data, including lattice parameters from peak positions, crystallite size from peak width, and site occupancy from peak area, providing valuable information about the sample.

The fitting process, known as Rietveld refinement, is employed to analyze the diffraction data and extract these parameters. The steps involved in the fitting process are as follows:

(1) Scaling factor: adjusting the intensity of the simulated pattern to match the experimental data.

(2) Background: modelling and subtracting the background contribution to the diffraction pattern, accounting for sources such as amorphous material or instrumental effects.

(3) Sample displacement: correcting for any positional errors (Z-position) in the sample during the experiment.

(4) Lattice parameters: fitting the lattice parameters of the identified phases to obtain accurate values.

(5) Peak full width at half maximum (FWHM): determining the peak width using the Caglioti formula, which considers the peak broadening with increasing 2theta.

(6) Peak shape: selecting an appropriate peak shape function (e.g., Gaussian, Lorentzian, or a mixed function) to accurately model the diffraction peaks.

(7) Site occupancies: estimating the relative site occupancies of different elements in the crystal structure by analyzing the peak areas. Constraints should be set when relaxing site occupancy values.[36]

By performing these steps and fitting the experimental data, we can gain insights into the phase content, lattice parameters, crystallite size, and other structural properties of the sample. This information is crucial for understanding the composition, crystal structure, and characteristics of materials studied using powder XRD.

1.4.1.2 Microstructure

Microstructure encompasses various material characteristics, including grain size, shape, orientation, packing (relative density), and grain boundaries. Each of these factors plays a significant role in determining the ionic conductivity of the solid electrolyte. Sintering is one of the factors that influence the microstructure.

Grain shape and orientation can impact the connectivity of the ionic pathways within the material. On the other hand, efficient packing with minimal void spaces (high relative density) can enhance ionic conductivity by providing continuous pathways for ion diffusion. Grain boundaries, which are the interfaces between adjacent grains, can significantly impact ionic conductivity. Grain boundaries may act as barriers to ion diffusion, impeding the transport of ions across the material. The nature of grain boundaries, including their structure, composition, and defect concentration, can either promote or hinder ion transport depending on their characteristics.

Understanding the relationship between microstructure and ionic conductivity is crucial for designing and optimizing solid electrolytes for all-solid-state batteries. It is possible to enhance ionic conductivity and improve the performance of solid electrolytes by tailoring the microstructural features, such as grain size, shape, orientation, packing, relative density, and grain boundaries

Sintering is a process in which powder particles fuse through diffusion reactions at temperatures below the melting point, leading to material densification. The driving force behind sintering is the reduction of interfacial free energy by replacing solid-gas interfaces with grain boundaries and decreasing the interfacial area per volume of grains through grain growth. Densification and grain growth are competing factors during sintering.[37]

In ceramics, grain boundary and surface diffusion are active at elevated temperatures. These types of diffusion involve similar atomic jumps as those occurring during the sintering process. Atoms moving across the boundary contribute to changes in grain size, while atoms moving along the boundary aid in densification. Surface diffusion occurs due to curvature reduction, while grain growth and grain boundary diffusion are driven by the reduction of grain boundary area and pore surface area, respectively. At the atomic scale, grain surfaces act as sources and sinks of material, with concave surfaces exhibiting higher energy and greater mobility than convex surfaces.[38]

Consequently, grain growth occurs as the grain boundary moves from the concave to the convex grain, while densification is achieved through mass diffusion along the grain boundaries to fill pores. Vacancies are generated at the pore surface (vacancy source) and diffuse from the pore to the grain boundary (vacancy sinks), where they are eliminated (collapsed) by short-range atomic forces. This collapse causes the center of mass of the grains to approach each other, resulting in densification.[39]

The stages of sintering encompass initial sintering, involving particle rearrangement and neck formation, followed by intermediate sintering, characterized by neck growth, pore reduction, and shrinkage. The final sintering stage entails eliminating pores closed in the grain bulk through volume diffusion, which is slower than grain boundary diffusion. The isolated pores elimination only occurs if the pore contains a soluble gas.[40]

Neck growth and coarsening of particles without densification can be attributed to vapor transport, surface diffusion, and lattice diffusion from the particle surfaces to the neck. Conversely, grain boundary diffusion, lattice diffusion from the grain boundary to the neck, and plastic flow contribute to neck growth and densification (shrinkage).[41] Three types of sintering exist solid-state sintering involving only a solid phase, liquid-phase sintering with a small amount of liquid phase, and viscous sintering occurring through viscous flow in nanocrystalline materials like glass.[42]

Effective densification cannot be achieved solely by increasing the temperature to accelerate diffusion rates, as it eventually becomes limited by ceramic evaporation or excessive grain growth. Evaporation can be mitigated to some extent by embedding the compact in a powder bed or utilizing a high-pressure sintering atmosphere.

Sintering aids can enhance the ratio of densification rate to grain growth rate by facilitating grain boundary diffusion and impeding diffusion across grain boundaries from one grain to another (restraining grain boundary movement).[43] In other words, sintering aids can control the separation of grain boundaries from pores by pinning them, thereby reducing grain growth. Specific sintering agents can expedite the sintering rate through liquid sintering, wherein a liquid phase is produced at a temperature lower than the sintering temperature. This viscous liquid may introduce an additional diffusion mechanism involving dissolution/precipitation particle rearrangement, acting as a lubricant, and exerting capillary force thus enhancing the densification process.

Dopants and secondary phases (intentionally added or naturally formed) are commonly found in materials, serving various purposes such as modifying electronic properties, aiding the sintering process, or enhancing mechanical properties. Their impact on sintering is multifaceted. When the concentration of impurities or dopants surpasses the solubility limit, a second phase precipitates, leading to reduced grain boundary mobility and slower grain growth. Dopants with charges differing from the crystalline lattice ions can induce concentration variations in vacancies or interstitial atoms, thereby influencing diffusion rates. Introducing foreign ions into a crystal generates stress fields around defects, enabling defects with opposing constraint fields to minimize their energy, thus immobilizing them and decreasing diffusion coefficients. Dopants tend to segregate at interfaces, where the disrupted crystalline structure facilitates their incorporation. This segregation diminishes grain boundary mobility and amplifies the effects of changes in point defect concentrations or defect immobilization. In conclusion, the effects of dopants and impurities on sintering are intricate, difficult to predict, and contingent upon the specific type and concentration of ions involved.

1.4.2 Sulfide solid electrolytes

Sulfide solid electrolytes have conductivities close to those of liquid electrolytes as shown in Figure **1.5**d. Some examples of sulfide solid electrolytes are $Li_{9.54}Si_{1.74}P_{1.44}S_{11.7}Cl_{0.3}$ (25 mS cm^{-1})[44] and argyrodite $Li_{5.5}PS_{4.5}Cl_{1.5}$ (9.4 mS cm^{-1})[45]. They form better contact (wetting) with electrodes and are easier to machine than oxide electrolytes due to their moderate deformability. However, they have a narrow intrinsic stability window due to the oxidation of sulfide anions at high potentials and the reduction of metal cations (such as Ge) at low potentials. The exception is metal free $Li_7P_3S_{11}$-type sulfide, its stability against metallic lithium is improved by the formation of a passivating interphase. By contrast, in metal containing sulfides the metal is reduced into metallic form forming an electronically conductive interphase that facilitates the propagation of the decomposition reaction.[46] The main disadvantage of sulfide solid electrolytes is that they are moisture sensitive and react with water to produce toxic H_2S gas which poses safety issues. This moisture sensitivity complicates the synthesis and processing of sulfide solid electrolytes because they need to be performed under an inert atmosphere. For these reasons, we did not study this system.

1.4.3 Halide solid electrolytes

Halide solid-state electrolytes have high ionic conductivity due to a weaker coulombic force between monovalent halogen anions of the framework and lithium ions compared to divalent sulfur or oxygen anions. This leads to a lower E_a for Li diffusion. Additionally, the longer Li-halogen ionic bond lengths in halide solid electrolytes, resulting from the larger ionic radii of halogens, contribute to their high ionic conductivity. Some examples of halide solid electrolytes with high ionic conductivity include Li_3ScCl_6 which has a conductivity of 3.02 mS cm^{-1},[47] oxyhalides, such as Li_3OX X:Cl, Br (antiperovskite structure),[48] and $LiMOCl_4$, which has conductivities reaching 12.4 mS cm^{-1} in $LiTaOCl_4$.[49] Moreover, halide anions offer higher oxidative stability than sulfide and oxide solid electrolytes because of the higher electrochemical redox potential of the halide anion. Despite these advantages, they are moisture sensitive and have low reductive stability (not stable against metallic lithium). For instance, Li_3InCl_6 reacts with H_2O to form In_2O_3, LiCl, and HCl.[50] This increases the complexity of working with these materials. They are of further interest for study with our methods developed herein but they were not selected for the initial studies included in this thesis.

1.4.4 Phosphide and hydride solid electrolytes

The phosphide solid electrolytes are composed of isolated MP_4 tetrahedra, which are separated by Li ions occupying both the tetrahedral and octahedral sites of the phosphide cubic closed packing. The metal could be trivalent or tetravalent known as phosphidotrielates and phosphidotetrelates respectively. An example of a phosphidotrielate is Li_9GaP_4, which has a conductivity of 4.5 mS cm^{-1}.[51] These electrolytes demonstrate high conductivity and exhibit stability when exposed to water and air. However, their low oxidative stability, which is due to the presence of the P^{3-} anion, makes them incompatible with most cathodes. These discouraged us from researching into this system.

Lastly, hydride solid electrolytes, such as monocarba-closo-borate salts with the formula $0.7Li(CB_9H_{10})$-$0.3Li(CB_{11}H_{12})$, have conductivities as high as 6.7 mS cm^{-1}.[52] Hydride solid electrolytes exhibit good stability against lithium metal and have good oxidative stability, but their high hygroscopicity and susceptibility to hydrolysis (depending on the composition) make their synthesis and processing quite challenging, which in turn poses difficulties in investigating this system.

1.4.5 Oxide solid electrolytes

Oxide solid electrolytes include garnets, perovskites, sodium superionic conductors (NASICON), and lithium superionic conductors (LISICON). These solid electrolytes exhibit moderate conductivity, above our threshold of 10^{-4} S cm^{-1} at room temperature surpassing that of polymers but falling short of the conductivity offered by current liquid electrolytes as shown in Figure **1.5**c.

Due to their brittle nature, they also exhibit poor interfacial contact with electrodes and are challenging to process. Additionally, they require high sintering temperatures, making their manufacturing difficult. Nonetheless, they demonstrate stability against lithium metal, as observed in LLZO, and can also exhibit high oxidative stability, as demonstrated by LLTO. Moreover, these electrolytes possess exceptional thermal stability and outstanding safety.

Garnets total conductivities can reach $>10^{-3}$ S cm^{-1} in doped-$Li_7La_3Zr_2O_{12}$ (LLZO). LLZO can take two structures a low conductivity ~10^{-6} S cm^{-1} tetragonal phase (space group I41/acd) or a high conductivity 10^{-4}-10^{-3} S cm^{-1} cubic phase (space group Ia-3d). The cubic phase can be stabilized by substitution. While LLZO is stable against lithium, it is unstable at high potentials (>4.1V).[53] On the other hand, lithium lanthanum titanate (LLTO) with a perovskite structure has high bulk conductivity of above 10^{-3} S cm^{-1}, but the grain boundary conductivity of ~10^{-5} S cm^{-1} is two orders of magnitude lower. LLTO is stable at high potentials, but Ti^{4+} gets reduced when in contact with lithium metal, converting it into a mixed conductor.[54]

Lithium lanthanum titanate (LLTO) has a chemical formula of $Li_{3x}La_{2/3-x}TiO_3$ and takes to perovskite structure with a generic formula of ABX_3. The A-sites are partially occupied by lithium and lanthanum, the B-sites are occupied by titanium, and the anion X is oxygen. The Ti octahedra connect at the vertices, and Li/La occupy the dodecahedral sites as shown in Figure **1.7**. The high temperature cubic phase (Pm-3m) of LLTO distorts when quenched, but Li and La stay disordered at the A-site (I4/mcm).[55] By contrast, when LLTO is slowly cooled, its structure converts into a double perovskite, due to Li and La ordering, resulting in an orthogonal phase (Pmmm) in the Li-poor region and a tetragonal phase (P4/mmm) in the lithium-rich region.[56]

The Li-ion conductivity in LLTO occurs via the single cation vacancy mechanism, where Li^+ hops through a high energy barrier (square 4 oxygen window) shown in Figure **1.7**.[57] The mobility of Li ions increases with the window size. LLTO bulk conductivity is highest (~10^{-3} S cm^{-1}) when x=0.11 corresponding to the optimal charge carrier concentration.[58] However, the grain boundary conductivity is 2 orders of magnitude lower. Despite good oxidation stability, LLTO is unstable against lithium metal. When in contact with lithium metal, Ti^{4+} reduces to Ti^{3+} by lithium insertion, converting LLTO into a mixed ionic/electronic conductor propagating through the solid electrolyte and causing an internal electric short.

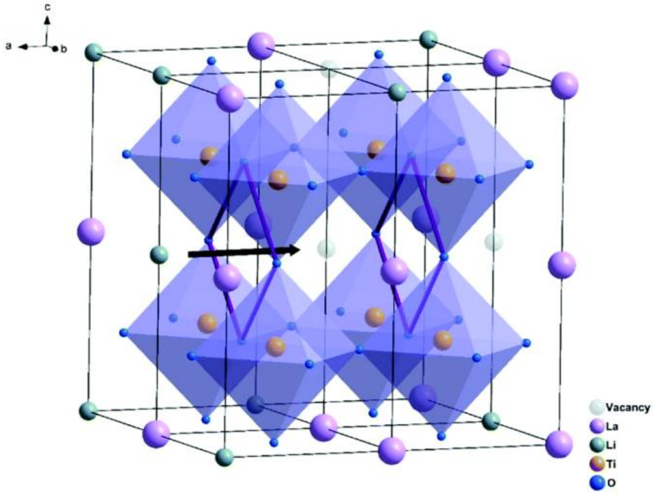

Figure 1.7 *Structure of LLTO and the energy barrier window made of 4 oxygens. Reproduced with permission from ref. [59].*

Efforts to shift the cathodic stability limit to lower potentials of LLTO by partially substituting the Ti site have been unsuccessful so far. B and A site substitutions have been investigated to enhance bulk and grain boundary conductivity summarized in Table **1.1**.[60] The bulk conductivity can be improved by increasing the size of the 4-oxygen window[61] and strengthening the bond between B-site cation and oxygen anion resulting in a weaker Li-O bond[62]. Larger cations at the A site can increase the bottleneck size, but excessively large cation substitutions can cause structural distortion and decrease the window size.[63] Unfortunately, most substitutions made in the LLTO system have only resulted in minor improvements in conductivity.

Table 1.1 *Substitutions in LLTO. Reproduced with permission from ref. [60].*

Composition	**Synthesis Method**	**Sintering temperature/time**	**σ_{Total} (S cm^{-1})**	**Ea (eV)**	**$\sigma_{electronic}$ (S cm^{-1})**	**ρ/ρ_o (%)**	**Ref.**
$Li_{0.5}La_{0.5}Nb_{0.04}Ti_{0.95}O_3$	Solid state	1350 °C for 12h	1.04×10^{-4}	-	-	-	64
$Li_{0.35}La_{0.35}Sr_{0.3}TiO_3$	Solid state	1300 °C for 6 h	2.78×10^{-5}	0.3	-	97.17	65
$Li_{0.355}La_{0.35}Sr_{0.3}Ti_{0.995}Al_{0.005}O_3$	Solid state	1300 °C for 6 h	2.05×10^{-5}	0.31	-	96.56	65
$Li_{0.355}La_{0.35}Sr_{0.3}Ti_{0.995}Co_{0.005}O_3$	Solid state	1300 °C for 6 h	1.37×10^{-5}	0.32	-	96.99	65
$Li_{0.355}La_{0.35}Sr_{0.3}Ti_{0.995}In_{0.005}O_3$	Solid state	1300 °C for 6 h	1.97×10^{-5}	0.31	-	97.15	65
$Li_{0.43}La_{0.56}Ti_{0.95}Ge_{0.05}O_3$	Solid state	1150 °C for 2 h	1.20×10^{-5}	-	5.2×10^{-7}	-	66
$(Li_{0.33}La_{0.56})_{1.005}Ti_{0.99}Al_{0.01}O_3$	Sol-gel	1350 °C for 6 h	3.17×10^{-4}	-	2.3×10^{-12}	-	67

This thesis will focus on understanding and improving the properties of perovskite solid electrolytes, one of the promising families of ceramic solid electrolytes. Perovskite solid electrolytes, as mentioned above, have high bulk conductivity, show stability at high potentials, and have outstanding safety making them an ideal candidate for further research and development for energy storage.

1.4.6 Synthesis and sintering techniques

Ceramic solid electrolytes can be synthesized through various methods, including solid-state synthesis, co-precipitation, and sol-gel. In solid-state synthesis, solid reagents (usually oxides) are mixed using ball milling or manual milling. Long high-temperature treatments are required to obtain a pure product due to the long diffusion paths involved. Sometimes, multiple intermediate grinding and re-pelleting steps are necessary.[68]

Co-precipitation involves mixing all reagents as solutions (such as nitrates) and adding a precipitator such as sodium hydroxide or ammonium hydroxide. The resulting precipitate, usually a hydroxide, is washed then mixed with a lithium source (Li_2CO_3 or LiOH) for the heat treatment step to form the oxide.[69] The drawback of the co-precipitation method is that some cations tend to precipitate out before adding the precipitator while other may precipitate very slowly or not at all leading to heterogeneity in the collected powder.

The sol-gel method typically also starts with nitrate solutions. However, it employs a chelating agent like citric acid, stabilizing the cations from precipitating, resulting in a homogeneous initial mixture. The solvent is then dried to form a gel, which is subsequently calcined. Sol-gel can be used with a far wider variety of cations than co-precipitation and will therefore be the method of choice herein.

Various sintering techniques are used to achieve a dense ceramic solid electrolyte, such as ultrafast high-temperature sintering (which minimizes lithium loss due to its short heating time),[70] spark plasma sintering (sintering under uniaxial pressure),[71] and conventional furnace sintering. These methods enable the production of high density ceramic solid electrolytes with desirable properties for use in all-solid-state batteries.

1.5 Characterization techniques for solid electrolytes

It is important to characterize the essential properties of solid electrolytes to ensure decent performance in a full battery. Good solid electrolytes should have high ionic conductivity, low electronic conductivity, a wide electrochemical stability window, be stable against lithium metal, and be deformable.

1.5.1 Electrical conductivity

Electrical conductivity of solid electrolyte is measured by electrochemical impedance spectroscopy (EIS). First, metal contacts (Au or Pt) are sputtered on two sides of pellets. AC current at low voltage (mV) is applied through the contacts and the frequency is swept while measuring AC current response (phase shift and amplitude). The EIS data can be presented in a

Nyquist plot and fitted to an equivalent circuit as shown in Figure **1.8**a. The Nyquist plot of a typical solid electrolyte consists of arcs at the high-mid-frequency regions and a spike at the low-frequency region. The arc can be fitted to an RC circuit, but due to non-ideal capacitor behavior of solid electrolytes the capacitor is replaced by a constant phase element (CPE).[72] If two arcs are present, the identity of each arc is assigned based on its capacitance value as being either due to the bulk (10^{-12} F) or grain boundary (10^{-11}-10^{-8} F).[73] The spike at low frequency is associated with the accumulation/depletion occurring at the solid electrolyte/blocking metal electrode interface. The conductivity σ (S cm^{-1}) is calculated by normalizing the resistance value R (Ω) measured by the geometric factors of the sample which are its thickness l (cm) and area of contact A (cm^2) using the following formula:

$$\sigma = \frac{l}{RA} \tag{2}$$

The activation energy of lithium conduction can be determined by measuring the conductivity at various temperatures, T, and then plotting $\ln\left(\sigma T\right)$ as a function of $\frac{1}{T}$. The y-intercept of the resulting linear plot corresponds to the pre-exponential factor and the activation energy is calculated from the slope using the following equation:

$$\sigma = \frac{\sigma_0}{T} e^{\left(-\frac{E_a}{kT}\right)} \tag{3}$$

where σ_0 (S cm^{-1} K^{-1}) is the pre-exponential factor, E_a(eV) is the activation energy of Li conduction, and k(eV K^{-1}) is Boltzmann constant.

Thus, the conductivity can be improved by tuning the activation energy and pre-exponential factor, $\sigma_0 = \sigma_{00} e^{(S_m/k_B)}$, which increases with σ_{00} and entropy of migration (S_m). Where σ_{00} is a function of the jump distance, the attempt frequency, and charge carrier concentration.[74] Therefore orders of magnitude increases in pre-exponential factor are usually due to increase of entropy of migration.

1.5.2 Electronic conductivity

Electronic conductivity is measured using the Hebb-Wagner method, where a reversible electrode like lithium and a blocking electrode like Cu are used in a (−)Li/SE/Cu(+) cell configuration.[75, 76] DC constant voltage is applied while measuring the current decay as shown in Figure **1.8**b. The initial current corresponds to total conductivity (electronic and ionic), while the steady-state current corresponds to electronic conductivity.[75, 76] The electronic resistance is calculated from the steady-state current using Ohm's law and then electronic conductivity is computed using eq (2).

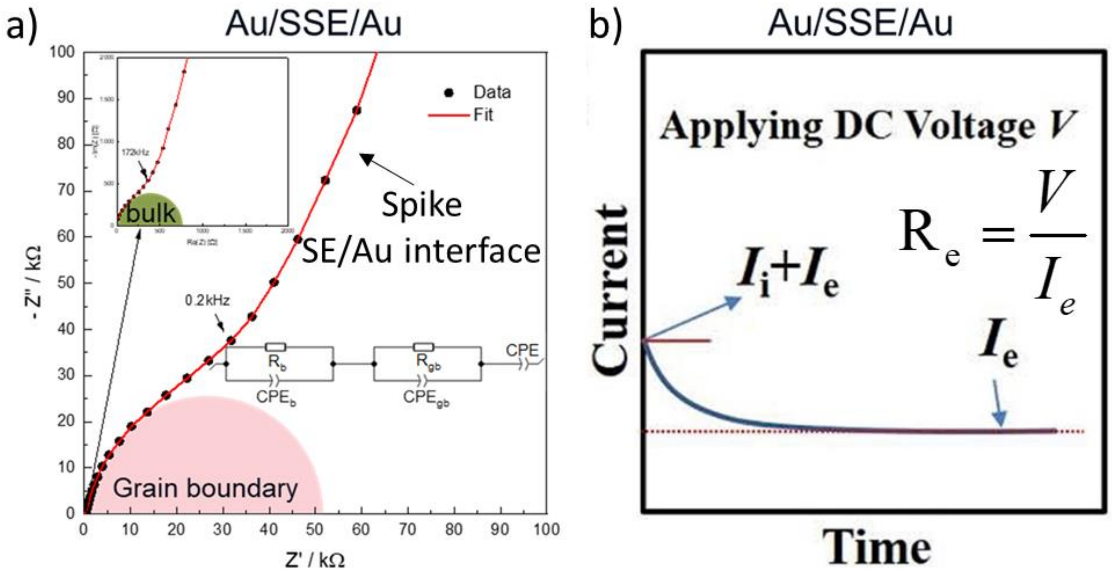

Figure 1.8 *(a) Nyquist plot for EIS spectrum of solid electrolyte shown with the equivalent circuit. The dots are the EIS data, and the red line is the fit. (b) Current vs time plot under applied constant voltage for electronic conductivity measurement. The electronic resistance is calculated by Ohm's law from the steady state current. Reproduced with permission from ref. [77].*

1.5.3 Electrochemical stability window

ESW is measured by depositing a metal contact on one side of a solid electrolyte pellet and cycling it against Li metal. This method should not be used because it overestimates the electrochemical stability due to limited ionic and electronic conductivity. Figure **1.9**a shows a wide ESW (0 to 5 V) for the sulfide base electrolyte $Li_{10}GeP_2S_{12}$ (LGPS) using this biased method.[78] To obtain accurate ESW, electrodes must be prepared from the solid electrolyte by mixing with a conducting powder (e.g. Pt, carbon black). Low electrode loadings and a slow sweeping rate should be used to ensure that the ESW is not overestimated by sluggish electronic or ionic paths. Figure **1.9**b shows the electrochemical stability of LGPS using the latter method. It is clear that LGPS starts to oxidize at voltages below 2.8 V (vs Li/Li$^+$).[79]

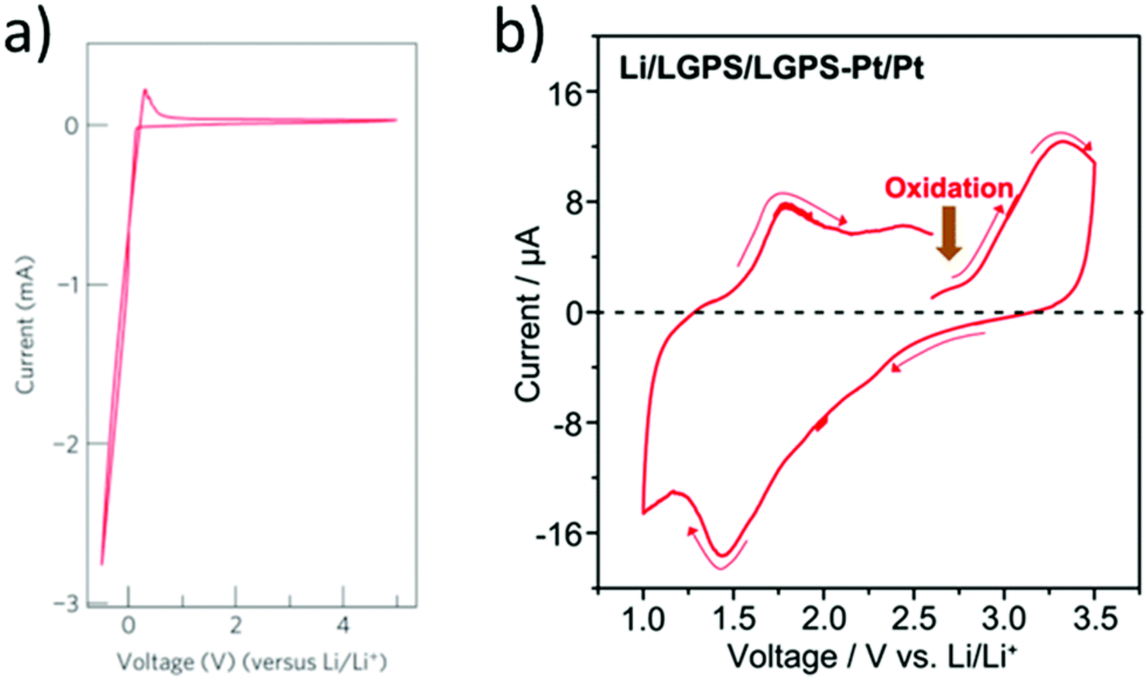

Figure 1.9 *Electrochemical stability window CV tests in Li/LGPS/Au configuration (a) and by preparing electrode in Li/LGPS/LGPS-Pt/Pt configuration (b). Due to sluggish ionic and electronic kinetics the stability window is overestimated in Li/LGPS/Au configuration. Reproduced with permission from ref. [78, 79].*

1.5.4 Stability against lithium metal

The stability of solid electrolytes against lithium metal is tested using EIS by measuring the impedance of a Li/SE/Li symmetric cell at various intervals starting from the time it comes in contact with lithium metal. Figure **1.10** shows the evolution of interfacial resistance between a Nb^{5+} substituted LLZO electrolyte and lithium metal electrode. The interfacial resistance increased over time while the bulk conductivity decreased, indicating the development of an electronically conductive phase progressing through the electrolyte.[80] Li/SE/Li cell configuration is also utilized to investigate the interfacial resistance between the lithium electrode and SE (with or without surface treatment) to assess lithium wettability.[81]

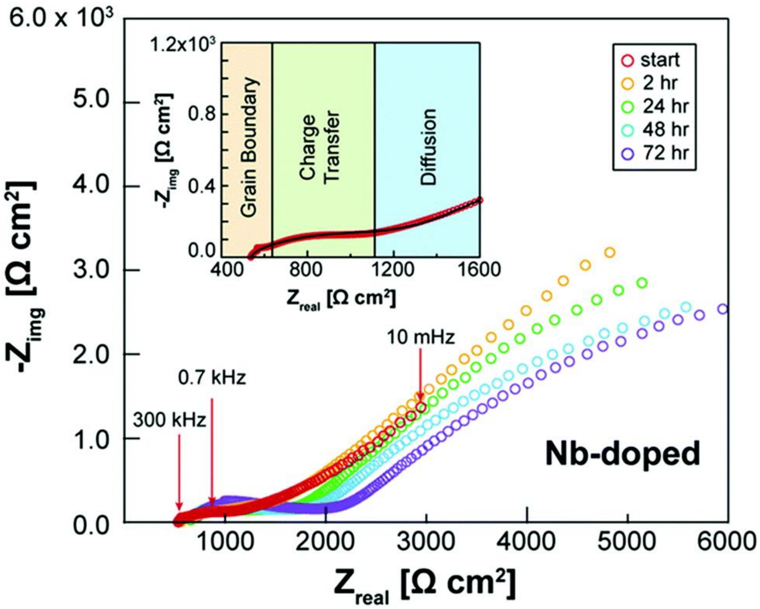

Figure 1.10 *EIS spectra of a symmetric Li/Nb-LLZO/Li cell demonstrate the variation of impedance over 72 hours as a result of the electrolyte and Li metal interaction. The inset shows the assignment of the different features of the EIS spectrum. Reproduced with permission from ref. [80].*

Evaluating all the properties mentioned above is critical to ensure that the tested solid electrolyte is suitable for use in a solid-state battery. By carefully measuring and analyzing these properties, we can identify solid electrolytes with the desired combination of properties for use in high-performance and safe solid-state batteries.

1.6 Intercalation cathodes

Commercialized intercalation cathode materials are categorized based on their crystal structures into layered, olivine, and spinel as shown in Figure **1.11**. The most common cathodes used in electric vehicles are layered oxides with a generic formula of $LiMO_2$, where M are transition metals such as nickel, manganese, and cobalt. This cathode consists of sheets of edge-sharing MO_6 octahedra with a Li layer between them. The diffusion paths of Li in these cathodes are two-dimensional. On the other hand, spinel type cathodes are made of edge shared MO_6 octahedra framework whilst LiO_4 tetrahedra are corner shared with MO_4 tetrahedra and face shared with empty octahedral sites. The lithium diffusion in spinel structures, such as $LiMn_2O_4$, is through 3D lithium channels. Finally, $LiMPO_4$ olivine-type cathodes consist of PO_4 polyanions, and the lithium mobility is through 1D lithium channels. This thesis will focus on studying olivine-type cathodes and developing strategies to improve their properties.

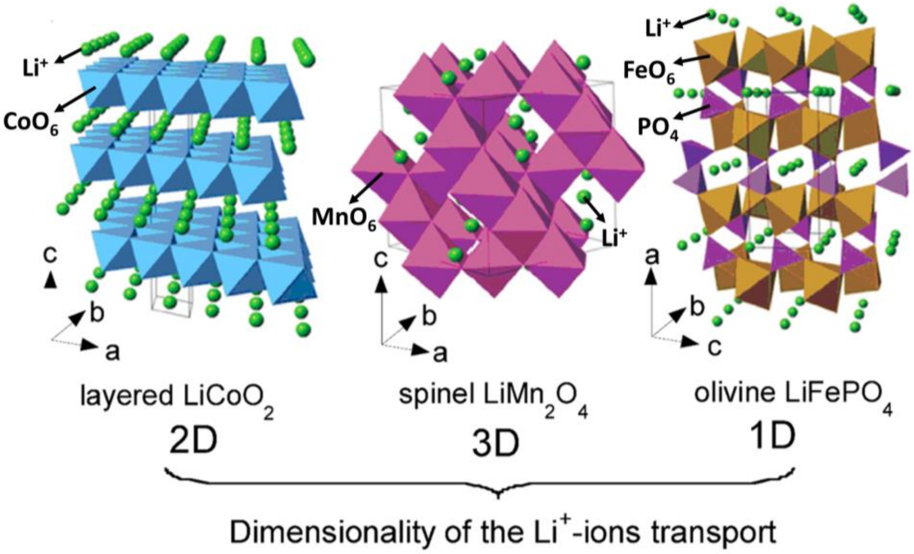

Figure 1.11 *Classification of intercalation-deintercalation cathodes for lithium-ion batteries and the lithium motion dimensionality in each. Reproduced with permission from ref. [82].*

1.6.1 Olivine cathodes

Olivine cathodes have a generic formula of $LiMPO_4$, containing MO_6, LiO_6, and PO_4 polyhedra as shown in Figure **1.12**a. The MO_6 octahedra are connected in the bc plane through shared corners whilst sharing edges with two LiO_6 and one PO_4. Antisite defects can block the 1D lithium-ion diffusion channels. Figure **1.12**a show the various possible configurations of antisite exchange pairs in $LiFePO_4$.[83] $LiFePO_4$ has poor ionic and electronic conductivities. One way to address the poor ionic conductivity of olivine-type cathodes is by preparing nanomaterials with a reduced lithium diffusion path. As depicted in Figure **1.12**b, the capacity of $LiFePO_4$ decreases as the sintering temperature rises above 550°C due to the formation of larger particles. On the other hand, carbon coating has been shown to improve poor electronic conductivity. Figure **1.12**c shows that carbon-coated $LiFePO_4$ with different carbon sources has a higher capacity compared to untreated $LiFePO_4$.[84-86] Nanosizing can be detrimental to the liquid electrolyte due to the large surface area on which solid electrolyte interphase forms, especially at high potentials, but $LiFePO_4$ operates near 3.5 V (vs. Li/Li^+) where the electrolyte is stable.

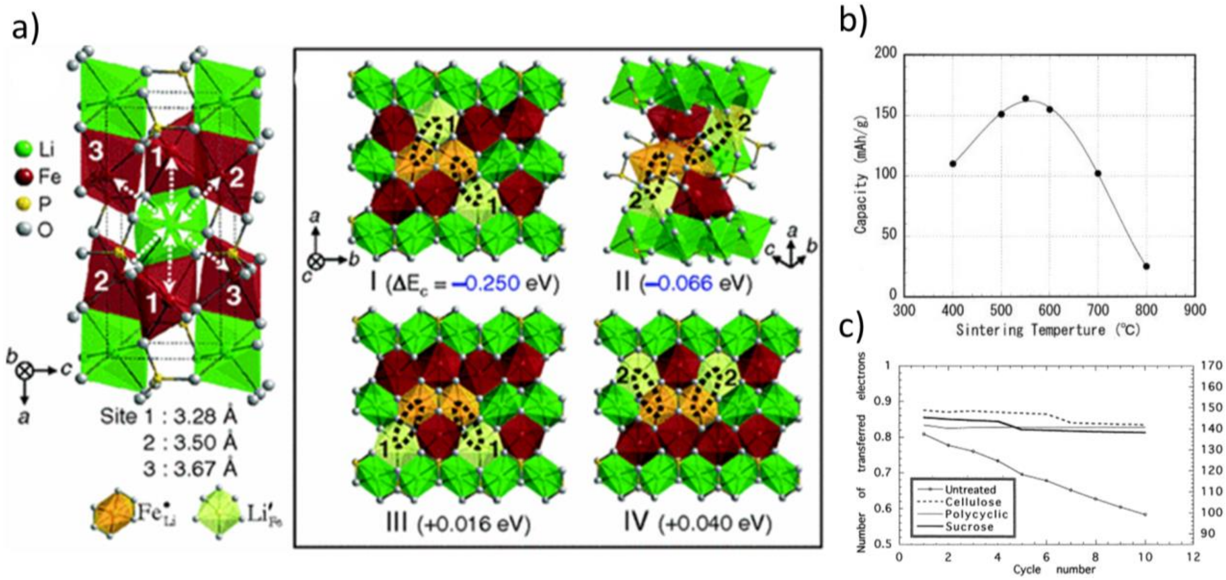

Figure 1.12 *(a) Various possible configurations of antisite exchange pairs in* $LiFePO_4$*. Reproduced with permission from ref. [83]. (b) 1st discharge capacity of different sized* $LiFePO_4$ *particles. Reproduced with permission from ref. [84]. (c) Discharge capacity of bare* $LiFePO_4$ *and carbon coated by various organic reagents. Reproduced with permission from ref. [85].*

$LiCoPO_4$ is a promising olivine cathode due to its high potential (4.8V vs. Li/Li^+) but its performance is hindered by its low ionic and electronic conductivities. Partial substitutions such as Fe, Mn, and Ni have been investigated as a strategy to improve the intrinsic ionic and electronic conductivity of $LiCoPO_4$.[86] However, even with these substitutions, the electrochemical performance of $LiCoPO_4$-based cathodes remains poor, especially in terms of long-term cycling stability.

1.6.2 Characterization techniques for cathodes

Galvanostatic and cyclic voltammetry (CV) measurements are commonly used for evaluating the electrochemical performance of cathode materials. In galvanostatic measurements, a constant current is supplied while recording the voltage over time to generate a charge/discharge curve. On the other hand, in CV measurements, the potential is swept while measuring the resulting current. The data obtained from CV measurements can be converted into a charge/discharge curve by integrating the current over time. These measurements provide valuable information about the electrochemical performance of the cathode, including discharge capacity, capacity retention, coulombic efficiency, charge/discharge voltages, and overpotential. Discharge capacity refers to the amount of charge that the cathode material can deliver. Coulombic efficiency measures the irreversible capacity loss, calculated as the ratio of discharge capacity to charge capacity. Charge/discharge voltages and overpotential are also important parameters, as they determine the energy density and power output of the battery.

1.7 High-throughput experimentation

Developing battery materials has been slow, as these materials are traditionally investigated one composition at a time. This approach can be both time-consuming and inefficient. Furthermore, the properties of these materials are frequently not examined under uniform testing conditions, making it difficult to compare their performances and impeding the development of novel and enhanced battery materials. However, high-throughput experimentation has the potential to overcome these hurdles by enabling the rapid screening of a large number of samples within a short time and under identical testing conditions. As a result, high-throughput experimentation can lead to more efficient and systematic screening of battery materials, ultimately speeding up the development of new and improved materials. Various high-throughput techniques have been used to study anode, cathode, and solid electrolyte materials in thin films[87] and bulk form. Co-sputtering is a common technique often used in high-throughput experimentation to produce thin films with composition gradients.[88] It uses multiple targets positioned at different positions/angles from the substrate to create a compositional gradient. This approach was used to study the LLTO composition space and map the conductivity.[89] In the bulk form, milligram scale samples are made in high-throughput using one of the synthesis methods mentioned above. One of the challenges in combinatorial synthesis at the milligram scale and high synthesis temperatures is mitigating lithium loss, which can be achieved by adjusting experimental parameters such as synthesis method, atmosphere, heat treatment, and adding excess lithium.[90]

High-throughput methodologies are useful for optimizing variables (such as synthesis conditions and electrolyte formulation), exploring defined composition spaces, and studying the effect of substitutions. Recently, high-throughput methods were employed to screen the effect of additives on the performance of liquid electrolytes by screening a large number of different additive combinations and measuring their performance in terms of coulombic efficiency.[91] Combinatorial methodologies for screening cathode[92] and anode[93] materials have also been recently developed. Figure **1.13**a shows a combinatorial cell designed for screening 64 cathode materials. The CV data in Figure **1.13**b obtained for two model cathode materials using this setup show high accuracy and reproducibility.[92] By implementing high-throughput experimentation, the development of cathode and solid electrolyte materials can be significantly accelerated, leading to more efficient and effective design of lithium-ion battery materials.

High throughput experimentation techniques have the potential to revolutionize the way that battery materials are discovered and developed and are likely to play an increasingly important role in the future of battery research and development.

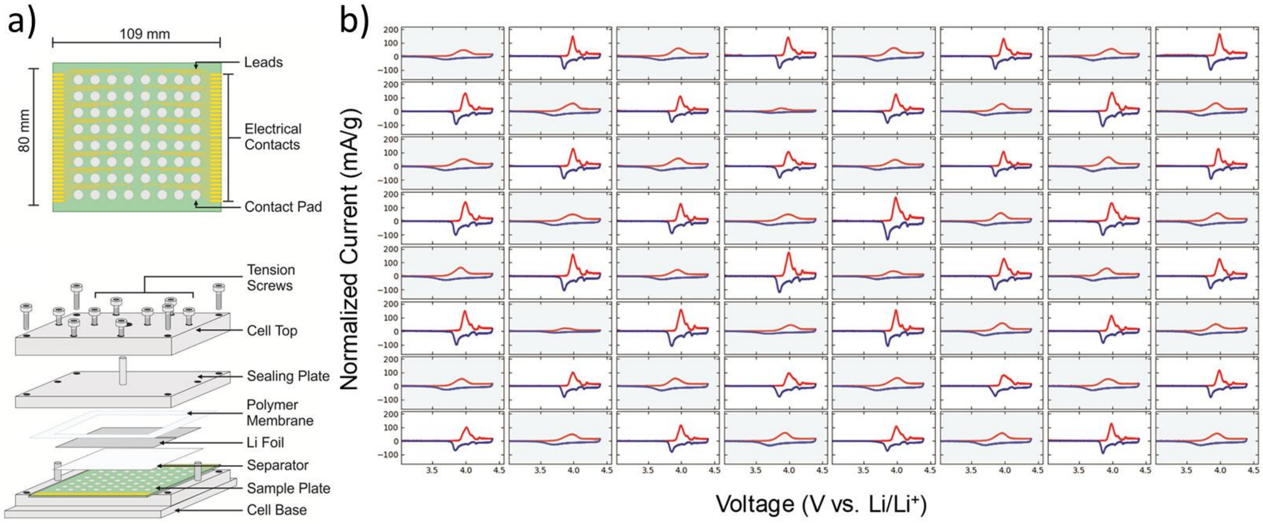

Figure 1.13 *(a) Combinatorial cell for screening battery materials 64 samples at a time. (b) CV data from 64 samples checkerboard made of two cathode materials showing reproducibility. Reproduced with permission from ref. [92].*

1.8 Context and scope of this thesis

Chapter 2 focuses on developing and validating a high-throughput suite of methods for synthesizing and screening solid-state electrolytes. It provides a detailed description of the methodologies and workflow for testing solid-state electrolytes. It presents the validation of the suite using two reference materials to assess its precision, accuracy, and versatility. The methods developed in this chapter will be used in Chapters 3 and 4 to optimize solid-state electrolytes for all-solid-state batteries.

Chapter 3 explores the impact of composition on the structure and ionic conductivity of LLTO solid electrolytes. The chapter describes the synthesis and characterization of over 576 samples in the Li-La-Ti-O pseudoternary phase diagram using XRD and the high throughput suite developed and validated in Chapter 2. The study revealed that LLTO is a metastable phase stabilized by secondary phases such as TiO_2 and that the cooling rate influences the stabilization process. The chapter also discusses the discovery that secondary phases enhance ionic conductivity, highlighting the importance of appropriate composition and synthesis conditions to improve ionic conductivity without using additional sintering steps, additives, or sacrificial powder beds. Overall, the chapter provides valuable insights into the composition-structure-conductivity relationship in LLTO solid electrolytes.

Chapter 4 investigates the effects of single partial substitutions at the Ti-site on the performance of the best LLTO from Chapter 3. The chapter outlines the synthesis and characterization of 50 single partial substitutions at 5 different levels and their impact on the properties of LLTO. The study found that some substitutions did not affect bulk conductivity, while others decreased it. K-substituted LLTO showed a minor enhancement in bulk conductivity, and Na-substituted LLTO showed improved grain boundary conductivity. The chapter also discusses the impact of substitutions such as Cr, Mn, Rh, and Cd on the electronic conductivity of LLTO, making them useful candidates for the electrolyte in composite electrodes in all-solid batteries. Additionally, the chapter identifies potential candidates for the first epitaxial battery. The study provides a guide for improving the performance of LLTO through partial substitutions for energy storage applications.

Chapter 5 aims to enhance the performance of $LiCoPO_4$, a high-potential cathode material that could be coupled with our ceramic electrolytes that is stable at high potentials. The study focuses on partial single and co-substitution at the Co site and optimization of synthesis conditions to overcome low intrinsic electronic and ionic conductivity. The study screens 1300 samples, including 263 distinct substituted samples to design an optimum material. Even a small amount of 1% In and 1% Mo partial co-substitution of Co showed a significant performance improvement compared to unsubstituted LCP. Traditional experimental and computational methods were used to understand the improved performance mechanism.

1.9 References

(1) Fan, L.; Tu, Z.; Chan, S. H. Recent Development of Hydrogen and Fuel Cell Technologies: A Review. *Energy Reports* **2021**, *7*, 8421.

(2) Chen, T.; Jin, Y.; Lv, H.; Yang, A.; Liu, M.; Chen, B.; Xie, Y.; Chen, Q. Applications of Lithium-Ion Batteries in Grid-Scale Energy Storage Systems. *Transactions of Tianjin University* **2020**, *26* (3), 208.

(3) Masias, A.; Marcicki, J.; Paxton, W. A. Opportunities and Challenges of Lithium Ion Batteries in Automotive Applications. *ACS Energy Letters* **2021**, *6* (2), 621.

(4) https://www.statista.com/statistics/1103218/global-battery-demand-forecast/ .

(5) Wang, F.; Harindintwali, J. D.; Yuan, Z.; Wang, M.; Wang, F.; Li, S.; Yin, Z.; Huang, L.; Fu, Y.; Li, L.; Chang, S. X.; Zhang, L.; Rinklebe, J.; Yuan, Z.; Zhu, Q.; Xiang, L.; Tsang, D. C. W.; Xu, L.; Jiang, X.; Liu, J.; Wei, N.; Kästner, M.; Zou, Y.; Ok, Y. S.; Shen, J.; Peng, D.; Zhang, W.; Barceló, D.; Zhou, Y.; Bai, Z.; Li, B.; Zhang, B.; Wei, K.; Cao, H.; Tan, Z.; Zhao, L.-b.; He, X.; Zheng, J.; Bolan, N.; Liu, X.; Huang, C.; Dietmann, S.; Luo, M.; Sun, N.; Gong, J.; Gong, Y.; Brahushi, F.; Zhang, T.; Xiao, C.; Li, X.; Chen, W.; Jiao, N.; Lehmann, J.; Zhu, Y.-G.; Jin, H.; Schäffer, A.; Tiedje, J. M.; Chen, J. M. Technologies and Perspectives for Achieving Carbon Neutrality. *The Innovation* **2021**, *2* (4), 100180.

(6) Liang, Y.; Zhao, C.-Z.; Yuan, H.; Chen, Y.; Zhang, W.; Huang, J.-Q.; Yu, D.; Liu, Y.; Titirici, M.-M.; Chueh, Y.-L.; Yu, H.; Zhang, Q. A Review of Rechargeable Batteries for Portable Electronic Devices. *InfoMat* **2019**, *1* (1), 6.

(7) Ramasubramanian, B.; Reddy, M. V.; Zaghib, K.; Armand, M.; Ramakrishna, S. Growth Mechanism of Micro/Nano Metal Dendrites and Cumulative Strategies for Countering Its Impacts in Metal Ion Batteries: A Review. In *Nanomaterials*, 2021; Vol. 11, p 2476.

(8) Owen, J. R. Rechargeable Lithium Batteries. *Chemical Society Reviews* **1997**, *26* (4), 259.

(9) Xu, K. Nonaqueous Liquid Electrolytes for Lithium-Based Rechargeable Batteries. *Chemical Reviews* **2004**, *104* (10), 4303.

(10) Roy, P.; Srivastava, S. K. Nanostructured Anode Materials for Lithium Ion Batteries. *Journal of Materials Chemistry A* **2015**, *3* (6), 2454.

(11) Stallworth, P. E.; Fontanella, J. J.; Wintersgill, M. C.; Scheidler, C. D.; Immel, J. J.; Greenbaum, S. G.; Gozdz, A. S. NMR, DSC and High Pressure Electrical Conductivity Studies of Liquid and Hybrid Electrolytes. *Journal of Power Sources* **1999**, *81-82*, 739.

(12) Zhang, X.; Kostecki, R.; Richardson, T. J.; Pugh, J. K.; Ross, P. N. Electrochemical and Infrared Studies of the Reduction of Organic Carbonates. *Journal of The Electrochemical Society* **2001**, *148* (12), A1341.

(13) Azcarate, I.; Yin, W.; Méthivier, C.; Ribot, F.; Laberty-Robert, C.; Grimaud, A. Assessing the Oxidation Behavior of EC:DMC Based Electrolyte on Non-Catalytically Active Surface. *Journal of The Electrochemical Society* **2020**, *167* (8), 080530.

(14) Feng, X.; Ouyang, M.; Liu, X.; Lu, L.; Xia, Y.; He, X. Thermal Runaway Mechanism of Lithium Ion Battery for Electric Vehicles: A Review. *Energy Storage Materials* **2018**, *10*, 246.

(15) Wang, Q.; Sun, J.; Yao, X.; Chen, C. Thermal Stability of $LiPF_6$/EC+DEC Electrolyte With Charged Electrodes for Lithium Ion Batteries. *Thermochimica Acta* **2005**, *437* (1), 12.

(16) Ramadass, P.; Haran, B.; White, R.; Popov, B. N. Capacity Fade of Sony 18650 Cells Cycled at Elevated Temperatures: Part I. Cycling Performance. *Journal of Power Sources* **2002**, *112* (2), 606.

(17) Zhou, G.; Sun, X.; Li, Q.-H.; Wang, X.; Zhang, J.-N.; Yang, W.; Yu, X.; Xiao, R.; Li, H. Mn Ion Dissolution Mechanism for Lithium-Ion Battery with $LiMn_2O_4$ Cathode: In Situ Ultraviolet–Visible Spectroscopy and Ab Initio Molecular Dynamics Simulations. *The Journal of Physical Chemistry Letters* **2020**, *11* (8), 3051.

(18) Yu, L.; Ong, S. J. H.; Liu, X.; Mandler, D.; Xu, Z. J. The Importance of the Dissolution of Polysulfides in Lithium-Sulfur Batteries and a Perspective on High-Energy Electrolyte/Cathode Design. *Electrochimica Acta* **2021**, *392*, 139013.

(19) Julien, C. M.; Mauger, A. Review of 5-V Electrodes for Li-Ion Batteries: Status and Trends. *Ionics* **2013**, *19* (7), 951.

(20) Schnell, J.; Günther, T.; Knoche, T.; Vieider, C.; Köhler, L.; Just, A.; Keller, M.; Passerini, S.; Reinhart, G. All-Solid-State Lithium-Ion and Lithium Metal Batteries – Paving the Way to Large-Scale Production. *Journal of Power Sources* **2018**, *382*, 160.

(21) Han, F.; Westover, A. S.; Yue, J.; Fan, X.; Wang, F.; Chi, M.; Leonard, D. N.; Dudney, N. J.; Wang, H.; Wang, C. High Electronic Conductivity as the Origin of Lithium Dendrite Formation Within Solid Electrolytes. *Nature Energy* **2019**, *4* (3), 187.

(22) Xue, Z.; He, D.; Xie, X. Poly(Ethylene Oxide)-Based Electrolytes for Lithium-Ion Batteries. *Journal of Materials Chemistry A* **2015**, *3* (38), 19218.

(23) Zhu, J.; Zhang, Z.; Zhao, S.; Westover, A. S.; Belharouak, I.; Cao, P.-F. Single-Ion Conducting Polymer Electrolytes for Solid-State Lithium–Metal Batteries: Design, Performance, and Challenges. *Advanced Energy Materials* **2021**, *11* (14), 2003836.

(24) Pringle, J. M.; Howlett, P. C.; MacFarlane, D. R.; Forsyth, M. Organic Ionic Plastic Crystals: Recent Advances. *Journal of Materials Chemistry* **2010**, *20* (11), 2056.

(25) Woolley, H. M.; Vargas-Barbosa, N. M. Hybrid Solid Electrolyte-Liquid Electrolyte Systems for (Almost) Solid-State Batteries: Why, How, and Where To? *Journal of Materials Chemistry A* **2023**, *11* (3), 1083.

(26) Tan, S.-J.; Wang, W.-P.; Tian, Y.-F.; Xin, S.; Guo, Y.-G. Advanced Electrolytes Enabling Safe and Stable Rechargeable Li-Metal Batteries: Progress and Prospects. *Advanced Functional Materials* **2021**, *31* (45), 2105253.

(27) Wang, C.; Liang, J.; Zhao, Y.; Zheng, M.; Li, X.; Sun, X. All-Solid-State Lithium Batteries Enabled by Sulfide Electrolytes: From Fundamental Research to Practical Engineering Design. *Energy & Environmental Science* **2021**, *14* (5), 2577.

(28) Monroe, C.; Newman, J. The Impact of Elastic Deformation on Deposition Kinetics at Lithium/Polymer Interfaces. *Journal of The Electrochemical Society* **2005**, *152* (2), A396.

(29) Jang, J.; Chen, Y.-T.; Deysher, G.; Cheng, D.; Ham, S.-Y.; Cronk, A.; Ridley, P.; Yang, H.; Sayahpour, B.; Han, B.; Li, W.; Yao, W.; Wu, E. A.; Doux, J.-M.; Nguyen, L. H. B.; Oh, J. A. S.; Tan, D. H. S.; Meng, Y. S. Enabling a Co-Free, High-Voltage $LiNi_{0.5}Mn_{1.5}O_4$ Cathode in All-Solid-State Batteries with a Halide Electrolyte. *ACS Energy Letters* **2022**, *7* (8), 2531.

(30) Ohno, S.; Zeier, W. G. Toward Practical Solid-State Lithium–Sulfur Batteries: Challenges and Perspectives. *Accounts of Materials Research* **2021**, *2* (10), 869.

(31) Wei, R.; Chen, S.; Gao, T.; Liu, W. Challenges, Fabrications and Horizons of Oxide Solid Electrolytes for Solid-State Lithium Batteries. *Nano Select* **2021**, *2* (12), 2256.

(32) Yu, T.; Ke, B.; Li, H.; Guo, S.; Zhou, H. Recent Advances in Sulfide Electrolytes Toward High Specific Energy Solid-State Lithium Batteries. *Materials Chemistry Frontiers* **2021**, *5* (13), 4892.

(33) Wang, C.; Liang, J.; Kim, J. T.; Sun, X. Prospects of Halide-Based All-Solid-State Batteries: From Material Design to Practical Application. *Science Advances 8* (36), eadc9516.

(34) Restle, T. M. F.; Sedlmeier, C.; Kirchhain, H.; Klein, W.; Raudaschl-Sieber, G.; Deringer, V. L.; van Wüllen, L.; Gasteiger, H. A.; Fässler, T. F. Fast Lithium Ion Conduction in Lithium Phosphidoaluminates. *Angewandte Chemie International Edition* **2020**, *59* (14), 5665.

(35) Pang, Y.; Liu, Y.; Yang, J.; Zheng, S.; Wang, C. Hydrides for Solid-State Batteries: A Review. *Materials Today Nano* **2022**, *18*, 100194.

(36) Bish, D. L.; Post, J. E. *Modern Powder Diffraction*; De Gruyter, 2018.

(37) Gupta, M.; Singapore, N. U. o.; Technology, S. I. o. M.; International, A. *Processing and Fabrication of Advanced Materials XIII: Proceedings of a Conference Organized by National University of Singapore, Singapore Institute of Manufacturing Technology, Co-sponsored by American Society for Materials International (ASM Int.) (The Materials Information Society), Held December 6-8, 2004 at Pan-Pacific Hotel, Singapore*; Stallion Press, 2005.

(38) Fang, Z. Z. *Sintering of Advanced Materials*; Elsevier Science, 2010.

(39) German, R. *Sintering: From Empirical Observations to Scientific Principles*; Elsevier Science, 2014.

(40) Zuckerman, J. J.; Atwood, J. D. *Inorganic Reactions and Methods, Formation of Ceramics*; Wiley, 2009.

(41) Kang, S. J. L. *Sintering: Densification, Grain Growth and Microstructure*; Elsevier Science, 2004.

(42) FTSE, D. Z. *Ultra-Supercritical Coal Power Plants: Materials, Technologies and Optimisation*; Elsevier Science, 2013.

(43) Tomsia, A. P.; Glaeser, A. M. *Ceramic Microstructures: Control at the Atomic Level*; Springer US, 2012.

(44) Kato, Y.; Hori, S.; Saito, T.; Suzuki, K.; Hirayama, M.; Mitsui, A.; Yonemura, M.; Iba, H.; Kanno, R. High-Power All-Solid-State Batteries Using Sulfide Superionic Conductors. *Nature Energy* **2016**, *1* (4), 16030.

(45) Adeli, P.; Bazak, J. D.; Park, K. H.; Kochetkov, I.; Huq, A.; Goward, G. R.; Nazar, L. F. Boosting Solid-State Diffusivity and Conductivity in Lithium Superionic Argyrodites by Halide Substitution. *Angewandte Chemie International Edition* **2019**, *58* (26), 8681.

(46) Wenzel, S.; Randau, S.; Leichtweiß, T.; Weber, D. A.; Sann, J.; Zeier, W. G.; Janek, J. Direct Observation of the Interfacial Instability of the Fast Ionic Conductor $Li_{10}GeP_2S_{12}$ at the Lithium Metal Anode. *Chemistry of Materials* **2016**, *28* (7), 2400.

(47) Liang, J.; Li, X.; Wang, S.; Adair, K. R.; Li, W.; Zhao, Y.; Wang, C.; Hu, Y.; Zhang, L.; Zhao, S.; Lu, S.; Huang, H.; Li, R.; Mo, Y.; Sun, X. Site-Occupation-Tuned Superionic Li_xScCl_{3+x}Halide Solid Electrolytes for All-Solid-State Batteries. *Journal of the American Chemical Society* **2020**, *142* (15), 7012.

(48) Xia, W.; Zhao, Y.; Zhao, F.; Adair, K.; Zhao, R.; Li, S.; Zou, R.; Zhao, Y.; Sun, X. Antiperovskite Electrolytes for Solid-State Batteries. *Chemical Reviews* **2022**, *122* (3), 3763.

(49) Tanaka, Y.; Ueno, K.; Mizuno, K.; Takeuchi, K.; Asano, T.; Sakai, A. New Oxyhalide Solid Electrolytes with High Lithium Ionic Conductivity >10 mS cm^{-1} for All-Solid-State Batteries. *Angewandte Chemie International Edition* **2023**, *62* (13), e202217581.

(50) Li, W.; Liang, J.; Li, M.; Adair, K. R.; Li, X.; Hu, Y.; Xiao, Q.; Feng, R.; Li, R.; Zhang, L.; Lu, S.; Huang, H.; Zhao, S.; Sham, T.-K.; Sun, X. Unraveling the Origin of Moisture Stability of Halide Solid-State Electrolytes by In Situ and Operando Synchrotron X-ray Analytical Techniques. *Chemistry of Materials* **2020**, *32* (16), 7019.

(51) Restle, T. M. F.; Strangmüller, S.; Baran, V.; Senyshyn, A.; Kirchhain, H.; Klein, W.; Merk, S.; Müller, D.; Kutsch, T.; van Wüllen, L.; Fässler, T. F. Super-Ionic Conductivity in ω-Li_9TrP_4 (Tr = Al, Ga, In) and Lithium Diffusion Pathways in Li_9AlP_4 Polymorphs. *Advanced Functional Materials* **2022**, *32* (46), 2112377.

(52) Kim, S.; Oguchi, H.; Toyama, N.; Sato, T.; Takagi, S.; Otomo, T.; Arunkumar, D.; Kuwata, N.; Kawamura, J.; Orimo, S.-i. A Complex Hydride Lithium Superionic Conductor for High-Energy-Density All-Solid-State Lithium Metal Batteries. *Nature Communications* **2019**, *10* (1), 1081.

(53) Smetaczek, S.; Pycha, E.; Ring, J.; Siebenhofer, M.; Ganschow, S.; Berendts, S.; Nenning, A.; Kubicek, M.; Rettenwander, D.; Limbeck, A.; Fleig, J. Investigating the Electrochemical Stability of $Li_7La_3Zr_2O_{12}$ Solid Electrolytes Using Field Stress Experiments. *Journal of Materials Chemistry A* **2021**, *9* (27), 15226.

(54) Inaguma, Y.; Liquan, C.; Itoh, M.; Nakamura, T.; Uchida, T.; Ikuta, H.; Wakihara, M. High Ionic Conductivity in Lithium Lanthanum Titanate. *Solid State Communications* **1993**, *86* (10), 689.

(55) Catti, M.; Sommariva, M.; Ibberson, R. M. Tetragonal Superstructure and Thermal History of $Li_{0.3}La_{0.567}TiO_3$ (LLTO) Solid Electrolyte by Neutron Diffraction. *Journal of Materials Chemistry* **2007**, *17* (13), 1300.

(56) Ibarra, J.; Várez, A.; León, C.; Santamaría, J.; Torres-Martínez, L. M.; Sanz, J. Influence of Composition on the Structure and Conductivity of the Fast Ionic Conductors $La_{2/3-x}Li_{3x}TiO_3$ ($0.03 \leq x \leq 0.167$). *Solid State Ionics* **2000**, *134* (3), 219.

(57) Stramare, S.; Thangadurai, V.; Weppner, W. Lithium Lanthanum Titanates: A Review. *Chemistry of Materials* **2003**, *15* (21), 3974.

(58) Inaguma, Y.; Chen, L.; Itoh, M.; Nakamura, T. Candidate Compounds With Perovskite Structure for High Lithium Ionic Conductivity. *Solid State Ionics* **1994**, *70-71*, 196.

(59) Zhang, S.; Zhao, H.; Guo, J.; Du, Z.; Wang, J.; Świerczek, K. Characterization of Sr-Doped Lithium Lanthanum Titanate With Improved Transport Properties. *Solid State Ionics* **2019**, *336*, 39.

(60) Jonderian, A.; McCalla, E. The Role of Metal Substitutions in the Development of Li Batteries, part II: Solid Electrolytes. *Materials Advances* **2021**, *2* (9), 2846.

(61) Itoh, M.; Inaguma, Y.; Jung, W.-H.; Chen, L.; Nakamura, T. High Lithium Ion Conductivity in the Perovskite-Type Compounds $Ln_{12}Li_{12}TiO_3$(Ln=La,Pr,Nd,Sm). *Solid State Ionics* **1994**, *70-71*, 203.

(62) Chung, H.-T.; Kim, J.-G.; Kim, H.-G. Dependence of the Lithium Ionic Conductivity on the B-Site Ion Substitution in $(Li_{0.5}La_{0.5})Ti_{1-x}M_xO_3$ (M=Sn, Zr, Mn, Ge). *Solid State Ionics* **1998**, *107* (1), 153.

(63) Katsumata, T.; Matsui, Y.; Inaguma, Y.; Itoh, M. Influence of Site Percolation and Local Distortion on Lithium Ion Conductivity in Perovskite-Type Oxides $La_{0.55}Li_{0.35} - xK_xTiO_3$ and $La_{0.55}Li_{0.35}TiO_3$-KMO_3 (M = Nb and Ta). *Solid State Ionics* **1996**, *86-88*, 165.

(64) Jiang, Y.; Huang, Y.; Hu, Z.; Zhou, Y.; Zhu, J.; Zhu, X. Effects of B-Site Ion (Nb^{5+}) Substitution on the Microstructure and Ionic Conductivity of $Li_{0.5}La_{0.5}TiO_3$ Solid Electrolytes. *Ferroelectrics* **2020**, *554* (1), 89.

(65) Yu, K.; Jin, L.; Li, Y.; Liu, G.; Wei, X.; Yan, Y. Structure and Conductivity of Perovskite $Li_{0.355}La_{0.35}Sr_{0.3}Ti_{0.995}M_{0.005}O_3$ (M = Al, Co and In) Ceramics. *Ceramics International* **2019**, *45* (18, Part A), 23941.

(66) Hu, Z.; Sheng, J.; Chen, J.; Sheng, G.; Li, Y.; Fu, X.-Z.; Wang, L.; Sun, R.; Wong, C.-P. Enhanced LI Ion Conductivity in Ge-Doped $Li_{0.33}La_{0.56}TiO_3$ Perovskite Solid Electrolytes for All-Solid-State Li-Ion Batteries. *New Journal of Chemistry* **2018**, *42* (11), 9074.

(67) Le, H. T. T.; Kalubarme, R. S.; Ngo, D. T.; Jang, S.-Y.; Jung, K.-N.; Shin, K.-H.; Park, C.-J. Citrate gel synthesis of aluminum-doped lithium lanthanum titanate solid electrolyte for application in organic-type lithium–oxygen batteries. *Journal of Power Sources* **2015**, *274*, 1188.

(68) Robertson, A. D.; Martin, S. G.; Coats, A.; West, A. R. Phase Diagrams and Crystal Chemistry in the Li^+ Ion Conducting Perovskites, $Li_{0.5-3}RE_{0.5+1}TiO_3$: Re=La, Nd. *Journal of Materials Chemistry* **1995**, *5* (9), 1405.

(69) Shao, C.; Liu, H.; Yu, Z.; Zheng, Z.; Sun, N.; Diao, C. Structure and Ionic Conductivity of Cubic $Li_7La_3Zr_2O_{12}$ Solid Electrolyte Prepared by Chemical Co-precipitation Method. *Solid State Ionics* **2016**, *287*, 13.

(70) Wang, C.; Ping, W.; Bai, Q.; Cui, H.; Hensleigh, R.; Wang, R.; Brozena, A. H.; Xu, Z.; Dai, J.; Pei, Y.; Zheng, C.; Pastel, G.; Gao, J.; Wang, X.; Wang, H.; Zhao, J.-C.; Yang, B.; Zheng, X.; Luo, J.; Mo, Y.; Dunn, B.; Hu, L. A General Method to Synthesize and Sinter Bulk Ceramics in Seconds. *Science* **2020**, *368* (6490), 521.

(71) Kobayashi, Y.; Takeuchi, T.; Tabuchi, M.; Ado, K.; Kageyama, H. Densification of $LiTi_2(PO_4)_3$-Based Solid Electrolytes by Spark-Plasma-Sintering. *Journal of Power Sources* **1999**, *81-82*, 853.

(72) Vadhva, P.; Hu, J.; Johnson, M. J.; Stocker, R.; Braglia, M.; Brett, D. J. L.; Rettie, A. J. E. Electrochemical Impedance Spectroscopy for All-Solid-State Batteries: Theory, Methods and Future Outlook. *ChemElectroChem* **2021**, *8* (11), 1930.

(73) Irvine, J. T. S.; Sinclair, D. C.; West, A. R. Electroceramics: Characterization by Impedance Spectroscopy. *Advanced Materials* **1990**, *2* (3), 132.

(74) Furusawa, S.-i.; Tabuchi, H.; Sugiyama, T.; Tao, S.; Irvine, J. T. S. Ionic Conductivity of Amorphous Lithium Lanthanum Titanate Thin Film. *Solid State Ionics* **2005**, *176* (5), 553.

(75) Hebb, M. H. Electrical Conductivity of Silver Sulfide. *The Journal of Chemical Physics* **1952**, *20* (1), 185.

(76) Wagner, J. B.; Wagner, C. Electrical Conductivity Measurements on Cuprous Halides. *The Journal of Chemical Physics* **1957**, *26* (6), 1597.

(77) Wang, S.; Yan, M.; Li, Y.; Vinado, C.; Yang, J. Separating Electronic and Ionic Conductivity in Mix-Conducting Layered Lithium Transition-Metal Oxides. *Journal of Power Sources* **2018**, *393*, 75.

(78) Kamaya, N.; Homma, K.; Yamakawa, Y.; Hirayama, M.; Kanno, R.; Yonemura, M.; Kamiyama, T.; Kato, Y.; Hama, S.; Kawamoto, K.; Mitsui, A. A Lithium Superionic Conductor. *Nature Materials* **2011**, *10* (9), 682.

(79) Han, F.; Zhu, Y.; He, X.; Mo, Y.; Wang, C. Electrochemical Stability of $Li_{10}GeP_2S_{12}$ and $Li_7La_3Zr_2O_{12}$ Solid Electrolytes. *Advanced Energy Materials* **2016**, *6* (8), 1501590.

(80) Zhu, Y.; Connell, J. G.; Tepavcevic, S.; Zapol, P.; Garcia-Mendez, R.; Taylor, N. J.; Sakamoto, J.; Ingram, B. J.; Curtiss, L. A.; Freeland, J. W.; Fong, D. D.; Markovic, N. M. Dopant-Dependent Stability of Garnet Solid Electrolyte Interfaces with Lithium Metal. *Advanced Energy Materials* **2019**, *9* (12), 1803440.

(81) Sharafi, A.; Kazyak, E.; Davis, A. L.; Yu, S.; Thompson, T.; Siegel, D. J.; Dasgupta, N. P.; Sakamoto, J. Surface Chemistry Mechanism of Ultra-Low Interfacial Resistance in the Solid-State Electrolyte $Li_7La_3Zr_2O_{12}$. *Chemistry of Materials* **2017**, *29* (18), 7961.

(82) Julien, C. M.; Mauger, A.; Zaghib, K.; Groult, H. Comparative Issues of Cathode Materials for Li-Ion Batteries. In *Inorganics*, 2014; Vol. 2, pp 132.

(83) Chung, S.-Y.; Choi, S.-Y.; Lee, S.; Ikuhara, Y. Distinct Configurations of Antisite Defects in Ordered Metal Phosphates: Comparison between $LiMnPO_4$ and $LiFePO_4$. *Physical Review Letters* **2012**, *108* (19), 195501.

(84) Yamada, A.; Chung, S. C.; Hinokuma, K. Optimized $LiFePO_4$ for Lithium Battery Cathodes. *Journal of The Electrochemical Society* **2001**, *148* (3), A224.

(85) Ravet, N.; Chouinard, Y.; Magnan, J. F.; Besner, S.; Gauthier, M.; Armand, M. Electroactivity of Natural and Synthetic Triphylite. *Journal of Power Sources* **2001**, *97-98*, 503.

(86) Zhang, M.; Garcia-Araez, N.; Hector, A. L. Understanding and Development of Olivine $LiCoPO_4$ Cathode Materials for Lithium-Ion Batteries. *Journal of Materials Chemistry A* **2018**, *6* (30), 14483.

(87) Moradi, S.; Kundu, S.; Saidaminov, M. I. High-Throughput Synthesis of Thin Films for the Discovery of Energy Materials: A Perspective. *ACS Materials Au* **2022**, *2* (5), 516.

(88) Borhani-Haghighi, S.; Kieschnick, M.; Motemani, Y.; Savan, A.; Rogalla, D.; Becker, H.-W.; Meijer, J.; Ludwig, A. High-Throughput Compositional and Structural Evaluation of a $Li_a(Ni_xMn_yCo_z)O_r$ Thin Film Battery Materials Library. *ACS Combinatorial Science* **2013**, *15* (8), 401.

(89) Beal, M. S.; Hayden, B. E.; Le Gall, T.; Lee, C. E.; Lu, X.; Mirsaneh, M.; Mormiche, C.; Pasero, D.; Smith, D. C. A.; Weld, A.; Yada, C.; Yokoishi, S. High Throughput Methodology for Synthesis, Screening, and Optimization of Solid State Lithium Ion Electrolytes. *ACS Combinatorial Science* **2011**, *13* (4), 375.

(90) McCalla, E.; Carey, G. H.; Dahn, J. R. Lithium Loss Mechanisms During Synthesis of Layered $Li_xNi_{2-x}O_2$ for Lithium Ion Batteries. *Solid State Ionics* **2012**, *219*, 11.
(91) Matsuda, S.; Nishioka, K.; Nakanishi, S. High-Throughput Combinatorial Screening of Multi-Component Electrolyte Additives to Improve the Performance of Li Metal Secondary Batteries. *Scientific Reports* **2019**, *9* (1), 6211.
(92) Potts, K. P.; Grignon, E.; McCalla, E. Accelerated Screening of High-Energy Lithium-Ion Battery Cathodes. *ACS Applied Energy Materials* **2019**, *2* (12), 8388.
(93) Rehman, S.; Sieffert, J. M.; Lang, C. J.; McCalla, E. $Nb_yW_{1-y}O_z$ and $Nb_xTi_{1-x}O_z$ Pseudobinaries as Anodes for Li-Ion Batteries. *Electrochimica Acta* **2023**, *439*, 141665.

Chapter 2

Suite of High-Throughput Experiments for Screening Solid Electrolytes for Li Batteries

Solid-state lithium batteries can potentially offer improved safety and lifespan over current lithium-ion batteries. Moreover, they can increase energy density by enabling the use of a lithium metal anode and high-potential cathodes. However, the development of solid electrolytes is slowed by experimentation where samples are made and studied one composition at a time. To accelerate their development, high-throughput methodologies for screening solid-state electrolytes are needed. Although high-throughput methods have been used to screen room temperature ionic conductivity, this single property is insufficient for ensuring proper function in a solid-state battery. Therefore, this chapter develops a suite of high-throughput methods to synthesize batches of 64 solid-state electrolytes and screen their essential properties for integration into solid batteries. These properties include ionic conductivity, the activation energy for lithium diffusion, electrochemical stability window, and stability against lithium metal. The precision, accuracy, and versatility of our suite are determined for two model materials (LLTO and tetragonal LLZO), which have contrasting properties, by comparing them with the literature.

Chapter 2 is produced with permission from "Jonderian, A.; Anderson, E.; Peng, R.; Xu, P.; Jia, S.; Cozea, V.; McCalla, E. Suite of High-Throughput Experiments for Screening Solid Electrolytes for Li Batteries. *Journal of The Electrochemical Society* **2022**, *169* (5), 050504".

2.1 Abstract

All-solid lithium batteries are an important technology to develop to achieve safer batteries with potentially longer life. Efforts over the past decade have generated a vast list of candidate solid

electrolytes. High-throughput methods have already been useful in this context, but studies have been limited to room temperature ionic conductivities. Although a high ionic conductivity is necessary, this single property is insufficient to ensure function in a solid battery. Herein, a suite of high-throughput methods is introduced where 64 samples are synthesized simultaneously. Herein, we demonstrate for the first time the high-throughput capability of obtaining: (1) ionic conductivities at and above room temperature to extract activation energies, (2) electronic conductivities to evaluate the risk of dendrite growth within pellets, (3) electrochemical stability window, and (4) chemical stability against lithium. Importantly, the stability window is obtained by testing the electrolyte in a composite electrode with conductive carbon, thereby avoiding the overestimations of stability that are rampant in the literature. Each method was validated using two reference materials chosen as they show high contrast for all properties. The results systematically show excellent reproducibility and good agreement with the literature. This suite of techniques provides meaningful properties necessary to evaluate candidate solid electrolytes.

2.2 Introduction

There is a global demand for safer and longer lasting energy storage devices for electric vehicles and grid energy due to the increasing reliance on intermittent renewable energy sources. Solid-state electrolyte based batteries are promising for fulfilling this demand. Commercial lithium-ion batteries are reaching their limits since important issues such as the flammable organic liquid electrolytes and limited electrochemical stability windows continue to limit their performance. Moreover, the liquid electrolyte cannot inhibit dendrite formation at fast-charging rates nor permit the use of lithium metal anodes. In contrast, solid electrolytes (SE) are inflammable and can potentially prevent dendrite formation thus they are considered a promising alternative. Over the past decades, a great deal of research has taken place to obtain solid electrolytes with the highest possible room temperature (RT) ionic conductivity. Indeed, the RT ionic conductivity and activation energy are essential properties to measure as SE with high ionic conductivity and low activation energy is needed to ensure minimal resistance at a wide temperature range. The total ionic conductivity is measured by electrochemical impedance spectroscopy (EIS) on a symmetric cell with two ion-blocking contacts. A few reports have performed these measurements in high-throughput.[1, 2]

However, there are a number of other key properties that must also be fulfilled for a solid electrolyte to be suitable for integration into a full battery.[3] The electronic conductivity, which is not frequently assessed, was shown to be correlated with dendrite formation from the bulk of the SE, with the smallest conductivity giving rise to dendrites being 2.2×10^{-9} S cm^{-1} at room temperature.[4] In the few cases where this property has been reported, DC polarization is used to measure electronic conductivity from the steady-state current. To date, no high-throughput paper has included this measurement. Similarly, solid electrolytes must have a suitable electrochemical stability window (ESW) to enable the use of the anode at low potentials and the desired cathode at high potentials. Recently, it has become abundantly evident that the ESW is overestimated when measured on a Li/SE/Au cell configuration due to the poor electronic conductivity of the SE shutting down the parasitic reactions.[3, 5] Despite this well known error from this method, this approach continues to be utilized in the literature, and this leads to confusion and a lack of attention to the true limits of the materials under study. Obtaining a meaningful result for the stability window requires preparing the solid electrolyte as a working electrode by mixing it with a conductive additive to overcome the poor electronic conductivity of the material.[5-9] To date, very few studies have used this approach and no high-throughput studies have been performed with a suitable method to determine the ESW.

It is also important to note that metallic lithium continues to be an extremely interesting anode given its very high capacities. A solid electrolyte can potentially be used with lithium anodes while its high bulk modulus can prevent dendrite growth from the surface of the lithium. Therefore, it is imperative to investigate the stability of the solid electrolytes against lithium metal. The metallic lithium compatibility is typically investigated by measuring the evolution of the impedance using EIS after bringing the SE in contact with lithium metal.[10]

The conventional method of screening solid electrolytes one composition at a time, coupled with an incomplete suite of property measurements, has slowed down the development of SEs. Consequently, there is a need for high-throughput synthesis and characterization tools for exploring a wide range of composition spaces and the effect of broad substitutions into promising but limited materials. The high-throughput characterization tools should include screening the essential properties mentioned above as illustrated in Figure **2.1**, with the resulting radar plots helping to shortlist promising SEs for additional tests such as compatibility tests with specific cathodes and full cell performance. The high-throughput tools will therefore help elucidate the structure-property relationships guiding the design of new materials. A previous report for high-throughput synthesis and characterization of solid electrolytes was done on thin films, and only structure and ionic conductivity were determined.[1] Previously, we have used the citrate sol-gel method as a versatile synthesis route to produce a variety of ceramics of high interest for battery materials.[2, 11-13] The characterization of solid electrolytes in our previous work was limited to room temperature ionic conductivities. Thus, herein, we developed high-throughput tools for screening solid-state electrolytes. We validated our setups by studying two model solid electrolytes: perovskite Li_{23}-La_{27}-Ti_{50} and garnet $Li_7La_3Zr_2O_{12}$. These two materials were chosen for their contrasting properties for the tests performed here. We optimized the citrate sol-gel method for synthesizing 64 samples and measured the key properties required for a good solid electrolyte using our developed high-throughput characterization tools, as illustrated in Figure **2.1**.

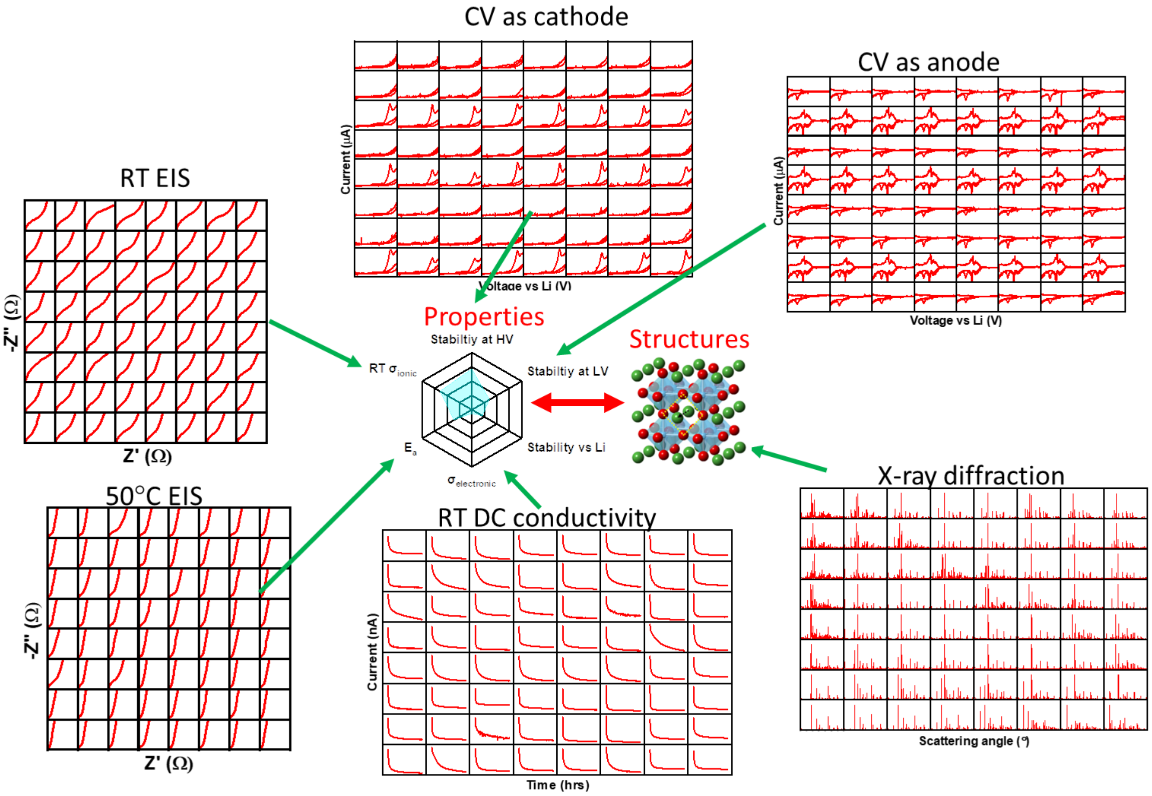

Figure 2.1 *High-throughput structural and electrochemical characterization tools for solid electrolyte discovery and screening. All measurements are performed on 64 samples at once and result in the properties shown in the radar plot: room temperature ionic conductivity (σ_{ionic}), activation energy (E_a), electronic conductivity ($\sigma_{electronic}$), stability at low voltage (LV) and high voltage (HV). Each measurement is shown in greater detail throughout this manuscript.*

2.3 Experimental methods

The various steps in Figure **2.2** illustrate the methods used throughout. This demonstrates the typical workflow in our high-throughput studies of SEs. The solid electrolytes were synthesized by the citrate sol-gel method described in detail in ref. [13]. Solutions were prepared from the starting reagents in DI or ethanol (Ti only). Two materials were made for the proof-of-concept herein: lithium lanthanum titanate (LLTO) and undoped tetragonal lithium lanthanum zirconate (LLZO). These two materials were selected for their contrast in properties (e.g. the undoped LLZO

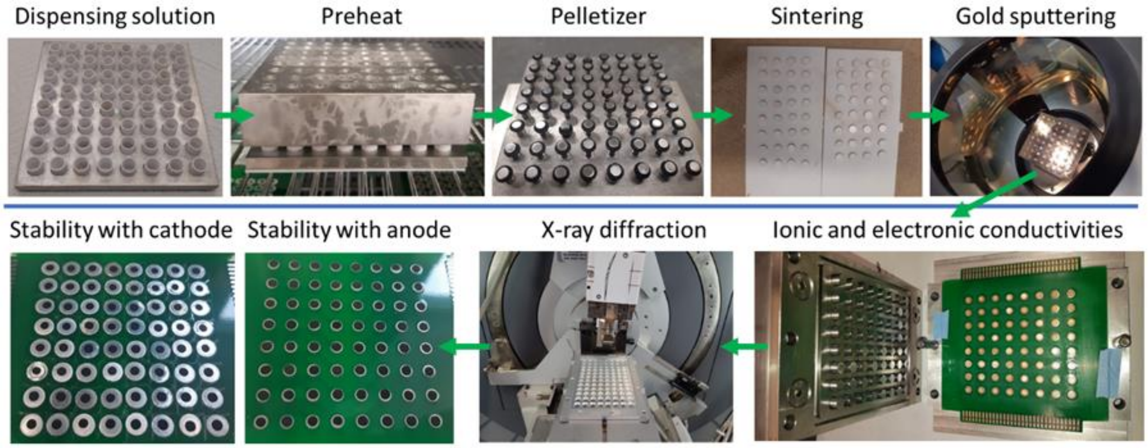

Figure 2.2 *The scheme of the high-throughput synthesis and structural/chemical/electrochemical characterization of solid electrolytes. Precursors are first dispensed into 64 alumina cups, then preheated with an aluminum plate to prevent mixing, samples are then pelletized in high-throughput, sintered to high temperature on alumina plates. Prior to conductivity tests, pellets are coated with gold, then assembled in the house-made cell with spring mounted contacts. After conductivity measurements, samples are crushed into powders and XRD is performed. Finally, the powders are mixed into slurries to make electrodes for the electrochemical stability tests on aluminum for HV, and on gold for LV.*

has a low ionic conductivity while the LLTO show a much higher conductivity as per refs. [24-25]) such that a high-throughput suite of methods must be able to obtain precise measures for both these materials in order to be useful in developing new materials that could start with poor properties and be improved with doping and/or changing synthesis conditions. For the synthesis of LLTO, first citric acid (4 M) was pipetted followed by the addition of $Ti(OCH_2CH_2CH_2CH_3)_4$ (98+% Acros Organics) (2M EtOH), $La(NO_3)_3$ (99.9% Alfa Aesar) (2M) and lastly $LiNO_3$ (99% Alfa Aesar) (2M) in mole percentages of 13/15/29/43 for Li/La/Ti/citric acid. For the synthesis of LLZO we used $LiNO_3$, $La(NO_3)_3$, and $Zr(OH)_2(OAc)_2$ (Sigma Aldrich) in a mole ratio of 7/3/2 respectively, followed by the addition of citric acid (4M) for a total cations to citric ratio of 1:0.75. The bulk content of the solvent was dried by heating at 80 °C for 12 hours after placing a smokestack above the cups to prevent cross-contamination during the heat treatments. After the powders were calcinated at 600 °C for 6 hours, green pellets were prepared in a homemade high-throughput pellet die (1 GPa maximum pressure). The LLTO pellets were sintered at 1200 °C for 6 hours while the LLZO were sintered at 900 °C for 3 hours. The surface of the sintered pellets was sanded with diamond sanding paper (800 grit). To determine reproducibility and precision, 64 LLTO pellets of identical composition were made herein. Furthermore, to demonstrate the contrast between materials for each characterization method, a few LLZO samples were also synthesized in the same high-throughput method.

Gold contacts were sputtered on the two faces of the polished pellets for the EIS and DC polarization measurements using the high-throughput cell described in refs. [13]. A Biologic SP150 potentiostat coupled with a Pickering multiplexer was used to measure the electrical response from 1MHz to 1Hz at 100 mV at RT and 50 °C to determine the activation energy from the Arrhenius plot. Prior to the 50 °C measurement, the cell was allowed to stabilize for 12 h (the high-throughput cell has a large thermal mass), such that the total measurement time is approximately 16 h (2 h per EIS for 64 samples, and 12 h stabilization). The EIS spectra were analyzed using the Z-fit tool of EC-Lab software in batch mode. The DC polarization measurements were done using a Keithley 213 quad voltage source with Keithley 2750 multimeter (the same high-throughput pseudo-potentiostat as used to do cyclic voltammetry for cathodes in refs. [13, 14]). However, to get the precision required, high resistance and high precision (10 kΩ) resistors were used to measure small currents through the pellets. Various DC voltages (0.5, 1, 1.5, 2, 2.5 V) were applied, and the current was measured for 1 h. The Keithley 2750 has an internal impedance of 10 GΩ in the voltage ranges utilized herein.[15] We, therefore, estimate the minimum measurable current to be 1 nA at 1 V (this corresponds to a resistance 10 times smaller than the internal impedance of the instrument). This low current corresponds to a conductivity of approximately 10^{-10} S cm^{-1} for our typical pellets with 5 mm diameters and thicknesses of about 0.4 mm. This is our estimate of the lowest measurable electronic conductivity for this instrument.

The gold contacts were then removed by sanding following the conductivity measurements, and the pellets were ground into powder. The powders were transferred into a high-throughput XRD holder where the samples lied on a thin mylar film. The XRD measurement of 64 samples required 10 h in transmission mode using a Panalytical goniometer equipped with a Mo X-ray source and a GaliPIX detector. The XRD data could be analyzed using either Rietveld or Pawley refinement methods as demonstrated in refs.[2, 12, 14]. The precision and reproducibility of the synthesis and XRD results have been shown to be excellent elsewhere.[13]

After XRD characterization, the powders were then transferred into stainless steel cups to prepare 64 electrode slurries for cycling to either a high or low potential for determining the stability window. Unlike our high-throughput studies on cathodes (e.g. refs.[11, 12, 14]) where a high loading was used to replicate industrial standards, we used here a low loading (approximately 1mg/cm^2) to ensure that poor transport within the electrode (that is composed of an insulating solid electrolyte) does not lead to overestimating the stability window. A PVDF and carbon black solution was prepared in NMP. This solution was pipetted into 64 cups containing pre-weighed sample powders. Stirring for 15 min using a stir bar followed. The weight ratios (wt. %) of the electrode mixture SE:CB:PVDF were 84:11:5. Next, 3 μL of electrode slurry were pipetted onto each of the 64 pads of two printed circuit boards serving as current collectors in our high-throughput cells (Figure **2.2**). The first PCB had pads covered with gold to test the electrolytes' stability at low potentials and the other with aluminum for the high potential stability test. After drying the electrodes at 80 °C, the high-throughput electrochemical half-cell was assembled using two Whatman microfiber separators, liquid electrolyte (LE) which consists of 1M LiPF6 in

EC/EMC = 3/7 (Soulbrain), and lithium foil. The electrochemical stability window test CVs were run on the same setup used for electronic conductivity measurement but with 1 kΩ resistors used to measure the current through each cell. The voltage was swept from 3 to 5.5 V for the high voltage (HV) test and from 3 to 0.1 V for the low voltage (LV) test at a sweeping rate of 0.1 V/h. Both cells were cycled for 1.5 cycles in order to be able to observe whether or not passivation occurred.

Importantly, all of the above could be performed on a single set of samples using the workflow proposed. In order to better identify the limitations of using carbonate-based electrolytes for these tests, a single sample of LLTO was also tested to high potential in a Swagelok cell using ionic liquid (IL) electrolyte (0.3 M bistrifluoromethanesulfonimide lithium salt from Sigma-Aldrich in 1-Butyl-1-methylpyrrolidinium bistrifluoromethanesulfonylimide ionic liquid from TCIchemicals). Finally, another batch of LLTO and LLZO samples was synthesized to test the chemical stability against lithium. Given the potential damage done by lithium contact and that this test required pellets, we saw no alternative but to prepare a second set when stability measurements vs. lithium were required. In this final test, one side of the pellets was sputtered with gold, and on the other side, a small disk of lithium foil was placed against the electrolyte. Then, the EIS measurement was performed at different time intervals to track the interfacial impedance evolution using the previous EIS parameters.

2.4 Results & discussion

2.4.1 Ionic conductivity

Screening the ionic conductivity of solid electrolytes is essential because high ionic conductivity is essential to minimize the internal resistance of the cell. The ionic conductivity of a solid electrolyte is measured by electrochemical impedance spectroscopy (EIS). The total electrical conductivity of 64 similar composition LLTO samples was measured by EIS on a symmetric cell with gold ion blocking electrodes. Due to the negligible electronic conductivity of LLTO measured in the following electronic conductivity test, the electrical conductivity is considered to correspond to the ionic conductivity. The Nyquist plots of the 64 LLTO samples shown in Figure **2.3** consist of two semicircle arcs and a tail at low, medium, and high frequencies, respectively. The EIS spectrum was fitted to an equivalent circuit consisting of two RC circuits in series with a capacitor (ref. [2, 13]). The capacitors were replaced by a constant phase element to model the non-ideal impedance response. The first semicircle arc is assigned to the bulk conductivity and the second to the grain boundary, while the tail corresponds to the polarization of the blocked ions at the SE/Au interface. The EIS measurements were performed at 22 °C and 50 °C, and the activation energy was extracted from the Arrhenius plot. The conductivities and activation energies obtained here and from the literature are given in Table **2.1**. The bulk and grain boundary conductivities

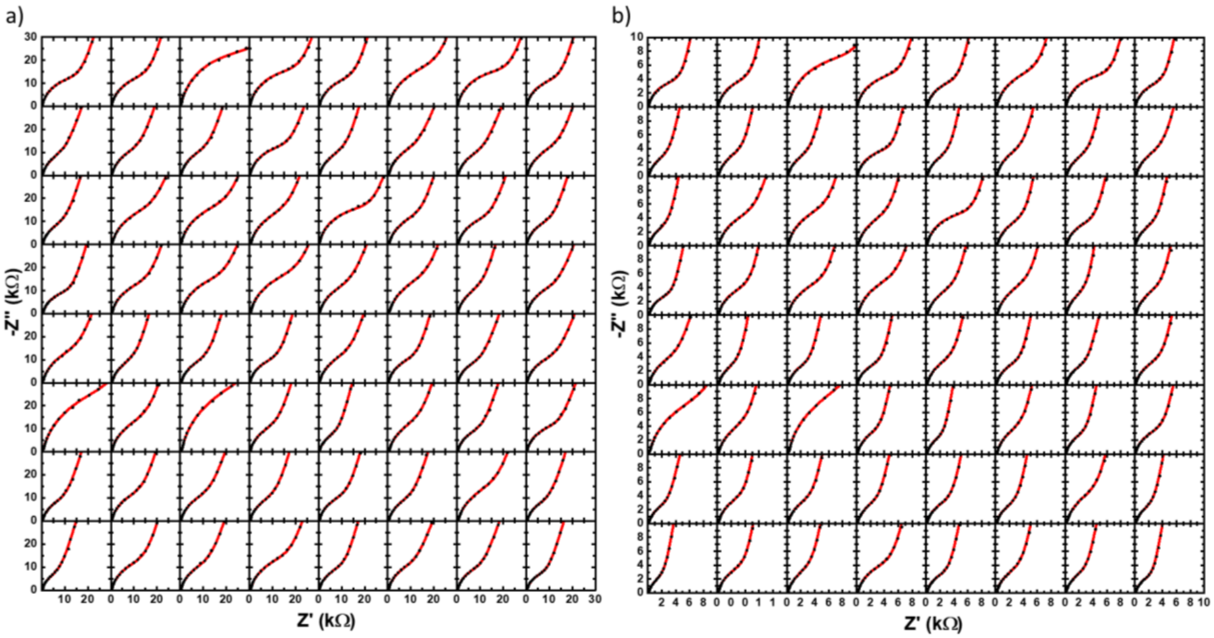

Figure 2.3 *Nyquist plots of identical LLTO samples measured on Au/LLTO/Au cell using EIS at (a) 22 °C, and (b) 50 °C. The red lines are the fits to the equivalent circuit. From the fits, ionic conductivity and activation energy are extracted and presented in* ***Table 2.1****.*

Table 2.1 *Ionic conductivity, activation energy, electronic conductivity, and electrochemical stability window of LLTO and LLZO, all obtained using our high-throughput methods in this study and compared to results from traditional studies in the literature. The uncertainties on all values from this study are the standard deviations on the measurements and therefore represent the precisions of the high-throughput techniques developed here.*

Parameter	LLTO		LLZO	
	This study	Literature	This study	Literature
σ_{bulk} (S cm^{-1})	$(1.28 \pm 0.27) \times 10^{-3}$	$(1.32 \pm 0.2) \times 10^{-3}$ (16)	1.36×10^{-6}	1.63×10^{-6} (17)
σ_{gb} (S cm^{-1})	$(4.37 \pm 1.22) \times 10^{-5}$	$(5.01 \pm 0.3) \times 10^{-5}$ (16)	-----	-----
$E_{a,bulk}$ (eV)	0.27 ± 0.01	0.27 (18)	0.51	0.54 (17)
$E_{a,gb}$ (eV)	0.38 ± 0.02	0.36 (18)		
ESW (V)	1.78 – 4.7*	1.8 (19) – **	0 – 4	0 – 4 (5)
σ_e (S cm^{-1})	$(3 \pm 2) \times 10^{-10}$ (<1.5V) $(8 \pm 4) \times 10^{-10}$ (2V) $(32 \pm 4) \times 10^{-10}$ (2.5V)	5.59×10^{-10} (1-2V) (20)	1.28×10^{-7} (1V)	1.2×10^{-7} (0.1V) (21)

of 64 LLTO samples obtained here are $(1.28 \pm 0.27) \times 10^{-3}$ S cm^{-1} and $(4.37 \pm 1.22) \times 10^{-5}$ S cm^{-1}, respectively. Note: the uncertainties here are standard deviations such that they give a good indication of the variations to be expected in single sample measurements. We found standard deviations about 20 % or lower for conductivity values. Given that the objective in screening solid electrolytes is to obtain ionic conductivities above a certain threshold, this level of precision is certainly sufficient. Furthermore, the activation energies were 0.28 eV for bulk conductivity and 0.37 eV for grain boundary conductivity. The activation energies are in excellent agreement with the literature values as shown in Table **2.1** while also showing very low standard deviations (0.02 eV at most) showcasing the high degree of reproducibility obtained in the activation energy

measurements. Furthermore, for LLZO, a bulk conductivity of 1.36 × 10^{-6} S cm^{-1} was obtained with an activation energy of 0.51 eV, again in excellent agreement with the literature for this

composition. These tests clearly show that the EIS setup is valid for a wide range of conductivity values as it has the reproducibility and precision necessary to effectively screen solid electrolytes. Furthermore, Figure **S2.1**a shows the result for a single LLTO sample in a Swagelok style cell obtained at 4 different temperatures. The resulting values for activation energy are 0.30 eV (bulk) and 0.36 eV (grain), in good agreement with the result obtained in high-throughput at 2 temperatures only. We, therefore, feel this setup is optimal and effective for both RT ionic conductivities and near RT activation energies.

2.4.2 Electronic conductivity

The electronic contribution to the total electrical conductivity was measured by the DC polarization method. The electronic conductivity was calculated from the steady-state currents after applying different DC polarizations: 0.5, 1, 1.5, 2, and 2.5 V were applied to a symmetric Au/SE/Au cell, while the current was recorded for 60 min. As shown in Figure **2.4**a, the total current decreases due to the decay of the ionic current until it reaches a steady-state current, which corresponds to the electronic contribution to conductivity. Li/Se/Au cell configuration is not recommended for high-throughput studies because of the instability of some SE against lithium preventing its systematic use. The I-t plots of the Au/LLTO/Au cell under 2V is shown in Figures **2.4** and **S2.2**. Clearly, the electronic conductivity lies well below the value of 2.2 ×10^{-9} S cm^{-1} where dendrite growth is a concern as discussed in the introduction, such that we can conclude that dendrite growth will be greatly mitigated in LLTO, especially in comparison to LLZO that shows conductivities well above this value. Figure **2.4** also shows the extracted electronic conductivities as a function of the applied voltages. The electronic conductivity of LLTO showed ohmic behavior between 0.5 V and 1.5 V, while the conductivities increased like a varistor at 2-2.5 V (Figure **2.4**b). The electronic conductivity measured for LLTO in the ohmic range is therefore (3 ± 2) × 10^{-10} S cm^{-1}. Again, this level of precision is excellent given that the required purpose is to determine if the electronic conductivity is below 3 × 10^{-9} S cm^{-1}. The value reported here is consistent with previous reports as shown in Table **2.1**; importantly, the best agreement is found for reports where the measurements were performed in the Ohmic range.[20, 22, 23] To make sure the setup is versatile and able to measure electronic conductivities above the dendrite threshold, the electronic conductivity of the LLZO was determined. The electronic conductivity of LLZO was 1.28 × 10^{-7} S cm^{-1} at 1 V, in good agreement with what was found by Chen.[21] It is well known in the literature that electronic conductivity is a concern in garnet LLZO materials while not for perovskite electrolytes.[3] The fact that the high-throughput setup here dramatically shows this contrast confirms that this system will be effective in screening this important property for ceramic solid electrolytes.

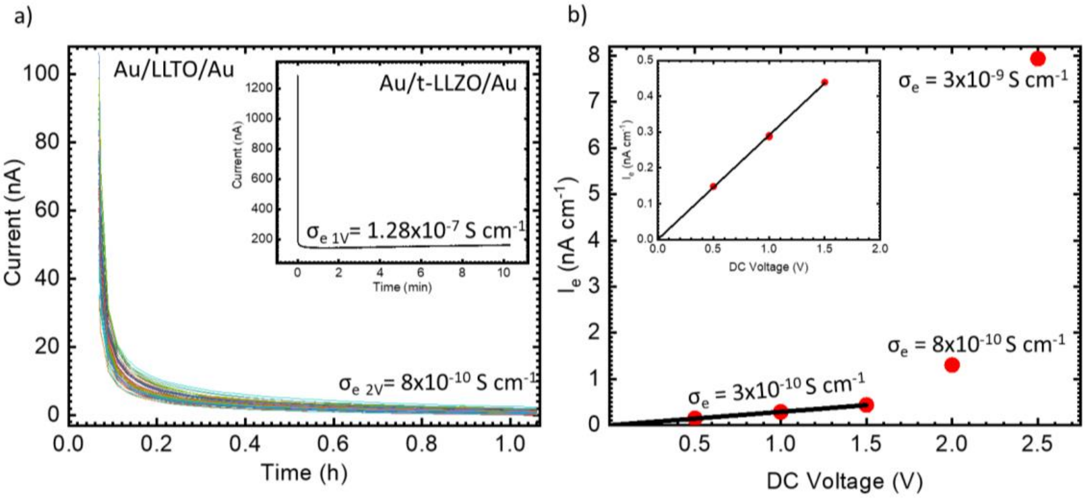

***Figure 2.4** (a) DC polarization curves for 64 identical LLTO samples and a single LLZO sample (inset) measured in Au/SE/Au cell configuration. (b) The average steady state current (I_e) for the LLTO samples vs the applied DC voltage. The inset is a zoom-in on the Ohmic region.*

2.4.3 Electrochemical stability window

Solid electrolytes should have a wide electrochemical stability window including the operation potentials of both electrodes. In our high-throughput methodology, the limits of the electrochemical stability window are determined by cyclic voltammetry of two cells. Working electrodes were prepared from the solid electrolytes by mixing them with carbon black to ensure sufficient electronic paths. Lithium half-cells were assembled using a liquid carbonate based electrolyte to ensure the ionic conduction does not limit current. Each sample was divided into two, one swept to 5.5 V and the other to 0.1 V as shown in Figure **2.5**. In each cell, we alternated a row of blank cells (carbon black and PVDF only, in the same quantities as in the electrodes with electrolyte) with rows of LLTO and LLZO. The Faradaic current of the solid electrolytes can then be compared to the blanks, and the point where the two diverge is identified as the end of the stability window. Figure **2.5** clearly shows (as in refs. [11, 14]) that there is no cross-contamination between neighboring samples and the CVs of duplicates are highly reproducible. For the low voltage tests, the CVs of Li/LE/LLTO-C cells in Figures **2.5**a, **2.6**, and **S2.3** a show a large reductive current (~-4.0 µA) below 1.78 V, which is reversible and shows in the second cycle, indicating its instability (interphase propagation). This value is close to the theoretical value 1.75 V[24] also consistent with the previous experimental value of 1.8 V[19]. In contrast, the CV of Li/LE/LLZO-C at low voltages does not show reductive current compared to the carbon black indicating that it remains stable all the way down to 0.1 V. However, it must be acknowledged that determining the stability of SE at voltages close to zero is challenging because of the interference provided by the significant electrolyte degradation as the SEI builds. Thus, in cases where rigorous confirmation of low voltage stability is required, then a repetition of the test will be performed with a more stable liquid electrolyte (e.g., ionic liquid). We do not propose ionic liquid electrolytes

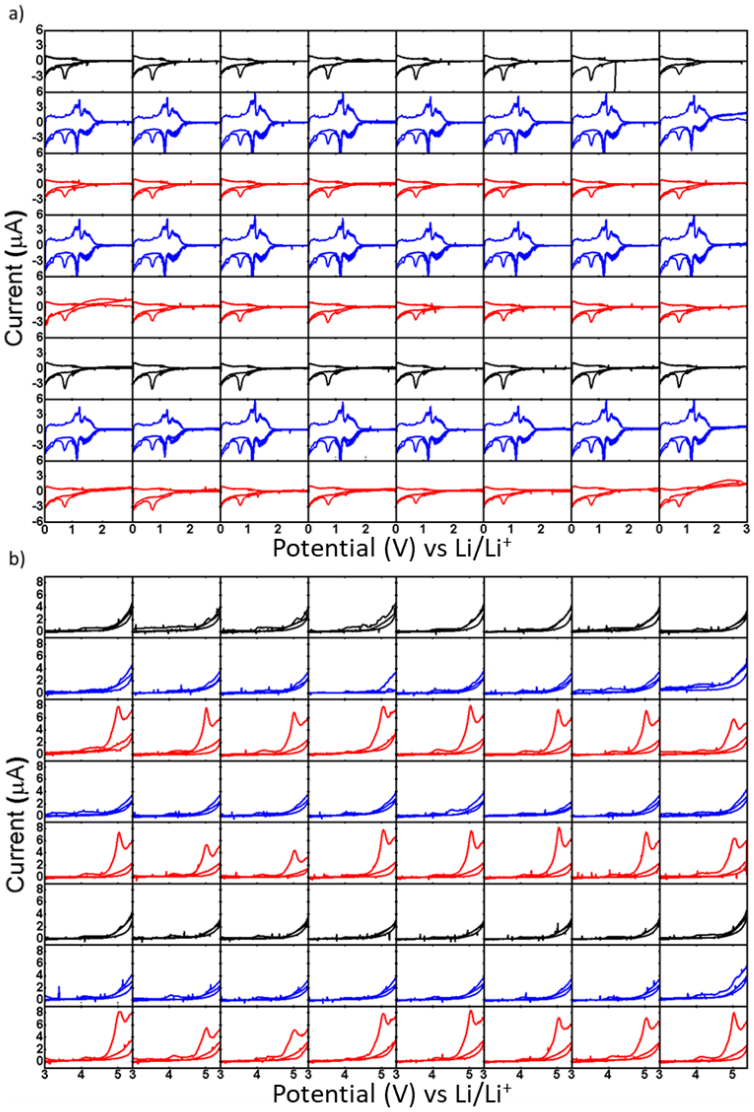

Figure 2.5 *(a) CV profiles of identical LLTO samples (blue), LLZO samples (red) and blank (carbon black and PVDF only, black) swept from 3 V down to 0.1 V at 0.1 V/h scan rate. The solid electrolytes were made into electrodes as described in the text for this electrochemical stability window test. (b) CV profiles from 3-5.5 V at 0.1 V/h scan rate in a half cell configuration with the solid electrolytes made into electrodes for electrochemical stability window test. Both sets of CVs were run for 1.5 cycles.*

for high-throughput screening given the high cost of ionic liquids, but we utilize it on occasion to confirm/refine high-throughput results (as illustrated below for the high voltage stability of LLTO). In the high voltage stability tests shown in Figures **2.5**b, **2.6**b, **S2.3**b and **S2.4** both LLTO and LLZO show small irreversible oxidative currents at 4.0 V (~0.5 μA), which do not appear on

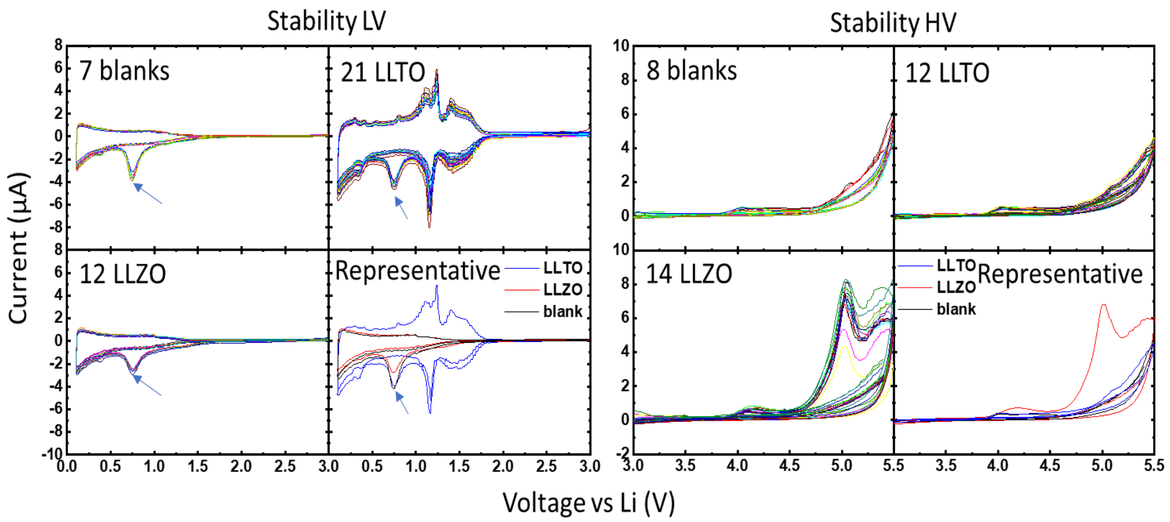

Figure 2.6 *Electrochemical stability of LLTO and LLZO at low and high voltage from Figure* ***2.5****, overlayed for comparison. The CVs of same composition LLTO, LLZO, and blank cycled as cathodes shows the accuracy of the tool. The arrow indicates the feature that appeared on the first cycle. The stability windows in Table* ***2.1*** *were extracted from this data.*

the second cycle and also appear in the blanks. The irreversibility could be caused by an irreversible process or the formation of a high impedance interphase (ionic and/or electronic insulating interphase causing sluggish kinetics). Figure **S2.3** shows clearly that LLZO exceeds the current of the blanks at 4.0 V and above, while LLTO does not exceed the blank at any voltage. Therefore, even in this case where electrolyte degradation interferes, we can establish the end of the stability window of our solid electrolytes: 4.0 V for LLZO, while the LLTO appears to be stable over the entire range. As shown in Table **2.1**, this is in good agreement with the few reports of ESW in the literature that use a reliable method as discussed in the introduction. This oxidation limit determined for LLZO by the CV test is the same as the value obtained by Han[5] showing that our high-throughput stability test is consistent with the few appropriate results in the literature. However, for LLTO it is difficult to be conclusive about the stability window's upper limit given the interference by electrolyte degradation. Therefore, in Figure **S2.4** we repeat the measurements in ionic liquid electrolyte that shows very little degradation in the blanks. The result shows that the upper limit of the stability window for LLTO is in fact 4.7 V.[24] The higher experimental limits compared to the theoretical could be explained by the sluggish kinetic (overpotential).[5, 24] We therefore intend to use the test with the ionic liquid in cases where the solid electrolyte appears to be stable over the entire range (or as stable as the blank) in the high-throughput screening.

2.4.4 Chemical compatibility with lithium

Solid electrolytes can achieve high energy density when used with lithium metal anodes, so checking their compatibility is crucial. The stability of the SE against lithium was explored by measuring the EIS of asymmetric cell Li/Se/Au at different time intervals. Figure **2.7**a shows the impedance evolution of Li/LLTO/Au and Li/LLZO/Au cell with time. The total electrical conductivity of Li/LLTO/Au increased by time while the low-frequency tail, as shown in Figure **2.7**b disappeared, indicating the presence of electronic conductivity. This signifies the formation and propagation of a mixed conductor phase as was previously explored.[25] On the other hand, the total electrical conductivity of the Li/LLZO/Au decreased initially and later remained constant similar to others' observation[26] indicating stable interphase formation. These results are again consistent with the well-known trends in the literature that LLTO shows instability vs. Li metal while LLZO does not.[10, 25]

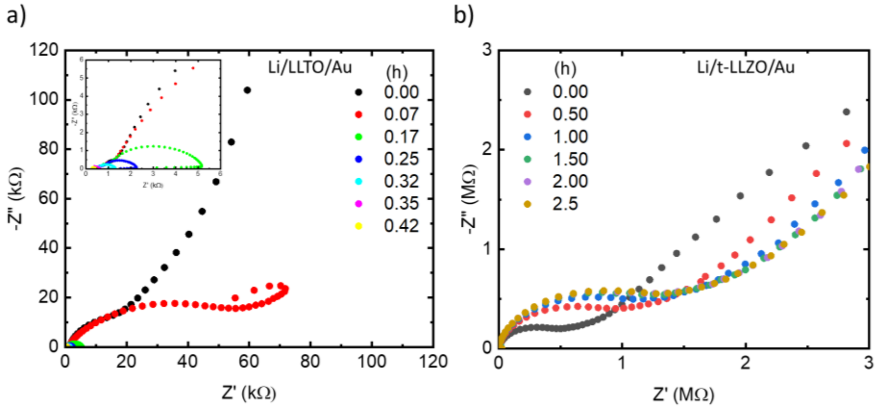

Figure 2.7 *The EIS spectra evolution as a function of time after contact with lithium. The Nyquist plots are shown for LLTO (the inset is an expanded view of the high frequency region) (a) and LLZO (b) in the asymmetric configuration Li/SE/Au.*

2.5 Conclusion

Although screening essential properties for solid electrolytes has emerged as a significant bottleneck in developing all-solid lithium batteries, no robust high-throughput methodology was previously reported for screening any property other than room temperature ionic conductivity. The tools introduced herein allow the high-throughput synthesis of solid electrolytes and screening various properties required for their integration into solid batteries. All methods are designed for sets of 64 samples and enable the fast automated testing of the ionic conductivity (2 h), activation energy (an extra 14 h), electronic conductivity (4 h to ensure we are in the Ohmic region), electrochemical stability window (2 cells running for 54 h) and the chemical stability against lithium (1 h per sample). The workflow is such that all tests (except lithium stability) can be performed on a single batch of samples in a 1-2 weeks time span). The stability against lithium is then to be utilized on a selection of samples that show promising stability at low potentials in the stability window test. The properties of two model materials LLTO and LLZO were measured in high-throughput using our infrastructure, and systematically the results showed excellent agreement with the literature, and produced small standard deviations thereby enabling effective and reproducible screening of these critical properties. The two materials were selected for their contrast in properties (e.g. the undoped LLZO showed a low ionic conductivity while the LLTO showed a much higher conductivity) such that the suite of methods has now been shown to be effective for materials over a wide range of properties’ values. Furthermore, low standard deviations obtained for repeats of the same compositions systematically show that the high-throughput methods will have high precision in identifying materials with improved properties. This system is therefore now optimized to advance the development of novel solid electrolyte chemistries.

2.6 Acknowledgments

This work was funded by a New Frontiers in Research Fund grant, by the Natural Sciences and Engineering Research Council of Canada under the auspices of a Discovery grant and by an FRQNT new researcher grant.

2.7 Supporting information

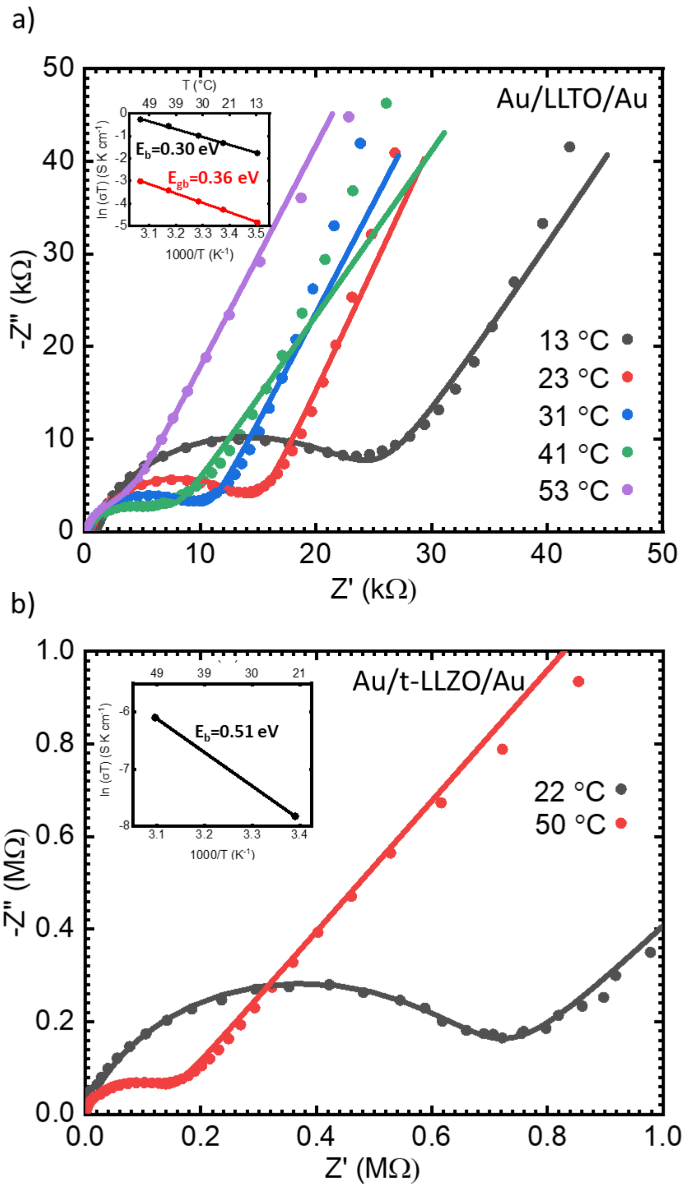

Figure S2.1 *Nyquist and Arrhenius (inset) plots of (a) LLTO and (b) t-LLZO measured in Au/SE/Au cell configuration. The dots are the experimental data, and the lines are the fits.*

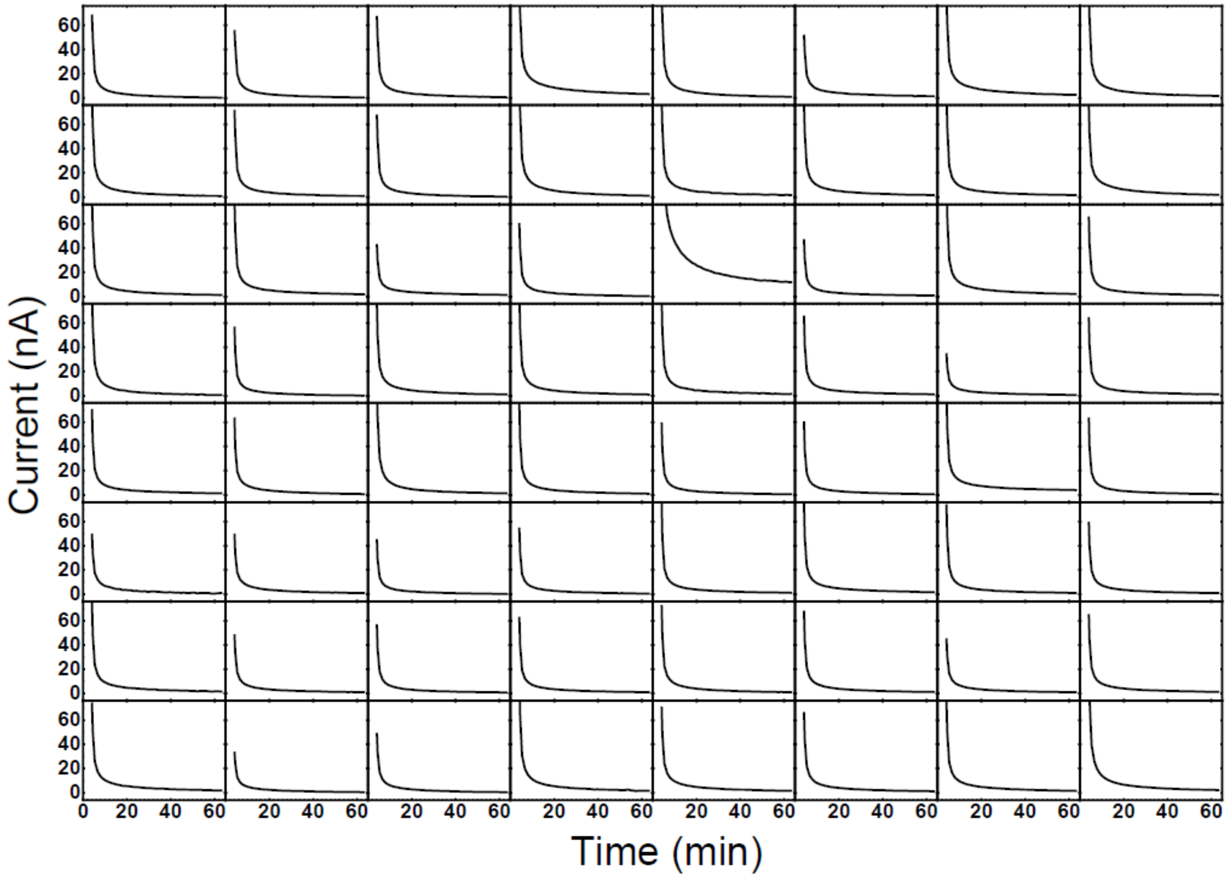

Figure S2.2 *DC polarization curves for 64 LLTO samples in Au/LLTO/Au configuration at 2 V for 60 min for electronic conductivity measurement. There is only 1 outlier (row3, column5). The electronic conductivities are calculated from the steady state currents using Ohm's Law.*

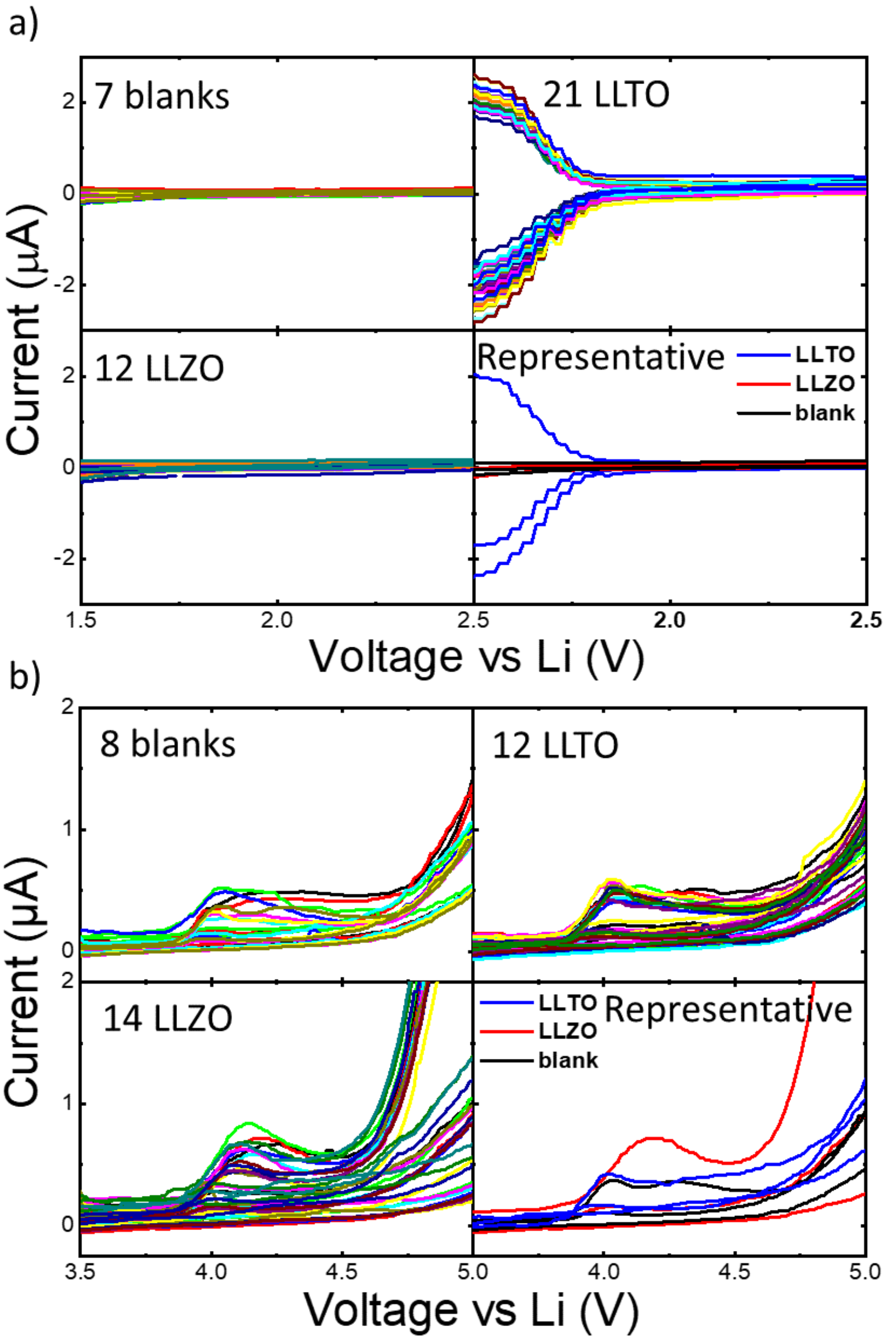

Figure S2.3 *Electrochemical stability of LLTO and LLZO at low and high voltage assessed via preparing a composite electrode (SE+CB+PVDF) and performing CVs at a scanning rate of 0.1 V/h. The blanks contain carbon black and PVDF without SE.*

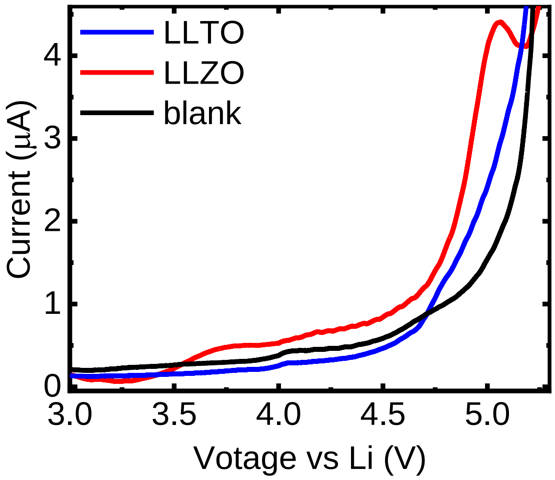

Figure S2.4 *High-voltage stability test of LLTO and LLZO in 0.3 M LiTFSI salt in ionic liquid electrolyte at 50 ℃ to overcome the viscosity of the ionic liquid.*

2.8 References

(1) Beal, M. S.; Hayden, B. E.; Le Gall, T.; Lee, C. E.; Lu, X.; Mirsaneh, M.; Mormiche, C.; Pasero, D.; Smith, D. C. A.; Weld, A.; Yada, C.; Yokoishi, S. High Throughput Methodology for Synthesis, Screening, and Optimization of Solid State Lithium Ion Electrolytes. *ACS Combinatorial Science* **2011**, *13* (4), 375.

(2) Jonderian, A.; Ting, M.; McCalla, E. Metastability in Li–La–Ti–O Perovskite Materials and Its Impact on Ionic Conductivity. *Chemistry of Materials* **2021**, *33* (12), 4792.

(3) Jonderian, A.; McCalla, E. The Role of Metal Substitutions in the Development of Li Batteries, part II: Solid Electrolytes. *Materials Advances* **2021**, *2* (9), 2846.

(4) Han, F.; Westover, A. S.; Yue, J.; Fan, X.; Wang, F.; Chi, M.; Leonard, D. N.; Dudney, N. J.; Wang, H.; Wang, C. High Electronic Conductivity as the Origin of Lithium Dendrite Formation Within Solid Electrolytes. *Nature Energy* **2019**, *4* (3), 187.

(5) Han, F.; Zhu, Y.; He, X.; Mo, Y.; Wang, C. Electrochemical Stability of $Li_{10}GeP_2S_{12}$ and $Li_7La_3Zr_2O_{12}$ Solid Electrolytes. *Advanced Energy Materials* **2016**, *6* (8), 1501590.

(6) Hakari, T.; Nagao, M.; Hayashi, A.; Tatsumisago, M. All-Solid-State Lithium Batteries With Li_3PS_4 Glass as Active Material. *Journal of Power Sources* **2015**, *293*, 721.

(7) Hakari, T.; Fujita, Y.; Deguchi, M.; Kawasaki, Y.; Otoyama, M.; Yoneda, Y.; Sakuda, A.; Tatsumisago, M.; Hayashi, A. Solid Electrolyte with Oxidation Tolerance Provides a High-Capacity Li_2S-Based Positive Electrode for All-Solid-State Li/S Batteries. *Advanced Functional Materials* **2022**, *32* (5), 2106174.

(8) Dewald, G. F.; Ohno, S.; Kraft, M. A.; Koerver, R.; Till, P.; Vargas-Barbosa, N. M.; Janek, J.; Zeier, W. G. Experimental Assessment of the Practical Oxidative Stability of Lithium Thiophosphate Solid Electrolytes. *Chemistry of Materials* **2019**, *31* (20), 8328.

(9) Swamy, T.; Chen, X.; Chiang, Y.-M. Electrochemical Redox Behavior of Li Ion Conducting Sulfide Solid Electrolytes. *Chemistry of Materials* **2019**, *31* (3), 707.

(10) Zhu, Y.; Connell, J. G.; Tepavcevic, S.; Zapol, P.; Garcia-Mendez, R.; Taylor, N. J.; Sakamoto, J.; Ingram, B. J.; Curtiss, L. A.; Freeland, J. W.; Fong, D. D.; Markovic, N. M. Dopant-Dependent Stability of Garnet Solid Electrolyte Interfaces with Lithium Metal. *Advanced Energy Materials* **2019**, *9* (12), 1803440.

(11) Adhikari, T.; Hebert, A.; Adamič, M.; Yao, J.; Potts, K.; McCalla, E. Development of High-Throughput Methods for Sodium-Ion Battery Cathodes. *ACS Combinatorial Science* **2020**, *22* (6), 311.

(12) Jia, S.; Counsell, J.; Adamič, M.; Jonderian, A.; McCalla, E. High-Throughput Design of Na–Fe–Mn–O Cathodes for Na-Ion Batteries. *Journal of Materials Chemistry A* **2022**, *10* (1), 251.

(13) McCalla, E.; Parmaklis, M.; Rehman, S.; Anderson, E.; Jia, S.; Hebert, A.; Potts, K.; Jonderian, A.; Adhikari, T.; Adamič, M. Combinatorial Methods in Advanced Battery Materials Design. *Canadian Journal of Chemistry* **2021**, *100* (2), 132.

(14) Potts, K. P.; Grignon, E.; McCalla, E. Accelerated Screening of High-Energy Lithium-Ion Battery Cathodes. *ACS Applied Energy Materials* **2019**, *2* (12), 8388.

(15) *Model 2750 Multimeter/Switch System User's Manual*. https://www.tek.com/en/switching-and-data-acquisition-systems/2700-multimeter-data-acquisition-switch-systems-manual/mode-3.

(16) Morata-Orrantia, A.; García-Martín, S.; Alario-Franco, M. Á. Optimization of Lithium Conductivity in La/Li Titanates. *Chemistry of Materials* **2003**, *15* (21), 3991.

(17) Awaka, J.; Kijima, N.; Hayakawa, H.; Akimoto, J. Synthesis and structure analysis of tetragonal Li7La3Zr2O12 with the garnet-related type structure. *Journal of Solid State Chemistry* **2009**, *182* (8), 2046.

(18) Aguesse, F.; López del Amo, J. M.; Roddatis, V.; Aguadero, A.; Kilner, J. A. Enhancement of the Grain Boundary Conductivity in Ceramic $Li_{0.34}La_{0.55}TiO_3$ Electrolytes in a Moisture-Free Processing Environment. *Advanced Materials Interfaces* **2014**, *1* (7), 1300143.

(19) Chen, C. H.; Amine, K. Ionic Conductivity, Lithium Insertion and Extraction of Lanthanum Lithium Titanate. *Solid State Ionics* **2001**, *144* (1), 51.

(20) Cheng, X.; Wang, J.; Qiang, W.; Huang, B. Improvement in electronic conductivity of perovskite electrolyte by variable-valence element doping. *Journal of the American Ceramic Society* **2020**, *103* (6), 3698.

(21) Chen, Y.-T.; Jena, A.; Pang, W. K.; Peterson, V. K.; Sheu, H.-S.; Chang, H.; Liu, R.-S. Voltammetric Enhancement of Li-Ion Conduction in Al-Doped $Li_{7-x}La_3Zr_2O_{12}$ Solid Electrolyte. *The Journal of Physical Chemistry C* **2017**, *121* (29), 15565.

(22) Sutorik, A. C.; Green, M. D.; Cooper, C.; Wolfenstine, J.; Gilde, G. The Comparative Influences of Structural Ordering, Grain Size, Li-Content, and Bulk Density on the Li^+-Conductivity of $Li_{0.29}La_{0.57}TiO_3$. *Journal of Materials Science* **2012**, *47* (19), 6992.

(23) Emery, J.; Buzare, J. Y.; Bohnke, O.; Fourquet, J. L. Lithium-7 NMR and Ionic Conductivity Studies of Lanthanum Lithium Titanate Electrolytes. *Solid State Ionics* **1997**, *99* (1), 41.

(24) Zhu, Y.; He, X.; Mo, Y. Origin of Outstanding Stability in the Lithium Solid Electrolyte Materials: Insights from Thermodynamic Analyses Based on First-Principles Calculations. *ACS Applied Materials & Interfaces* **2015**, *7* (42), 23685.

(25) Inaguma, Y.; Liquan, C.; Itoh, M.; Nakamura, T.; Uchida, T.; Ikuta, H.; Wakihara, M. High Ionic Conductivity in Lithium Lanthanum Titanate. *Solid State Communications* **1993**, *86* (10), 689.

(26) Sharafi, A.; Yu, S.; Naguib, M.; Lee, M.; Ma, C.; Meyer, H. M.; Nanda, J.; Chi, M.; Siegel, D. J.; Sakamoto, J. Impact of Air Exposure and Surface Chemistry on Li–$Li_7La_3Zr_2O_{12}$ Interfacial Resistance. *Journal of Materials Chemistry A* **2017**, *5* (26), 13475.

Chapter 3

Metastability in Li–La–Ti–O Perovskite Materials and Its Impact on Ionic Conductivity

In Chapter 2, we demonstrated that while LLTO has high bulk conductivity, its total ionic conductivity is significantly limited by orders of magnitude lower grain boundary conductivity (Table **2.1**). In this chapter, we further investigate the effect of composition on structure and ionic conductivity by preparing and characterizing over 576 samples in the Li-La-Ti-O pseudoternary phase diagram using the high throughput suite developed and validated in Chapter 2. We also demonstrate that good conductivities can be obtained via a single relatively short and low-temperature sintering step, thereby decoupling the impact of composition and synthesis conditions. Therefore, choosing the correct composition and synthesis conditions can help reduce grain boundary resistance without requiring extra sintering steps, additives, or a sacrificial powder bed. This study provides valuable insights into LLTO solid electrolytes.

Chapter 3 is produced with permission from “Jonderian, A.; Ting, M.; McCalla, E. Metastability in Li–La–Ti–O Perovskite Materials and Its Impact on Ionic Conductivity. *Chemistry of Materials* **2021**, *33* (12), 4792”.

3.1 Abstract

A great number of candidates exist for solid electrolytes in all-solid Li batteries. This study represents the first in a series using combinatorial synthesis, XRD, and impedance spectroscopy to screen for better solid electrolytes. Herein, over 576 Li-La-Ti-O samples are synthesized and characterized by XRD. Phase compositions are determined using automated Rietveld refinement, and the resulting phase stabilities provide important insights in this class of materials. This system

includes LLTO perovskite structures. Of highest importance, we find that the perovskite structure is not stabilized as a pure phase at any composition, but rather as composites wherein the LLTO is stabilized by the presence of secondary phases at high temperature, and at some compositions, these composites are further favored during slow cooling. This new means of stabilizing metastable phases is of interest in itself, but it also proves important in designing solid electrolytes as the ionic conductivities vary dramatically with changes in secondary phase content. We find ionic conductivities as high as 5 x 10^{-5} S cm^{-1} in total and >10^{-3} S cm^{-1} in the bulk in a sample where the secondary phase is TiO_2 with a composition of 9 wt. %. Both conductivity values are highly competitive with the state-of-the-art even though more cost-effective sintering protocols are used herein (far shorter times, and lower temperatures). We find that TiO_2 helps lower the grain boundary energy in the composite electrolytes and speculate that it may be acting as a sintering agent. This study therefore helps to decouple the effects of composition and synthesis conditions that have plagued the understanding of this class of material. Thus, this work not only serves as a proof of concept for the use of combinatorial methods in studying solid electrolytes, but also gives significant insight into the importance of secondary phases in ionic transport, and this is done for a class of materials that has proven to be particularly challenging. Given the negligible focus on secondary phases in the literature of solid electrolytes, these findings will be of use in further explorations of other classes of solid electrolytes.

3.2 Introduction

The increasing demand for energy storage solutions is associated with the shift to renewable energy sources, leading to a great deal of research into advanced lithium-ion batteries, among others, as a promising candidate for renewable applications.[1] The growing market of electric vehicles alongside the grid storage demand urges the development of safer, more energy dense, and longer life batteries. The replacement of a traditional flammable organic liquid electrolyte with an inorganic solid one makes batteries safer because of their non-flammable nature and better mechanical properties, which may suppress dendrite formation that eventually causes cell shortage.[2] Additionally, some solid electrolytes are compatible with metallic Li anodes as well as higher potential cathodes, both of which enable higher energy density batteries. Furthermore, solid-state electrolytes enable the advancements of new battery chemistries beyond Li-ion such as Li-S and Li-O_2.[3, 4] The challenges for a good inorganic solid electrolyte are that they should have high ionic conductivity, low electronic conductivity, low interfacial area specific resistance with the electrodes and a wide electrochemical stability window. A very wide variety of materials are currently being explored as potential solid electrolytes, including sulfides, phosphates, and various metal oxides (garnet and perovskite structures both garnering interest).[5] No clear winner has emerged to date and metal oxide solid electrolytes are currently being extensively studied as an alternative to the sulfide electrolytes because of their stability against moisture and inherent safety. The work presented herein is the first installment of a wide exploration of solid electrolytes using combinatorial methods. We focus herein on the LLTO perovskite materials.

Figure **3.1a** shows the structure of perovskite LLTO, which is made up of a network of connected TiO_6 octahedra with Li, La, and vacancies all located at the A-sites, which are surrounded by 12 oxygen anions. Li occupying A-sites results in Li diffusion occurring through a 3D network of channels, which is ideal as they are difficult to block entirely with occasional defects. The black arrow shows the path of lithium through one such channel, with the highest energy point on the path corresponding to lithium passing through a window formed by oxygen atoms (yellow lines). The activation energy for ionic conduction is determined by the size of the

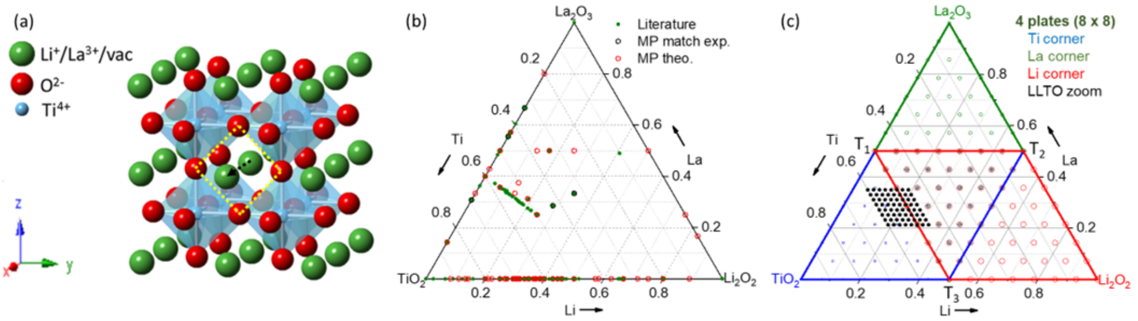

Figure 3.1 *(a) The structure of perovskite LLTO, with the oxygen window representing the barrier to Li diffusion indicated in yellow and the path followed by lithium as a black arrow. (b) The Li-La-Ti-O pseudo-ternary phase diagram with the previously studied compositions by both computational means (the materials project, MP) and experiment. (c) The compositions studied during this study. The axes are Li, La, and Ti metal molar fractions. The triangle defined by the three points T_1, T_2 and T_3 represents the triplicate region (all three of the Li, Ti and La corner plates contain these triplicates) and serves as verification that the synthesis is consistent between plates.*

oxygen window (lattice volume) and the positions of the oxygen atoms (octahedral tilting).[6-8] Such a window will be impacted by substitutions, such that a screening across many compositions is expected to impact the bulk conductivity in these materials. To our surprise, the compositions spanning the entire Li-La-Ti-O system studied herein also impacted the grain boundary contributions to conduction.

Figure **3.1**b shows all experimental and computational compositions studied in the Li-La-Ti-O system prior to the current study extracted from the ICSD, COD and Materials Project MP. The solid electrolyte candidates all lie on the composition line (thick black lines shown in Figure **3.2**a, b) given by $Li_{3x}La_{(2/3)-x}\square_{(1/3)-2x}TiO_3$ with $1/25 < x < 1/6$ (for easy reference: the $x = 1/25$ end-member is above and to the left of the $x = 1/6$ end-member in the phase diagrams here). This family of perovskite materials is one class of metal oxide solid electrolytes being explored due to their high bulk ionic conductivity exceeding 10^{-3} S cm^{-1}.[9] On the composition line defined by $Li_{3x}La_{(2/3)-x}TiO_3$, the oxidation states of La and Ti are 3+ and 4+, respectively. It will be of note for this article that to lie above this line a pure phase perovskite material would require Ti to be reduced to 3+, while below the line there would be a need for oxygen vacancies to stabilize the structure (this is based solely on balancing oxidation states). Despite the exceptional high bulk ionic conductivity of LLTO, the total ionic conductivity remains low due to the grain boundaries.[10] Thus, the limitation to the total conductivity is linked to the microstructure of the inorganic solid electrolyte with the grain boundaries generally accepted as being the source of limited total conductivity. Although we originally selected this system for high-throughput studies in an attempt to engineer more vacancies, it rapidly became clear that the combinatorial study would help explain another important question: why has the composition line of highest interest ($Li_{3x}La_{(2/3)-x}TiO_3$) been notoriously difficult to synthesize as a solid solution with contaminant phases often being present?[11-14] In fact, the few cases where contaminant phases are not present required extremely aggressive synthesis conditions resulting in severe lithium losses that prove difficult to reproduce and scale-up.[15] When starting with a nominal composition of $Li_{0.5}La_{0.5}TiO_3$, many studies end up with lithium contents of 0.3 or lower and a significant proportion of Ti^{3+} , the reason for which has not been satisfactorily explained.[11] In fact, some of the best conductivities (> 10^{-4} S cm^{-1}) were obtained under conditions that yielded more than 33% Ti^{3+} which results in an increased electronic conductivity making the material impractical as a solid electrolyte.[11, 16] The result of the body of work on LLTO is a great deal of confusion in the literature and difficulty in reproducing high ionic conductivity materials. The current study aims to systematically explore the impact of composition and synthesis condition on the phases present and the performance of solid LLTO electrolytes by using combinatorial methods to rapidly screen many compositions.

A high throughput methodology consisting of synthesis and characterization has proven to be a great tool for screening specific battery property and has been used to screen cathodes for Li-ion and Na-ion batteries,[17-19] as well as anodes.[20-22] In such studies, high-throughput synthesis of powders proves essential as the battery performance of thin film electrodes does not scale-up well to bulk materials. This limitation arises from the distinct microstructure between the two. Thin films often exhibit anisotropic properties due to the preferred orientation of grains (originated from the substrate) within the film and the presence of nano-sized grains. Here, for the first time, we adapt the combinatorial synthesis of powders to the screening of solid electrolytes. Previously, combinatorial studies of solid electrolytes were limited to thin films meant as passivating layers in the perovskite materials.[23] Although this work showed that high throughput methodology can yield meaningful results in tuning the interface properties of solid electrolytes, it has yet to be used in the screening of the solid electrolytes themselves. The synthesis method used herein is based on a recent success in synthesizing combinatorial Na-ion cathodes using the sol-gel method.[17] The sol-gel method starts with forming a stable sol after the solvent is removed to form a gel consisting of a homogenous network of the metal ions which can be later processed by calcination followed by sintering. Compared to the solid-state synthesis, which involves ball milling of the solid reagent, the sol-gel method consumes less energy and forms a homogenous precursor for the sintering step. Furthermore, specifically the citrate sol-gel method stabilizes high valence metal cations (such as Ti^{4+}, Si^{4+}…) which precipitate out in the aqueous co-precipitation method leading to heterogeneity.[24] Recently, it has been shown that the sol-gel method can be scaled down to a few milligrams making it feasible for the high throughput methodology for Na-ion battery cathodes.[17] The primary concern in applying this method here is the extreme temperatures required for the synthesis of the LLTO materials (>1150 °C) such that lithium loss from the small samples is a major concern and will be mitigated herein. In-situ XRD during synthesis (both from solid state synthesis and also solution based co-precipitation) has been performed in the literature for

$Li_{0.5}La_{0.5}TiO_3$ and the results demonstrate that the LLTO perovskite phase is well crystallized above 1150 °C for both synthesis routes.[25] This supports the decision taken herein to not explore lower temperatures.

Previous studies have shown that many factors such as chemical composition, doping, and sintering conditions play role in reducing the grain boundary resistance in LLTO.[26, 27] Given that LLTO suffers from low diffusion across grain boundaries,[9] we therefore expect secondary phases to play an essential role by changing the energy landscape at the grain boundaries, in essence playing the role of sintering agent. Thus, the current study, which systematically looks at the impact of composition on electrolyte performance, also helps to explore the role of secondary phases by studying the entire composition space around the LLTO composition line. Thus, a large part of the current study deals with how LLTO is stabilized and we find in fact that it is metastable at all compositions and conditions studied here. There has been a significant push in recent years to better understand the stabilization mechanisms for metastable materials from a computational point of view.[28] Traditionally, metastable materials are considered to be stabilized by reaching equilibrium at high temperature, followed by cooling sufficiently quickly to prevent conversion at lower temperatures such that at room temperature the kinetics of conversion can be considered to be zero. Herein, we find this mechanism present in vast areas of the Li-La-Ti-O phase diagram, but this does not account for the stabilization of LLTO structures in the phase diagram. In fact, at numerous compositions, the LLTO is stabilized (more LLTO was obtained) more during slow cooling rather than at high temperature. This work will therefore provide a new mechanism for the stabilization of metastable phases.

In this work, we therefore report the first full sampling of the Li-La-Ti-O pseudoternary phase space including a dense sampling in the LLTO region. The ionic conductivity was also mapped as a function of the composition space. This work not only serves as a demonstration of the feasibility of combinatorial solid electrolyte studies, but also provides means to make quality solid electrolytes under far shorter sintering methods and also provides significant insights into the challenges met in the literature in the study of these materials.

3.3 Experimental methods

The entire Li-La-Ti-O pseudo-ternary composition space was sampled by making 3 sets of samples; each containing 64 samples with different compositions. This sampling is shown in Figure **3.1c** where the 3 sets are the $TiT_1T_2T_3$, the $LiT_3T_1T_2$ and the $LaT_2T_3T_1$ parallelograms. This yields 192 samples with 120 distinct compositions and numerous samples on each plate lying in the triplicate region defined by the $T_1T_2T_3$ triangle; these are used to test reproducibility, which is found to be excellent as shown in Figure **S3.1**. These three sets of samples serve to map out the entire phase diagram. In order to thoroughly study the LLTO materials of the highest interest for solid batteries, a 4th set was also made, called the LLTO zoom plate and it is shown as the black points in Figure **3.1**c. The citrate sol-gel method was used to prepare all samples with an approximate mass of 30 mg. $Ti(OCH_2CH_2CH_2CH_3)_4$ (2M) solution was freshly prepared by dissolving 98% $Ti(OCH_2CH_2CH_2CH_3)_4$ in absolute ethanol. $LiNO_3$ (2M), $La(NO_3)_3$ (2M), and citric acid (4M) solutions were prepared with deionized water. The sol-gel method in these perovskite materials typically involves crystalline phases only at 700 °C and above. We therefore expect solid-state reactions only above this temperature.[29]

The concentrations of the prepared solutions were determined by ICP-OES. The optimal molar ratio of total metal ions to citric acid was found to be 0.75. The solutions were either pipetted by hand or by an automatic dispensing system (Opentrons OT-2 robot) into sixty-four 400 µL stainless steel cups arranged in an 8x8 array. First, the citric acid solution was dispensed into the cups, followed by the titanium solution, then the lanthanum nitrate, and finally, the lithium nitrate. These solutions were left to dry for 12 h at 65 ºC in air and then placed in a vacuum oven at 160 ºC for 1 h to obtain solid material. The samples were ground briefly with a spatula and transferred onto an alumina plate for the pyrolysis step. The powder samples were heated in air at 600 °C for 12 h at a heating and cooling rate of 2 ºC/min. The obtained samples were then transferred to a house-built high-throughput pressing die to form 64 pellets with a diameter of 3/16” under 2 tons of force (approximate pressure of 1 GPa). The pellets were heated in air on an alumina plate to either 1200 or 1150 °C at a rate of 5 ºC/min and held at that temperature for either 6 or 12 h. Two cooling rates are explored in this study: slow cool and quench. Slow cooling involved simply turning off the furnace after the 6 h hold giving a cooling rate of approximately 3 ºC/min. The quench cooling was performed by dropping the hot pellets on a copper slab at room temperature, which results in a moderate quench (cooling to below 100 ºC in less than a minute). In order to determine the extent of Li loss and aluminum contamination taking place during synthesis ICP-OES was performed on a number of compositions after synthesis at 1200°C and slow cooled (*i.e.* the conditions giving highest lithium loss). In all cases the lithium content was 500-2000 times above the detection limit of the ICP instrument.

To perform XRD measurements, newly synthesized pellets were ground and transferred into a sample holder wherein the samples were held between two thin mylar sheets. The powder XRD measurements were performed in transmission mode using a Panalytical Empyrean diffractometer equipped with Mo anode (60 kV, 40 mA) and PIXcel3D detector. For ease of comparison with the rest of the literature, all XRD patterns shown in this manuscript have been adjusted for scattering angles that would have been obtained with copper radiation with the $k\alpha_2$ peak having been subtracted. In total, 576 XRD patterns were collected in this study and they were all analyzed qualitatively for phase matching and quantitatively with Rietveld refinements. Fits were performed on the raw data. The average intensity of the largest peak was around 3500 counts (>1000 counts is typically considered sufficient for Rietveld refinement). The HighScore Plus software was used for the Rietveld refinements performed in batch mode as described in detail in the SI, section I and Table **S3.1**, and the effectiveness of this fitting approach is demonstrated in Figures **S3.2 -S3.3**, and Table **S3.2**.

To perform the EIS measurements, both sides of newly synthesized pellets were polished by 800-grit diamond sandpaper to give flat surfaces. Gold was sputtered on the two faces of the polished pellets as contacts for the impedance measurement using a Q150T sputterer. The room temperature AC conductivities of the samples were measured in high throughput using a house-assembled system consisting of a Biologic SP-150 potentiostat and a Pickering 64-channel multiplexer, operated by house-written software. The impedance measurements were performed at frequencies ranging from 1 MHz to 1 Hz with a voltage amplitude of 100 mV. The EIS spectra obtained were batch fitted to an equivalent electrical circuit using the Z-fit tool in the EC-Lab software.

Further characterization was performed on a few key samples. XPS was used to observe the near-surface chemistry of carbon in order to identify whether or not lithium carbonate is present in the pellets prior to EIS measurements. Specifically, we performed XPS on 4 samples: a pellet made in air and one made in oxygen within 1 week of synthesis, one made in air and then exposed to air for 3 months (all 3 pellets were fractured prior to XPS measurements and then observed in cross-section in order to see if lithium carbonate forms within the pores throughout the pellet), and a pellet made in air was ground to powder and left in air for 6 months. Analysis was performed using both the XPSPEAK4.1 and Avantage software. Density measurements of pellets were performed using the Archimedes method in absolute ethanol. The pellets were weighed in air and in ethanol and the density was calculated using the following equation $\rho_{pellet} = \frac{Weight\ in\ Air}{Weight\ in\ Air - Weight\ in\ ethanol} \times \rho_{ethanol}$. Finally, Hitachi SU3500 variable pressure scanning electron microscope (SEM) equipped with Oxford energy dispersive x-ray detector (EDS) was used to confirm the low porosity and also to identify contaminants, if present.

3.4 Results and discussion

3.4.1 Li-La-Ti-O pseudoternary phase diagram

Figure **3.2**a,b show the phase stabilities as determined in this study for synthesis at 1200 °C for 6 h followed by either slow cooling or quenching in which the black dots corresponds to single phases, red dash lines to two phase regions (tie-lines) and any region within 3 tie-lines representing three phase regions. Figure **3.2**c shows the results of the ICP-OES measurements at 1200°C with slow cooling as black dots and the solid black line tying between the dispensed and ICP composition. Any such black line that extrapolates back to the Li corner, represents lithium loss that occurs during high temperature synthesis. It is first important to note that Li loss is negligible in the region of highest interest where the LLTO materials form. Furthermore, the Li loss is extreme in any region where the materials form a multiphase material where one of the phases lies at the Li corner (presumably Li_2O which converts to volatile Li_2O_2 under these conditions[30]). This region of extreme lithium loss is shown in gray in Figures **3.2**c, **3.3**, and **3.4** show phase maps in molar % (*i.e.* the percentage of metal atoms that are in a particular phase) obtained by Rietveld refinement of all samples (excluding the zoom-in plates to be discussed separately below) at 1200 °C under both slow cooled and quenched cooling, respectively. These phase maps form the basis used to produce the phase stabilities shown in Figure **3.2**a,b. We discuss this large body of data step-by-step in the following paragraphs, starting with materials on the binaries.

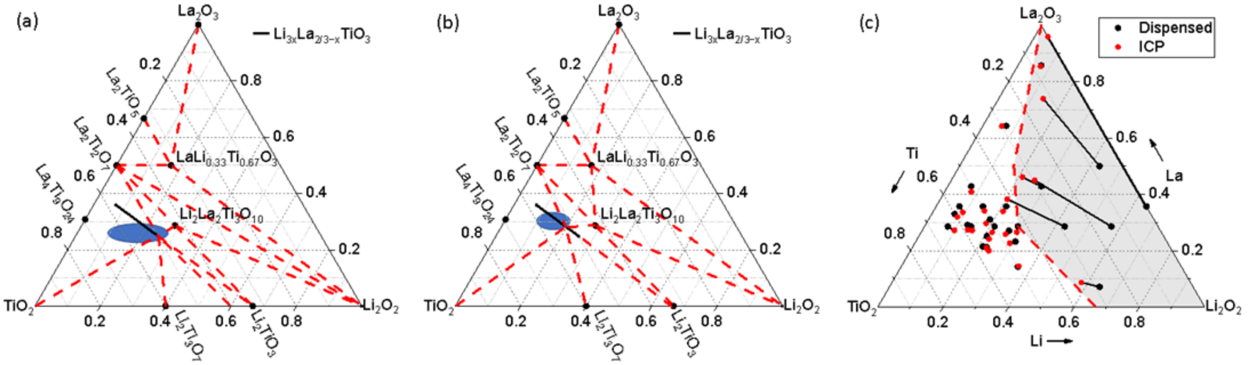

Figure 3.2 The complete phase stabilities obtained by quenching from 1200 °C. The red dashed lines are tie-lines, the black line represents the $Li_{3x}La_{(2/3)-x}TiO_3$ composition line (note that this is not a solid solution), and the blue oval shows the region of stabilization of the LLTO-TiO_2 composites discussed throughout the text. (b) The corresponding complete phase stabilities for samples obtained by slow cooling from 1200 °C. (c) The compositions obtained for slow cooling: the black points are the as-dispensed compositions while the red symbols are the compositions after synthesis as measured by ICP-OES. The lines shown that extrapolates back to the Li corner indicates Li loss during synthesis, and the gray region represents the part of the composition space showing extreme Li loss.

Firstly, two of the corners contain phases seen inside the ternary system: TiO_2 and La_2O_3. TiO_2 is of particular interest in the current study as it appears in the region of the ternary where the LLTO phases are also stabilized. The corresponding molar phase fraction maps for TiO_2 are shown in Figures **3.3**e, and **3.4**e. This phase will be of particular interest below in discussing the LLTO stabilization. Next, both the Ti-La and Li-Ti binaries have been well studied in the literature[31, 32] and thus the current article will only focus on pseudobinary materials if they are stabilized somewhere within the ternary. This includes 5 materials only: La_2TiO_5 (Figure **S3.4**), $Li_{1+x}Ti_{1-x}O_2$ ($x \approx 0.2$, Figure **S3.5**), Li_2TiO_3 (Figure **S3.5**), $La_2Ti_2O_7$ (Figures **3.3**, **3.4**, and **S3.6**), and $Li_2Ti_3O_7$ (Figures **3.3**, **3.4**, and **S3.6**). Let it be noted that $Li_{1+x}Ti_{1-x}O_2$ ($x \approx 0.2$) and Li_2TiO_3 are separated by a miscibility gap at 1200 °C as seen in ref. [32]. Furthermore, based on the same reference, $Li_{1+x}Ti_{1-x}O_2$ ($x \approx 0.2$) is not stable at lower temperatures and thus this phase is left off of the slow cool phase diagram as explained with Figures **S3.5**, and **S3.7**. All XRD patterns shown in the Supporting Information are obtained by slow cooling, but very comparable patterns are obtained at these compositions when quenching is used. Each of these binary phases co-exist somewhere in the ternary part of the phase diagram under both quenched and slow cooled conditions. The tie-lines shown in Figure **3.2**a,b are consistent with phase fraction maps shown in Figures **3.3**, **3.4**, **S3.4**, and **S3.5** for all phases lying on the binaries. By contrast, the Li-La pseudobinary shows only the presence of La_2O_3. Figure **3.2**c shows that this is a result of extreme lithium loss in all Li-containing samples on this binary such that all the lithium content is lost and we are left with La_2O_3 only. It should also be noted that $La_4Ti_9O_{24}$ was found along the binary as expected based on the literature, but this phase was not found in any sample containing each of Li, Ti, and La (i.e. lying within the ternary); this surprising fact will be discussed below in the context of the stabilization mechanism of metastable LLTO materials.

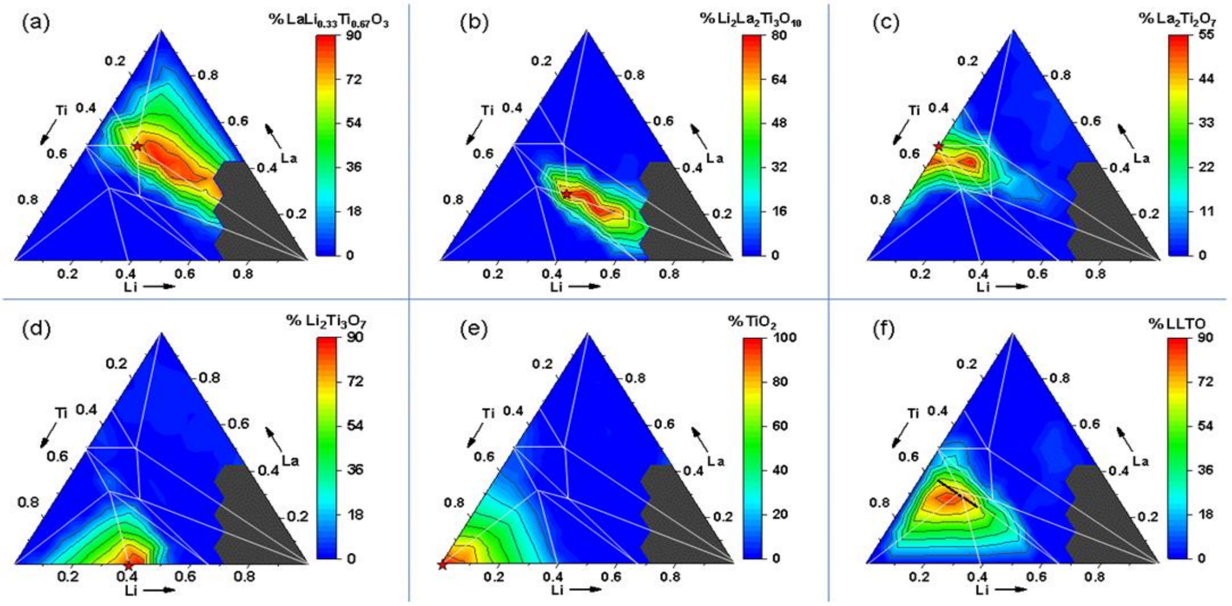

Figure 3.3 *Molar phase fractions obtained with Rietveld refinement for samples made by heating at 1200 ℃ for 6 h and slow cooling. Includes results for all samples except those made in the zoomed-in region. The red stars indicate the single-phase compositions in each contour. The white lines correspond to the two-phase regions and are corrected for the lithium loss (from ICP-OES).*

Next we consider known compositions in the ternary space: $LaLi_{0.33}Ti_{0.66}O_3$ (Figure**S3.4**b), $Li_2La_2Ti_3O_{10}$ (Figure **S3.5**) and the LLTO of interest. In both Figures **S3.4**b, and **S3.5**, the X represents the composition where we find the highest phase content, and the * represents the composition based on the cif file; and we find that the X in both cases is at a higher lithium content than that expected from the cif file. These therefore show that for $LaLi_{0.33}Ti_{0.66}O_3$ and $Li_2La_2Ti_3O_{10}$, we need excess lithium to account for lithium loss during synthesis consistent with the map of lithium loss in Figure **3.2**c as they both lie on the edge of the region of extreme lithium loss. The phase stabilities in Figures **3.2**, **3.3**, and **3.4** take this lithium loss into account. It is also important to note that $LaLi_{0.33}Ti_{0.66}O_3$ has a perovskite structure with La at the A-site and Ti/Li showing mixed occupation at the B-site. This phase is present in a large area of the triangle, but there is no indication of a solid solution such that it appears to only be stabilized due to the ordering permitted by having 1/3 Li and 2/3 Ti on the B-sites and no off-stoichiometry is possible. It should also be

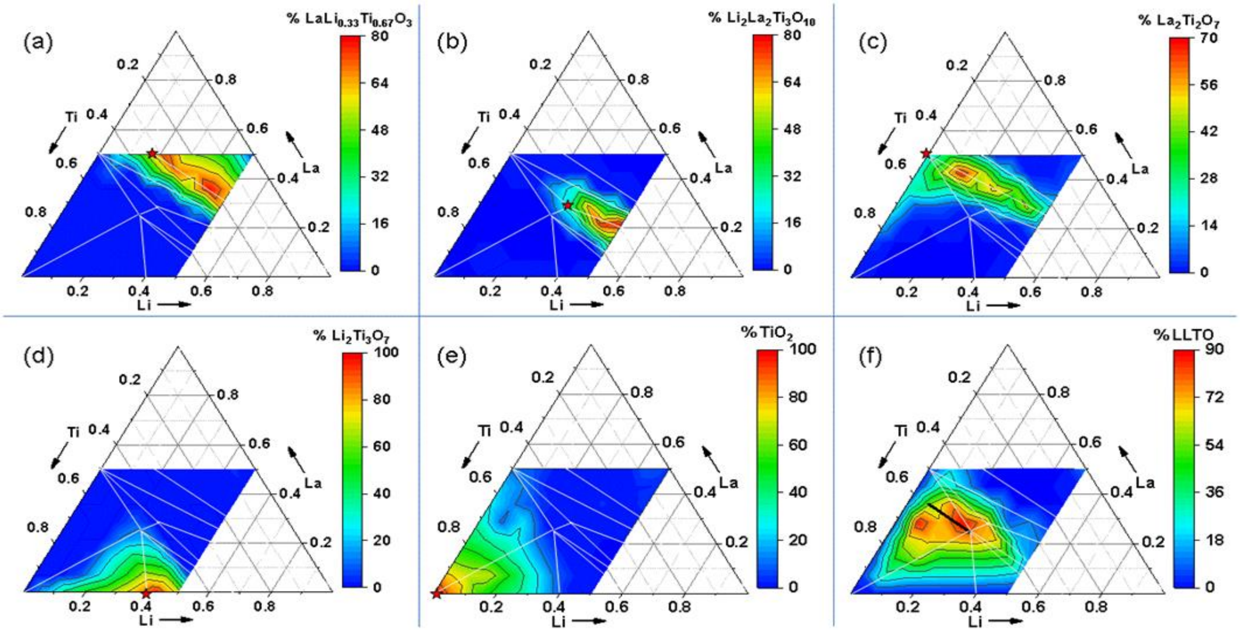

Figure 3.4 *Molar phase fractions obtained with Rietveld refinement for samples made by heating at 1200 °C for 6 h and quenching. Includes results for the* $TiT_1T_2T_3$ *plate only. This serves to better understand how the LLTO phases are stabilized at high temperature. The red stars indicate the single-phase compositions in each contour. The white lines correspond to the two-phase regions and corrected for the lithium loss (from ICP-OES).*

mentioned that in the region near this $LaLi_{0.33}Ti_{0.66}O_3$ phase, the automated phase identification method used as the first step in fitting the data struggled to distinguish between this phase and the low-lithium content LLTO phases. As a result, the phase maps for $La_2Ti_2O_7$ and $Li_2La_2Ti_3O_{10}$ proved essential to determine the tie-lines involving $LaLi_{0.33}Ti_{0.66}O_3$.

Finally, this leaves the LLTO phases. The phase stabilities in the region containing LLTO proved to be far more difficult to interpret. First, despite the fact that we prepared zoom-in plates focused solely on the LLTO region under various synthesis conditions (Figures **3.5**, **3.6**, **3.7**, and **S3.8**), we find no single phase LLTO material. It should also be mentioned that an *in-situ* high temperature study at 1250 °C also failed to yield a single phase material[25] and that the few reports that convincingly show single phases involved quite complex sintering protocols and much higher temperatures.[15] Figures **3.5**, **S3.2** , and **S3.3** show XRD patterns for materials with varying % LLTO obtained here, including the sample with the highest LLTO fraction of 95% with labels showing the other phases present. Figure **S3.2** shows a zoom on the strongest TiO_2 peak in this sample that contained only 5 % TiO_2. Despite this low content the strongest XRD peak for TiO_2 was 23 times above the noise in the background, such that the precision in detecting secondary phases is judged to be extremely high with the Mo XRD system used in this study (Figure **S3.2** shows other secondary phases in order to better judge the sensitivity of these). Figures **S3.2** , and **S3.3** also demonstrate the high quality fits obtained with the automatic fitting describing in the SI, section I. Table **S3.2** shows fitting parameters obtained through the entire zoom-in region with R_{wp} values; this table demonstrated that high quality fits were obtained throughout the ternary and the uncertainty on extracted lattice parameters is small (typically 0.001 – 0.003 Å).

The small TiO_2 peaks in Figure **3.5** demonstrate that great care that must be taken in analyzing these patterns, the small TiO_2 peaks seen in Figure **3.5**c, for example, can also clearly

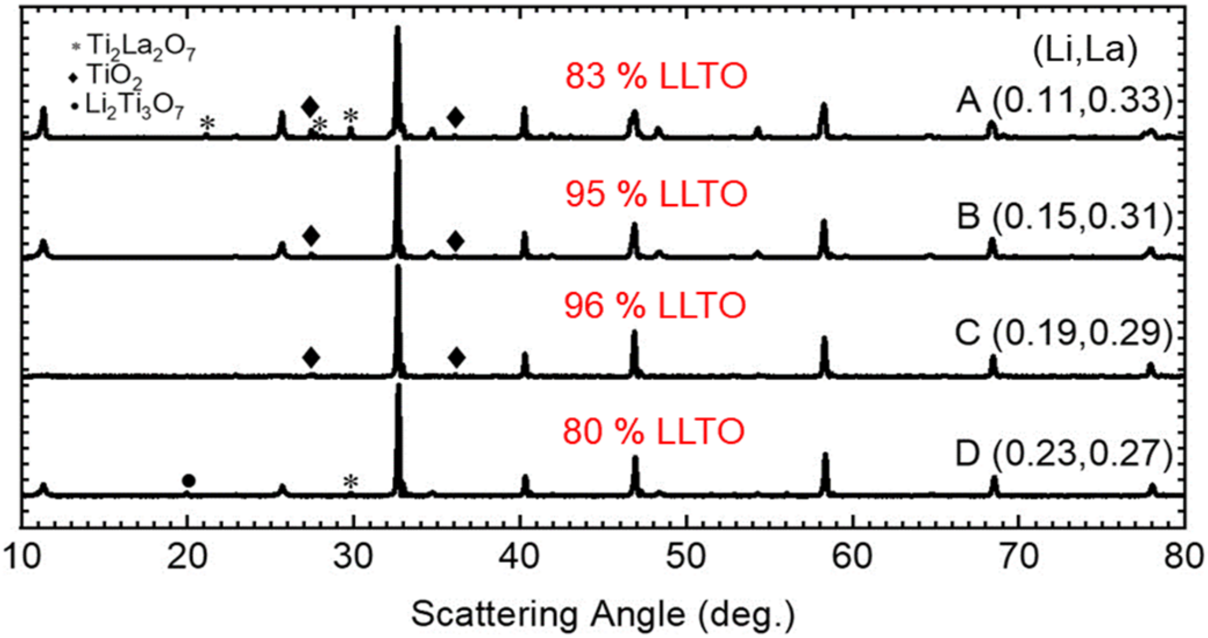

***Figure 3.5** Powder XRD patterns of samples along the composition line with various fractions of LLTO. The compositions are shown as metal molar fractions: (Li,La), where the titanium fraction is Ti = 1-Li-La. The legend shows contaminant peaks present, all other peaks index well to the perovskite LLTO phases. The compositions A,B,C, and D have increasing lithium content as shown in Figure **3.8** and the fits for these patterns are included in Figures **S3.2** and **S3.3**.*

be seen in comparable amounts in prior results.[11, 12, 14] where the authors treat their materials as single phase. The presence of secondary phases is therefore prevalent in the literature for LLTO electrolytes but the impact of these phases has not been sufficiently explored. We consider 3 possible reasons why single phase materials were not found in the current study: 1- the composition was never right (in this case the co-existence should yield a phase-pure composition very near to those with the highest LLTO fraction, as discussed below), 2- equilibrium conditions were not reached (*e.g. insufficient quench rate*, this will also be considered below), 3- the LLTO phases are not stable on their own at any condition and require the presence of the secondary phases in order to be stabilized. To evaluate whether 1 occurred we use the lever rule. The lever rule uses the phase compositions in a co-existence region to extrapolate to where the single-phase materials are found in the phase diagram. Figure **3.6** shows the points obtained using the lever rule to determine where the pure LLTO phase should be by extrapolating from where LLTO/TiO_2 composites exist to where the TiO_2 fraction goes to zero (this method proved infallible in previous pseudoternary studies[33, 34]). Figure **3.6** therefore shows the pure LLTO compositions extrapolated using the lever rule in the co-existence regions for both the quench and slow cool. For the quench materials, let us focus on two compositions: E and F. Composition F is very near to the traditional LLTO composition line's end-member: $Li_{0.5}La_{0.5}TiO_3$, which has been extensively studied. Here, the lever rule yields a point very nearby, suggesting that a phase pure LLTO may in fact have been found (we still feel this is unlikely given our extensive search near point F, but it remains possible). For point E, however, the lever rule yields a point well above the LLTO composition line discussed in the literature (and note that point E shows 2 phases only as shown in Figure **3.7**, such that the extrapolated point does represent the composition of the LLTO present in the composite at point E, based on conservation of atoms). However, the samples made at the composition where E predicts a single phase LLTO shows only about 60% LLTO (Figure **3.3**). This implies that the mixture at point E includes an LLTO phase that is not stable on its own. This further implies that either the thermodynamics or the kinetics of the LLTO-TiO_2 composite is improved compared to

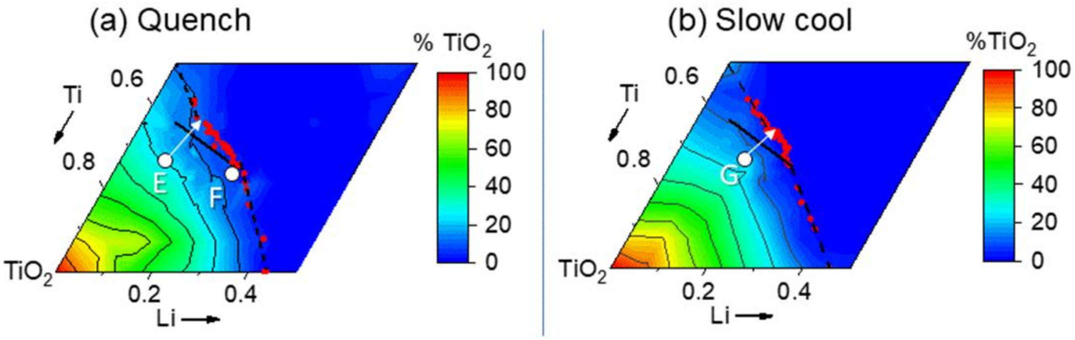

Figure 3.6 *Phase maps for the TiO_2 molar fraction obtained by heating at 1200 ℃ for 6 h and then quenching (a) or slow cooling (b). The red points represent the result of using the lever rule on all samples that showed co-existence between TiO_2 and LLTO (each sample yields 1 red point). The labels E, F and G correspond to the points with highest LLTO content in Figures* ***3.3*** *and* ***3.4*** *and are used in the main text to discuss the significance of these results.*

that of the two end-members on their own. This conclusively demonstrates that the LLTO material stabilized at point E cannot be stabilized on its own as a pure phase but requires a secondary phase to be present in order to obtain the LLTO phase.

There are two possible explanations for this need of a secondary phase to stabilize LLTO: (1) free energy of the mixture of LLTO and the secondary phase is lowered by the interaction between the two phases (this implies thermodynamic stabilization), or (2) the secondary phase is needed simply to first nucleate the LLTO phase and then continued growth of LLTO is possible

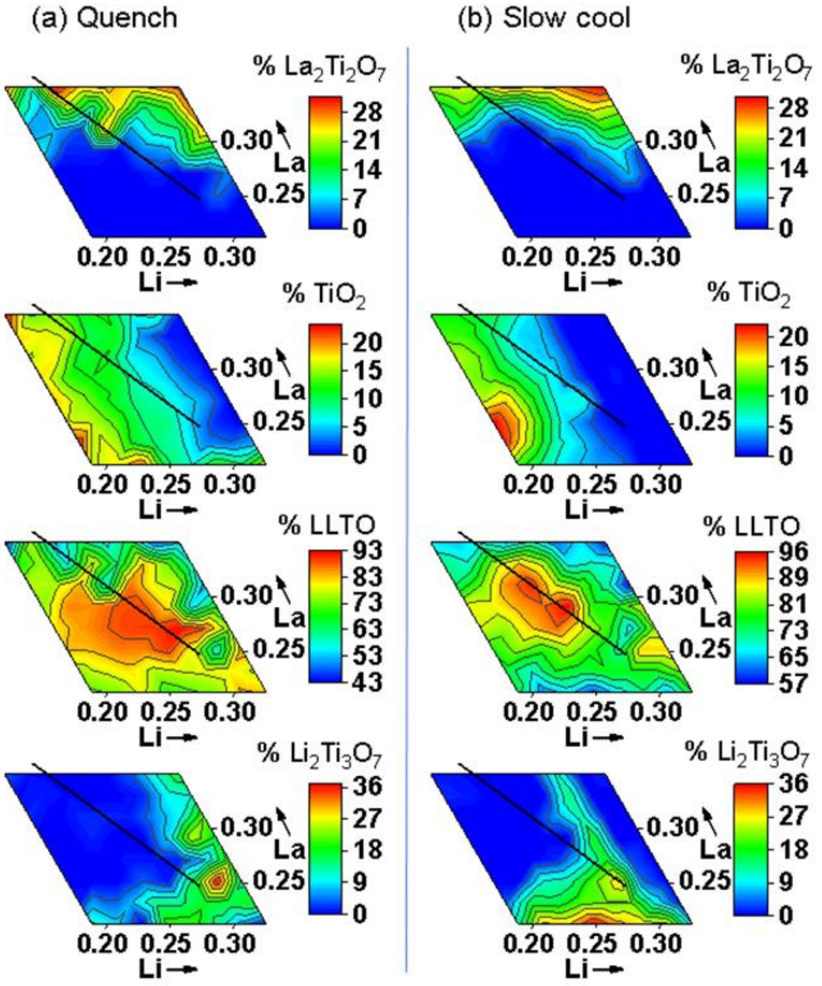

Figure 3.7 *Phase maps obtained in the zoomed-in LLTO region of the phase diagram after heating at 1200 ℃ for 6 h and then either quenching (a) or slow cooling (b). The black line represents the* $Li_{3x}La_{(2/3)-x}TiO_3$ *composition line. The highest LLTO content in quenched samples is 93% while 96% in the slow cooled.*

(this implies kinetic stabilization). Either mechanism is plausible given our data, however, there is no question that a second phase is required in order to obtain the LLTO phase. Given that we know the phase boundaries of LLTO are high energy barriers to Li diffusion,[35] we propose that in either mechanism, the secondary phase brings down the energy of the phase boundaries of LLTO to the point of either stabilizing the LLTO phase or nucleating its growth. This stabilization of this composite also explains why $La_4Ti_9O_{24}$ is present on the binary but not in the ternary: TiO_2 continues to be present because of its role in stabilization LLTO, whereas on the binary the $La_4Ti_9O_{24}$ on its own proves more energetically favorable than a TiO_2-$La_2Ti_2O_7$ composite. It should be noted that the presence of TiO_2 phase at the LLTO grain boundaries was detected previously by Schell *et al.* using electron back-scatter diffraction (EBSD).[27] We are currently pursuing a detailed EBSD study of a number of our materials from the current study to further understand the impact of composition and sintering condition/atmosphere on the microstructure.

Figure **3.6**b shows that this occurs in slow cooled samples as well: the highest LLTO concentration is found at point G and the lever rule leads us to conclude that this contains an LLTO phase above the composition line. This stabilization of low Li content LLTO can therefore only occur if the secondary phase is present in sufficient quantities as is the case for points E, G. Therefore, the phase stabilities in Figure **3.2**a only shows tie-lines to one LLTO composition: $Li_{0.5}La_{0.5}TiO_3$. It is important to recognize though that this does not mean that all LLTO's found in the phase diagram have this composition, this fact will be made clear below in discussing the lattice parameters of the LLTO phases. Instead, we depict the rest of the LLTO phases that are stabilized with a blue oval in the phase stabilities, these represent compositions where the LLTO-composites can be stabilized with high LLTO concentrations.

Figures **3.7**, and **S3.8** show phase maps in the zoomed-in region under a variety of heating conditions different temperature, dwell time, and cooling rate. The results show that a maximum LLTO content of 91% can be obtained at 1150 °C when quenched, but that this drops to 81% when slow cooling is used. This shows that the high-lithium content LLTO nearly-stabilized at 1150 °C (Figure **S3.8**a) decomposes during cooling. Interestingly, the same effect is seen at 1200 °C where the materials near the $Li_{0.5}La_{0.5}TiO_3$ end-member show as high as 92% LLTO when quenched and closer to 80% when slow cooled (Figure **3.7**a,b). By contrast, the material showing the highest LLTO content in Figure **3.7**b (1200 °C, slow cooling) of 96% showed closer to 80% LLTO when quenched (Figure **3.7**a), and this effect is not seen at 1150 °C in Figure **S3.8**. This occurs at lower Li content and helps explain a great deal of the results in the literature. The low-Li LLTO is therefore not primarily stabilized at high temperature, but is in fact stabilized *during cooling from high temperature*. Thus, the pathway used primarily to date to make a near-single phase LLTO is to begin at the composition of $Li_{0.5}La_{0.5}TiO_3$ and then heat to extreme temperatures (say >1350 °C) where Li loss brings the lithium content down significantly to about $Li_{0.3}La_{0.56}TiO_3$ where the composition is stabilized during cooling to lower temperatures. By staying below the temperatures where Li loss is high in this region of the phase diagram, we are able to de-couple the effects of cooling conditions and composition for the first time. The impact on the design of solid electrolytes will be discussed in the next section, but from a materials point of view it is critical to recognize that the materials stabilized are impacted by both the cooling rate and the stabilization due to the secondary TiO_2 phase. It is also important to recognize that the fact that the maximum LLTO content at 1200 °C and quenching does not increase when the sintering time increases from 6 to 12 h (93 % in Figure **3.7**a for 6 h, and 92 % in Figure **S3.8** for 12 h). This demonstrates that 6 h was sufficient to reach equilibrium at these temperatures, such that the secondary phases found cannot be explained by insufficient sintering times.

The lattice parameters extracted for the LLTO phases after heating at 1200 °C are shown in Figure **3.8** after converting them into pseudo-cubic values to permit comparison across space groups. In the quenched materials, minimal variation in lattice parameters is seen in much of the plate, consistent with co-existence with the high-lithium $Li_{0.5}La_{0.5}TiO_3$ material. Figure **S3.9** shows lattice parameter ratios (for a cubic structure all ratios would be exactly 1) and clearly demonstrates that much of the LLTO region does in fact contain cubic materials with all ratios being very near to 1, especially in the region near $Li_{0.5}La_{0.5}TiO_3$. However, the upper left corner shows strong variations away from the cubic structure due to high lanthanum content causing A-

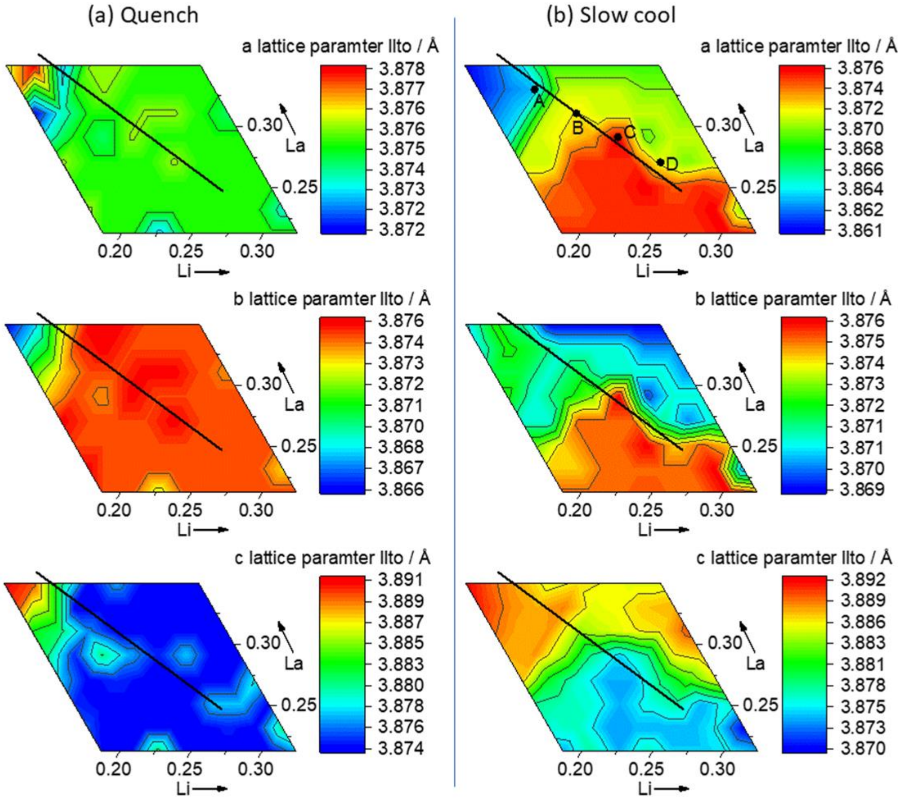

Figure ***3.8*** *The contour map of the a, b and c lattice parameters as a function of composition in the zoomed-in plates discussed in Figure* ***3.7*** *Phase maps obtained in the zoomed-in LLTO region of the phase diagram after heating at 1200 ℃ for 6 h and then either quenching (a) or slow cooling (b). The black line represents the* $Li3xLa_{(2/3)-xTiO3}$ *composition line. The lattice parameters are reported as pseudo cubic (conversions shown in Table* ***S3.1****).*

site ordering. In this region, contours point towards the region of high LLTO-TiO_2 composites identified in Figure **3.4**f (point E in Figure **3.6**) and these lattice parameters confirm distortion away from the cubic structure (Figure **S3.9**a). The fact that the contours point towards this region suggests tie-lines leading to the composites discussed above (lattice parameters must remain constant along tie-lines as the co-existence implies the same perovskite is present in all samples on the tie-line). Thus, though complex, the lattice parameter maps do re-inforce the phase stabilities shown in Figure **3.2**a and are consistent with the LLTO-TiO_2 composite model presented above. By contrast, the lattice parameter maps obtained after slow cooling (Figures **3.8**b and **S9**b) show a much greater variation throughout the entire zoom-in region with much of the LLTO region showing non-cubic LLTO. This is a result of the transformation during cooling discussed above wherein the lower-lithium containing LLTOs form primarily during cooling from high temperature. These results are in good agreement with previous results along the well-studied $Li_{3x}La_{(2/3)-x}TiO_3$ composition line. The directions of the contours again hint at the directions of tie-lines with much of them pointing towards the high LLTO content composition seen in Figure **3.6**b (this lies roughly in the middle of the black composition line shown in Figure **3.8**). Thus, once again, the lattice parameter maps are consistent with the phase stability maps in Figure **3.2**.

We therefore conclude that the LLTO phase can be stabilized in a very large portion of the Li-La-Ti-O composition space, even though they cannot be made single phase at any composition. The metastability results not from phase separation during cooling, but in fact due to stabilization by at least one secondary phase: TiO_2, though the phase maps at 1150 °C suggest that other phases may also play this role. We emphasize the TiO_2-LLTO composites in large part due to the improved conductivities in these samples as discussed in the next section. Given the known function of TiO_2 as a sintering additive for perovskite materials, it is now of high interest to consider the impacts of these composites on the ionic conductivity of these potential solid electrolytes.

3.4.2 Lithium conductivity

Figures **3.9**, **3.10**, **S3.10**, and **S3.11** show the EIS spectra obtained after heating for 6 h at 1200 °C for slow cooled and quenched samples, respectively, both in the entire frequency range measured and also zoomed spectra showing the bulk contributions. The red lines are the product of fitting the spectra using the $(CPE_{bulk}//R_{bulk})(CPE_{gb}//R_{gb})CPE_{be}$ equivalent circuit well established in the literature where R is resistance, CPE is a constant phase element, gb represents grain boundary, and be represents an ion blocking electrode.[14, 36] The spectra can be divided into three frequency domains high, medium, and low which are dominated by bulk, grain boundary, and ion blocking

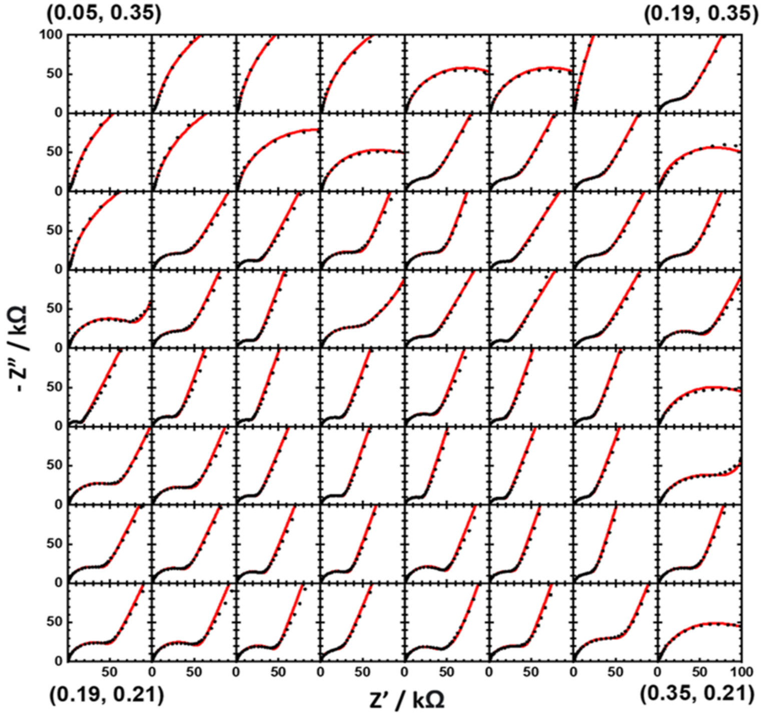

Figure 3.9 *EIS spectra obtained in the zoomed-in LLTO region for samples heated at 1200 ℃ for 6 h and then slow cooled to room temperature. The four corners are labeled by compositions using molar metal fractions: (Li, La) where Ti = 1 – Li – La. The red lines are the results of fitting as described in the main text and the dots are the EIS data.*

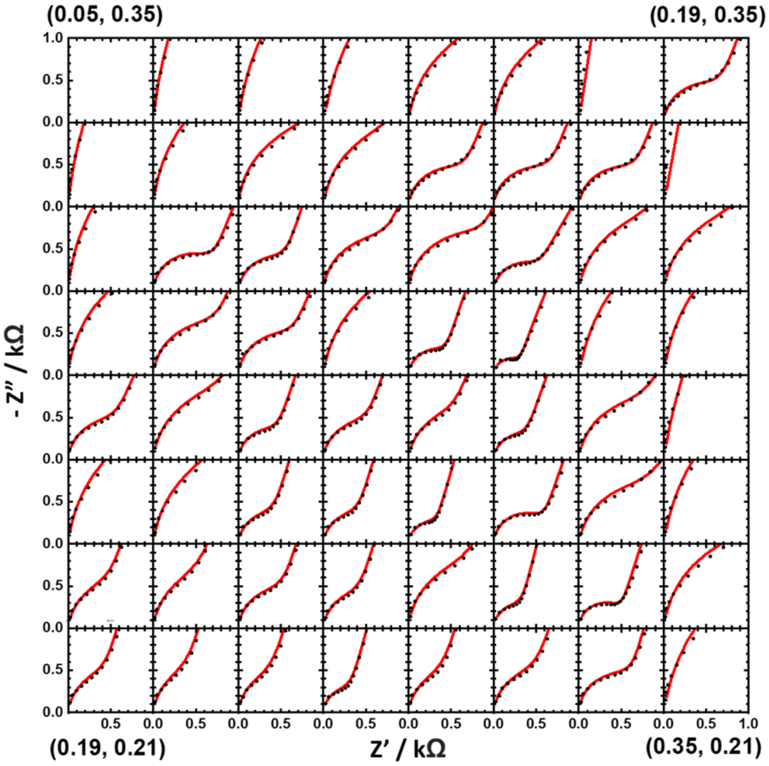

Figure 3.10 *EIS spectra obtained in the zoomed-in LLTO region for samples heated at 1200 °C for 6 h and then slow cooled to room temperature. The spectra are zoomed-in (high frequency region) in order to show the bulk contributions to the EIS data. The dots are the EIS data, and the red lines are the fits.*

electrode kinetics respectively.[28] The model was able to fit all three ranges well for all spectra. Figure **3.11** shows the resulting contour maps for both bulk and grain boundary Li-conductivities of both quenched (average of two batches) and slow cooled samples (average of three batches). The bulk conductivities are extremely high as expected for this class of material (> 10^{-3} S cm^{-1}). More interestingly, the total conductivities vary dramatically over the plates.

Prior to investigating the significance of the trends in conductivity with composition, let us first verify that other factors are not responsible for the variations of 2 orders in magnitude seen in the total conductivity. We consider 3 important concerns that could result in variations in conductivity with no correlation to our phase diagram: (1) Al contamination from the alumina substrate, (2) other contaminants from the precursors used during synthesis, (3) Li_2CO_3 formation

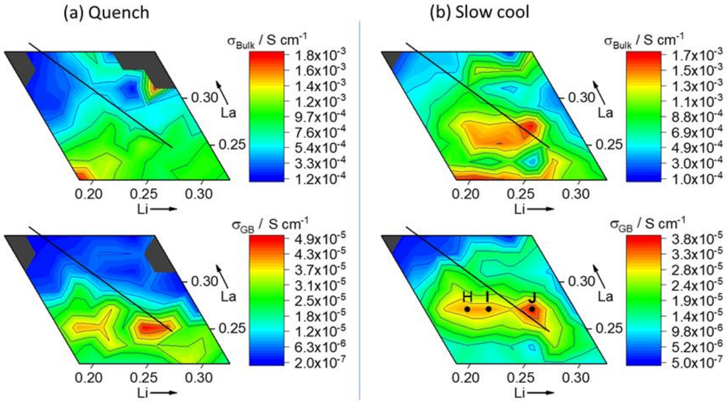

Figure 3.11 *The contour map of bulk and total ionic conductivities of quenched (a) and slow cooled (b) samples after heating to 1200 ℃ for 6 h extracted by fitting the EIS spectra. The line indicates* $Li_{3x}La_{2/3-x}TiO_3$ *composition line.*

in the pores of low density pellets such that variations in conductivity could be due to variation in pellet quality. Regarding contaminants, Figure **S3.12** shows EDS results on a typical pellet. We find no contaminant other than aluminum such that we suspect that other contaminations are very low. Aluminum contamination is therefore a serious concern and Table **S3.3** shows ICP results for 10 different pellets in the LLTO zoom region. All show very low Al:Ti ratios (one outlier is at 0.0078, all others are below 0.004); these are close to but all are clearly above the detection limit of the ICP instrument. Since Al:Ti ratios below 0.1 show no measurable impact on structure (ref. [37]), and a ratio of 0.012 shows minimal impact on conductivity (about 10% based on ref. [38]), we conclude that the level of aluminum contamination in our samples is mitigated and is in no way sufficient to explain the trends of multiple orders of magnitude seen in the conductivity values in our phase diagram. Finally, the pellet quality was explored by characterizing the cross section of fractured pellets using SEM as shown in Figure **3.12**. All samples show very high packing, with relative densities above 92% such that we do not believe large variations in porosity were at play across our samples. To confirm that Li_2CO_3 was not present in significant quantities in the pores of the pellets, we performed XPS measurements on pellets at composition J immediately after

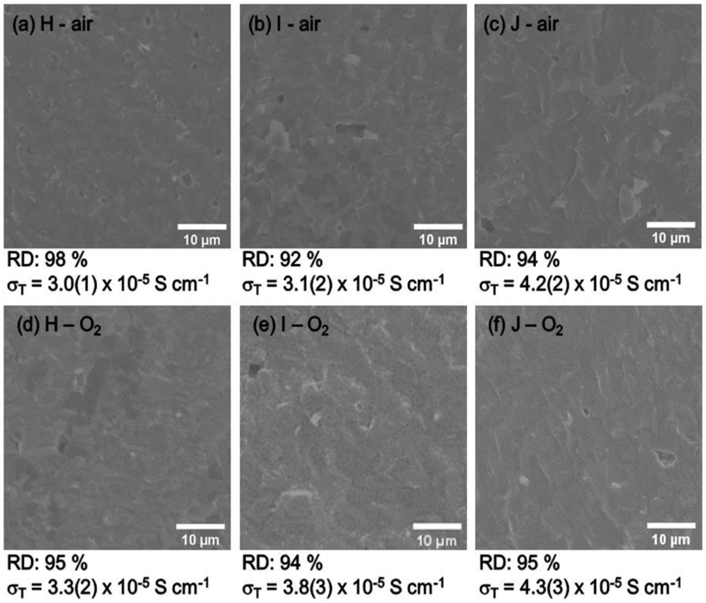

RD: 98 %
$\sigma_T = 3.0(1) \times 10^{-5}$ S cm^{-1}

RD: 92 %
$\sigma_T = 3.1(2) \times 10^{-5}$ S cm^{-1}

RD: 94 %
$\sigma_T = 4.2(2) \times 10^{-5}$ S cm^{-1}

RD: 95 %
$\sigma_T = 3.3(2) \times 10^{-5}$ S cm^{-1}

RD: 94 %
$\sigma_T = 3.8(3) \times 10^{-5}$ S cm^{-1}

RD: 95 %
$\sigma_T = 4.3(3) \times 10^{-5}$ S cm^{-1}

Figure 3.12 *SEM images of 6 pellets made at each of compositions H, I and J from Figure* ***3.11****, and either synthesized at 1200 ℃ in either air or oxygen. Below each image, we include the average total conductivity values obtained by making 8 replicates, as well as the average relative densities.*

fracturing after various exposure times in air as shown in Figure **S3.14**. The only sample that shows lithium carbonate was ground to a powder and left in air for 6 months; all others show no lithium carbonate even after 3 months in air prior to fracturing. The powder sample exposed for 6 months demonstrates that lithium carbonate formation in these materials is an important concern, but the samples exposed to air for a week or 3 months show that this cannot explain the conductivity results from Figure **3.11**. The < 1 week exposure to air is consistent with the sample preparation prior to EIS measurements. Furthermore, our high-throughput samples are all synthesized at the same time such that they are all exposed to air for the same period of time such that large variations in lithium carbonate formation are not responsible for the variations in conductivity seen in Figure **3.11**. We therefore conclude that the trends in Figure **3.11** are in fact due to various in composition and not to other factors that could be overshadowing the composition effects.

Let us now consider the consequences of the results shown in Figure **3.11**. The highest conductivity obtained is about 4.9 x 10^{-5} S cm^{-1} and obtained by quenching a sample with phase composition: 90% LLTO, 9% TiO_2, and 1% $Li_2Ti_3O_7$. It is of note that this highest conductivity value is *not* obtained for the highest LLTO fraction; in fact this result supports the theory that a certain fraction of TiO_2 co-existence helps improve the grain boundary conductivity. We speculate that TiO_2 may be acting as a sintering additive during material synthesis but further research into the microstructure is required to confirm this. Furthermore, this conductivity value is very close to the state-of-the-art for undoped LLTO of 7 x 10^{-5} S cm^{-1}.[5] It is significant that oftentimes very complex sintering protocols were used to achieve such high conductivities. For example, Morata-Orrantia *et al.* obtained a high total conductivity of $(5.1 \pm 0.3) \times 10^{-5}$ S cm^{-1} for undoped LLTO by first heating in platinum boats for 6 h for decarbonation, then the samples were reground, pelleted, covered with a powder of the same composition and fired at 1150 °C for 12 h followed by further grinding, re-pelleting, and re-firing for another 12 h at 1275 °C.[39] It is therefore of high significance that equivalent conductivities are obtained here in a single sintering step without regrinding nor re-pelletizing nor using a sacrificial powder bed, but by simply starting at optimized compositions and remaining at conditions where Li loss is mitigated.

There is another recent result from the literature that requires further consideration in the context of the current study. Kwon *et al.* obtained very high conductivities as high as 4 x 10^{-4} S cm^{-1} in undoped LLTO but with an unexpectedly high proportion of Ti^{3+} that proves detrimental as it results in electronic conduction making it unsuitable for battery operation. In that study, a sample was mixed at the composition $Li_{0.5}La_{0.5}TiO_3$ (near point F in Figure **3.6** here), and heated to 1400 °C such that the final composition extracted by ICP-MS was $Li_{0.18}La_{0.61}TiO_3$ and this would suggest an oxidation state for Ti of 4+ given that La takes a 3+ state. However, the authors find a Ti 3+/4+ ratio of 0.61 in this sample based on XPS. Figure **3.6** of the current study sheds light on these results. The sample with metallic composition $Li_{0.18}La_{0.61}Ti_1$ (near point E in Figure **3.6** here, though closer to the stoichiometric line) should, according to our phase stabilities, contain a small amount of TiO_2 and a perovskite lying on the $Li_{0.5}La_{0.5}TiO_3$-$LaTiO_3$ composition line. Such an LLTO would contain a significant proportion of Ti in the 3+ state: for example, the sample in the middle of that line has a composition of $Li_{0.25}La_{0.75}TiO_3$ having an average Ti oxidation state of 3.5+. We therefore propose that samples made near $Li_{0.5}La_{0.5}TiO_3$ under extreme conditions that result in a high lithium loss show Ti^{3+} due to the fact that the samples have moved into composition spaces where the co-existing LLTO phase lies above the stoichiometric line $Li_{3x}La_{(2/3)-x}TiO_3$. Furthermore, the XRD patterns from Kwon *et al.* do in fact show small peaks at 27 and 36° consistent with small amounts of TiO_2 (qualitatively consistent with our results for 4-5 % TiO_2 shown in Figure **3.5**). The phase stabilities presented here therefore fully explain the results obtained by Kwon *et al.* This both reinforces the care that must be taken in examining XRD patterns of these materials and demonstrates the usefulness of ternary phase stabilities in understanding complex solid electrolytes.

To further explore what factors might be causing the conductivity changes with composition, 3 compositions were studied further: H, I and J as labelled in Figure **3.11**. These show high total ionic conductivity in the slow cooled samples. We prepared replicates (sets of 8) synthesized either in air or oxygen. Figures **3.12** and **S14** shows SEM images of 6 such samples in cross-section after fracturing the pellets. As shown in the SEM images, all pellets are highly dense with very low porosity. This is confirmed by the relative densities that are all > 92 % (assuming a crystallographic density of 5.1 g cm^{-1}). The density values and conductivity values in Figures **3.12** and **S14** are all averages of the replicates. It should also be noted that in Figure **3.12**, the uncertainties on the conductivity values are the standard errors, such that the standard deviation are in the range 10 - 20%. As such, the values obtained in the systematic screening in Figure **3.11** at point H, I and J all lie within one standard deviation of the corresponding average values in Figure **3.12** (note the grain boundary conductivity is at most only 1 x 10^{-6} S cm^{-1} larger than the total conductivity for these materials). For example, for point J, Figure **3.11** yields a total conductivity of 3.7 x 10^{-5} S cm^{-1} which is within 1 standard deviation (0.85 x 10^{-5} S cm^{-1}) of the average value of 4.2 x 10^{-5} S cm^{-1} from Figure **3.12**. We therefore use these replicates to determine that our precision in a single high-throughput screening is 20 %, such that for higher precision replicates are required. This level of precision is more than sufficient to identify regions of further interest given that total conductivity varies by 2 orders of magnitude over the LLTO zoom region. Figure **3.12** shows that uncertainties on the mean as small as 5 % can be obtained from 8 replicates.

We can also see that the relative densities for all 6 pellets do not correlate at all to the conductivities (in fact the most dense pellet shows the lowest conductivity), but in all cases the trends in conductivities match those from the high-throughput screening in Figure **3.11** (J > I > H). This indicates that the trends in total conductivity are very much composition dependent and not a consequence of some pellets having been pressed more effectively than others. That being said, it is currently unclear as to why composition J (with 18% $Li_2Ti_3O_7$) shows the highest conductivity. The impact of the phase compositions identified herein on the microstructure is the subject of on-going study as mentioned previously. However, the current study undeniably demonstrates that secondary phases can play an important role in improving the grain boundary conductivity in LLTO solid electrolytes.

As a final point of discussion, Aguesse *et al.*[40] found an improved ionic conductivity in $Li_{0.34}La_{0.55}TiO_3$ materials synthesized at 1350 °C in oxygen over those synthesized in air

(1.47×10^{-5} S cm^{-1} in air, and 6.86×10^{-5} S cm^{-1} in oxygen). Firstly, it is of note that our best conductivities obtained in air here (4.2×10^{-5} S cm^{-1}) is considerably higher than those obtained by Aguesse *et al*. even though we use a lower sintering temperature. Furthermore, the dramatic improvement in conductivity obtained in oxygen as seen by Aguesse *et al*. was attributed to a higher density preventing the formation of Li_2CO_3 in the pores. Interestingly, in Figure **3.12**, we only find a weak improvement in conductivities in oxygen and only for compositions with lower lithium content: H and I both show an improved conductivity in the materials synthesized in oxygen, while the more lithium rich composition (J) shows equally high conductivities in air and oxygen. This implies that the mechanism found by Aguesse *et al*. in a material with lower lithium content ($Li_{0.34}La_{0.55}TiO_3$ corresponds to a point near H in our phase diagram) is in fact composition dependent and is not unavoidable in LLTO perovskites. Again, ideal compositions must be determined in order to prevent this deterioration of the pellets when made in air.

3.5 Conclusions

Herein, over 576 samples in the Li-La-Ti-O pseudoternary phase diagram were synthesized and characterized by XRD. The resulting phase stabilities show that perovskite LLTOs of interest as solid electrolytes can be stabilized in a large portion of the phase space, but never as pure phase. Instead, we find that LLTO-composites are stabilized wherein a secondary phase such as TiO_2 is required in order to make LLTO. The best conductivities obtained herein are competitive with the literature even though a single short lower temperature sintering step is utilized here. This study helps to decouple the impact of composition and synthesis conditions that remains a point of confusion due to complex sintering protocols used in the literature. It is also of note that much of the LLTO stabilization occurs during slow cooling rather than at high temperature, in contrast to expectations for metastable materials. This new instance of stabilization of metastable LLTO is of interest both from the materials science point of view but also from the solid electrolyte engineering view given that TiO_2 has been used as a sintering agent to improve the ionic conductivity of LLTO. Thus, by choosing the correct composition and synthesis conditions, one can now better reduce the grain boundary resistance without resorting to extra sintering steps, nor requiring an additive, nor a sacrificial powder bed. Further studies in this system examining the impact of composition on the microstructure, as well as the impact of various dopants are of interest.

3.6 Acknowledgments

This work was funded by a New Frontiers in Research Fund grant and by the Natural Sciences and Engineering Research Council of Canada under the auspices of a Discovery grant.

3.7 Supporting information

Section I: Rietveld fitting approach

The phases present in each 64-sample plate were first identified by the search & match tool embedded in HighScore Plus using the COD and ICSD databases. After, the matched patterns were converted into phases for the automatic Rietveld refinement routine performed in batch mode using HighScore Plus. The steps of the refinement included: scale factor, baseline (background), and peak profile but not site occupations. The challenge with this approach to fitting is to not allow poor fits in cases where the LLTO phase in a particular pattern happens to be at a different composition than the cif file selected for the automated fitting. In order to avoid this problem, 10 different cif files were used for the LLTO phase (these are obtained for 10 different compositions) and each was attempted in an automated fashion for every sample. Then, the fit yielding the lowest Rwp was selected. The list of cif files for the LLTO phases are: $Li_{1.44}La_{4.82}Ti_{8.00}O_{24.00}$ / Cmmm

(ICSD: 99397), $Li_{1.44}La_{4.87}Ti_{8.00}O_{24.00}$ / Cmmm (ICSD: 99399), $Li_{1.20}$ $La_{2.27}Ti_{4.00}O_{12.00}$ / I4/mcm (ICSD:172043), $La_{1.00}Ti_{2.00}O_{6.00}$ / P4/mmm (ICSD: 92237), $Li_{0.48}La_{1.17}Ti_{2.00}O_{6.00}$ / P4/mmm (COD:1000438), $Li_{0.26}La_{1.24}Ti_{2.00}O_{6.00}$ / P4/mmm (ICSD: 50436), $Li_{1.20}Ti_{4.00}La_{2.27}O_{12.00}$ / P4/nbm (ICSD: 236452), $Li_{0.50}La_{0.50}Ti_{1.00}O_{3.00}$ / Pm-3m (ICSD: 254044), $La_{1.28}Ti_{2.00}O_{6.00}$ / Pmmm (ICSD: 92228), $Li_{2.59}La_{3.13}Ti_{6.00}O_{18.00}$ / R-3c (ICSD: 98263). In order to compare lattice parameters across these different space groups, for all fitting results of the LLTO phases we calculated the pseudo-cubic lattice parameters (detailed values used for each cif is given in Table **S3.1**).

The other cif files also used in the automated fitting were: $La_{1.12}Li_{0.62}Ti_2O_6$ (ICSD: 88837), $Li_2Ti_3O_7$ (ICSD: 431128), La_2TiO_5 (ICSD:195207), β-Li_2TiO_3 (ICSD:257014), γ-Li_2TiO_3 (ICSD:31148), La_2O_3(COD:2002286), $La_2Ti_2O_7$ (ICSD:4132), TiO_2 (ICSD:51934), $Li_{0.333}LaTi_{0.667}O_3$ (COD:1531699),and $Li_2La_2Ti_3O_{10}$ (ICSD:82907)

The resulting fits for all 576 XRD patterns had an average R_{wp} value of 11 % with a standard deviation of 2 %, which represents excellent quality fits as supported by Figure **S3.3** where excellent fits are obtained for R_{WP} values ranging from 11-15 %.

Table S3.1 *Pseudo-cubic lattice parameters for the cif files used in the automated fitting of perovskite LLTO.*

ICSD/COD code	Space group	Lattice parameters
254044	Pm-3m	a, a, a
98263	R-3c	√2a, √2a, 2√3a
172043	I4/mcm	√2a, √2a, 2a
50436,92237,1000438	P4/mmm	a, a, 2a
236452	P4/nbm	√2a, √2a, 2a
92228	Pmmm	a, a, 2a
99397,99399	Cmmm	2a,2a,2a

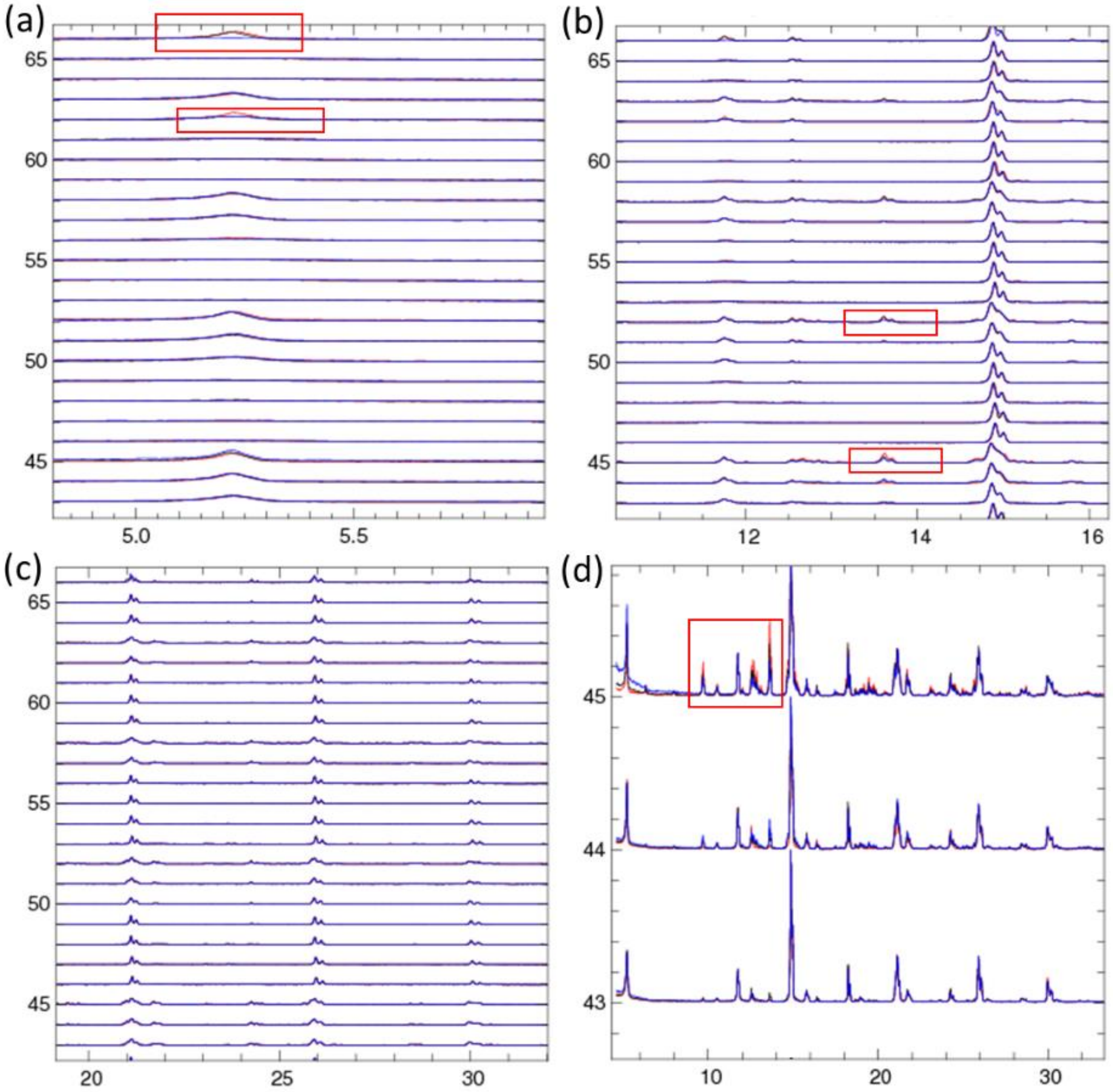

Figure S3.1 *24 sets of triplicate XRD patterns. For each pattern, the triplicates are overlayed in 3 different colors: red, blue and black. The red boxes indicate the few cases where a single outlier exists (the other 2 always overlap well). (a,b,c) Various angle ranges used to zoom enough to make meaningful comparison across all sets, while (d) shows a zoom on 3 particular sets: 2 with excellent overlaps and one showing what we deem to be an outlier in red.*

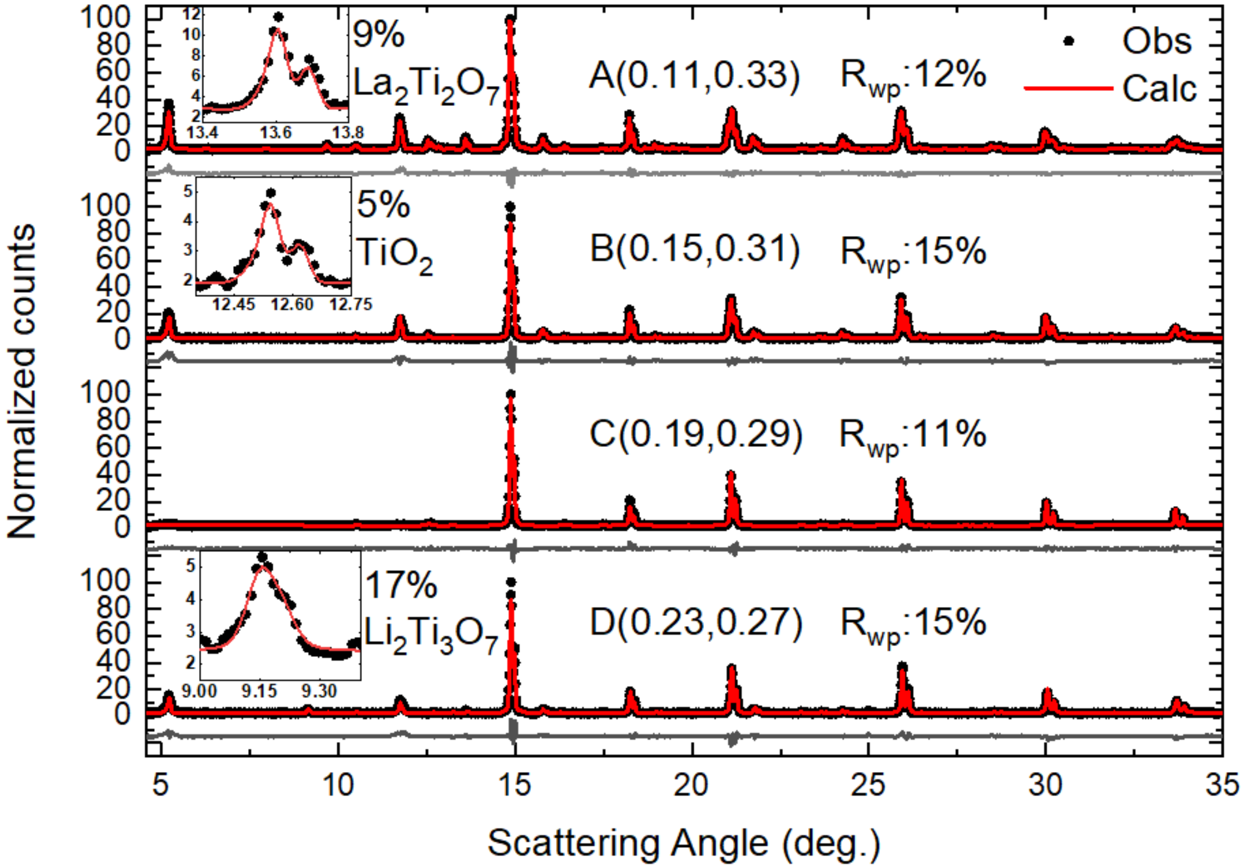

Figure S3.2 *Rietveld fits of the 4 patterns shown in* ***3.5*** *of the main text. Scattering angle here is for Mo radiation. Scan B shows that 5 %* TiO_2 *shows a peak that is 23 times above the noise (the noise on the background is the square root of the counts which is 0.14 in terms of normalized counts). By contrast, the sensitivity to lithium containing phases is lower, with 17%* $Li_2Ti_3O_7$ *also yielding a peak that is approximately 30 times above the noise.*

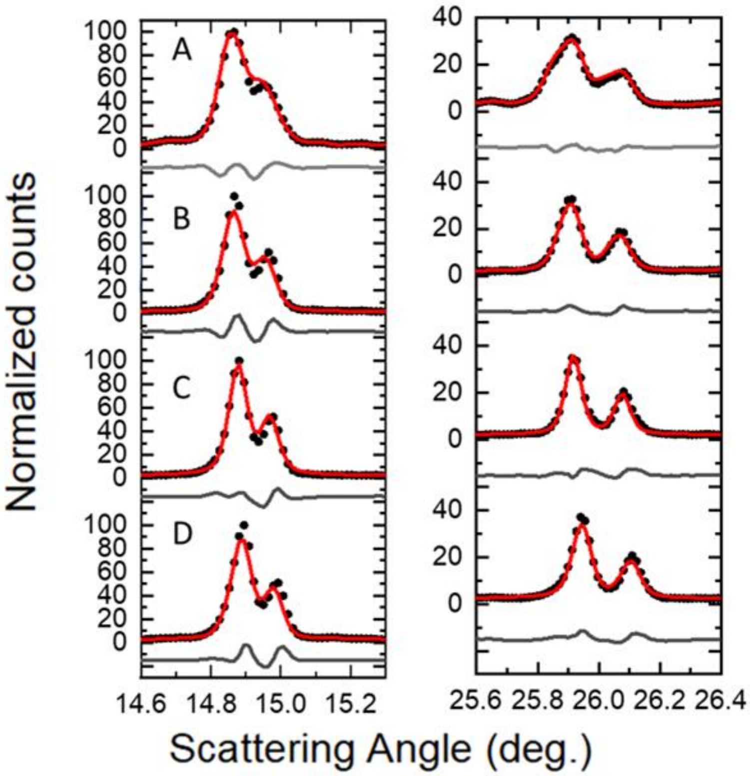

Figure S3.3 *Zoom of the Rietveld fits of the 4 patterns shown in* ***3.5*** *of the main text focusing on two main peaks of the LLTO perovskite phase. In all cases the difference plot is no more that 10 % of the peaks, indicative of a quality fit (and the error in peak area is clearly much smaller than this). The four samples shown above cover the full range of lithium content of interest in the literature, so the fact that excellent fits are obtained for all is indicative that the use of the multiple cifs in the literature gave the refinement enough flexibility to give quality fits. It should also be pointed out that the noise with Mo radiation is exceedingly small (Mo does not fluoresce with the Ti, while copper does), this results in* R_{WP} *values that are artificially inflated for our data (if we add the same background as typical for Cu we find that* R_{WP} *changes from 12 to 2%). Therefore, these figures should establish for the reader that* R_{WP} *values in the vicinity of 15% here are in fact excellent fits.*

Table S3.2 *Results for parameters obtained by Rietveld fits of XRD data of all 64 samples in the zoomed-in region after synthesis to 1200 ℃ and slow cooling. a, b, c are the pseudo-cubic lattice parameters of the LLTO phase with uncertainties indicated in brackets. (Li,La,Ti) represents the dispensed composition.* R_{wp} *is a quality parameter for the fits and is considered to be excellent in the range <15% for the Mo radiation diffractometer used throughout this study. The average* R_{wp} *value is 11% with a standard deviation of 2%.*

Li	**La**	**Ti**	**R_{wp} (%)**	**a (Å)**	**b (Å)**	**c (Å)**
0.32	0.21	0.46	12.9	3.874(3)	3.874(3)	3.874(3)
0.30	0.21	0.48	15.5	3.875(1)	3.875(1)	3.875(3)
0.29	0.21	0.50	16.3	3.874(2)	3.874(2)	3.874(3)
0.27	0.21	0.52	16.6	3.874(1)	3.874(1)	3.874(2)
0.25	0.21	0.54	14.6	3.8750(5)	3.8750(5)	3.877(1)
0.23	0.21	0.56	16.8	3.874(3)	3.874(3)	3.874(3)
0.21	0.21	0.58	15.2	3.874(1)	3.874(1)	3.877(1)
0.19	0.21	0.60	15.2	3.874(3)	3.874(3)	3.874(3)
0.30	0.23	0.46	12.2	3.870(1)	3.870(1)	3.870(1)
0.29	0.23	0.48	10.7	3.875(2)	3.875(2)	3.875(3)
0.27	0.23	0.50	10.0	3.874(5)	3.874(5)	3.870(6)
0.25	0.23	0.52	16.7	3.874(2)	3.874(2)	3.874(3)
0.23	0.23	0.54	16.1	3.874(3)	3.874(3)	3.874(3)
0.21	0.23	0.56	14.4	3.874(3)	3.874(3)	3.874(3)
0.19	0.23	0.58	14.9	3.874(1)	3.874(1)	3.877(2)
0.17	0.23	0.60	13.8	3.874(1)	3.874(1)	3.876(2)
0.29	0.25	0.46	16.1	3.874(1)	3.874(1)	3.876(1)
0.27	0.25	0.48	14.5	3.874(2)	3.874(2)	3.874(3)
0.25	0.25	0.50	14.6	3.874(1)	3.874(1)	3.877(2)
0.23	0.25	0.52	15.1	3.875(1)	3.875(1)	3.876(2)
0.21	0.25	0.54	15.5	3.874(3)	3.874(3)	3.874(3)
0.19	0.25	0.56	14.7	3.874(1)	3.874(1)	3.876(2)
0.17	0.25	0.58	15.7	3.874(1)	3.874(1)	3.877(1)
0.15	0.25	0.60	16.9	3.873(1)	3.873(1)	3.878(2)
0.27	0.27	0.46	14.0	3.8711(6)	3.8711(6)	3.885(1)
0.25	0.27	0.48	14.8	3.870(2)	3.870(2)	3.882(2)
0.23	0.27	0.50	15.4	3.871(1)	3.871(1)	3.878(1)
0.21	0.27	0.52	16.9	3.874(4)	3.874(4)	3.874(3)
0.19	0.27	0.54	14.6	3.874(3)	3.874(3)	3.874(3)
0.17	0.27	0.56	13.2	3.874(1)	3.874(1)	3.876(2)
0.15	0.27	0.58	15.8	3.871(1)	3.871(1)	3.880(2)
0.13	0.27	0.60	13.7	3.871(1)	3.871(1)	3.887(2)

0.25	0.29	0.46	11.9	3.871(1)	3.871(1)	3.887(1)
0.23	0.29	0.48	12.9	3.871(2)	3.871(2)	3.886(2)
0.21	0.29	0.50	15.1	3.8695(6)	3.8695(6)	3.8780(5)
0.19	0.29	0.52	10.7	3.875(1)	3.875(1)	3.874(2)
0.17	0.29	0.54	17.7	3.873(1)	3.873(1)	3.878(1)
0.15	0.29	0.56	14.1	3.872(2)	3.872(2)	3.884(2)
0.13	0.29	0.58	13.4	3.871(1)	3.871(1)	3.888(1)
0.11	0.29	0.60	12.3	3.868(2)	3.869(3)	3.886(1)
0.23	0.31	0.46	10.8	3.870(2)	3.870(2)	3.889(3)
0.21	0.31	0.48	13.3	3.871(2)	3.871(2)	3.886(2)
0.19	0.31	0.50	12.2	3.871(2)	3.871(2)	3.886(3)
0.17	0.31	0.52	12.5	3.871(1)	3.871(1)	3.885(1)
0.15	0.31	0.54	15.0	3.872(2)	3.872(2)	3.884(2)
0.13	0.31	0.56	12.9	3.871(1)	3.871(1)	3.888(2)
0.11	0.31	0.58	10.6	3.868(2)	3.869(2)	3.886(2)
0.09	0.31	0.60	11.1	3.864(3)	3.872(3)	3.887(3)
0.21	0.33	0.46	10.1	3.870(2)	3.870(2)	3.887(3)
0.19	0.33	0.48	10.9	3.870(1)	3.870(1)	3.887(2)
0.17	0.33	0.50	13.0	3.871(2)	3.871(2)	3.886(2)
0.15	0.33	0.52	12.7	3.871(1)	3.871(1)	3.885(1)
0.13	0.33	0.54	11.9	3.871(2)	3.871(2)	3.888(2)
0.11	0.33	0.56	11.8	3.868(3)	3.868(4)	3.886(2)
0.09	0.33	0.58	10.4	3.863(2)	3.872(2)	3.887(2)
0.07	0.33	0.60	10.7	3.862(2)	3.872(2)	3.888(2)
0.19	0.35	0.46	10.6	3.870(1)	3.870(1)	3.887(2)
0.17	0.35	0.48	10.6	3.870(2)	3.870(2)	3.886(2)
0.15	0.35	0.50	9.8	3.870(3)	3.870(3)	3.887(3)
0.13	0.35	0.52	10.7	3.870(2)	3.870(2)	3.888(2)
0.11	0.35	0.54	9.9	3.871(2)	3.871(2)	3.887(3)
0.09	0.35	0.56	10.4	3.870(5)	3.870(5)	3.885(3)
0.07	0.35	0.58	9.9	3.864(3)	3.871(3)	3.887(3)
0.05	0.35	0.60	10.1	3.862(2)	3.872(2)	3.889(2)

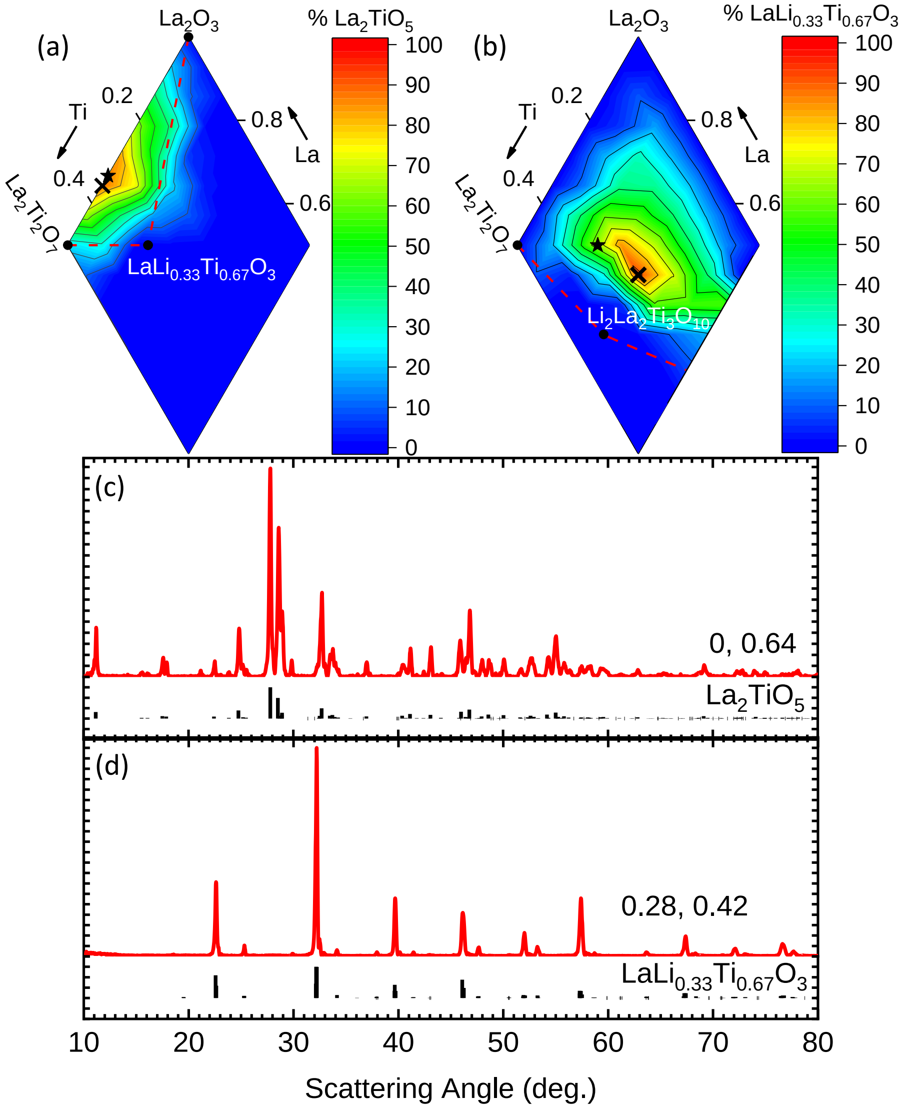

Figure S3.4 *The contour map of the La_2TiO_5 (a) and $LaLi_{0.33}Ti_{0.67}O_3$ (b) phase fractions after heating at 1200 ℃ and slow cooling. (c) The powder XRD pattern of the sample lying at the Xs in panel a with the reference pattern for La_2TiO_5 (d) The XRD pattern obtained at the X in panel b along with the reference pattern for $LaLi_{0.33}Ti_{0.67}O_3$. The * in each of a,b indicate the position of the phase based on the reference pattern. In the case of $LaLi_{0.33}Ti_{0.67}O_3$. the difference in position between the * (reference) and X (highest phase fraction obtained experimentally) is attributed to Li loss as the line between the two points extrapolates to the Li corner.*

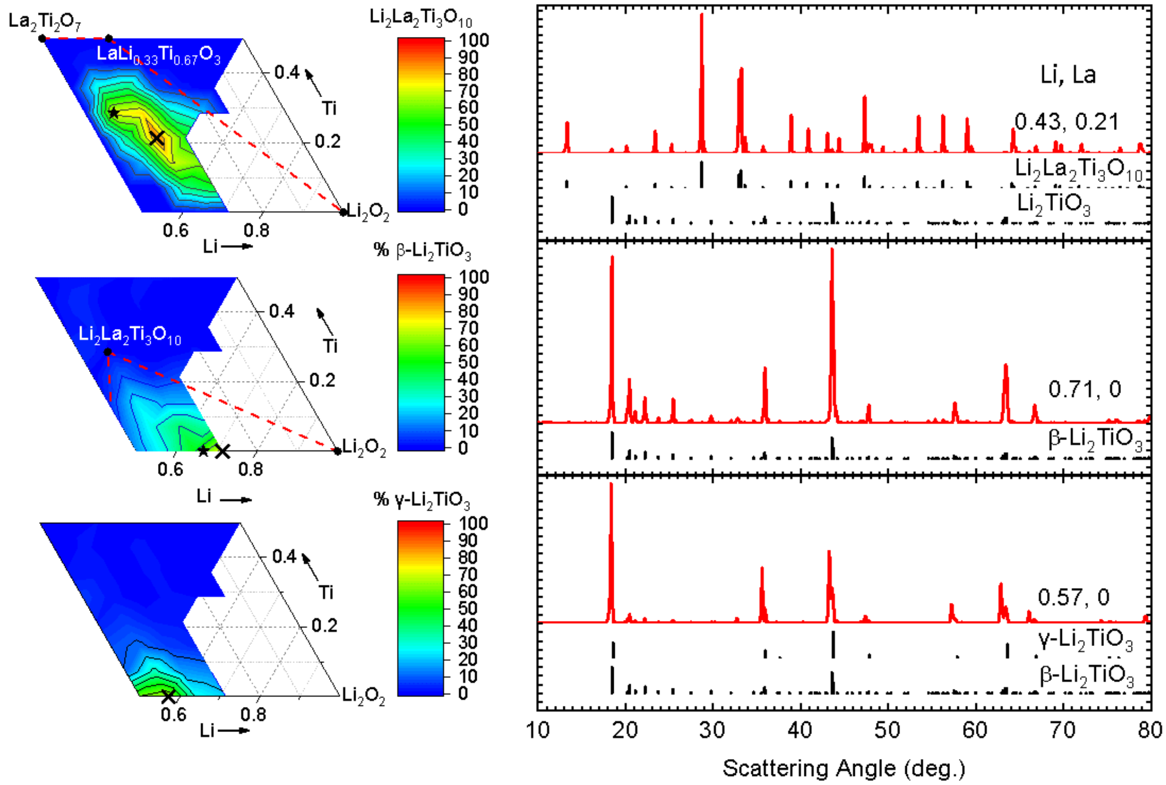

Figure S3.5 *The contour maps of* $Li_2La_2Ti_3O_{10}$ *and* Li_2TiO_3 *(two different phases:* β*, and* γ*). The* β *phase is found to be stabilized at 100% at a composition of (Li,Ti) = (0.71,0.29), consistent with a small amount of lithium loss such that we attribute this phase to the actual* Li_2TiO_3 *composition. The* γ *phase however can be stabilized at lower Li contents. Here, we find that this phase has a composition of Li:Ti = 0.6:0.4 based on the phase map in Figure* ***3.4*** *of the main text. This corresponds to* $Li_{1.2}Ti_{0.8}O_2$ *and explains why the superstructure peaks seen in the* β *phase (due to ordering of Li on the Ti layers) are greatly diminished in the* γ *phase. We also find that this phase is metastable and begins to disappear during slow cooling as shown by the lever rule in Figure* ***S3.7****.*

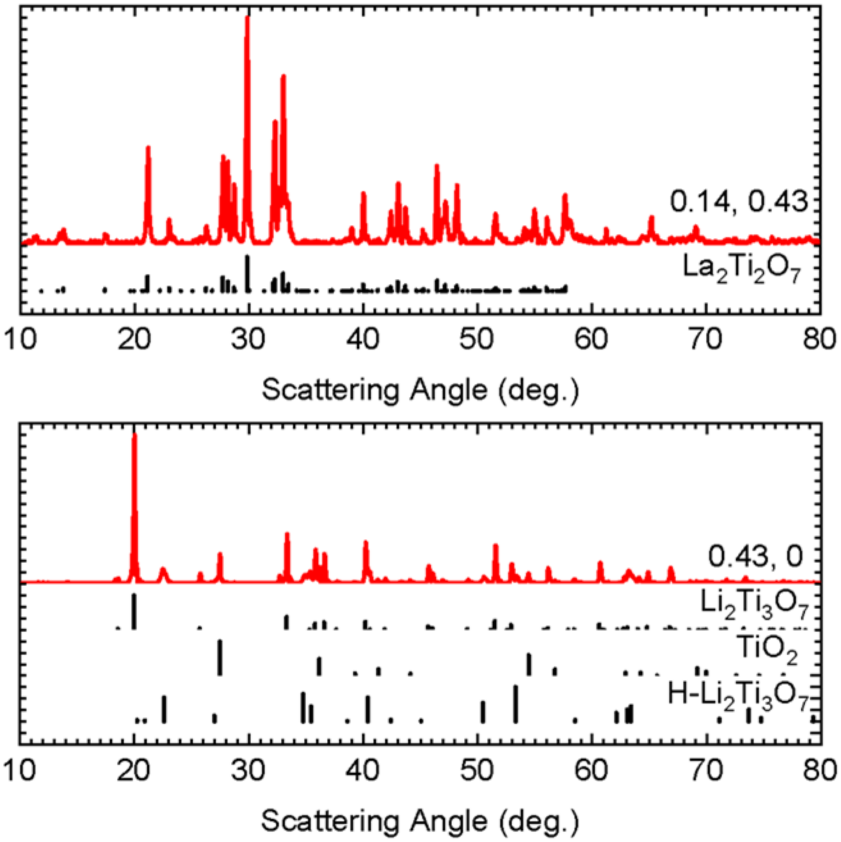

Figure S3.6 *XRD patterns showing the highest presence of* $La_2Ti_2O_7$ *(upper panel) and* $Li_2Ti_3O_7$ *(lower panel). The black lines are the reference patterns for the phases present.*

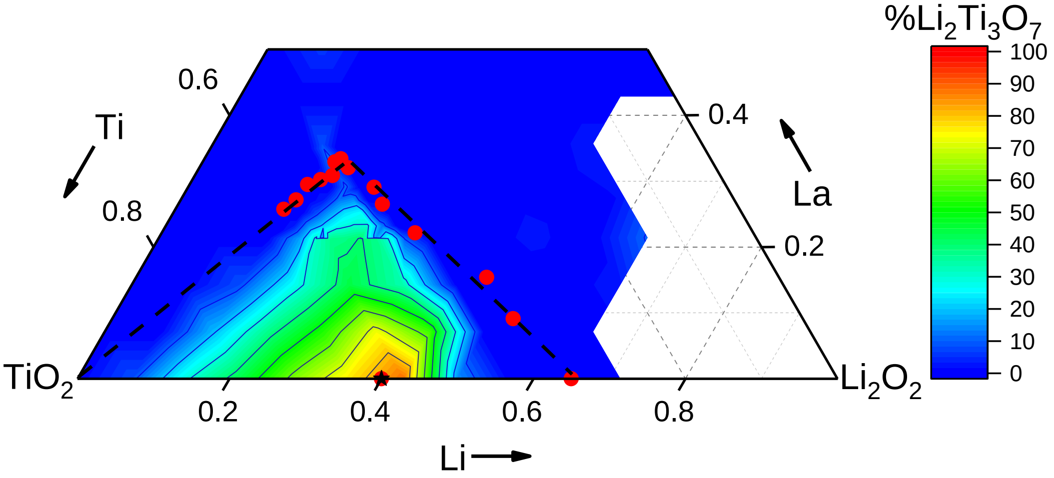

Figure S3.7 *Phase map obtained for* $Li_2Ti_3O_7$ *after heating at 1200 ℃ for 6 h and then slow cooling. The red points show the result of using the lever rule to extrapolate to where the phase is no longer present. The two linear fits extrapolate to* TiO_2 *and* Li_2TiO_3*.*

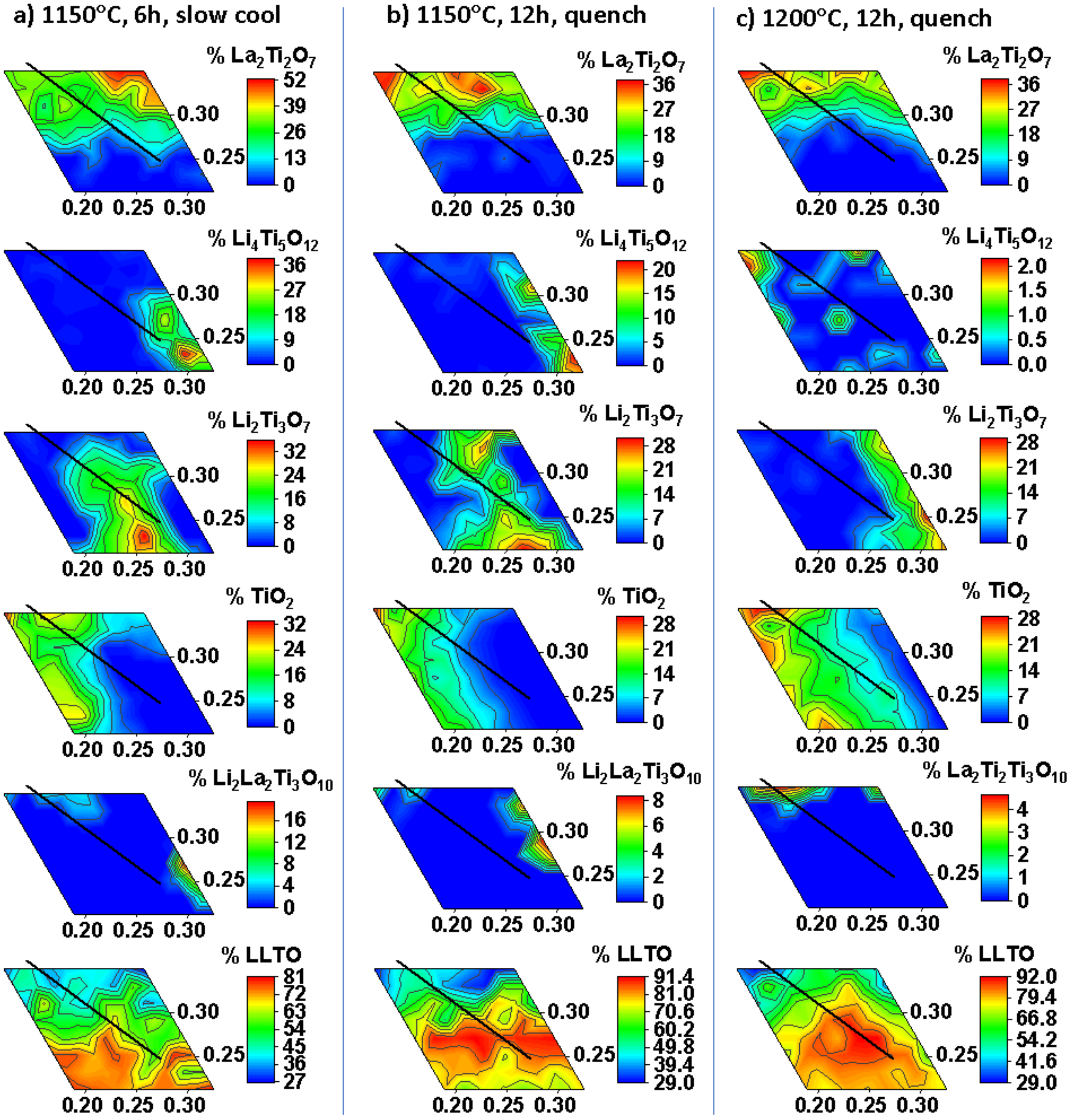

Figure S3.8 *Phase composition maps found in the zoomed-in region under various sintering conditions. In all cases, the black line shows the composition line typically studied for LLTO materials as detailed in the main text.*

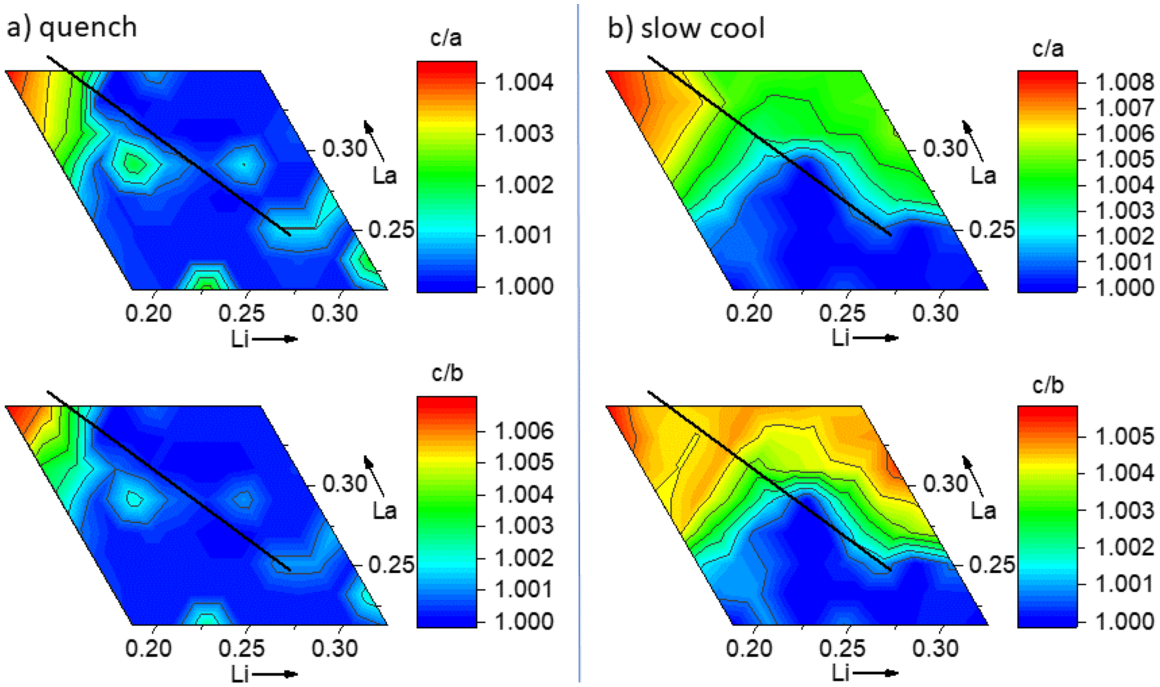

Figure S3.9 *Lattice parameter ratios obtained for materials made in the zoomed-in LLTO region after heating to 1200 ℃ for 6 h. The mid and high lithium regions (bottom, right) of quenched samples are almost cubic. While the low lithium region (top, left) of both quenched and slow cooled samples are orthorhombic.*

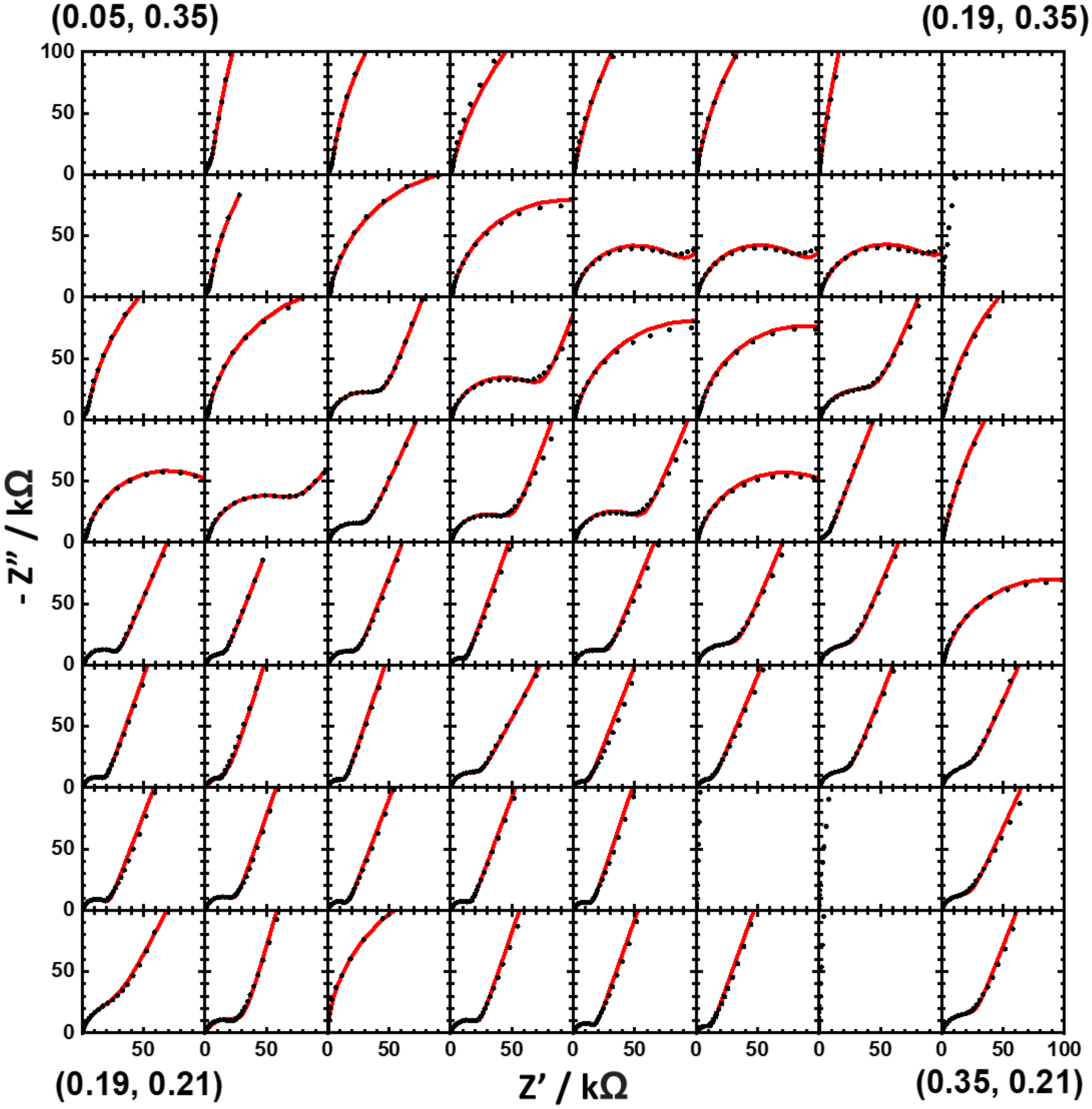

__Figure S3.10__ EIS spectra obtained in the zoomed-in LLTO region for samples heated at 1200 ℃ for 6 h and then quenched to room temperature. The four corners are labelled by compositions using molar fractions: (Li, La) where Ti = 1 – Li – La. The red lines are the results of fitting as described in the main text.

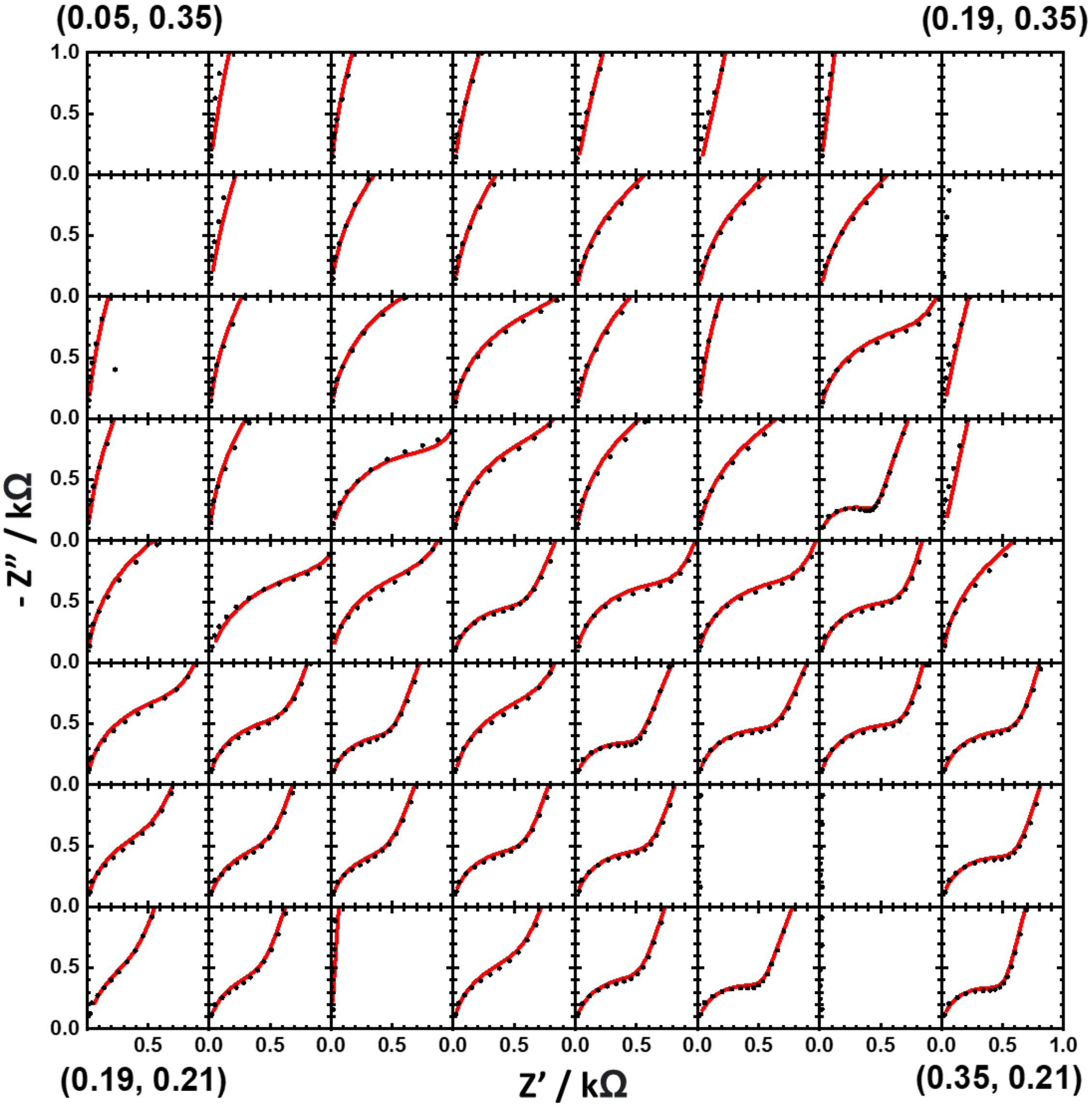

__Figure S3.11__ EIS spectra obtained in the zoomed-in LLTO region for samples heated at 1200 ℃ for 6 h and then quenched to room temperature. The spectra have been zoomed in (high frequency region) in order to show the bulk contributions to the EIS data.

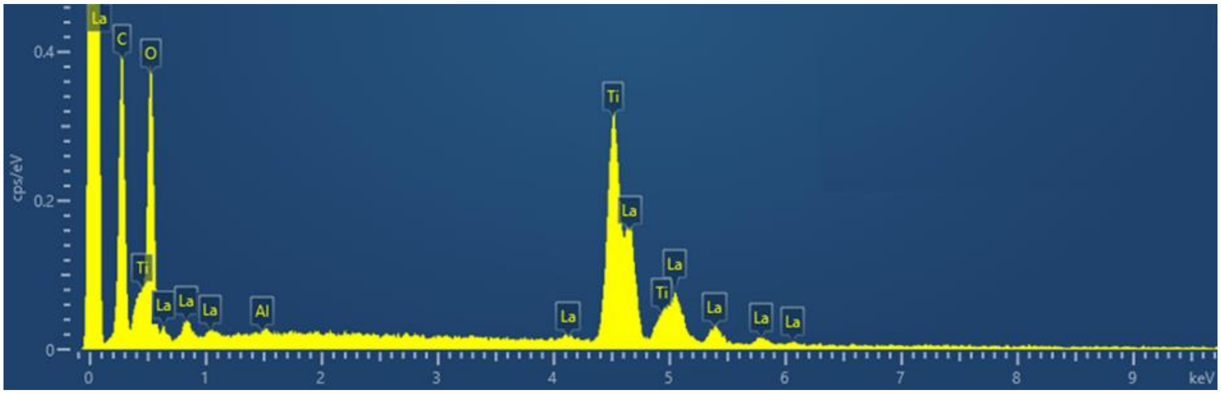

Figure S3.12 *EDS results from a typical pellet of LLTO in this study. A small peak is found for Al, otherwise no peak is recognized within the detection limit of the instrument other than the expected Li, La, Ti, and O.*

Table S3.3 *ICP results of 10 pellets after synthesis at 1200 °C and slow cooling. The first four columns are metallic molar ratios adding up to 1, while x is the aluminum:titanium metal ratio.*

Al	Li	La	Ti	x: (Al_xTi_{1-x})
0.00381	0.29034	0.22544	0.48042	0.00786
0.00200	0.24002	0.19900	0.55898	0.00357
0.00180	0.20624	0.24807	0.54388	0.00330
0.00220	0.18689	0.26473	0.54617	0.00401
0.00090	0.13731	0.32066	0.54113	0.00166
0.00170	0.17961	0.24475	0.57394	0.00295
0.00170	0.12446	0.26705	0.60679	0.00280
0.00170	0.17226	0.31719	0.50886	0.00333
0.00190	0.12765	0.28664	0.58380	0.00325
0.00090	0.13963	0.29196	0.56751	0.00158

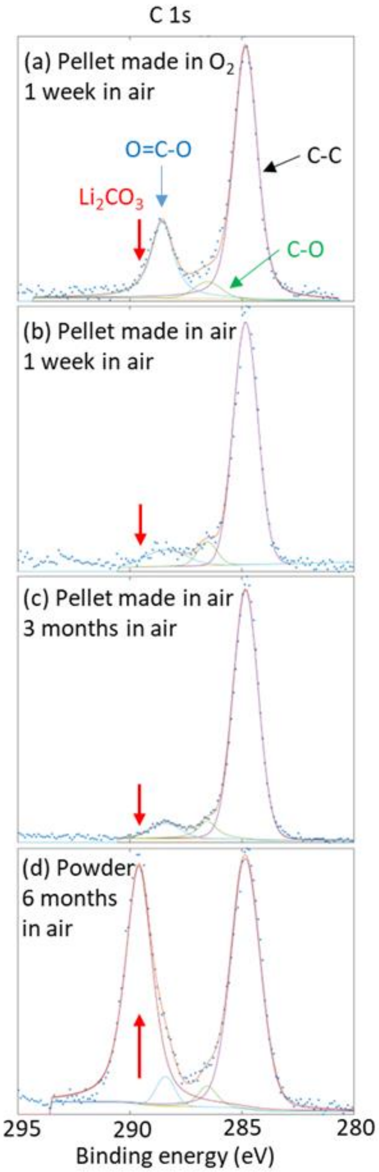

Figure S3.13 *XPS results for the carbon 1s peak on samples made at composition J (0.23,0.27) in air at 1200 C for 6 h followed by slow cooling. The peaks are labelled according to the identification from ref. [S41]. The powder sample left in air for 6 months clearly shows a large amount of lithium carbonate, this supports the reviewers' concerns. However, our 3 pellet samples (all at composition J, 2 made in air and 1 in oxygen) all show no lithium carbonate whatsoever. The samples after 1 week are particularly meaningful as we always perform EIS quicker than this. We therefore conclude that lithium carbonate was not at play in our results.*

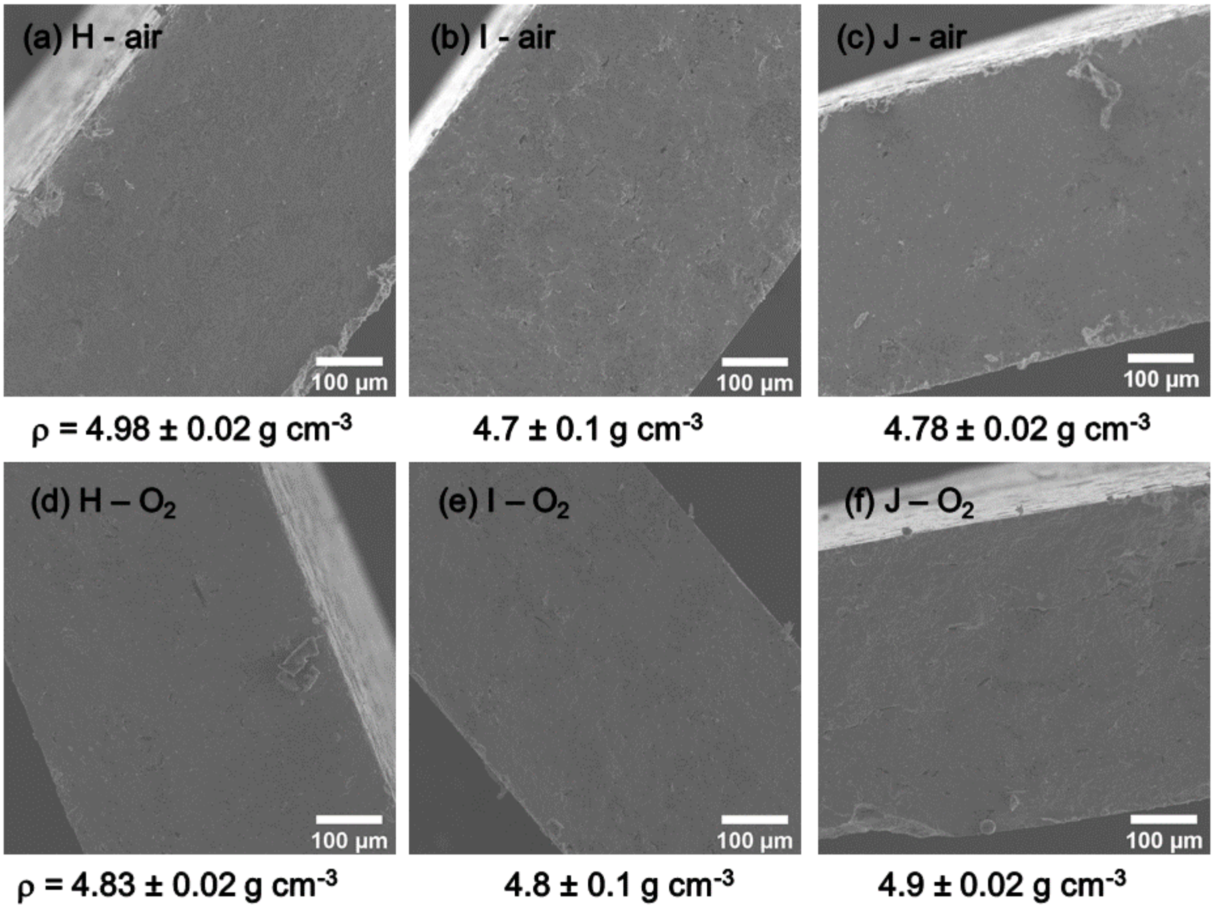

Figure S3.14 *Cross-sectional SEM images of six freshly fractured pellets shown in* ***3.12*** *of the main text. Below each image is the average density obtained from the replicates.*

3.8 References

(1) Chen, T.; Jin, Y.; Lv, H.; Yang, A.; Liu, M.; Chen, B.; Xie, Y.; Chen, Q. Applications of Lithium-Ion Batteries in Grid-Scale Energy Storage Systems. *Transactions of Tianjin University* **2020**, *26* (3), 208.
(2) Monroe, C.; Newman, J. The Impact of Elastic Deformation on Deposition Kinetics at Lithium/Polymer Interfaces. *Journal of The Electrochemical Society* **2005**, *152* (2), A396.
(3) Phuc, N. H. H.; Takaki, M.; Muto, H.; Reiko, M.; Kazuhiro, H.; Matsuda, A. Sulfur–Carbon Nano Fiber Composite Solid Electrolyte for All-Solid-State Li–S Batteries. *ACS Applied Energy Materials* **2020**, *3* (2), 1569.
(4) Song, H.; Wang, S.; Song, X.; Wang, J.; Jiang, K.; Huang, S.; Han, M.; Xu, J.; He, P.; Chen, K.; Zhou, H. Solar-Driven All-Solid-State Lithium–Air Batteries Operating at Extreme Low Temperatures. *Energy & Environmental Science* **2020**, *13* (4), 1205.
(5) Bachman, J. C.; Muy, S.; Grimaud, A.; Chang, H.-H.; Pour, N.; Lux, S. F.; Paschos, O.; Maglia, F.; Lupart, S.; Lamp, P.; Giordano, L.; Shao-Horn, Y. Inorganic Solid-State Electrolytes for Lithium Batteries: Mechanisms and Properties Governing Ion Conduction. *Chemical Reviews* **2016**, *116* (1), 140.

(6) Inaguma, Y.; Chen, L.; Itoh, M.; Nakamura, T. Candidate Compounds With Perovskite Structure for High Lithium Ionic Conductivity. *Solid State Ionics* **1994**, *70-71*, 196.

(7) Itoh, M.; Inaguma, Y.; Jung, W.-H.; Chen, L.; Nakamura, T. High Lithium Ion Conductivity in the Perovskite-Type Compounds $Ln_{12}Li_{12}TiO_3$(Ln=La,Pr,Nd,Sm). *Solid State Ionics* **1994**, *70-71*, 203.

(8) Inaguma, Y.; Yu, J.; Shan, Y. J.; Itoh, M.; Nakamuraa, T. The Effect of the Hydrostatic Pressure on the Ionic Conductivity in a Perovskite Lanthanum Lithium Titanate. *Journal of The Electrochemical Society* **1995**, *142* (1), L8.

(9) Inaguma, Y.; Liquan, C.; Itoh, M.; Nakamura, T.; Uchida, T.; Ikuta, H.; Wakihara, M. High Ionic Conductivity in Lithium Lanthanum Titanate. *Solid State Communications* **1993**, *86* (10), 689.

(10) Gao, X.; Fisher, C. A. J.; Kimura, T.; Ikuhara, Y. H.; Kuwabara, A.; Moriwake, H.; Oki, H.; Tojigamori, T.; Kohama, K.; Ikuhara, Y. Domain Boundary Structures in Lanthanum Lithium Titanates. *Journal of Materials Chemistry A* **2014**, *2* (3), 843.

(11) Kwon, W. J.; Kim, H.; Jung, K.-N.; Cho, W.; Kim, S. H.; Lee, J.-W.; Park, M.-S. Enhanced Li+ Conduction in Perovskite $Li_{3x}La_{2/3-x}\square_{1/3-2x}TiO_3$ Solid-Electrolytes via Microstructural Engineering. *Journal of Materials Chemistry A* **2017**, *5* (13), 6257.

(12) Guo, X.; Maram, P. S.; Navrotsky, A. A Correlation Between Formation Enthalpy and Ionic Conductivity in Perovskite-Structured $Li_{3x}La_{0.67-x}TiO_3$ Solid Lithium Ion Conductors. *Journal of Materials Chemistry A* **2017**, *5* (25), 12951.

(13) Vijayakumar, M.; Inaguma, Y.; Mashiko, W.; Crosnier-Lopez, M.-P.; Bohnke, C. Synthesis of Fine Powders of $Li_{3x}La_{2/3-x}TiO_3$ Perovskite by a Polymerizable Precursor Method. *Chemistry of Materials* **2004**, *16* (14), 2719.

(14) Wu, J.-F.; Guo, X. Origin of the Low Grain Boundary Conductivity in Lithium Ion Conducting Perovskites: $Li_{3x}La_{0.67-x}TiO_3$. *Physical Chemistry Chemical Physics* **2017**, *19* (8), 5880.

(15) García-Martín, S.; Alario-Franco, M. A.; Ehrenberg, H.; Rodríguez-Carvajal, J.; Amador, U. Crystal Structure and Microstructure of Some $La_{2/3-x}Li_{3x}TiO_3$ Oxides: An Example of the Complementary Use of Electron Diffraction and Microscopy and Synchrotron X-ray Diffraction To Study Complex Materials. *Journal of the American Chemical Society* **2004**, *126* (11), 3587.

(16) Wang, M. J.; Wolfenstine, J. B.; Sakamoto, J. Mixed Electronic and Ionic Conduction Properties of Lithium Lanthanum Titanate. *Advanced Functional Materials* **2020**, *30* (10), 1909140.

(17) Adhikari, T.; Hebert, A.; Adamič, M.; Yao, J.; Potts, K.; McCalla, E. Development of High-Throughput Methods for Sodium-Ion Battery Cathodes. *ACS Combinatorial Science* **2020**, *22* (6), 311.

(18) Potts, K. P.; Grignon, E.; McCalla, E. Accelerated Screening of High-Energy Lithium-Ion Battery Cathodes. *ACS Applied Energy Materials* **2019**, *2* (12), 8388.

(19) Fleischauer, M. D.; Hatchard, T. D.; Bonakdarpour, A.; Dahn, J. R. Combinatorial Investigations of Advanced Li-Ion Rechargeable Battery Electrode Materials. *Measurement Science and Technology* **2004**, *16* (1), 212.

(20) Du, Z.; Hatchard, T. D.; Dunlap, R. A.; Obrovac, M. N. Combinatorial Investigations of Ni-Si Negative Electrode Materials for Li-Ion Batteries. *Journal of The Electrochemical Society* **2015**, *162* (9), A1858.

(21) Al-Maghrabi, M. A.; Suzuki, J.; Sanderson, R. J.; Chevrier, V. L.; Dunlap, R. A.; Dahn, J. R. Combinatorial Studies of $Si_{1-x}O_x$ as a Potential Negative Electrode Material for Li-Ion Battery Applications. *Journal of The Electrochemical Society* **2013**, *160* (9), A1587.

(22) Todd, A. D. W.; Ferguson, P. P.; Fleischauer, M. D.; Dahn, J. R. Tin-Based Materials as Negative Electrodes for Li-Ion Batteries: Combinatorial Approaches and Mechanical Methods. *International Journal of Energy Research* **2010**, *34* (6), 535.

(23) Beal, M. S.; Hayden, B. E.; Le Gall, T.; Lee, C. E.; Lu, X.; Mirsaneh, M.; Mormiche, C.; Pasero, D.; Smith, D. C. A.; Weld, A.; Yada, C.; Yokoishi, S. High Throughput Methodology for Synthesis, Screening, and Optimization of Solid State Lithium Ion Electrolytes. *ACS Combinatorial Science* **2011**, *13* (4), 375.

(24) Danks, A. E.; Hall, S. R.; Schnepp, Z. The Evolution of 'Sol–Gel' Chemistry as a Technique for Materials Synthesis. *Materials Horizons* **2016**, *3* (2), 91.

(25) Belous, A.; Yanchevskiy, O.; V'Yunov, O.; Bohnke, O.; Bohnke, C.; Le Berre, F.; Fourquet, J.-L. Peculiarities of $Li_{0.5}La_{0.5}TiO_3$ Formation during the Synthesis by Solid-State Reaction or Precipitation from Solutions. *Chemistry of Materials* **2004**, *16* (3), 407.

(26) Ban, C. W.; Choi, G. M. The Effect of Sintering on the Grain Boundary Conductivity of Lithium Lanthanum Titanates. *Solid State Ionics* **2001**, *140* (3), 285.

(27) Schell, K. G.; Lemke, F.; Bucharsky, E. C.; Hintennach, A.; Hoffmann, M. J. Microstructure and Mechanical Properties of $Li_{0.33}La_{0.567}TiO_3$. *Journal of Materials Science* **2016**, *52* (4), 2232.

(28) Sun, W.; Dacek, S. T.; Ong, S. P.; Hautier, G.; Jain, A.; Richards, W. D.; Gamst, A. C.; Persson, K. A.; Ceder, G. The Thermodynamic Scale of Inorganic Crystalline Metastability. *Science Advances* **2016**, *2* (11), e1600225.

(29) Kitaoka, K.; Kozuka, H.; Hashimoto, T.; Yoko, T. Preparation of $La_{0.5}Li_{0.5}TiO_3$ Perovskite Thin Films by the Sol–Gel Method. *Journal of Materials Science* **1997**, *32* (8), 2063.

(30) McCalla, E.; Carey, G. H.; Dahn, J. R. Lithium Loss Mechanisms During Synthesis of Layered $Li_xNi_{2-x}O_2$ for Lithium Ion Batteries. *Solid State Ionics* **2012**, *219*, 11.

(31) Škapin, S. D.; Kolar, D.; Suvorov, D. Phase Stability and Equilibria in the La_2O_3–TiO_2 System. *Journal of the European Ceramic Society* **2000**, *20* (8), 1179.

(32) Mikkelsen Jr, J. C. Pseudobinary Phase Relations of $Li_2Ti_3O_7$. *Journal of the American Ceramic Society* **1980**, *63* (5-6), 331.

(33) McCalla, E.; Rowe, A. W.; Shunmugasundaram, R.; Dahn, J. R. Structural Study of the Li–Mn–Ni Oxide Pseudoternary System of Interest for Positive Electrodes of Li-Ion Batteries. *Chemistry of Materials* **2013**, *25* (6), 989.

(34) McCalla, E.; Lowartz, C. M.; Brown, C. R.; Dahn, J. R. Formation of Layered–Layered Composites in the Li–Co–Mn Oxide Pseudoternary System during Slow Cooling. *Chemistry of Materials* **2013**, *25* (6), 912.

(35) Ma, C.; Chen, K.; Liang, C.; Nan, C.-W.; Ishikawa, R.; More, K.; Chi, M. Atomic-Scale Origin of the Large Grain-Boundary Resistance in Perovskite Li-Ion-Conducting Solid Electrolytes. *Energy & Environmental Science* **2014**, *7* (5), 1638.

(36) Irvine, J. T. S.; Sinclair, D. C.; West, A. R. Electroceramics: Characterization by Impedance Spectroscopy. *Advanced Materials* **1990**, *2* (3), 132.

(37) Sotomayor, M. E.; Levenfeld, B.; Varez, A.; Sanz, J. Study of the $La_{1/2+1/2x}Li_{1/2-1/2x}Ti_{1-x}Al_xO_3$ ($0 \leq x \leq 1$) Solid Solution. A New Example of Percolative System in Fast Ion Conductors. *Journal of Alloys and Compounds* **2017**, *720*, 460.

(38) He, L. X.; Yoo, H. I. Effects of B-Site Ion (M) Substitution on the Ionic Conductivity of $(Li_{3x}La_{2/3-x})_{1+y/2}(M_yTi_{1-y})O_3$ (M=Al, Cr). *Electrochimica Acta* **2003**, *48* (10), 1357.

(39) Morata-Orrantia, A.; García-Martín, S.; Alario-Franco, M. Á. Optimization of Lithium Conductivity in La/Li Titanates. *Chemistry of Materials* **2003**, *15* (21), 3991.

(40) Aguesse, F.; López del Amo, J. M.; Roddatis, V.; Aguadero, A.; Kilner, J. A. Enhancement of the Grain Boundary Conductivity in Ceramic $Li_{0.34}La_{0.55}TiO_3$ Electrolytes in a Moisture-Free Processing Environment. *Advanced Materials Interfaces* **2014**, *1* (7), 1300143.

(41) Lee, M. J.; Shin, D. O.; Kim, J. Y.; Oh, J.; Kang, S. H.; Kim, J.; Kim, K. M.; Lee, Y. M.; Kim, S. O.; Lee, Y.-G. Interfacial Barrier Free Organic-Inorganic Hybrid Electrolytes for Solid State Batteries. *Energy Storage Materials* **2021**, *37*, 306.

Chapter 4

226 Substitutions Into Li-La-Ti-O Perovskites: Benefits and Limitations

Chapter 3 revealed that low grain boundary conductivity in LLTO can be improved by carefully selecting composition and synthesis conditions. Additionally, Chapter 2 demonstrated that LLTO is not stable at low potential. Building on this foundation, this chapter further enhances charge transport properties and increases reductive stability through single partial substitutions in the LLTO perovskite. To systematically investigate this, we perform substitutions with 50 different elements at 5 different substitution levels, utilizing bond valence mismatch to predict the ideal site for each substituent. Interestingly, while Chapter 3 uncovered the metastability of the perovskite phase, our findings reveal that partial substitutions can stabilize pure LLTO, resulting in a single-phase perovskite material. We explore the impact of these substitutions on bulk and grain boundary ionic conductivity, electronic conductivity, and electrochemical stability window, paving the way for the discovery of new materials for various components, including solid electrolytes, catholytes, and cathodes, of bulk and epitaxial solid-state batteries. With this new knowledge, we are one step closer to unlocking the full potential of LLTO solid electrolytes.

Chapter 4 is submitted for publication under the title “226 substitutions into Li-La-Ti-O perovskites: benefits and limitations” by Jonderian, A.; Peng, R.; Davies D.; McCalla, E.

4.1 Abstract

Lithium lanthanum titanate solid electrolyte has high bulk conductivity and stability at high potentials but suffers from low grain boundary conductivity and instability at low potentials. In order to mitigate these two limitations, the effect of single partial substitutions on perovskite (Li-

La-Ti-O) materials was studied. The XRD patterns showed that numerous substituents enable pure-phase perovskite, a feat that could not previously be accomplished in the unsubstituted materials. Bond valence mismatch is used as a simple predictor of the substitution site, and shows that remarkably high mismatches can be tolerated by the perovskite structure. The best substitutions had minimal impact on bulk conductivity but induced minor enhancements in the grain boundary conductivity. Some elements, such as Cr and Mn increased the electronic conductivity producing good candidates for the electrolyte in the composite cathode for an all-solid-state battery. The electrochemical stability limits were also shifted either to higher or lower potentials by substitutions. Cr substitution resulted in the electrolyte becoming a cathode material with a highly reversible redox peak near 3.43 V (vs. Li/Li^+). The thorough screening, therefore, yields a combination of materials (unsubstituted as the anode/electrolyte and Cr-substituted as the cathode) that represents a strong candidate for the elusive epitaxial battery (the components of the battery grown epitaxially layer by layer), an ideal application of this class of materials given the very high bulk conductivities. Some substitutions also extended the low potential stability limit to below 1.5 V, a shift that would allow the use of $Li_4Ti_5O_{12}$ and Nb-based anodes without a buffer layer. Overall, this work shows to what extent the properties of LLTO perovskites can be tuned with substitution in order to meet various application requirements.

4.2 Introduction

Current lithium-ion batteries are limited in safety by the flammable nature of the carbonate-based electrolytes. These electrolytes have a limited electrochemical stability window that restricts the usage of cathodes that operate at high potentials, thereby capping the energy densities achieved.[1] Ceramic solid electrolytes are a safer alternative to the current electrolyte. They can have wider electrochemical stability windows, potentially allowing the use of high-potential cathodes such as

$LiNiPO_4$ operating above 5 V vs. Li and metallic lithium as the anode. In contrast to liquid electrolytes, ceramics may prevent dendrite growth.[2] Lithium lanthanum titanates (LLTOs) are one of the heavily studied solid electrolytes, taking the perovskite structure with Ti octahedra surrounded by a 12-fold coordinated site shared by Li/La/vacancies. These materials have high bulk conductivity (~10^{-3} S cm^{-1}) and are stable at high potentials. However, they suffer from low grain boundary conductivities in the range of 10^{-6} - 10^{-4} S cm^{-1} and they are unstable at potentials lower than 1.7 V limiting their integration in all-solid-state batteries.[3-5] LLTO has recently been used as an anode for lithium-ion batteries exhibiting a high specific capacity of 225 mA h g^{-1}.[6] There have been a number of attempts to enhance the conductivity of LLTO by performing partial substitutions on both La- and Ti-sites, but only minor improvements were reported as summarised in our previous review article.[7] The bulk conductivity in LLTO is dictated by the optimal charge carrier concentration Li/vacancy, lithium percolation path, and lithium mobility barrier energy. Lithium mobility barrier energy is determined by migration bottleneck size (the highest energy point along the migration path) and lithium path electrostatic (energy) landscape. A larger migration bottleneck (made of square planar oxygens) size can be achieved by substituting La-site with large ionic radius elements that can expand the bottleneck size.[8] On the other hand, substituting Ti with a cation that forms strong bonds with oxygen can lower the Li-O bond strength causing less electrostatic potential on the Li-ion hence lowering the lithium mobility energy barrier.[9] Generally, as summarized above, the limiting contribution to conductivity comes from the grain boundaries rather than the bulk in LLTO materials. Previous studies showed that the grain boundary conductivity could be enhanced by: introducing an amorphous phase at the grain boundary,[10] decreasing the height of the Schottky barrier (potential barrier at grain boundary due to its atomic structure) in the space charge,[11] and/or increasing lithium path dimensionality[12].

Efforts were made to stabilize LLTO against lithium metal by trying partial substitutions such as Zr and Sn at the Ti-site but no success was reported.[5]

High-throughput experimentation has proven to be an effective method of accelerating the development of anodes,[13, 14] cathodes,[15-17] and solid electrolytes[4, 18-20] in both bulk materials and thin films. Our lab has developed a high-throughput suite that enables us to screen solid electrolytes accurately and precisely.[4] This suite has been utilized to explore the stability phase diagrams and conductivity of Li-La-Ti-O [20] and Li-La-Zr-O [19] pseudoternary, yielding new insights. Using high-throughput experimentation can significantly reduce the time and cost associated with developing advanced materials for energy storage applications. We have recently used these methods to investigate the impact of up to 52 different dopants on Na-Mn-O and $LiCoPO_4$ cathodes, improving electrochemical performance.[16, 17] Herein, this same broad substitution approach is applied to tune the properties of LLTO perovskites. We conducted systematic single partial substitution for Ti with 50 elements at 5 different levels and screened their essential properties, including ionic/electronic transport and electrochemical stability. This study is a dramatic step towards fully understanding the effect of substitution in Li-La-Ti-O system.

4.3 Experimental

The high-throughput synthesis was done using a methodology we have presented previously.[4,20,21] All reagents (with all substituents listed in Table **S4.1**) were purchased from Sigma-Aldrich with more than purities of more than 99%; only titanium butoxide was 98%. In brief, the sol-gel method was used, starting with lithium nitrate, lanthanum nitrate, a citric acid solution prepared in deionized water, and titanium butoxide prepared in ethanol. The reagents were mixed in a ratio of 1:0.75 total cations to citric acid ratio. The unsubstituted composition was $Li_{3x}La_{2/3-x}TiO_3$ with $x = 0.126$, selected as it showed the highest conductivities along the composition line in our previous study of the Li-La-Ti-O system[20]. The stoichiometry of the Ti was reduced when adding the substituent elements as shown in Tables 4.1 and 4.2 (note: charge was compensated for by both Li and La): $\left(\mathrm{Li}_{3x}\mathrm{La}_{2/3\text{-}x}\right)_{\left[1+\left(\frac{4\text{-}z}{2}\right)y\right]}\mathrm{M}_y\mathrm{Ti}_{1\text{-}y}\mathrm{O}_3$ where x = 0.126, M is the substituent and z is the charge of the substituent. After dispensing, the solvent was evaporated overnight in a 70 °C oven for 12 hrs, then dried under vacuum at 200 °C for 2 hrs. The powders were calcined at 650 °C for 6 hrs, then pelletized and sintered at 1200 °C for 6 hrs.

The essential transport and electrochemical properties of the samples were screened using the tools developed in our lab, and their precision and accuracy were validated in our previous study.[4] In brief, the two sides of the pellets were polished and sputtered with gold and placed in the high-throughput cell. The ionic conductivity was measured by applying AC current at 100 mV and sweeping the frequency from 1MHz to 1Hz using Biologic SP150 potentiostat. The electrochemical impedance measurement was plotted as Nyquist and fitted to RQ + RQ + Q equivalent circuit corresponding to bulk conductivity, grain boundary conductivity, and electrode, respectively, from high frequency to low. The resistances were assigned to bulk or grain boundary according to the capacitance values. These fits were done using EC-lab biologic software. This electrochemical impedance spectroscopy (EIS) measurement was done at two temperatures 22℃ and 50℃; after that, using the Arrhenius equation, the activation energy for Li-diffusion was calculated. The electronic conductivity was measured by applying 2 V DC current while measuring the current decay. The electronic resistance was calculated from the steady-state current.

After measuring the transport properties, the gold electrodes were sanded off, and the pellets were crushed into powder. The powders were transferred into a high-throughput XRD holder. The XRD measurements were performed in transmission mode using a Panalytical diffractometer with a Mo X-ray source and 2D GaliPIX detector. First, the phases were identified using ICSD database then Rietveld refinement was performed using batch mode in Highscore plus. Next, slurries were prepared from the powders, and two electrodes were prepared with 1 mg cm^{-2} loading. One swept to 0.1 V, the other to 0.1 V at a sweep rate of 0.1 V h^{-1}.

4.4 Results and discussions

4.4.1 Structure

The XRD patterns of the perovskites were fit using the tetragonal P4/mmm space group and high-quality fits were obtained as demonstrated with χ^2 values in the range 1.4-1.7 in Figure **4.1**. The two broad peaks at 10.4° and 26° shown in the insets of Figure **4.1** correspond to the superstructure peaks and the broadening is due to stacking fault. The XRD patterns of unsubstituted LLTO and

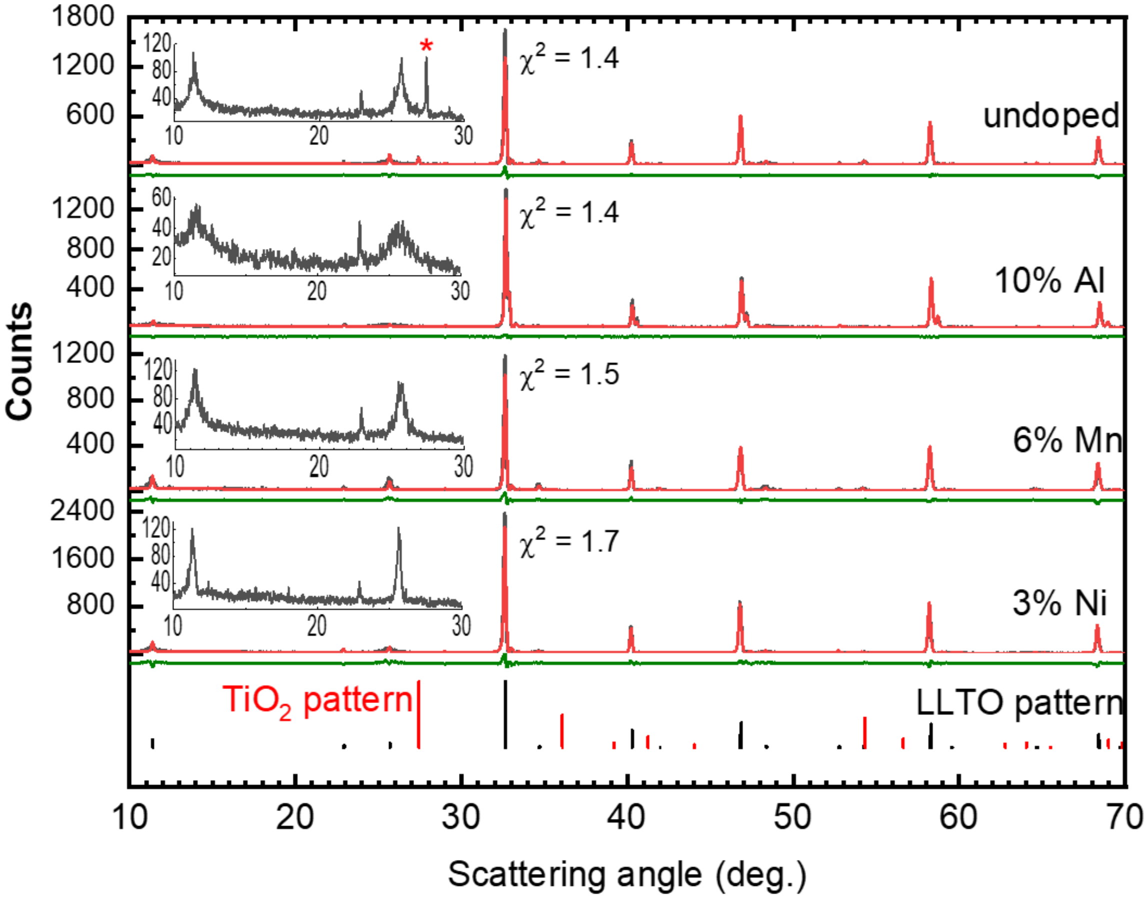

__Figure 4.1__ XRD patterns of undoped, 10% Al, 6%Mn and 3%Ni with reference patterns at the bottom of LLTO and TiO$_2$. Inset: zoomed-in region at the low angles where only LLTO peaks and a TiO$_2$ peak near 27.5° are seen. The red asterisk indicates the TiO$_2$ Phase. The goodness of fit $\chi^2$is reported at the center.

selected substitutions are shown in Figure **4.1** with the insets zoomed to the low-angle region. Unsubstituted LLTO contained 92% LLTO and 8% TiO_2 , consistent with our previous work that showed that unsubstituted LLTO cannot be made without the presence of secondary phases to stabilize it.[20] It is therefore highly significant that a number of substitutions here produce pure perovskite samples as shown in Figure **4.1**. The peak at 27.5° indicated by a red asterisk, corresponds to TiO_2, as seen in the pattern for the unsubstituted sample, while all 3 substituted samples in Figure **4.1** did not show the presence of any secondary phases. In our previous study, we discovered that unsubstituted LLTO is a metastable phase and secondary phases are needed to stabilize it such phase is TiO_2.[20] Recently, Warburton *et al*. in their computational study similarly found that LLTO is metastable.[21] In the current study, we conclude that a number of substitutions stabilize the perovskite, enabling single-phase perovskites to form.

Figures **4.2**, and **S4.1** show the perovskite phase fractions at 3, 6, 10, 15 and 20 % substitution levels for all substituents. The red dashed line corresponds to the unsubstituted LLTO such that 39 substituents at the 3% level increased the fraction of perovskite. Although Ge substitution was attempted, no measurements were collected because these samples at all substitution levels were fused onto the alumina plate. Possibly due to GeO_2 having a melting point of 1115 °C, and it may therefore act as a sintering agent. Thus, these samples would require a lower sintering temperature. 12 (Na, Mg, Al, Sc, Cr, Mn, Fe, Ni, Ga, Sr, Ag, Pb) formed pure perovskites. The perovskite weight fractions obtained from the higher substitution contents are shown in Figure **S4.1** and 6 elements (Mg, Al, Sc, Cr, Mn, Ga) at the 20% substitution level produced pure perovskite. The lattice parameters extracted by Rietveld refinement of the substituted perovskite patterns are shown in Figure **4.2** and distortion from cubic is shown in

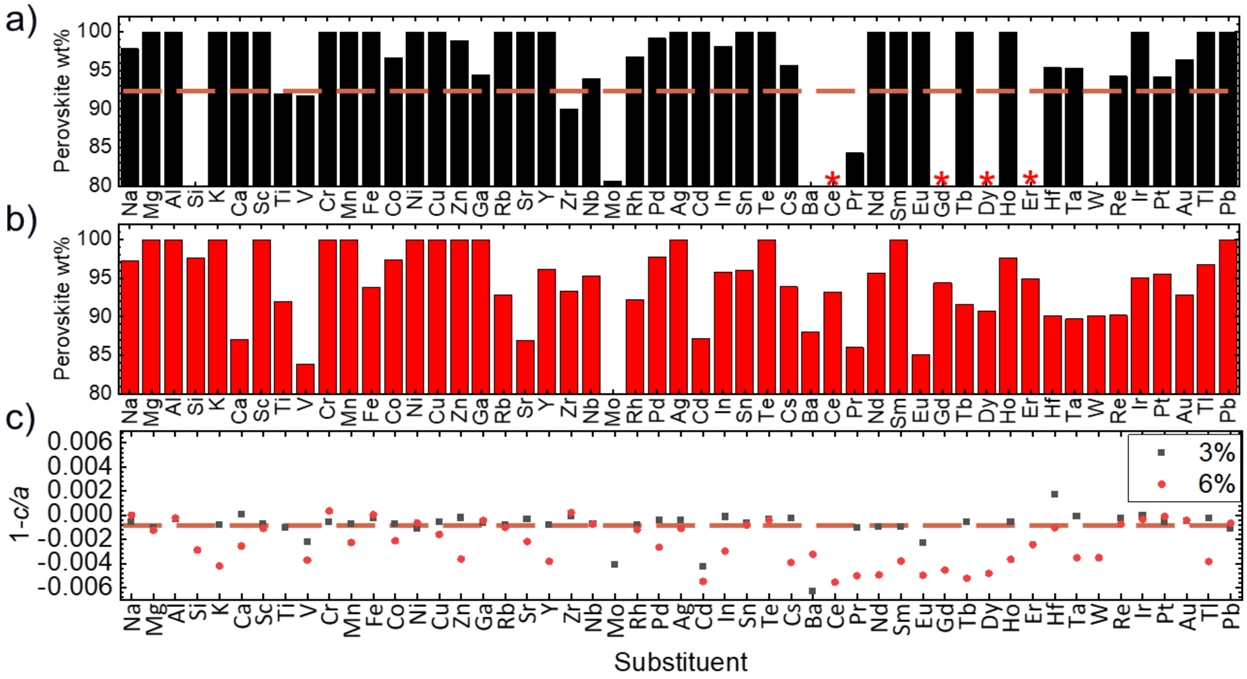

Figure 4.2 *Perovskite phase fraction in 3% (a) and 6% (b) substitutions. The red dashed line indicates the perovskite content in unsubstituted samples. A lot of substitutions show improved perovskite stabilization. Red asterisks indicate samples that were not made. The samples with 3%Si and 3%W substitution were stuck on the alumina plate. 1-c/a indicating how much close to perfect cubic the perovskite is (c). The red dashed line indicates the 1-c/a of substituted LLTO.*

Figure **4.2**c. The lattice parameter of Mg, Ca, Sc, Co, Ga, and Sr increased by increasing the substitution level.

As shown in Table **4.1**, the substitutions performed herein result in less Ti such that substitution on the Ti site is promoted; however, we also introduce vacancies on the La/Li sites such that unintentional substitutions on the La site is also possible while maintaining a pure perovskite material. The bond valence mismatch (BVM) of the two sites was calculated by subtracting the ideal valence from the calculated total bond valence. For the total valence calculation, Ti-site is 6-fold coordinated while La-site is 12-fold coordinated. We used BVM as a simple descriptor to determine if a specific substitution would work. Figure **4.3** shows the BVM values for both sites for all substituents. As has been seen elsewhere,[22] ionic radii mismatch and tolerance factor also prove to be similarly effective descriptors as BVM as demonstrated in Figure

S4.3. Figure **4.3** shows that some elements with large BVM at Ti-site formed 100% perovskite such as Na, K and Rb. When comparing the BVM at both sites Ti and La (Figure **4.3**a) we observed that these elements have a much lower La-site BVM. We, therefore, conclude that these elements likely occupied the La-site instead of the Ti-site, which is possible because of the available La-site vacancies introduced by charge compensation as per Table **4.1**. Taking this into account, the largest BVM (1.77 at Ti-site) that led to pure perovskite was Sc. It is also important to note that numerous elements with small BVM values led to phase separation, with some showing less LLTO than in the unsubstituted such as 6% W with BVM of 0.27 at Ti-site and 6% Ta with BVM of 0.78. This

Table 4.1 *Stoichiometry of 3% and 6% Ti-site substituted samples. Empty cells indicate samples that were not made.*

M^{z}	**y = 0.030**
Na^{+1}	$Li_{0.396}La_{0.565}Na_{0.030}Ti_{0.970}O_3$
Mg^{+2}	$Li_{0.390}La_{0.557}Mg_{0.030}Ti_{0.970}O_3$
Al^{+3}	$Li_{0.384}La_{0.549}Al_{0.030}Ti_{0.970}O_3$
Si^{+4}	$Li_{0.379}La_{0.540}Si_{0.030}Ti_{0.970}O_3$
K^{+1}	$Li_{0.396}La_{0.565}K_{0.030}Ti_{0.970}O_3$
Ca^{+2}	$Li_{0.390}La_{0.557}Ca_{0.030}Ti_{0.970}O_3$
Sc^{+3}	$Li_{0.384}La_{0.549}Sc_{0.030}Ti_{0.970}O_3$
V^{+5}	$Li_{0.373}La_{0.532}V_{0.030}Ti_{0.970}O_3$
Cr^{+3}	$Li_{0.384}La_{0.549}Cr_{0.030}Ti_{0.970}O_3$
Mn^{+2}	$Li_{0.390}La_{0.557}Mn_{0.030}Ti_{0.970}O_3$
Fe^{+3}	$Li_{0.384}La_{0.549}Fe_{0.030}Ti_{0.970}O_3$
Co^{+2}	$Li_{0.390}La_{0.557}Co_{0.030}Ti_{0.970}O_3$
Ni^{+2}	$Li_{0.390}La_{0.557}Ni_{0.030}Ti_{0.970}O_3$
Cu^{+2}	$Li_{0.390}La_{0.557}Cu_{0.030}Ti_{0.970}O_3$
Zn^{+2}	$Li_{0.390}La_{0.557}Zn_{0.030}Ti_{0.970}O_3$
Ga^{+3}	$Li_{0.384}La_{0.549}Ga_{0.030}Ti_{0.970}O_3$
Rb^{+1}	$Li_{0.396}La_{0.565}Rb_{0.030}Ti_{0.970}O_3$
Sr^{+2}	$Li_{0.390}La_{0.557}Sr_{0.030}Ti_{0.970}O_3$
Y^{+3}	$Li_{0.384}La_{0.549}Y_{0.030}Ti_{0.970}O_3$
Zr^{+4}	$Li_{0.379}La_{0.540}Zr_{0.030}Ti_{0.970}O_3$
Nb^{+5}	$Li_{0.373}La_{0.532}Nb_{0.030}Ti_{0.970}O_3$
Mo^{+6}	$Li_{0.367}La_{0.524}Mo_{0.030}Ti_{0.970}O_3$
Rh^{+3}	$Li_{0.384}La_{0.549}Rh_{0.030}Ti_{0.970}O_3$
Pd^{+2}	$Li_{0.390}La_{0.557}Pd_{0.030}Ti_{0.970}O_3$
Ag^{+1}	$Li_{0.396}La_{0.565}Ag_{0.030}Ti_{0.970}O_3$
Cd^{+2}	$Li_{0.390}La_{0.557}Cd_{0.030}Ti_{0.970}O_3$
In^{+3}	$Li_{0.384}La_{0.549}In_{0.030}Ti_{0.970}O_3$
Sn^{+4}	$Li_{0.379}La_{0.540}Sn_{0.030}Ti_{0.970}O_3$
Te^{+4}	$Li_{0.379}La_{0.540}Te_{0.030}Ti_{0.970}O_3$
Cs^{+1}	$Li_{0.396}La_{0.565}Cs_{0.030}Ti_{0.970}O_3$
Ba^{+2}	$Li_{0.390}La_{0.557}Ba_{0.030}Ti_{0.970}O_3$
Ce^{+3}	$Li_{0.384}La_{0.549}Ce_{0.030}Ti_{0.970}O_3$
Pr^{+3}	$Li_{0.384}La_{0.549}Pr_{0.030}Ti_{0.970}O_3$
Nd^{+3}	$Li_{0.384}La_{0.549}Nd_{0.030}Ti_{0.970}O_3$
Sm^{+3}	$Li_{0.384}La_{0.549}Sm_{0.030}Ti_{0.970}O_3$
Eu^{+3}	$Li_{0.384}La_{0.549}Eu_{0.030}Ti_{0.970}O_3$
Gd^{+3}	
Tb^{+3}	$Li_{0.384}La_{0.549}Tb_{0.030}Ti_{0.970}O_3$
Dy^{+3}	
Ho^{+3}	$Li_{0.384}La_{0.549}Ho_{0.030}Ti_{0.970}O_3$
Er^{+3}	
Hf^{+4}	$Li_{0.379}La_{0.540}Hf_{0.030}Ti_{0.970}O_3$
Ta^{+5}	$Li_{0.373}La_{0.532}Ta_{0.030}Ti_{0.970}O_3$
W^{+6}	$Li_{0.367}La_{0.524}W_{0.030}Ti_{0.970}O_3$
Re^{+7}	$Li_{0.362}La_{0.516}Re_{0.030}Ti_{0.970}O_3$
Ir^{+4}	$Li_{0.379}La_{0.540}Ir_{0.030}Ti_{0.970}O_3$
Pt^{+4}	$Li_{0.379}La_{0.540}Pt_{0.030}Ti_{0.970}O_3$
Au^{+3}	$Li_{0.384}La_{0.549}Au_{0.030}Ti_{0.970}O_3$
Tl^{+1}	$Li_{0.396}La_{0.565}Tl_{0.030}Ti_{0.970}O_3$
Pb^{+2}	$Li_{0.390}La_{0.557}Pb_{0.030}Ti_{0.970}O_3$

M^{z}	**y = 0.060**
Na^{+1}	$Li_{0.413}La_{0.589}Na_{0.060}Ti_{0.940}O_3$
Mg^{+2}	$Li_{0.401}La_{0.573}Mg_{0.060}Ti_{0.940}O_3$
Al^{+3}	$Li_{0.390}La_{0.557}Al_{0.060}Ti_{0.940}O_3$
Si^{+4}	$Li_{0.379}La_{0.540}Si_{0.060}Ti_{0.940}O_3$
K^{+1}	$Li_{0.413}La_{0.589}K_{0.060}Ti_{0.940}O_3$
Ca^{+2}	$Li_{0.401}La_{0.573}Ca_{0.060}Ti_{0.940}O_3$
Sc^{+3}	$Li_{0.390}La_{0.557}Sc_{0.060}Ti_{0.940}O_3$
V^{+5}	$Li_{0.367}La_{0.524}V_{0.060}Ti_{0.940}O_3$
Cr^{+3}	$Li_{0.390}La_{0.557}Cr_{0.060}Ti_{0.940}O_3$
Mn^{+2}	$Li_{0.401}La_{0.573}Mn_{0.060}Ti_{0.940}O_3$
Fe^{+3}	$Li_{0.390}La_{0.557}Fe_{0.060}Ti_{0.940}O_3$
Co^{+2}	$Li_{0.401}La_{0.573}Co_{0.060}Ti_{0.940}O_3$
Ni^{+2}	$Li_{0.401}La_{0.573}Ni_{0.060}Ti_{0.940}O_3$
Cu^{+2}	$Li_{0.401}La_{0.573}Cu_{0.060}Ti_{0.940}O_3$
Zn^{+2}	$Li_{0.401}La_{0.573}Zn_{0.060}Ti_{0.940}O_3$
Ga^{+3}	$Li_{0.390}La_{0.557}Ga_{0.060}Ti_{0.940}O_3$
Rb^{+1}	$Li_{0.413}La_{0.589}Rb_{0.060}Ti_{0.940}O_3$
Sr^{+2}	$Li_{0.401}La_{0.573}Sr_{0.060}Ti_{0.940}O_3$
Y^{+3}	$Li_{0.390}La_{0.557}Y_{0.060}Ti_{0.940}O_3$
Zr^{+4}	$Li_{0.379}La_{0.540}Zr_{0.060}Ti_{0.940}O_3$
Nb^{+5}	$Li_{0.367}La_{0.524}Nb_{0.060}Ti_{0.940}O_3$
Mo^{+6}	$Li_{0.356}La_{0.508}Mo_{0.060}Ti_{0.940}O_3$
Rh^{+3}	$Li_{0.390}La_{0.557}Rh_{0.060}Ti_{0.940}O_3$
Pd^{+2}	$Li_{0.401}La_{0.573}Pd_{0.060}Ti_{0.940}O_3$
Ag^{+1}	$Li_{0.413}La_{0.589}Ag_{0.060}Ti_{0.940}O_3$
Cd^{+2}	$Li_{0.401}La_{0.573}Cd_{0.060}Ti_{0.940}O_3$
In^{+3}	$Li_{0.390}La_{0.557}In_{0.060}Ti_{0.940}O_3$
Sn^{+4}	$Li_{0.379}La_{0.540}Sn_{0.060}Ti_{0.940}O_3$
Te^{+4}	$Li_{0.379}La_{0.540}Te_{0.060}Ti_{0.940}O_3$
Cs^{+1}	$Li_{0.413}La_{0.589}Cs_{0.060}Ti_{0.940}O_3$
Ba^{+2}	$Li_{0.401}La_{0.573}Ba_{0.060}Ti_{0.940}O_3$
Ce^{+3}	$Li_{0.390}La_{0.557}Ce_{0.060}Ti_{0.940}O_3$
Pr^{+3}	$Li_{0.390}La_{0.557}Pr_{0.060}Ti_{0.940}O_3$
Nd^{+3}	$Li_{0.390}La_{0.557}Nd_{0.060}Ti_{0.940}O_3$
Sm^{+3}	$Li_{0.390}La_{0.557}Sm_{0.060}Ti_{0.940}O_3$
Eu^{+3}	$Li_{0.390}La_{0.557}Eu_{0.060}Ti_{0.940}O_3$
Gd^{+3}	$Li_{0.390}La_{0.557}Gd_{0.060}Ti_{0.940}O_3$
Tb^{+3}	$Li_{0.390}La_{0.557}Tb_{0.060}Ti_{0.940}O_3$
Dy^{+3}	$Li_{0.390}La_{0.557}Dy_{0.060}Ti_{0.940}O_3$
Ho^{+3}	$Li_{0.390}La_{0.557}Ho_{0.060}Ti_{0.940}O_3$
Er^{+3}	$Li_{0.390}La_{0.557}Er_{0.060}Ti_{0.940}O_3$
Hf^{+4}	$Li_{0.379}La_{0.540}Hf_{0.060}Ti_{0.940}O_3$
Ta^{+5}	$Li_{0.367}La_{0.524}Ta_{0.060}Ti_{0.940}O_3$
W^{+6}	$Li_{0.356}La_{0.508}W_{0.060}Ti_{0.940}O_3$
Re^{+7}	$Li_{0.345}La_{0.492}Re_{0.060}Ti_{0.940}O_3$
Ir^{+4}	$Li_{0.379}La_{0.540}Ir_{0.060}Ti_{0.940}O_3$
Pt^{+4}	$Li_{0.379}La_{0.540}Pt_{0.060}Ti_{0.940}O_3$
Au^{+3}	$Li_{0.390}La_{0.557}Au_{0.060}Ti_{0.940}O_3$
Tl^{+1}	$Li_{0.413}La_{0.589}Tl_{0.060}Ti_{0.940}O_3$
Pb^{+2}	$Li_{0.401}La_{0.573}Pb_{0.060}Ti_{0.940}O_3$

shows that a low BVM may very well be necessary, but it is certainly not sufficient to overcome the metastability in the unsubstituted LLTO materials.

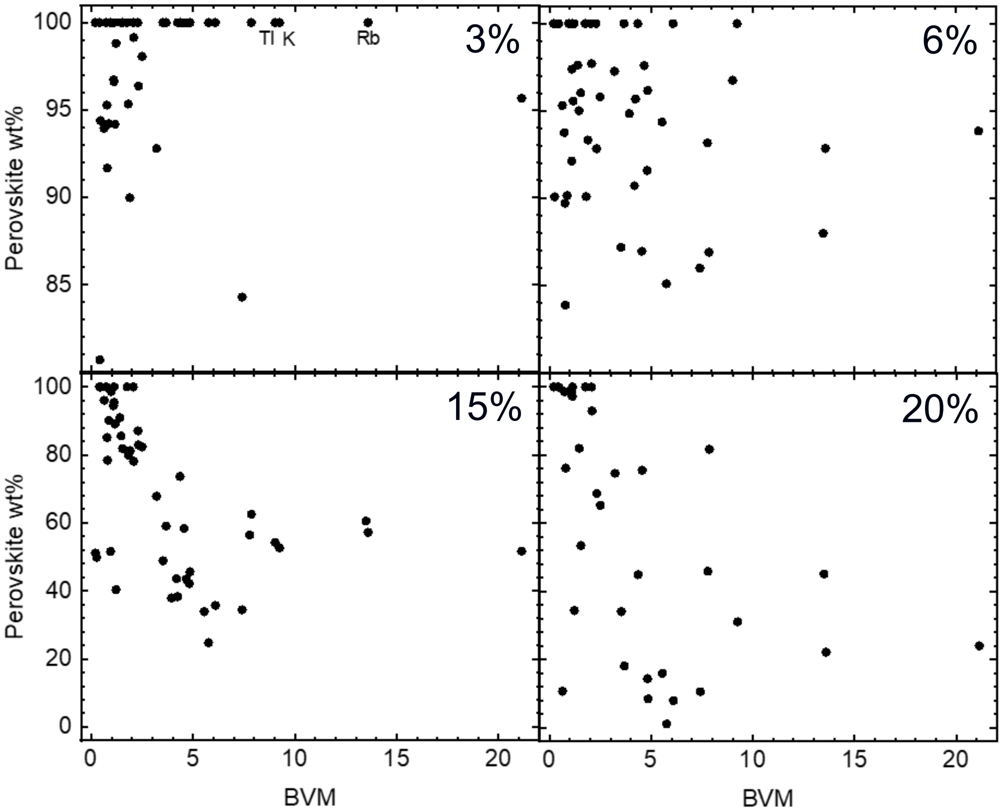

Figure 4.3 *Perovskite weight fraction at 3%, 6%, 15%, and 20% substitution levels vs. BVM on the Ti-site. Some substituents with large BVM still manage to incorporate into the structure. The BVM on the La-site is depicted in Figure* ***S4.3a****.*

4.4.2 Transport properties

The bulk conductivity in Figure **4.4**a shows that substitutions did not enhance the bulk conductivity significantly, with only minor enhancement for the 15% Nb sample. In fact the bulk conductivity decreased for a number of substitutions both at the La and Ti sites based on BVM values (e.g. Sr 0.244 at La and 7.863 at Ti). We speculate that the unintended La-site substitutions at high substitution levels predicted by BVM decreased the bulk conductivity by blocking Li ions pathways because they occupy La-site through which lithium ions hope and via reducing charge carriers concentration, as reported in ref. [23]. We also propose that the decrease of bulk

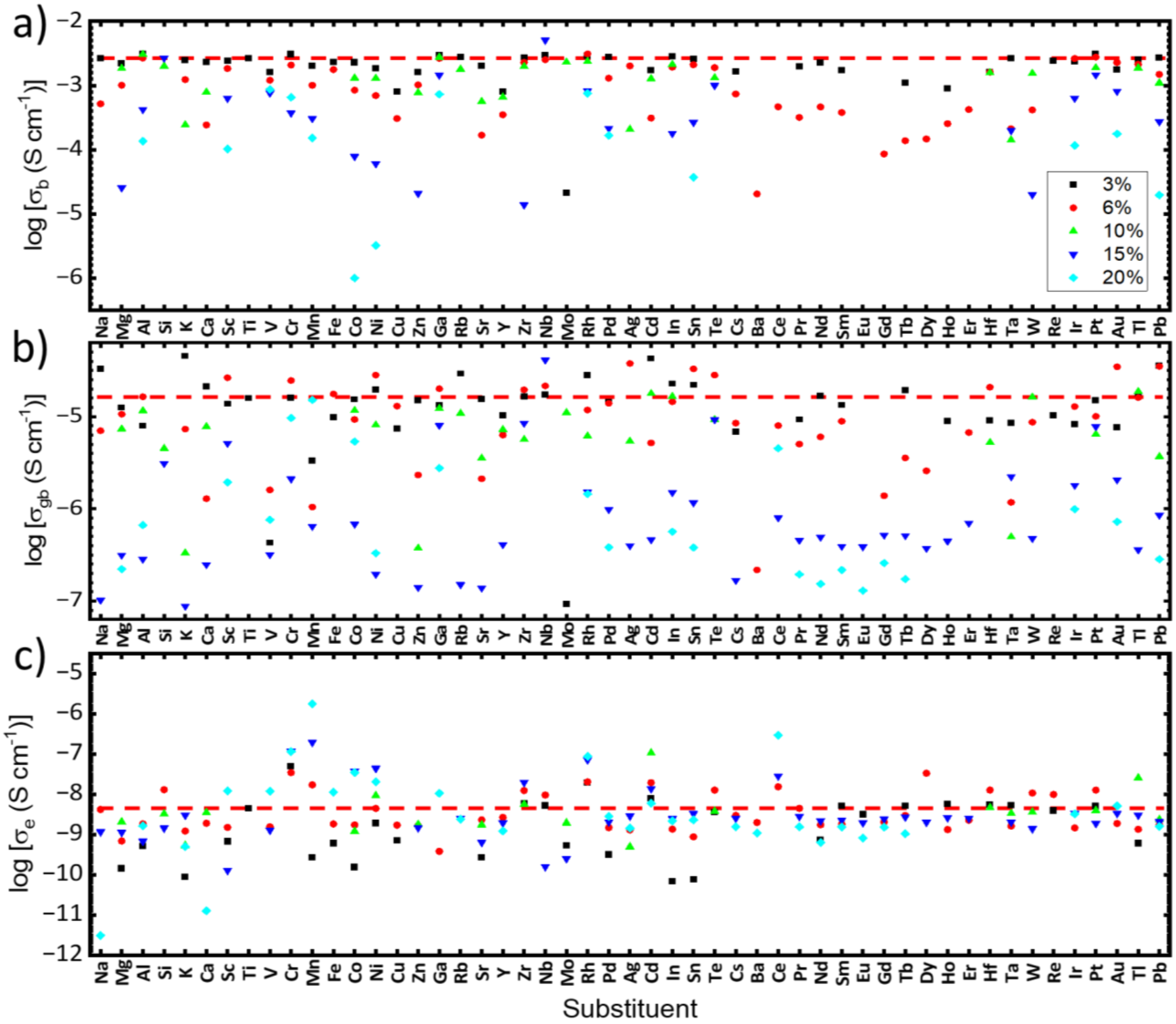

Figure 4.4 *Transport properties: bulk conductivity (a), grain boundary conductivity (b) and electronic conductivity (c) for 5 substitution levels. The red dashed line corresponds to the unsubstituted sample.*

conductivity for Ti-site substitutions is due to Ti octahedra distortion induced by the larger and smaller ionic radius elements thereby decreasing the bottleneck (four oxygen window) for Li diffusion and increasing the lithium transport energy barrier as seen in refs. [11, 24, 25]. The reduced bulk conductivity in both site substitutions at high substitution levels could be due to decreased charge carrier numbers because the charge was compensated by the Li/La, but it is also undoubtedly related to a decrease in LLTO content.[23] Hence, previously known mechanisms such as larger lithium mobility barriers and/or lower charge carrier numbers account for the reduced bulk conductivity seen here. Even though Mn has an ionic radius close to Ti and the lattice parameters did not change (Figure **S4.1**), the bulk conductivity dropped (Figure **4.4**a) which could be due to weaker Mn-O bond compared to Ti-O strengthening the Li-O bonding. Li-O bond strengthening increases the electrostatic force on the Li, increasing the mobility energy reflected by high activation energy.[9]

The fact that bulk conductivity did not improve is not so important here given that LLTO has high bulk conductivities; it is in fact, other properties that need optimizing by substitutions. Figure **4.4**b shows that minor enhancements of the grain boundary conductivity was achieved with substitutions. Na, K, and In at a 3% content and Sc, Ag, and Sn at 6% content all had higher grain boundary conductivities than unsubstituted LLTO. Figure **4.5** shows that Na and Sn substitutions at 3% and 6% contents respectively had higher grain boundary conductivity than many substitutions that gave pure perovskite materials. In those cases, introducing a small amount of secondary phase 3%-5% was beneficial for grain boundary conductivities. This demonstrates the impact of secondary phases on grain boundary conductivity, as we revealed in our previous study where a sample with 18% $Li_2Ti_3O_7$ had higher grain boundary conductivity than the sample with the highest fraction of LLTO.[20] It is significant that, here, within the set of samples where substitutions formed pure perovskite, the grain boundary conductivities changed by orders of magnitude moving from the highest (K) to the lowest (Mn) at 3% substitution level. This reveals the dramatic impact that substituents have at the grain boundary. The changes of the grain boundary conductivity of the substituted pure perovskite samples could be due to changing the Schottky barrier height. A possible mechanism for this was proposed by Wu *et al.*[11] who suggest that the origin of the low grain boundary conductivity in LLTO is due to the lithium (charge carrier) depletion at the space charge region. Additionally, the grain boundary conductivity trend within substituted pure perovskite can also indicate the role the substituents play in enhancing the sintering process, changing lithium diffusion dimensionality, or creating bigger grains thereby reducing the fraction of grain boundaries. Therefore substitution can tune the grain boundary conductivity within pure perovskite and they can also be beneficial through introducing a small amount of secondary phases. However, higher contents of secondary phases >5% generally drastically decreases the grain boundary conductivity as seen in Figure **4.5**. The promising candidates need to be further characterized to understand the exact mechanism of enhancement.

The EIS spectra of 10% substituted LLTO samples at 22 °C and 50 °C are shown in Figure Figure **S4.7** as black and red dots, respectively. The quality and reproducibility of these data here are highly comparable to our previous reports. From these data, the activation energies were calculated using the Arrhenius equation. The activation energies for bulk and grain boundary conductivities are shown in Figure **S4.4**. The bulk conductivity activation energy of Cr and Ga

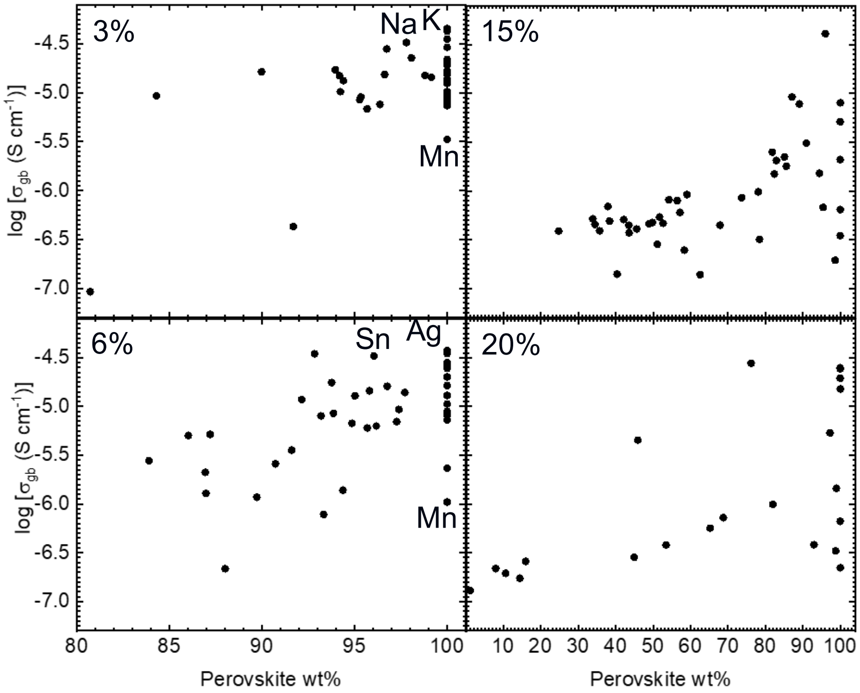

Figure 4.5 *Grain boundary conductivity changes by the fraction of substituted perovskite. Substitutions affected the grain boundary conductivity in pure perovskite and by introducing secondary phases.*

substituted samples decreased with increasing substitution levels, but the bulk conductivity decreased as well. Although the lithium mobility energy barrier is dropped in these two substitutions, we propose that the reduced charge carrier concentration and/or blocked lithium percolation path was detrimental to the bulk conductivity. The blocking of the Li percolation pathway can likely be excluded in this case because Cr and Ga are substituted for Ti in LLTO based on the BVM analysis. In other substitutions, such as Ca and Y, the bulk conductivity decreased due to the increased bulk conductivity activation energy. Thus, it is crucial to tailor charge carrier concentration, lithium percolation pathway, and Li mobility energy barrier to achieve high bulk conductivity. The results for grain boundary activation energies show that numerous dopants increase the activation energy slightly, while the dopants showing the best room temperature grain boundary conductivities (K at 3% and Ag at 6%) showed very minor changes in activation compared to the unsubstituted. Overall, substitutions resulted in moderate gains in grain boundary transport and thus in total transport given that grain boundaries are limiting in LLTO materials.

The electronic conductivity was measured to check if substitutions converted LLTO into a mixed conductor. Solid electrolytes should have low electronic conductivity ($<10^{-10}$ S cm^{-1}) to prevent dendrite growth from the bulk (at 1 mA cm^{-2}).[26] Most substitutions did not increase the electronic conductivity except for Cr, Mn, Rh, and Cd partial substitutions as shown in Figure **4.4**c. These elements increased the electronic conductivity by probably introducing oxygen vacancies.[27] The mixed ionic and electronic conductivity samples can be considered candidates for electrolyte to be mixed in with the active material to form composite cathodes and anodes in all-solid batteries.

4.4.3 Electrochemical stability window

The electrochemical stability limits at high and low potentials were measured by preparing low-loading (2.5 mg/cm^2) electrodes from our samples and performing cycling voltammetry at a slow sweep rate of 0.1 V/h. The limits to the stability window are determined by checking the potential where the sample first results in more current than the blank (carbon black+binder). Unsubstituted LLTO is stable at high potentials to 5.5 V (vs. Li/Li$^+$), as demonstrated in our previous study.[4] Most substitutions did not shift the high potential stability limit, but Cr had a dramatic impact. Figure **4.6**a shows that Cr-substituted perovskite had a reversible redox peak starting at 3.43 V (vs. Li/Li$^+$). This material is unsuitable for a solid electrolyte but could be a candidate as a cathode

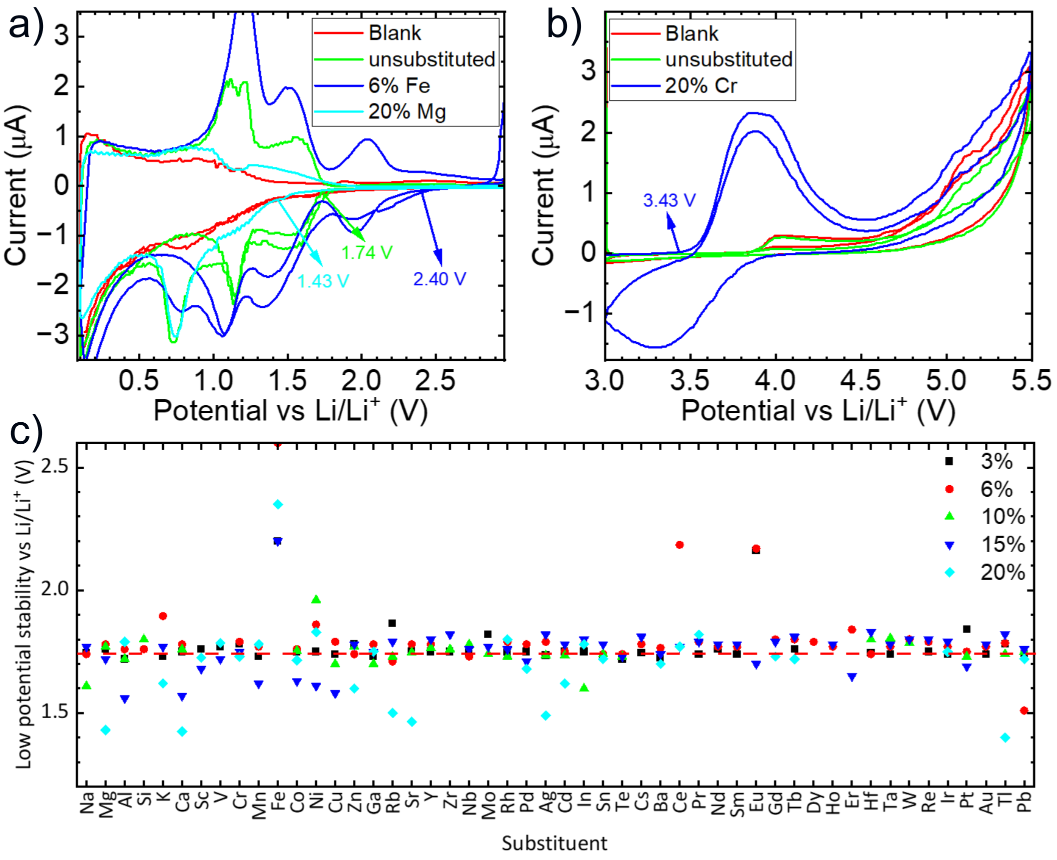

Figure 4.6 *Electrochemical stability at the low potential limit for unsubstituted, 6% Fe and 20% Mg substitutions (a) at the high potential for unsubstituted, and 20% Cr substituted sample (b). (c)The low stability limit potential (extracted from CVs) of 50 substituents at 5 different substitution levels in LLTO with the dashed line corresponding to the unsubstituted sample.*

material. In fact, LLTO has also been proposed as a coating for Ni-rich NMC cathodes for Li-ion batteries[28], the Cr-substituted material developed here could therefore serve as an electrochemically active shell.

Figure **4.6** also reveals that at low potentials, a few substituents such as Fe shifted the low potential stability limit to a higher potential (thereby reducing the stability window). For example, the Fe-substituted material results in a reversible redox peak starting at 2.4 V (vs. Li/Li^+). The unsubstituted material shows a highly reversible peak of its own starting 1.74 V, making it a candidate for the anode as proposed previously.[6] Although these potentials are not competitive with the common anode for high energy applications (graphite, 0.1 V), they are comparable to the potential of $Li_4Ti_5O_{12}$ (LTO, near 1.5 V) which is the state-of-the-art for high power and high safety applications. Combining the Cr-substituted and unsubstituted materials to potentially make the first epitaxial battery will be discussed further below. High levels of some substitution (15% and 20%) also shifted the low potential stability limit to lower potentials; one of these elements is Mg. In Mg substituted sample, the low stability limit shifted from 1.7 for the unsubstituted sample to 1.43 V vs. Li/Li^+ (Figure **4.6**a). This is significant, as this shift could allow its integration with LTO anode in an all-solid-state battery. These changes in the electrochemical stability limits in the case of homogenous microstructure could be due to a change of Ti-O local environment moving its redox potential.[29] As in the case of heterogeneous microstructure, introduced elements preferentially located on the surface of the grains form an electrochemically inert interphase. The distribution of substituents can either be evenly distributed throughout the bulk of the material (soluble/solid solution), phase separated (insoluble/secondary phase) or concentrated at the surface. For example, in W-doped $LiNiO_2$, W was found to be mainly concentrated at the surface of both primary and secondary particles.[30] There were trade-offs between low potential stability limit and total conductivity; however, that could be overcome by tuning the sintering temperature and time. Finally, this study acts as an initial screen to find which substitutions in LLTO can improve the electrochemical stability window and the transport properties and discover trends. Good candidates will need further experimental conditions optimization to get the best of a specific system. This work certainly demonstrates that only moderate progress can be made on the stability window limits, such that coupling with LTO may be possible, but use with lower potential anodes such as graphite will undoubtedly require a buffer layer such a PEO based polymer electrolyte.

Finally, the screening performed here has revealed a potential candidate for epitaxial battery. The unsubstituted LLTO with lattice parameters $a = 3.874$ Å, $c = 3.878$ Å can act as the anode with reversible redox peaks occurring between 1.7 and 0.5 V.[6] These transitions result in a transition to an electronically conducting phase such that it is not self-passivating.[4, 5] The 20% Cr-substituted LLTO is phase pure and results in lattice parameters ($a = 3.875$ Å, $c = 3.878$ Å) remarkably close to those of the undoped such that there exist minimal mismatches of 0.026 % and 0 % in the *a* and *c* lattice parameters, respectively. The Cr-substituted sample has a highly reversible peak near 3.5-4 V making it an interesting cathode material. Although higher Cr substitution should be explored to enhance the capacities of this material, it seems like a battery composed of Cr-substituted LLTO (cathode) with excess unsubstituted LLTO (anode[6] and electrolyte) may serve as an excellent first demonstration of an epitaxial battery. Given the excellent bulk conductivities of LLTO (and relatively poor grain boundary conductivities), an epitaxial design is an ideal way to benefit from this material's strengths.

4.5 Conclusion

A vast array of partial substitutions (50 substituents, 212 unique compositions) into perovskite $Li_{0.379}La_{0.540}TiO_3$ were performed. Numerous substitutions stabilized the perovskite phase to make single-phase materials, a feat previously found impossible in the Li-La-Ti-O system. Bond valence mismatch was used to predict which site was occupied by the different substituents (the chosen stoichiometries left vacancies on either site such that both were possible). Substitutions either had no impact or decreased bulk conductivities. Possible reasons for this include decreasing charge carrier concentration, hindering the lithium diffusion pathway, increasing Li-O bond strength and/or distorting Ti octahedra, thus reducing bottleneck sizes. On the other hand, a minor enhancement in the grain boundary conductivity (the limiting property in this class of electrolyte) was achieved in pure perovskites such as the K-substituted LLTO. The substituent in pure perovskites dramatically impacts grain boundary conductivities with impacts over multiple orders of magnitude, showing to what extent moderate substitutions can play important roles when acting at grain boundaries. It was also noted that numerous cases were found where introducing a secondary phase such as in Na-substituted LLTO also improved the grain boundary conductivities, demonstrating yet again the complex nature of transport at the grain surfaces. It is also noteworthy that Cr, Mn, Rh, and Cd substitutions increased the electronic conductivity of LLTO dramatically, perhaps by introducing oxygen vacancies and leading to useful candidates for the electrolyte in the composite electrodes in all solid batteries. The high potential stability limit did not shift with most substitutions except for Cr, which led to a potential cathode for solid batteries with a reversible redox peak near 3.8 V (vs. Li/Li$^+$). On the contrary, the low potential stability limit was shifted by substitution such as Mg allowing the usage of lithium titanate anode. The screening herein of over 226 materials also helped identify potential candidates for the first epitaxial battery, a potentially ideal use for this electrolyte that has such poor grain boundary conductivities. The results of this study provide a guide for improving the performance of LLTO by partial substitutions for energy storage applications. Therefore, this work shows the power of such an approach and helps identify the limits to how far each property can be tuned.

4.6 Acknowledgments

This work was funded by NSERC under the auspices of a discovery grant and the Canadian Foundation for Innovation. Also funded by a New Frontiers Research Fund, by the Natural Sciences and Engineering Research Council of Canada under the auspices of a Discovery grant, and by the FRQNT.

4.7 Supporting information

Table S4.1 *Precursors used to make the 50 substituents.*

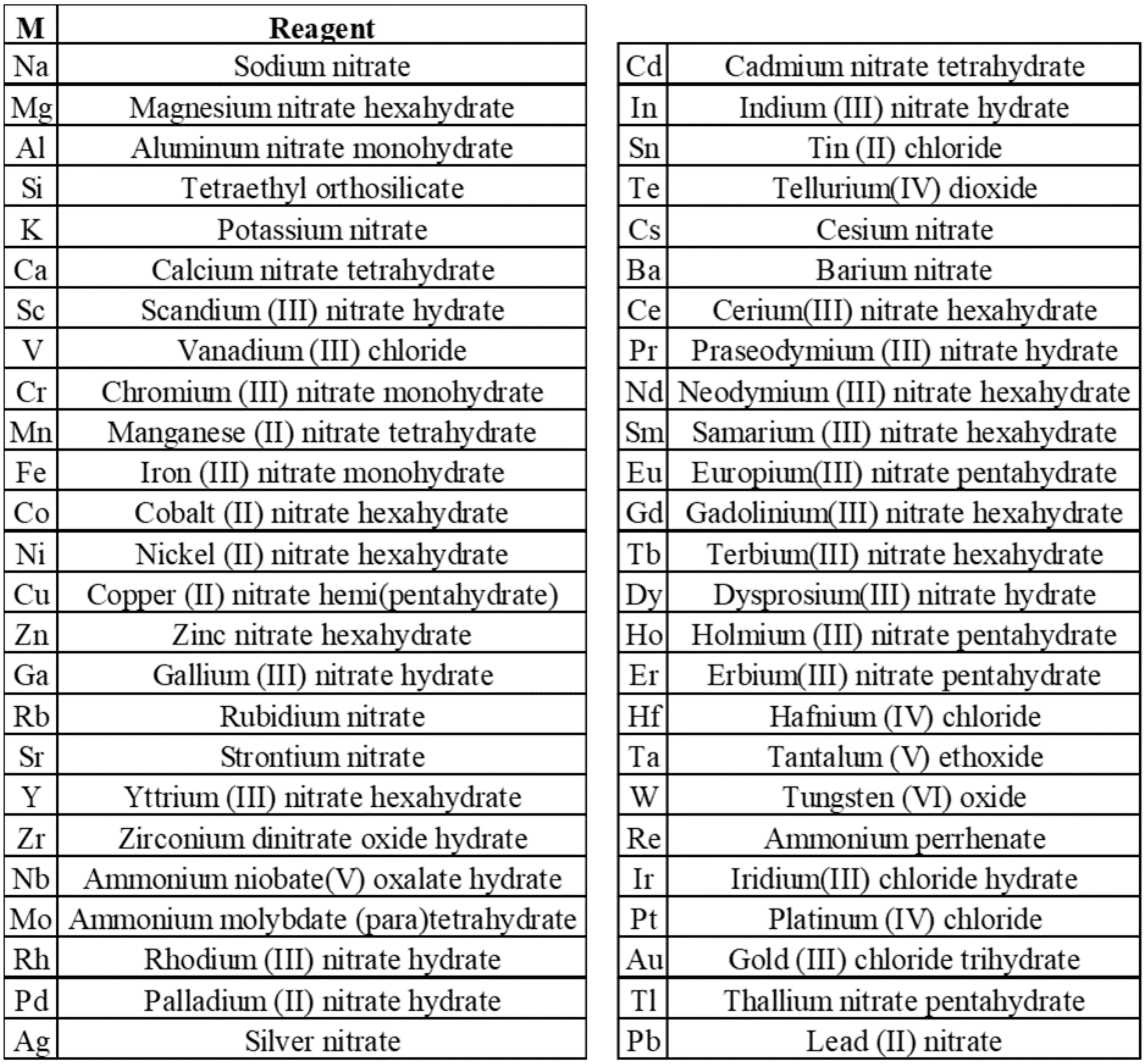

M	Reagent
Na	Sodium nitrate
Mg	Magnesium nitrate hexahydrate
Al	Aluminum nitrate monohydrate
Si	Tetraethyl orthosilicate
K	Potassium nitrate
Ca	Calcium nitrate tetrahydrate
Sc	Scandium (III) nitrate hydrate
V	Vanadium (III) chloride
Cr	Chromium (III) nitrate monohydrate
Mn	Manganese (II) nitrate tetrahydrate
Fe	Iron (III) nitrate monohydrate
Co	Cobalt (II) nitrate hexahydrate
Ni	Nickel (II) nitrate hexahydrate
Cu	Copper (II) nitrate hemi(pentahydrate)
Zn	Zinc nitrate hexahydrate
Ga	Gallium (III) nitrate hydrate
Rb	Rubidium nitrate
Sr	Strontium nitrate
Y	Yttrium (III) nitrate hexahydrate
Zr	Zirconium dinitrate oxide hydrate
Nb	Ammonium niobate(V) oxalate hydrate
Mo	Ammonium molybdate (para)tetrahydrate
Rh	Rhodium (III) nitrate hydrate
Pd	Palladium (II) nitrate hydrate
Ag	Silver nitrate
Cd	Cadmium nitrate tetrahydrate
In	Indium (III) nitrate hydrate
Sn	Tin (II) chloride
Te	Tellurium(IV) dioxide
Cs	Cesium nitrate
Ba	Barium nitrate
Ce	Cerium(III) nitrate hexahydrate
Pr	Praseodymium (III) nitrate hydrate
Nd	Neodymium (III) nitrate hexahydrate
Sm	Samarium (III) nitrate hexahydrate
Eu	Europium(III) nitrate pentahydrate
Gd	Gadolinium(III) nitrate hexahydrate
Tb	Terbium(III) nitrate hexahydrate
Dy	Dysprosium(III) nitrate hydrate
Ho	Holmium (III) nitrate pentahydrate
Er	Erbium(III) nitrate pentahydrate
Hf	Hafnium (IV) chloride
Ta	Tantalum (V) ethoxide
W	Tungsten (VI) oxide
Re	Ammonium perrhenate
Ir	Iridium(III) chloride hydrate
Pt	Platinum (IV) chloride
Au	Gold (III) chloride trihydrate
Tl	Thallium nitrate pentahydrate
Pb	Lead (II) nitrate

Table S4.2 *Stoichiometry of 10%, 15%, and 20% Ti-site substituted samples. Empty cells indicate samples that were not made.*

M^z	y = 0.100	M^z	y = 0.150
Na^{+1}	$Li_{0.435}La_{0.622}Na_{0.100}Ti_{0.900}O_3$	Na^{+1}	$Li_{0.464}La_{0.662}Na_{0.150}Ti_{0.850}O_3$
Mg^{+2}	$Li_{0.417}La_{0.594}Mg_{0.100}Ti_{0.900}O_3$	Mg^{+2}	$Li_{0.435}La_{0.622}Mg_{0.150}Ti_{0.850}O_3$
Al^{+3}	$Li_{0.398}La_{0.567}Al_{0.100}Ti_{0.900}O_3$	Al^{+3}	$Li_{0.407}La_{0.581}Al_{0.150}Ti_{0.850}O_3$
Si^{+4}	$Li_{0.379}La_{0.540}Si_{0.100}Ti_{0.900}O_3$	Si^{+4}	$Li_{0.379}La_{0.540}Si_{0.150}Ti_{0.850}O_3$
K^{+1}	$Li_{0.435}La_{0.622}K_{0.100}Ti_{0.900}O_3$	K^{+1}	$Li_{0.464}La_{0.662}K_{0.150}Ti_{0.850}O_3$
Ca^{+2}	$Li_{0.417}La_{0.594}Ca_{0.100}Ti_{0.900}O_3$	Ca^{+2}	$Li_{0.435}La_{0.622}Ca_{0.150}Ti_{0.850}O_3$
Sc^{+3}		Sc^{+3}	$Li_{0.407}La_{0.581}Sc_{0.150}Ti_{0.850}O_3$
V^{+5}		V^{+5}	$Li_{0.350}La_{0.500}V_{0.150}Ti_{0.850}O_3$
Cr^{+3}		Cr^{+3}	$Li_{0.407}La_{0.581}Cr_{0.150}Ti_{0.850}O_3$
Mn^{+2}		Mn^{+2}	$Li_{0.435}La_{0.622}Mn_{0.150}Ti_{0.850}O_3$
Fe^{+3}		Fe^{+3}	$Li_{0.407}La_{0.581}Fe_{0.150}Ti_{0.850}O_3$
Co^{+2}	$Li_{0.417}La_{0.594}Co_{0.100}Ti_{0.900}O_3$	Co^{+2}	$Li_{0.435}La_{0.622}Co_{0.150}Ti_{0.850}O_3$
Ni^{+2}	$Li_{0.417}La_{0.594}Ni_{0.100}Ti_{0.900}O_3$	Ni^{+2}	$Li_{0.435}La_{0.622}Ni_{0.150}Ti_{0.850}O_3$
Cu^{+2}	$Li_{0.417}La_{0.594}Cu_{0.100}Ti_{0.900}O_3$	Cu^{+2}	$Li_{0.435}La_{0.622}Cu_{0.150}Ti_{0.850}O_3$
Zn^{+2}	$Li_{0.417}La_{0.594}Zn_{0.100}Ti_{0.900}O_3$	Zn^{+2}	$Li_{0.435}La_{0.622}Zn_{0.150}Ti_{0.850}O_3$
Ga^{+3}	$Li_{0.398}La_{0.567}Ga_{0.100}Ti_{0.900}O_3$	Ga^{+3}	$Li_{0.407}La_{0.581}Ga_{0.150}Ti_{0.850}O_3$
Rb^{+1}	$Li_{0.435}La_{0.622}Rb_{0.100}Ti_{0.900}O_3$	Rb^{+1}	$Li_{0.464}La_{0.662}Rb_{0.150}Ti_{0.850}O_3$
Sr^{+2}	$Li_{0.417}La_{0.594}Sr_{0.100}Ti_{0.900}O_3$	Sr^{+2}	$Li_{0.435}La_{0.622}Sr_{0.150}Ti_{0.850}O_3$
Y^{+3}	$Li_{0.398}La_{0.567}Y_{0.100}Ti_{0.900}O_3$	Y^{+3}	$Li_{0.407}La_{0.581}Y_{0.150}Ti_{0.850}O_3$
Zr^{+4}	$Li_{0.379}La_{0.540}Zr_{0.100}Ti_{0.900}O_3$	Zr^{+4}	$Li_{0.379}La_{0.540}Zr_{0.150}Ti_{0.850}O_3$
Nb^{+5}		Nb^{+5}	$Li_{0.350}La_{0.500}Nb_{0.150}Ti_{0.850}O_3$
Mo^{+6}		Mo^{+6}	$Li_{0.322}La_{0.459}Mo_{0.150}Ti_{0.850}O_3$
Rh^{+3}	$Li_{0.398}La_{0.567}Rh_{0.100}Ti_{0.900}O_3$	Rh^{+3}	$Li_{0.407}La_{0.581}Rh_{0.150}Ti_{0.850}O_3$
Pd^{+2}		Pd^{+2}	$Li_{0.435}La_{0.622}Pd_{0.150}Ti_{0.850}O_3$
Ag^{+1}	$Li_{0.435}La_{0.622}Ag_{0.100}Ti_{0.900}O_3$	Ag^{+1}	$Li_{0.464}La_{0.662}Ag_{0.150}Ti_{0.850}O_3$
Cd^{+2}	$Li_{0.417}La_{0.594}Cd_{0.100}Ti_{0.900}O_3$	Cd^{+2}	$Li_{0.435}La_{0.622}Cd_{0.150}Ti_{0.850}O_3$
In^{+3}	$Li_{0.398}La_{0.567}In_{0.100}Ti_{0.900}O_3$	In^{+3}	$Li_{0.407}La_{0.581}In_{0.150}Ti_{0.850}O_3$
Sn^{+4}	$Li_{0.379}La_{0.540}Sn_{0.100}Ti_{0.900}O_3$	Sn^{+4}	$Li_{0.379}La_{0.540}Sn_{0.150}Ti_{0.850}O_3$
Te^{+4}	$Li_{0.379}La_{0.540}Te_{0.100}Ti_{0.900}O_3$	Te^{+4}	$Li_{0.379}La_{0.540}Te_{0.150}Ti_{0.850}O_3$
Cs^{+1}	$Li_{0.435}La_{0.622}Cs_{0.100}Ti_{0.900}O_3$	Cs^{+1}	$Li_{0.464}La_{0.662}Cs_{0.150}Ti_{0.850}O_3$
Ba^{+2}		Ba^{+2}	$Li_{0.435}La_{0.622}Ba_{0.150}Ti_{0.850}O_3$
Ce^{+3}		Ce^{+3}	$Li_{0.407}La_{0.581}Ce_{0.150}Ti_{0.850}O_3$
Pr^{+3}		Pr^{+3}	$Li_{0.407}La_{0.581}Pr_{0.150}Ti_{0.850}O_3$
Nd^{+3}		Nd^{+3}	$Li_{0.407}La_{0.581}Nd_{0.150}Ti_{0.850}O_3$
Sm^{+3}		Sm^{+3}	$Li_{0.407}La_{0.581}Sm_{0.150}Ti_{0.850}O_3$
Eu^{+3}		Eu^{+3}	$Li_{0.407}La_{0.581}Eu_{0.150}Ti_{0.850}O_3$
Gd^{+3}		Gd^{+3}	$Li_{0.407}La_{0.581}Gd_{0.150}Ti_{0.850}O_3$
Tb^{+3}		Tb^{+3}	$Li_{0.407}La_{0.581}Tb_{0.150}Ti_{0.850}O_3$
Dy^{+3}		Dy^{+3}	$Li_{0.407}La_{0.581}Dy_{0.150}Ti_{0.850}O_3$
Ho^{+3}		Ho^{+3}	$Li_{0.407}La_{0.581}Ho_{0.150}Ti_{0.850}O_3$
Er^{+3}		Er^{+3}	$Li_{0.407}La_{0.581}Er_{0.150}Ti_{0.850}O_3$
Hf^{+4}	$Li_{0.379}La_{0.540}Hf_{0.100}Ti_{0.900}O_3$	Hf^{+4}	$Li_{0.379}La_{0.540}Hf_{0.150}Ti_{0.850}O_3$
Ta^{+5}	$Li_{0.360}La_{0.513}Ta_{0.100}Ti_{0.900}O_3$	Ta^{+5}	$Li_{0.350}La_{0.500}Ta_{0.150}Ti_{0.850}O_3$
W^{+6}	$Li_{0.341}La_{0.486}W_{0.100}Ti_{0.900}O_3$	W^{+6}	$Li_{0.322}La_{0.459}W_{0.150}Ti_{0.850}O_3$
Re^{+7}		Re^{+7}	$Li_{0.293}La_{0.419}Re_{0.150}Ti_{0.850}O_3$
Ir^{+4}		Ir^{+4}	$Li_{0.379}La_{0.540}Ir_{0.150}Ti_{0.850}O_3$
Pt^{+4}	$Li_{0.379}La_{0.540}Pt_{0.100}Ti_{0.900}O_3$	Pt^{+4}	$Li_{0.379}La_{0.540}Pt_{0.150}Ti_{0.850}O_3$
Au^{+3}		Au^{+3}	$Li_{0.407}La_{0.581}Au_{0.150}Ti_{0.850}O_3$
Tl^{+1}	$Li_{0.435}La_{0.622}Tl_{0.100}Ti_{0.900}O_3$	Tl^{+1}	$Li_{0.464}La_{0.662}Tl_{0.150}Ti_{0.850}O_3$
Pb^{+2}	$Li_{0.417}La_{0.594}Pb_{0.100}Ti_{0.900}O_3$	Pb^{+2}	$Li_{0.435}La_{0.622}Pb_{0.150}Ti_{0.850}O_3$

$\mathbf{M}^{z}$	**y = 0.200**
Na^{+1}	$Li_{0.492}La_{0.703}Na_{0.200}Ti_{0.800}O_3$
Mg^{+2}	$Li_{0.454}La_{0.649}Mg_{0.200}Ti_{0.800}O_3$
Al^{+3}	$Li_{0.417}La_{0.594}Al_{0.200}Ti_{0.800}O_3$
Si^{+4}	
K^{+1}	$Li_{0.492}La_{0.703}K_{0.200}Ti_{0.800}O_3$
Ca^{+2}	$Li_{0.454}La_{0.649}Ca_{0.200}Ti_{0.800}O_3$
Sc^{+3}	$Li_{0.417}La_{0.594}Sc_{0.200}Ti_{0.800}O_3$
V^{+5}	$Li_{0.341}La_{0.486}V_{0.200}Ti_{0.800}O_3$
Cr^{+3}	$Li_{0.417}La_{0.594}Cr_{0.200}Ti_{0.800}O_3$
Mn^{+2}	$Li_{0.454}La_{0.649}Mn_{0.200}Ti_{0.800}O_3$
Fe^{+3}	$Li_{0.417}La_{0.594}Fe_{0.200}Ti_{0.800}O_3$
Co^{+2}	$Li_{0.454}La_{0.649}Co_{0.200}Ti_{0.800}O_3$
Ni^{+2}	$Li_{0.454}La_{0.649}Ni_{0.200}Ti_{0.800}O_3$
Cu^{+2}	$Li_{0.454}La_{0.649}Cu_{0.200}Ti_{0.800}O_3$
Zn^{+2}	$Li_{0.454}La_{0.649}Zn_{0.200}Ti_{0.800}O_3$
Ga^{+3}	$Li_{0.417}La_{0.594}Ga_{0.200}Ti_{0.800}O_3$
Rb^{+1}	$Li_{0.492}La_{0.703}Rb_{0.200}Ti_{0.800}O_3$
Sr^{+2}	$Li_{0.454}La_{0.649}Sr_{0.200}Ti_{0.800}O_3$
Y^{+3}	$Li_{0.417}La_{0.594}Y_{0.200}Ti_{0.800}O_3$
Zr^{+4}	
Nb^{+5}	
Mo^{+6}	
Rh^{+3}	$Li_{0.417}La_{0.594}Rh_{0.200}Ti_{0.800}O_3$
Pd^{+2}	$Li_{0.454}La_{0.649}Pd_{0.200}Ti_{0.800}O_3$
Ag^{+1}	$Li_{0.492}La_{0.703}Ag_{0.200}Ti_{0.800}O_3$
Cd^{+2}	$Li_{0.454}La_{0.649}Cd_{0.200}Ti_{0.800}O_3$
In^{+3}	$Li_{0.417}La_{0.594}In_{0.200}Ti_{0.800}O_3$
Sn^{+4}	$Li_{0.379}La_{0.540}Sn_{0.200}Ti_{0.800}O_3$
Te^{+4}	
Cs^{+1}	$Li_{0.492}La_{0.703}Cs_{0.200}Ti_{0.800}O_3$
Ba^{+2}	$Li_{0.454}La_{0.649}Ba_{0.200}Ti_{0.800}O_3$
Ce^{+3}	$Li_{0.417}La_{0.594}Ce_{0.200}Ti_{0.800}O_3$
Pr^{+3}	$Li_{0.417}La_{0.594}Pr_{0.200}Ti_{0.800}O_3$
Nd^{+3}	$Li_{0.417}La_{0.594}Nd_{0.200}Ti_{0.800}O_3$
Sm^{+3}	$Li_{0.417}La_{0.594}Sm_{0.200}Ti_{0.800}O_3$
Eu^{+3}	$Li_{0.417}La_{0.594}Eu_{0.200}Ti_{0.800}O_3$
Gd^{+3}	$Li_{0.417}La_{0.594}Gd_{0.200}Ti_{0.800}O_3$
Tb^{+3}	$Li_{0.417}La_{0.594}Tb_{0.200}Ti_{0.800}O_3$
Dy^{+3}	
Ho^{+3}	
Er^{+3}	
Hf^{+4}	
Ta^{+5}	
W^{+6}	
Re^{+7}	
Ir^{+4}	$Li_{0.379}La_{0.540}Ir_{0.200}Ti_{0.800}O_3$
Pt^{+4}	
Au^{+3}	$Li_{0.417}La_{0.594}Au_{0.200}Ti_{0.800}O_3$
Tl^{+1}	$Li_{0.492}La_{0.703}Tl_{0.200}Ti_{0.800}O_3$
Pb^{+2}	$Li_{0.454}La_{0.649}Pb_{0.200}Ti_{0.800}O_3$

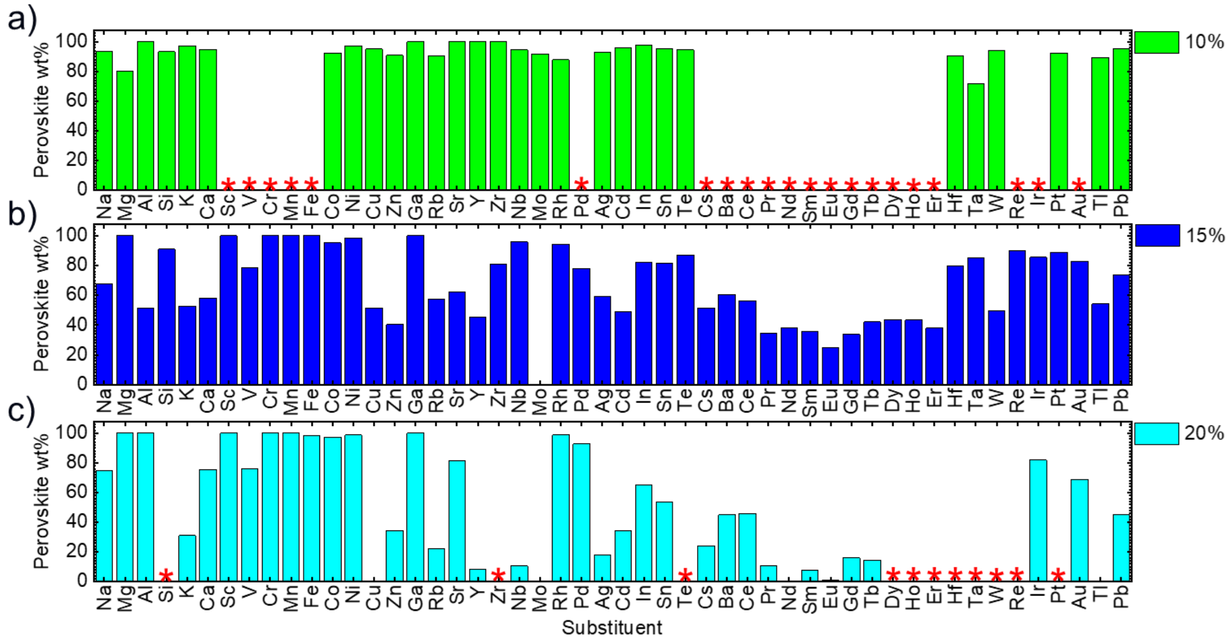

***Figure S4.1** Perovskite phase fraction of 10% (a), 15% (b), and 20% (c) substitutions. Red asterisks indicate samples that were not made. The 20% Cu substituted sample was stuck on the alumina plate.*

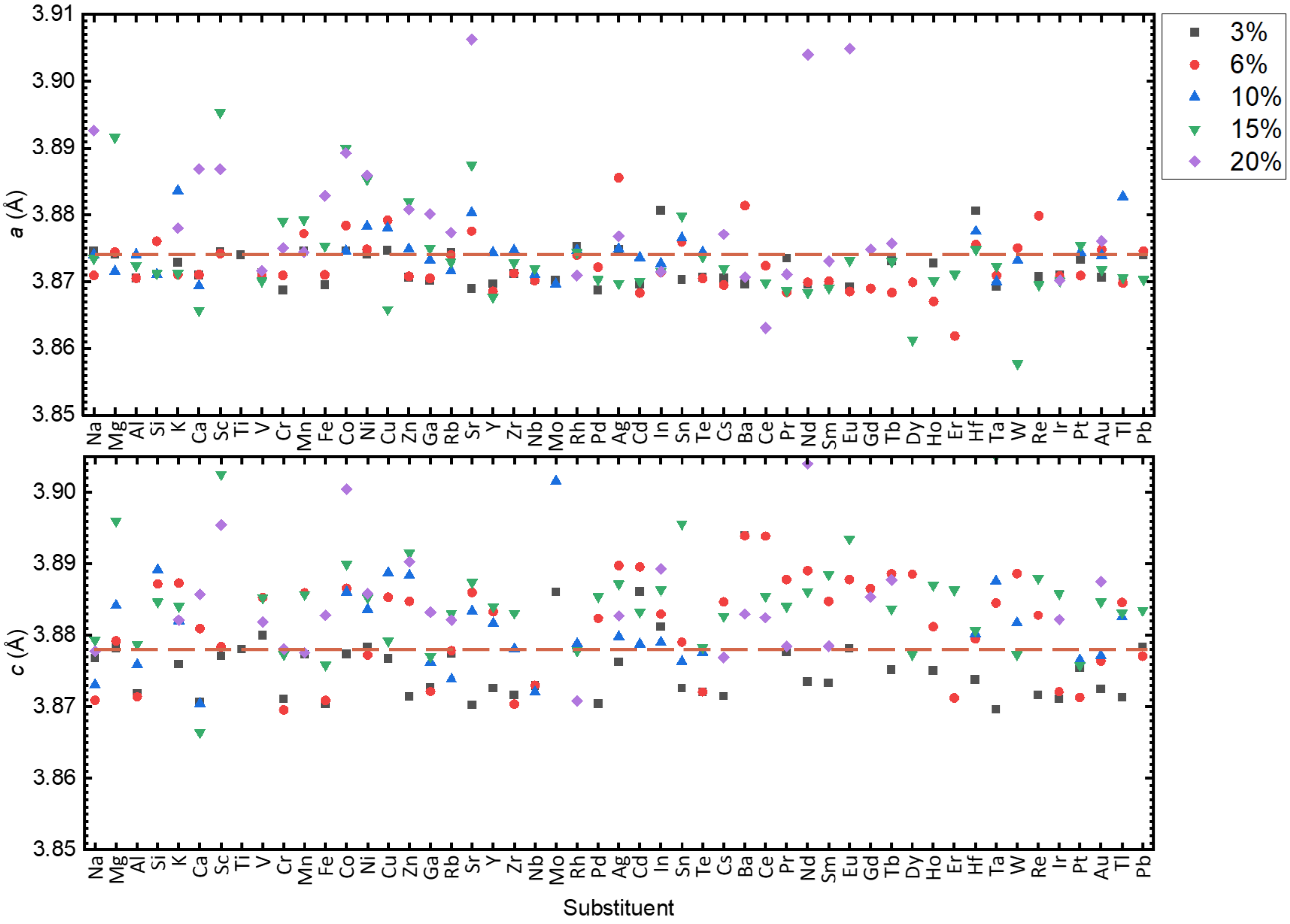

***Figure S4.2** a and c lattice parameters of substituted LLTO at 5 different levels. Red dashed line corresponds to the unsubstituted perovskite. The lattice parameters are reported for the pseudocubic lattice (lattice parameter conversions shown in Table **S3.1**).*

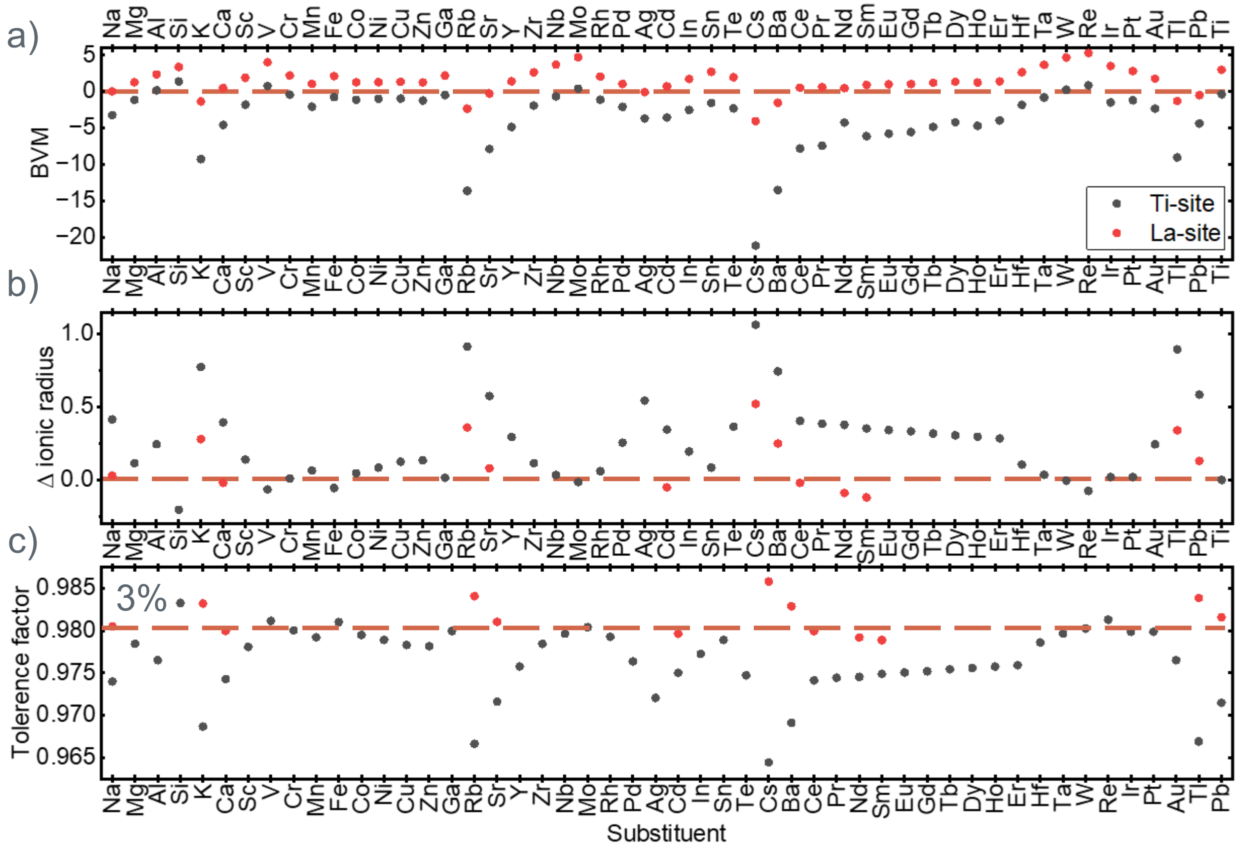

Figure S4.3 *BVM of different substituents at both Ti and La sites (a). Ionic lattice difference between substituent Ti and La with 6 coordination and 12 coordination respectively (b). Tolerance factor calculated at Ti and La sites by using average weighted ionic radius for 3% substitution (c). The tolerance factor was calculated from the ionic radii of the oxygen and the elements occupying Ti-site and La-site. In the case of mixed occupancy, the weighted average of the ionic radii was used.*

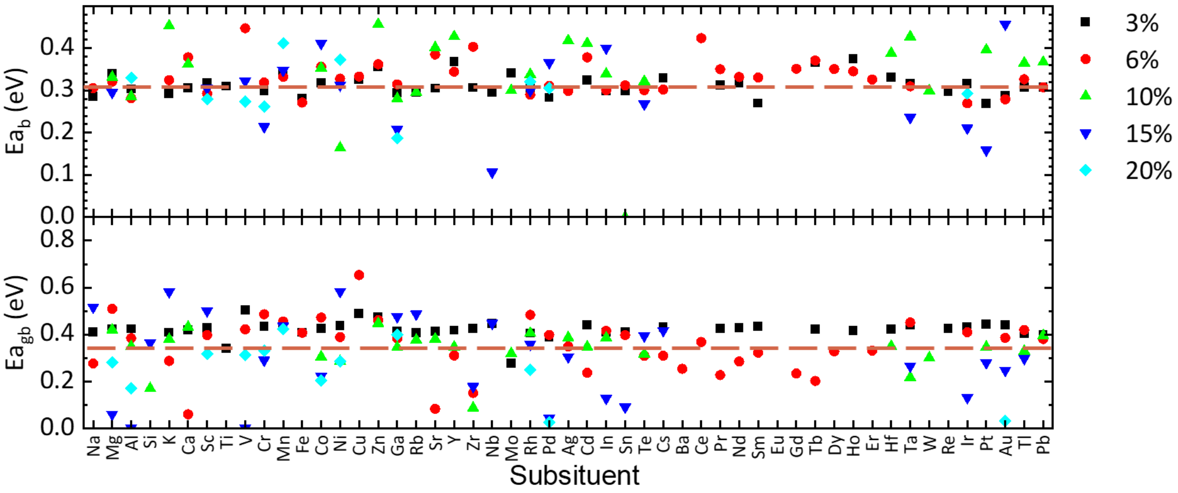

Figure S4.4 *Activation energy of bulk and grain boundary conductivities at 5 different substitution levels. Dashed line corresponds to the unsubstituted sample.*

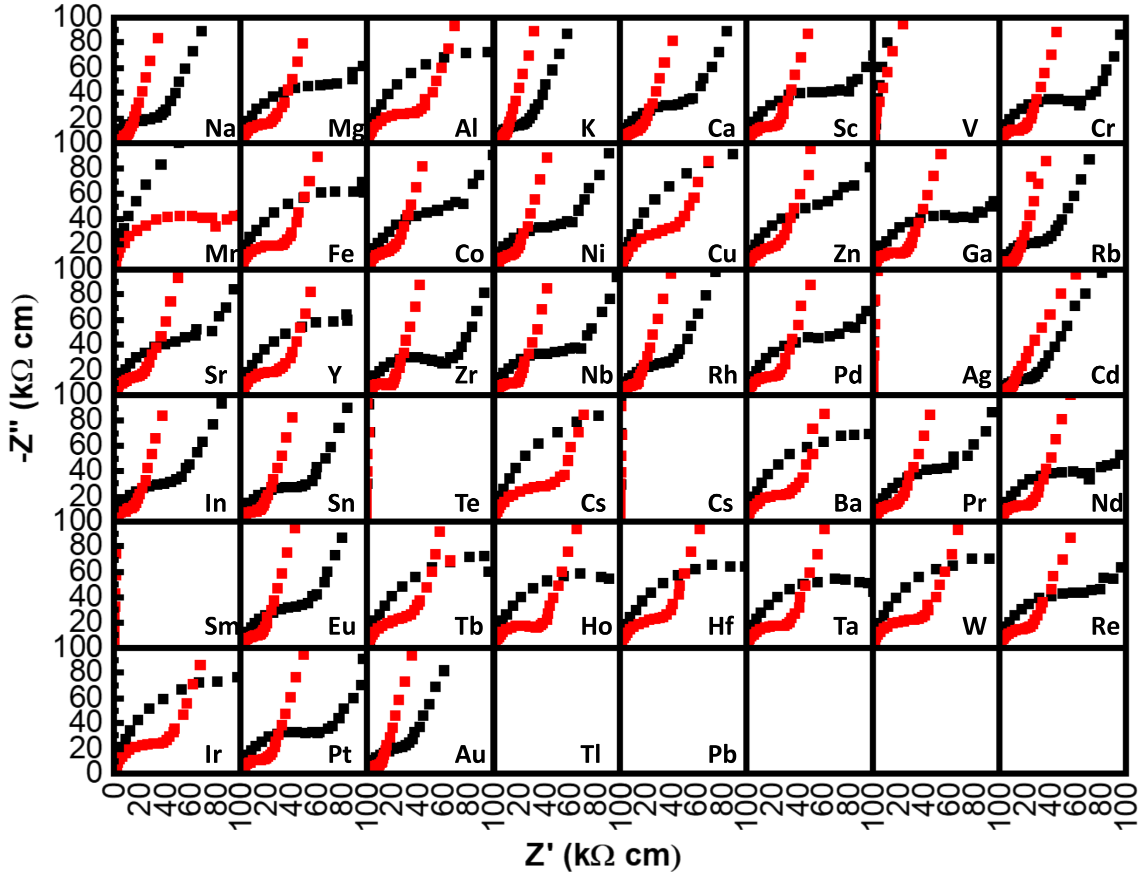

Figure S4.5 *Nyquist plots of 3% substituted perovskite at 22 ℃ black scatter plot and at 50 ℃ red scatter plot.*

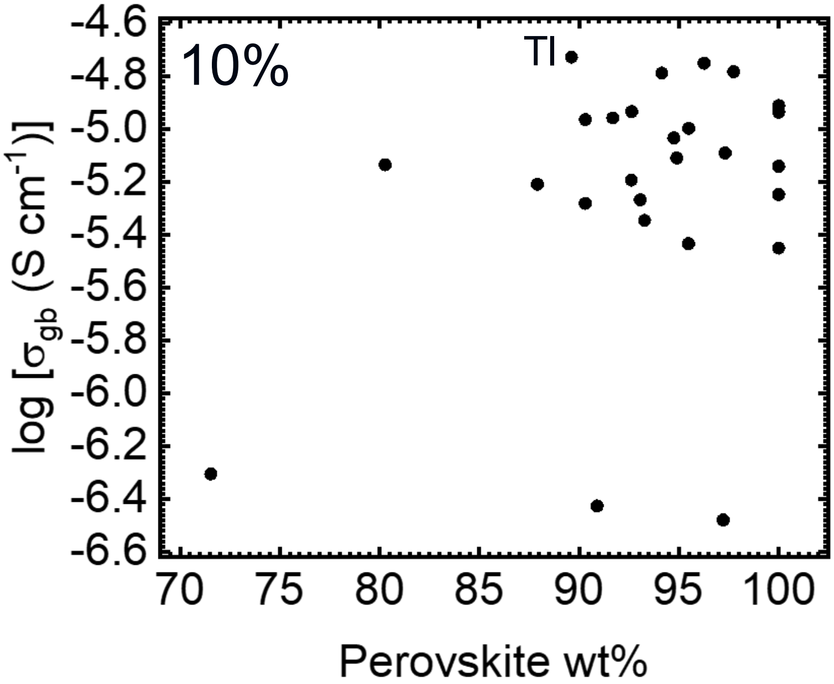

Figure S4.6 *Grain boundary conductivities of 10% substituted LLTO samples with varying perovskite phase content.*

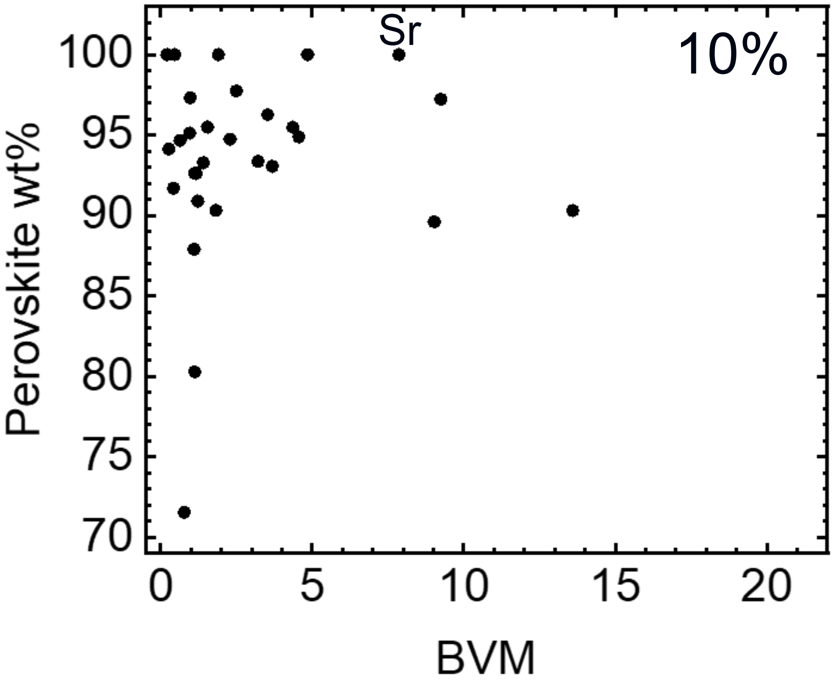

Figure S4.7 *Grain boundary conductivities of 10% substituted LLTO samples vs calculated BVM at Ti-site.*

4.8 References

(1) Xia, L.; Yu, L.; Hu, D.; Chen, G. Z. Electrolytes for Electrochemical Energy Storage. *Materials Chemistry Frontiers* **2017**, *1* (4), 584.
(2) Yu, S.; Schmidt, R. D.; Garcia-Mendez, R.; Herbert, E.; Dudney, N. J.; Wolfenstine, J. B.; Sakamoto, J.; Siegel, D. J. Elastic Properties of the Solid Electrolyte $Li_7La_3Zr_2O_{12}$ (LLZO). *Chemistry of Materials* **2016**, *28* (1), 197.
(3) Zhu, Y.; He, X.; Mo, Y. Origin of Outstanding Stability in the Lithium Solid Electrolyte Materials: Insights from Thermodynamic Analyses Based on First-Principles Calculations. *ACS Applied Materials & Interfaces* **2015**, *7* (42), 23685.
(4) Jonderian, A.; Anderson, E.; Peng, R.; Xu, P.; Jia, S.; Cozea, V.; McCalla, E. Suite of High-Throughput Experiments for Screening Solid Electrolytes for Li Batteries. *Journal of The Electrochemical Society* **2022**, *169* (5), 050504.
(5) Inaguma, Y.; Liquan, C.; Itoh, M.; Nakamura, T.; Uchida, T.; Ikuta, H.; Wakihara, M. High Ionic Conductivity in Lithium Lanthanum Titanate. *Solid State Communications* **1993**, *86* (10), 689.
(6) Zhang, L.; Zhang, X.; Tian, G.; Zhang, Q.; Knapp, M.; Ehrenberg, H.; Chen, G.; Shen, Z.; Yang, G.; Gu, L.; Du, F. Lithium Lanthanum Titanate Perovskite as an Anode for Lithium Ion Batteries. *Nature Communications* **2020**, *11* (1), 3490.
(7) Jonderian, A.; McCalla, E. The Role of Metal Substitutions in the Development of Li Batteries, part II: Solid Electrolytes. *Materials Advances* **2021**, *2* (9), 2846.

(8) Itoh, M.; Inaguma, Y.; Jung, W.-H.; Chen, L.; Nakamura, T. High Lithium Ion Conductivity in the Perovskite-Type Compounds $Ln_{12}Li_{12}TiO_3$(Ln=La,Pr,Nd,Sm). *Solid State Ionics* **1994**, *70-71*, 203.

(9) Thangadurai, V.; Weppner, W. Effect of B-Site Substitution of $(Li,La)TiO_3$ Perovskites by Di-, Tri-, Tetra- and Hexavalent Metal Ions on the Lithium Ion Conductivity. *Ionics* **2000**, *6* (1), 70.

(10) Mei, A.; Wang, X.-L.; Lan, J.-L.; Feng, Y.-C.; Geng, H.-X.; Lin, Y.-H.; Nan, C.-W. Role of Amorphous Boundary Layer in Enhancing Ionic Conductivity of Lithium–Lanthanum–Titanate Electrolyte. *Electrochimica Acta* **2010**, *55* (8), 2958.

(11) Wu, J.-F.; Guo, X. Origin of the Low Grain Boundary Conductivity in Lithium Ion Conducting Perovskites: $Li_{3x}La_{0.67-x}TiO_3$. *Physical Chemistry Chemical Physics* **2017**, *19* (8), 5880.

(12) Inaguma, Y.; Matsui, Y.; Shan, Y.-J.; Itoh, M.; Nakamura, T. Lithium Ion Conductivity in the Perovskite-Type $LiTaO_3$-$SrTiO_3$ Solid Solution. *Solid State Ionics* **1995**, *79*, 91.

(13) Al-Maghrabi, M. A.; Suzuki, J.; Sanderson, R. J.; Chevrier, V. L.; Dunlap, R. A.; Dahn, J. R. Combinatorial Studies of $Si_{1-x}O_x$ as a Potential Negative Electrode Material for Li-Ion Battery Applications. *Journal of The Electrochemical Society* **2013**, *160* (9), A1587.

(14) Rehman, S.; Sieffert, J. M.; Lang, C. J.; McCalla, E. $Nb_yW_{1-y}O_z$ and $Nb_xTi_{1-x}O_z$ Pseudobinaries as Anodes for Li-Ion Batteries. *Electrochimica Acta* **2023**, *439*, 141665.

(15) Kim, D.; Shim, H. C.; Yun, T. G.; Hyun, S.; Han, S. M. High Throughput Combinatorial Analysis of Mechanical and Electrochemical Properties of $Li[Ni_xCo_yMn_z]O_2$ Cathode. *Extreme Mechanics Letters* **2016**, *9*, 439.

(16) Jonderian, A.; Jia, S.; Yoon, G.; Cozea, V. T.; Galabi, N. Z.; Ma, S. B.; McCalla, E. Accelerated Development of High Voltage Li-Ion Cathodes. *Advanced Energy Materials* **2022**, *12* (40), 2201704.

(17) Jia, S.; Yao, E.; Peng, R.; Jonderian, A.; Abdolhosseini, M.; McCalla, E. Chemical Speed Dating: The Impact of 52 Dopants in Na–Mn–O Cathodes. *Chemistry of Materials* **2022**, *34* (24), 11047.

(18) Beal, M. S.; Hayden, B. E.; Le Gall, T.; Lee, C. E.; Lu, X.; Mirsaneh, M.; Mormiche, C.; Pasero, D.; Smith, D. C. A.; Weld, A.; Yada, C.; Yokoishi, S. High Throughput Methodology for Synthesis, Screening, and Optimization of Solid State Lithium Ion Electrolytes. *ACS Combinatorial Science* **2011**, *13* (4), 375.

(19) Anderson, E.; Jonderian, A.; Khaliullin, R. Z.; McCalla, E. Combinatorial Study of the Li-La-Zr-O System. *Solid State Ionics* **2022**, *388*, 116087.

(20) Jonderian, A.; Ting, M.; McCalla, E. Metastability in Li–La–Ti–O Perovskite Materials and Its Impact on Ionic Conductivity. *Chemistry of Materials* **2021**, *33* (12), 4792.

(21) Warburton, R. E.; Kim, J. J.; Patel, S.; Howard, J. D.; Curtiss, L. A.; Wolverton, C.; Buchholz, D. B.; Vaughey, J. T.; Fenter, P.; Fister, T. T.; Greeley, J. Tailoring Interfaces in Solid-State Batteries Using Interfacial Thermochemistry and Band Alignment. *Chemistry of Materials* **2021**, *33* (21), 8447.

(22) McCalla, E.; Walter, J.; Leighton, C. A Unified View of the Substitution-Dependent Antiferrodistortive Phase Transition in $SrTiO_3$. *Chemistry of Materials* **2016**, *28* (21), 7973.

(23) Sotomayor, M. E.; Levenfeld, B.; Varez, A.; Sanz, J. Study of the $La_{1/2+1/2x}Li_{1/2-1/2x}Ti_{1-x}Al_xO_3$ $(0 \leq x \leq 1)$ Solid Solution. A New Example of Percolative System in Fast Ion Conductors. *Journal of Alloys and Compounds* **2017**, *720*, 460.

(24) Jiang, Y.; Huang, Y.; Hu, Z.; Zhou, Y.; Zhu, J.; Zhu, X. Effects of B-Site Ion (Nb^{5+}) Substitution on the Microstructure and Ionic Conductivity of $Li_{0.5}La_{0.5}TiO_3$ Solid Electrolytes. *Ferroelectrics* **2020**, *554* (1), 89.

(25) Yu, K.; Jin, L.; Li, Y.; Liu, G.; Wei, X.; Yan, Y. Structure and Conductivity of Perovskite $Li_{0.355}La_{0.35}Sr_{0.3}Ti_{0.995}M_{0.005}O_3$ (M = Al, Co and In) Ceramics. *Ceramics International* **2019**, *45* (18, Part A), 23941.

(26) Han, F.; Westover, A. S.; Yue, J.; Fan, X.; Wang, F.; Chi, M.; Leonard, D. N.; Dudney, N. J.; Wang, H.; Wang, C. High Electronic Conductivity as the Origin of Lithium Dendrite Formation Within Solid Electrolytes. *Nature Energy* **2019**, *4* (3), 187.

(27) Wexler, R. B.; Gautam, G. S.; Stechel, E. B.; Carter, E. A. Factors Governing Oxygen Vacancy Formation in Oxide Perovskites. *Journal of the American Chemical Society* **2021**, *143* (33), 13212.

(28) Fan, Z.; Xiang, J.; Yu, Q.; Wu, X.; Li, M.; Wang, X.; Xia, X.; Tu, J. High Performance Single-Crystal Ni-Rich Cathode Modification via Crystalline LLTO Nanocoating for All-Solid-State Lithium Batteries. *ACS Applied Materials & Interfaces* **2022**, *14* (1), 726.

(29) Vallez, L.; Jimenez-Villegas, S.; Garcia-Esparza, A. T.; Jiang, Y.; Park, S.; Wu, Q.; Gill, T. M.; Sokaras, D.; Siahrostami, S.; Zheng, X. Effect of Doping TiO_2 With Mn for Electrocatalytic Oxidation in Acid and Alkaline Electrolytes. *Energy Advances* **2022**, *1* (6), 357.

(30) Zaker, N.; Geng, C.; Rathore, D.; Hamam, I.; Chen, N.; Xiao, P.; Yang, C.; Dahn, J. R.; Botton, G. A. Probing the Mysterious Behavior of Tungsten as a Dopant Inside Pristine Cobalt-Free Nickel-Rich Cathode Materials. *Advanced Functional Materials* **2023**, *n/a* (n/a), 2211178.

Chapter 5

Accelerated Development of High Voltage Li-Ion Cathodes

The solid electrolytes developed in Chapters 3 and 4 have high oxidative stability (5.5V), making them suitable for high-potential cathodes incompatible with conventional liquid electrolytes. This chapter aims to improve the performance of a challenging high-potential cathode material, $LiCoPO_4$, which operates at about 4.8V and is limited by low intrinsic electronic and ionic conductivity. First, we explore the effect of single partial substitution of the Co site in LCP on its electrochemical performance. This involved first optimizing the synthesis conditions Next, the performance of the best single-substituted LCP is further enhanced by adding co-substituents. Finally, the co-substitution level is optimized. The underlying mechanism of improved performance is investigated using traditional experimentation, such as measuring charge transport properties and computational simulations. The results show that a low content of co-substitution can drastically improve the performance of LCP.

Chapter 5 is produced with permission from "Jonderian, A.; Jia, S.; Yoon, G.; Cozea, V. T.; Galabi, N. Z.; Ma, S. B.; McCalla, E. Accelerated Development of High Voltage Li-Ion Cathodes. *Advanced Energy Materials* **2022**, *12* (40), 2201704".

5.1 Abstract

High voltage cathodes are attractive for high energy density Li-ion batteries. However, candidates such as $LiCoPO_4$ have presented numerous challenges stemming from poor electronic/ionic conductivities such that typical solutions involving nanosizing result in extremely poor cycling performance. Here, we apply high-throughput methods to develop near-micron sized carbon-coated $LiCoPO_4$ with improved energy density and capacity retention. In total, 1300 materials with

46 different substituents were synthesized and characterized. A number of substituents showed greatly improved capacity (e.g. 160 mAh/g for 1% In substitution vs. 95 mAh/g for the pristine). However, co-doping was required to improve extended cycling. $Li_{1-3x}Co_{1-2x}In_xMo_xPO_4$ was found to be particularly effective with dramatically improved cycling (as high as 100 % after 10 cycles, vs. ~50 % in unsubstituted). While In improved the electronic conductivity of the carbon-coated materials, Mo co-doping gave larger particles and DFT calculations showed that Mo impedes the formation of Li/Co antisite defects.

5.2 Introduction

There is a global demand for higher energy storage devices for electric vehicles in order to improve their range and become attractive for widespread use. One of the primary approaches to increasing energy density is to use cathodes that operate at higher voltages. $LiCoPO_4$ (LCP) has garnered a great deal of attention in this regard, as it operates near 4.8 V *vs*. Li.[1] To date, liquid electrolytes have not been able to operate at such high potentials although significant progress is being made.[2] Furthermore, the promise of stable solid electrolytes also serves to renew our interest in LCP. However, the challenges are numerous, with the key problems being that LCP is an electronic and ionic insulator. The only commercialized cathode with such poor intrinsic transport properties is $LiFePO_4$ (LFP) for which the limitations are overcome by nanosizing and carbon-coating the particles such that the poor transport takes place over very short length scales.[3] In the case of LFP, the greatly increased surface area due to nano-sizing is not detrimental given that the cathode operates at 3.45 V where liquid electrolytes are perfectly stable.[3] By contrast, LCP operates outside of the stability window of typical electrolytes such that nanosizing may indeed improve the first cycle capacity (e.g. capacities ranging from 80 mAh/g for 1-2 micron sized particles up to 125 mAh/g for 100-200 nm particles), but it is disastrous for extended cycling.[4] Typically, in the undoped materials, when the first cycle capacities of the approach 130 mAh/g due to nanosizing, the capacity retention is very poor (e.g. approximately 25% retention after 10 cycles in ref. [5]). As there is also a dramatic range of results in the literature for the impact of dopants in this material[1,6–18], there is a need for a systematic study where synthesis and test conditions are uniform to truly determine the impact of all the potential dopants. Previous computational work[6] demonstrated that a number of dopants are expected to be possible and interestingly all those explored lowered the redox voltage compared to the undoped. Herein, we report the first systematic study of 46 different dopants (shown in the periodic table in Figure **S5.1**) and co-dopants into micron sized LCP.

5.3 Experimental section

Synthesis

A citrate sol-gel method was used to prepare the samples. The optimal mole ratio of total metals to citric acid was 1:1. $LiNO_3$ (2M), $Co(NO_3)_2$(2M), $(NH_4)_2HPO_4$ (2M), and citric acid (4M) solutions were prepared in deionized water. The concertation of the initial metal solutions was quantified by inductively coupled plasma–optical emission spectroscopy (ICP–OES). First, 40 μL of citric acid was pipetted into 64 (400 μL alumina) cups followed by the addition of 40 μL of cobalt nitrate, 40 μL of lithium nitrate, and lastly 40 μL of ammonium phosphate dibasic. An aluminum smokestack was placed on the cups to prevent cross-contamination during gel swelling. The bulk of the water was reduced by heating to 70 °C for 12 h yielding a viscous gel. The rest of the trapped water was removed by incremental heating starting from 100 °C to 200 °C under vacuum, producing brown color powder that was ground before further heat treatment in air. These powder samples were heated to 750 °C or 850 °C for 4 h at a ramp/cool rate of 5 °/min. The violet colored powder formed was ground and placed on top of an alumina plate in clamps (~10 mg) and then wetted with 12 μL of 104 g/L citric acid corresponding to 13%wt citric acid content (10 %wt carbon). The wetted clamps were mixed by a pin forming a slurry. These slurries were transferred to a tube furnace and heated to 650 °C for 30 min at a ramp rate of 2 °C/min under an $Ar:H_2$ (95:5) atmosphere. After the coating step, the black/gray samples were ground for the structural and subsequently electrochemical analysis.

Characterization

The carbon-coated samples were transferred into a high throughput XRD holder. Their diffraction patterns were collected in transmission mode using PANalytical diffractometer equipped with a Mo anode X-ray source (60 kV, 40 mA) and GaliPIX3D area detector. The phases present were identified using the matching tool in HighScore Plus by searching against open crystal and ICSD databases. Once all the phases were identified, Rietveld refinement was performed to determine the content of each phase and their lattice parameters. For convenience, the patterns shown in this paper are K-alpha stripped and wavelength converted from Mo to Cu. The morphology of the samples was characterized by scanning electron microscopy (SEM) using a Hitachi SU3500 at 30 keV. The XPS measurement was done using a Thermo Scientific K-Alpha spectrometer equipped with Al Kα micro-focused monochromator. The XPS measurement was done at a pressure of <~ 10^{-7} mbar with an X-ray spot size of 200 μm. The survey and high-resolution spectra were collected with a pass energy of 200 eV and 50 eV, respectively. All binding energies were calibrated using the C 1s peak (284.8 eV).

High-throughput cyclic voltammetry

The high-throughput electrochemical analysis was performed by the lab-build high-throughput cyclic voltammetry system, which was designed by the Dahn lab[19] and adapted for use with cathode powders by the McCalla lab[20–22]. In detail, the custom-designed printed circuit board

(PCB) covered with aluminum pads has the capability to test 64 channels simultaneously, as illustrated in Figure **S5.12**. To prepare the electrodes, about 8 mg of each active material (AM) were weighed out and mixed with a slurry containing 80 μL N-methyl-2-pyrrolidone (NMP) (Alfa Aesar) containing 0.45 mg polyvinylidene fluoride (PVDF) (Kynar 1100), and 1.04 mg carbon black (TIMCAL). After mixing with a stirring rod for 15 min, the cathode was prepared by drop-casting 3 μL of the above-mentioned slurry onto the appropriate pad of the PCB. The electrodes were then dried at 80 °C for 12 h. The resulting electrode formulation is 84 wt % AM, 11 wt % carbon black, and 5 wt % PVDF, and the AM loading was typically 2.4 mg/cm^2 with a thickness of about 100 μm (minor variations were seen due to the shape of the electrode after drying, see Figure **S5.12** as an example). The combinatorial cell was then assembled in an argon-filled glovebox with the electrolyte (1M LiPF6 in 1:1 EC: DMC, SoulBrain MI) soaking two Whatman microfiber separators, and Li metal as the counter electrode. The cell is shown schematically in Figure **S5.15**. The CVs were performed with the voltage range from 3.0 V to 5.3 V vs. Li/Li$^+$ at a scan rate of 0.2 V h^{-1}.

Galvanostatic cycling

In order to ensure that the high performance of the In/Mo co-doped samples is maintained in galvanostatic cycling conditions, a slurry was made from 30 mg of LCP (multiple HT samples were combined to achieve this) with a formulation of 85 % AM, 7.5 % carbon black and 7.5 % PVDF. Electrodes with a mass loading of 2.5 mg/cm^2 were prepared using a doctor blade and then assembled into LIR2032 type coin cells (MTI Corp.) with the same electrolyte as in the HT voltammetry measurements. Galvanostatic cycling was performed at 10 mA/g in the range 3.0 – 5.0 V on a Biologic potentiostat.

Conductivity measurements

The electronic and ionic conductivities were measured by cold pressing 30 mg samples using a 3 mm pressing die and coating two gold blocking electrodes as contacts. The total electrical conductivity was determined by electrochemical impedance spectroscopy (EIS) using Biologic SP150. The EIS spectra were collected by scanning from 1 MHz to 100 mHz with an AC amplitude of 100 mV. The EIS Nyquist plots were fitted to the proper equivalent circuit using EC-lab. The electronic conductivity was determined by applying 1.5 V DC polarization for 15 min while measuring the current decay. From the steady-state current, the electronic contribution was calculated.

Density functional theory

First-principles calculations were performed with the Perdew–Burke–Ernzerhof (PBE) exchange-correlation functional using the spin-polarized GGA[23]. The projector-augmented wave pseudopotentials were used as implemented in the Vienna Ab initio Simulation Package (VASP)[24]. A Hubbard-type U parameter (GGA + U)[25] was added to correct the on-site Coulomb interactions, with U[Co] = 5.7 eV[26], U[In] = 7.0 eV[27], U[Mo] = 3.5 eV[28] and U[Nb] = 3.02 eV[29]. The supercell of LCP was 2a x 2b x 1c, comprising 112 atoms ($Li_{16}Co_{16}P_{16}O_{64}$). The magnetic ordering preference of LCP was calculated to demonstrate the intrinsic antiferromagnetism in LCP. [30] The activation barriers of Li migration were calculated using the CI-NEB method[31,32]. All the lattice parameters were fixed, but all the atomic positions were relaxed within the supercell during the CI-NEB calculations. To avoid the charge ordering problem on transition metals within GGA + U, the elastic band was calculated without U correction[26].

5.4 Results and discussion

As described in the methods section, a sol-gel synthesis is used wherein uncoated LCP is first made in air at either 750 or 850 °C. The resulting LCP materials are then mixed with a carbon source before being heated under forming gas to make carbon-coated LCP. Figure **5.1**a shows the typical workflow followed here wherein wide substitutions are explored using high-throughput methods, followed by characterization/DFT on key compositions prior to proposing/performing further high-throughput on co-doped samples. Figure **5.1**b shows that the undoped material is pure phase LCP, while the cyclic voltammogram (CV) performed in high-throughput between 3.0 and

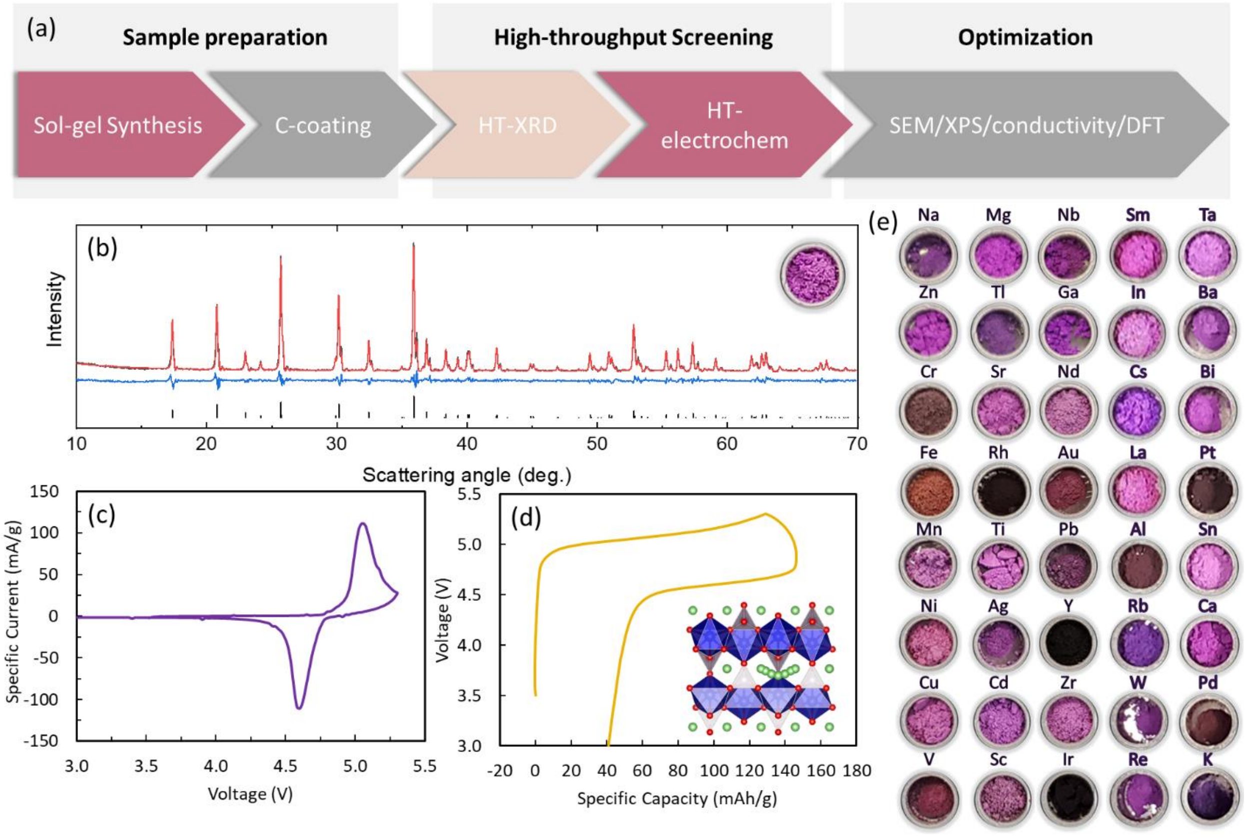

Figure 5.1 *(a) Workflow for the current study where high-throughput (HT) synthesis/characterization is used to screen cathode materials, followed by traditional experiments/computations to motivate further HT tests. (b) XRD (the fits in red and the difference plots in blue), (c) CV, and (d) corresponding voltage curve of the undoped sample made at 850 ℃ show limited capacity and high overpotentials, while the Li diffusion path in the undoped is shown in (d). (e) Pictures of the* $Li_yCo_{0.9}M_{0.1}PO_4$ *samples after heating in air to 750 ℃ (prior to carbon coating).*

5.3 V at 0.2 V/h is also shown in Figure **5.1**. The results for undoped LCP yield a first discharge capacity of 95 mAh/g at 850 °C, and 104 mAh/g at 750 °C, consistent with undoped materials with micron sized particles (shown in the SEM image in Figure **5.2**) as per ref. [4]. The capacity retention after 10 cycles are only 47 % (850 °C) and 43 % (750 °C). The slightly improved capacity and diminished retention at the lower synthesis temperature are attributed to smaller particles. It is important to recognize that a CV up to 5.3 V is a cycling protocol that leads to extremely poor extended cycling (i.e. all samples will spend 3 h above 5.0 V on every cycle, this is in contrast to galvanostatic cycling where LCP materials spend no time above 5.0 V). This cycling protocol is therefore ideal to rapidly obtain discrimination (i.e. any significant improvement in extended cycling will be measurable in a few cycles under these extremely aggressive conditions). Therefore, although direct comparison to retention from galvanostatic studies is impossible,

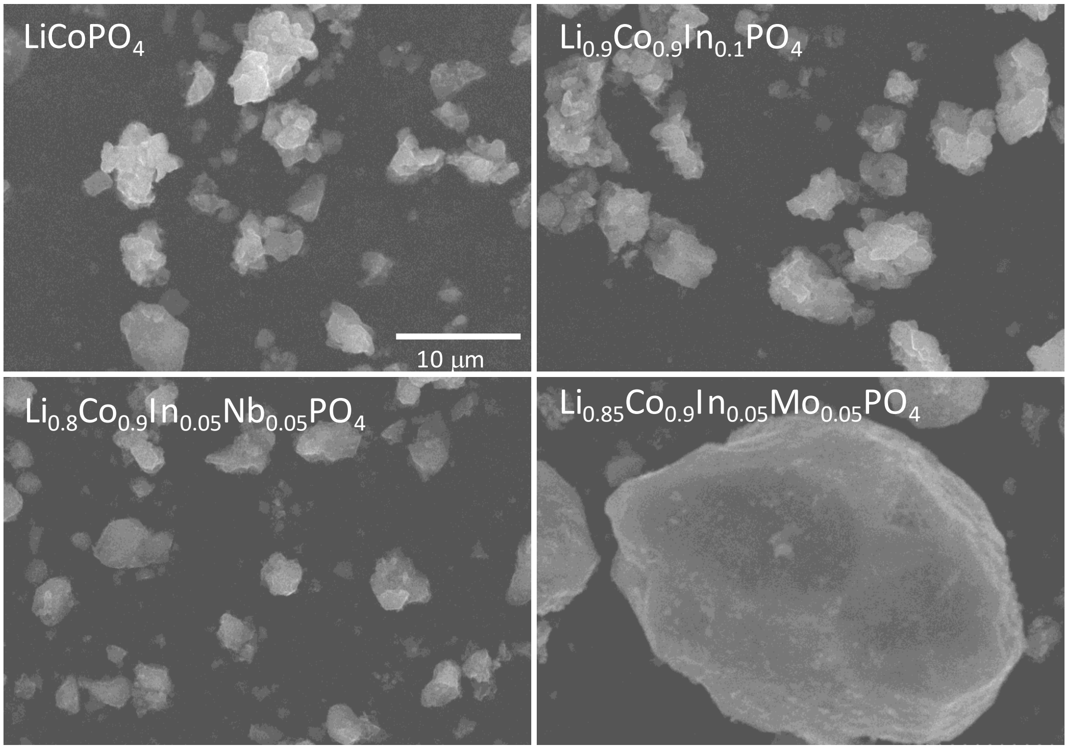

Figure 5.2 *SEM images of unsubstituted LCP along with 10% In-doped, as well as In/Mo and In/Nb co-doped samples. In all cases the images are representative. The scale bar applies to all four SEM images. The zoomed-out SEM image of the In/Mo substituted LCP is depitcted in Figure* ***S5.11***.

comparisons herein for our 1300 samples over 10 cycles are highly meaningful. Density functional theory was used to study the diffusion path of Li in the undoped LCP (Figure **5.1**d) and yields an energy barrier of 0.30 eV as shown in Figure **S5.2**. It should also be noted that these aggressive cycling conditions contribute to the overpotential which can be seen to be large in Figure **5.1**c.

Having benchmarked the undoped material with our high-throughput methods, a single dopant screening was performed at a 10% substitution for Co, denoted as $Li_yCo_{0.9}M_{0.1}PO_4$ yielding the samples shown in Figure **5.1**e. In total, 46 elements were attempted, covering a very large portion of the periodic table as shown in Figure **S5.1**. The Li content (y) self-adjusts to compensate for the oxidation state of the M dopant (excess Li evaporates during synthesis in air at or above 750 °C).[33] Detailed XRD analysis is required to determine to what extent substitution into LCP takes place. It is highly useful for us here that LCP exists as a single composition in the Li-Co-PO_4 pseudoternary phase diagram[34] such that any change in lattice parameter can be attributed to the substituent being integrated (at least partially) into the LCP structure. Multi-phase Rietveld refinement was utilized to obtain phase percentages based on known CIF files in the ICSD database and extract lattice parameters. A full list of the results for 750 and 850 °C are shown in Tables **S5.1**-**S5.2** with a complete list of secondary phases, and Figures **5.3**, and Figure **S5.3**. The phase fractions were then used with their cobalt and dopant contents to calculate what fraction of the dopant was present in the LCP phase. This is considered to be precise except for the patterns that had peaks that could not be indexed (these are marked by a * in Figures **5.3**, and **S5.3**). We find that 57 % of dopants were integrated in LCP (> 5 % doping) at 750 °C, while 67 % were integrated at 850 °C. This large set of data therefore leads to some important conclusions: (i) the solubility of dopants is generally quite high, (ii) many dopants show better solubility at 850 °C than 750 °C (though a few, like Ti, decreased at the higher temperature), (iii) a few dopants like Al show quite

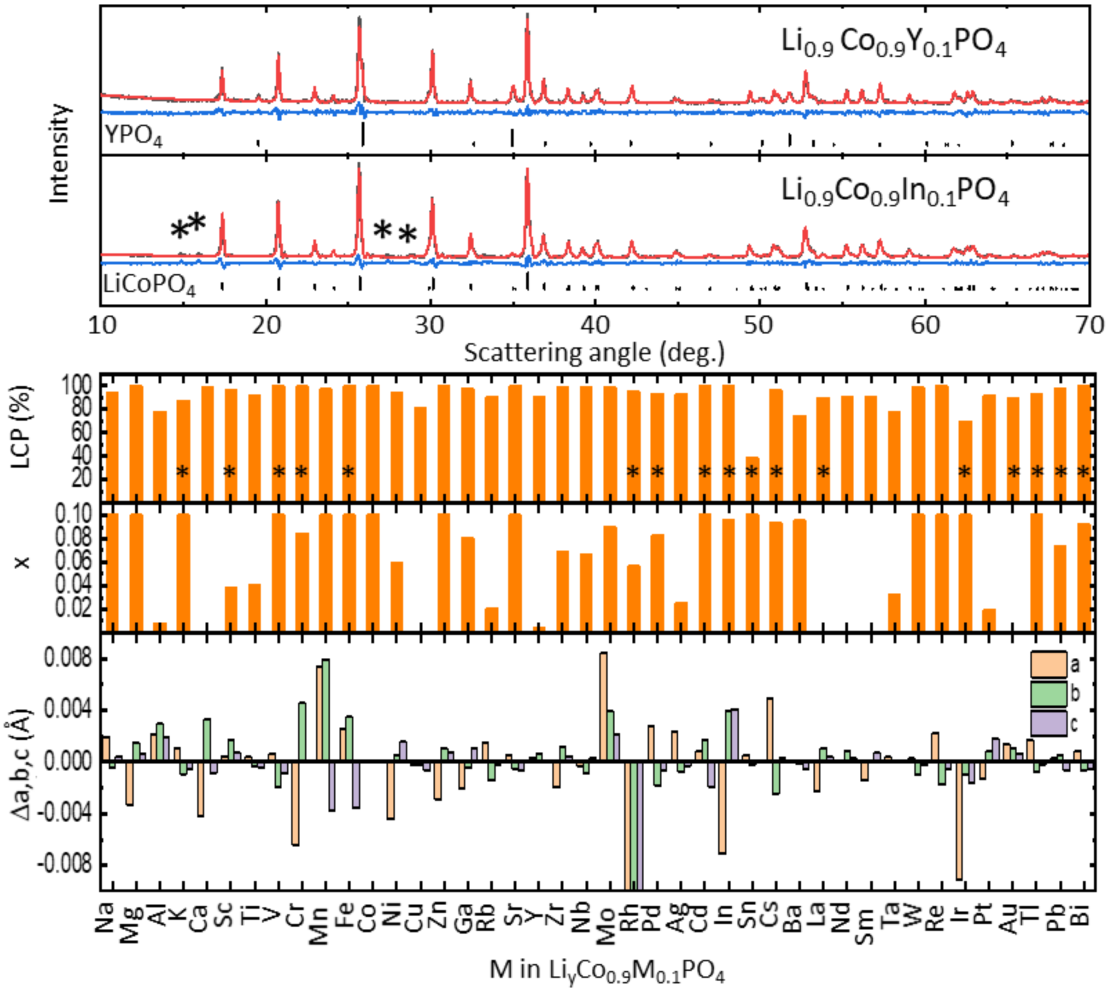

Figure 5.3 *XRD results for single dopant samples heated at 850 ℃ and carbon coated. Top: two representative XRD patterns along with the fits in red and the difference plots in blue. The * indicates small peaks corresponding to the unidentified phase in the In-doped sample. Lower: extracted values for molar phase % of the olivine LCP phase, * indicates the presence of an unidentified phase, x (the calculated x-value in* $Li_yCo_{1-x}M_xPO_4$ *as detailed in Table* ***S5.2****), and the shift in lattice parameters with respect to the undoped samples (standard deviations in undoped duplicates were less than 0.0002 Å).*

low solubility. As will be discussed below, a number of the samples of highest interest for improved electrochemistry also show high doping (e.g. In, Re, Zn). It should also be noted that the unidentified phase in the In-substituted sample is quite small and is not seen when the In content is < 10 % as discussed below.

Combinatorial cyclic voltammetry was performed on the single-dopant samples as shown in Figures **5.4**, **S5.4**, and **S5.5**. Average discharge voltage, average overpotential (charge – discharge), specific capacity on first discharge, reversible capacity on the first cycle, and capacity retention after 10 cycles are all extracted from the CVs and plotted in Figures **5.4**, and **S5.6**. The first cycle was analyzed because the cathode samples were cycled against a Li metal anode such

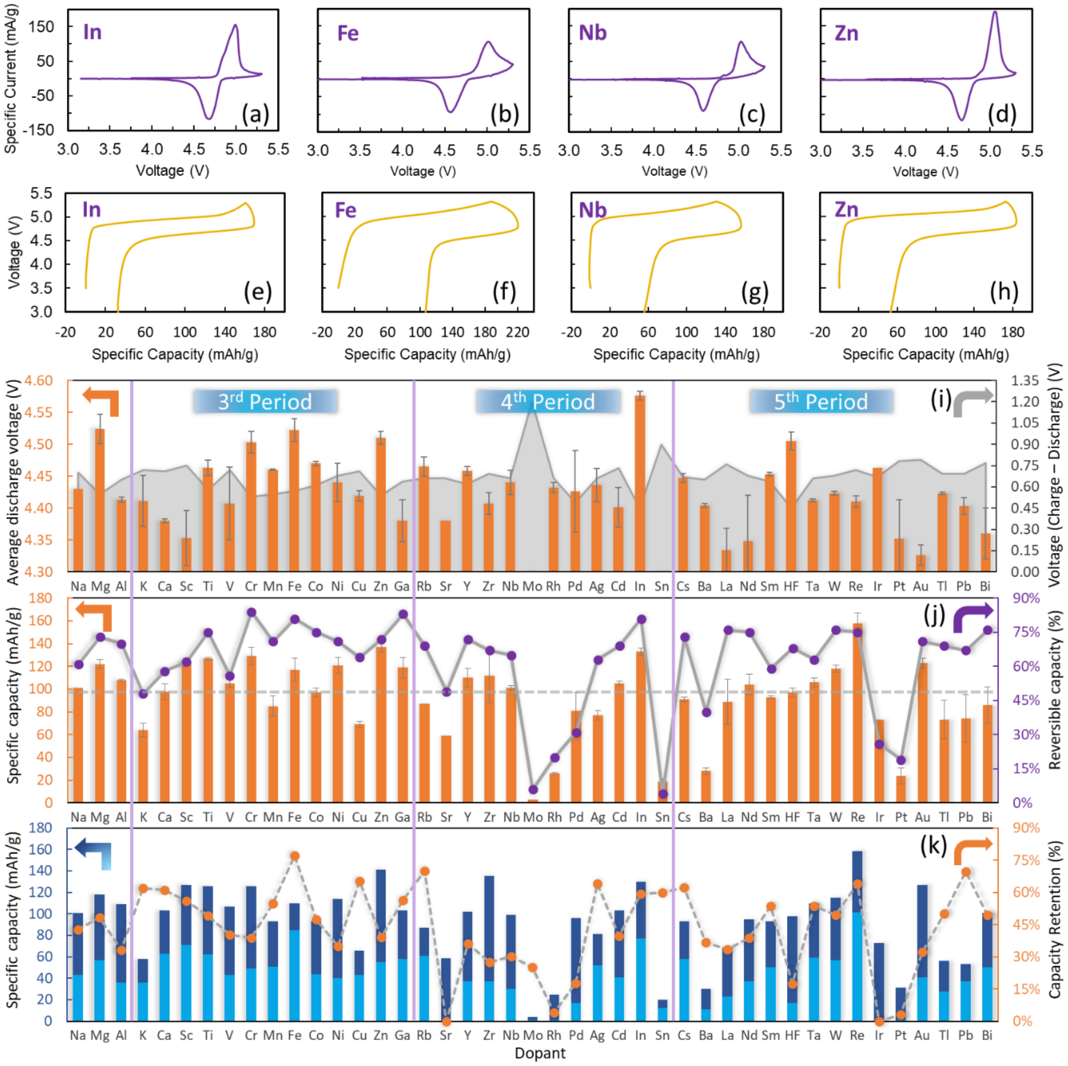

Figure 5.4 *Results of the high-throughput electrochemical testing on the* $Li_yCo_{0.9}M_{0.1}PO_4$ *samples prepared at 850 ℃ in air prior to carbon coating. Representative CVs (a-d) and corresponding voltage curves (e-h) are shown. The properties extracted for the first cycle are shown in (i,j) while (k) shows the retention after 10 cycles. The grey dashed line in (j) indicates the discharge capacity of the undoped sample as a reference. While a number of samples show significantly improved capacities, the retention continues to be poor.*

that the absence of lithium SEI formation does not affect the lithium inventory. Consequently, all the charge/discharge capacity observed can be attributed to the cathode materials (plus electrolyte decomposition contribution). Compared to the undoped samples with capacities near 100 mAh/g and capacity retention around 45 %, many of the substituted samples show a dramatically improved capacity, despite the fact that the theoretical capacity has dropped from 167 mAh/g to 150 mAh/g assuming the substituent is electrochemically inactive. There are definite trends in the properties evolution in Figure **5.4**, such as the inverted volcano in the capacity in the 4th period where In and Y at either end show higher capacities with a minima in the middle of the period (Mo, Rh). Ultimately, while 3d metals, which have been well studied as dopants in LCP, do show some improvement over the undoped, it is of high interest that we find greatly improved performance for a number of substituents that have generally been ignored including Ga, In, Re, and Au. In also shows an increased discharge voltage (highest average discharge voltage among dopants), a low overpotential, and an increased reversibility; all despite the fact that In^{3+} is electrochemically inactive.

To better understand the role of indium, samples with various In content were prepared ranging from 0.1 % to 100 %, as shown in Figure **5.5**. The XRD patterns show clear phase co-existence above 10 % (quantified in Figure **S5.7**), but 5 % substitution and below yielded single phase LCP, with the lattice parameters showing significant changes up to 5 % as shown in Figure **5.5**b (even 0.1 % expands *a* while contracting *b* and *c*). Importantly, Figure **5.5**d clearly shows that the benefits of indium are seen over a wide range of doping levels, with the theoretical capacities being fully achieved at both 1 and 5 %, and the highest capacity of 161 mAh/g at 1 % In substitution being particularly competitive. Figure **S5.7** shows the corresponding average discharge potentials, which generally increase with In content, in contrast to previous computational predictions[6] such

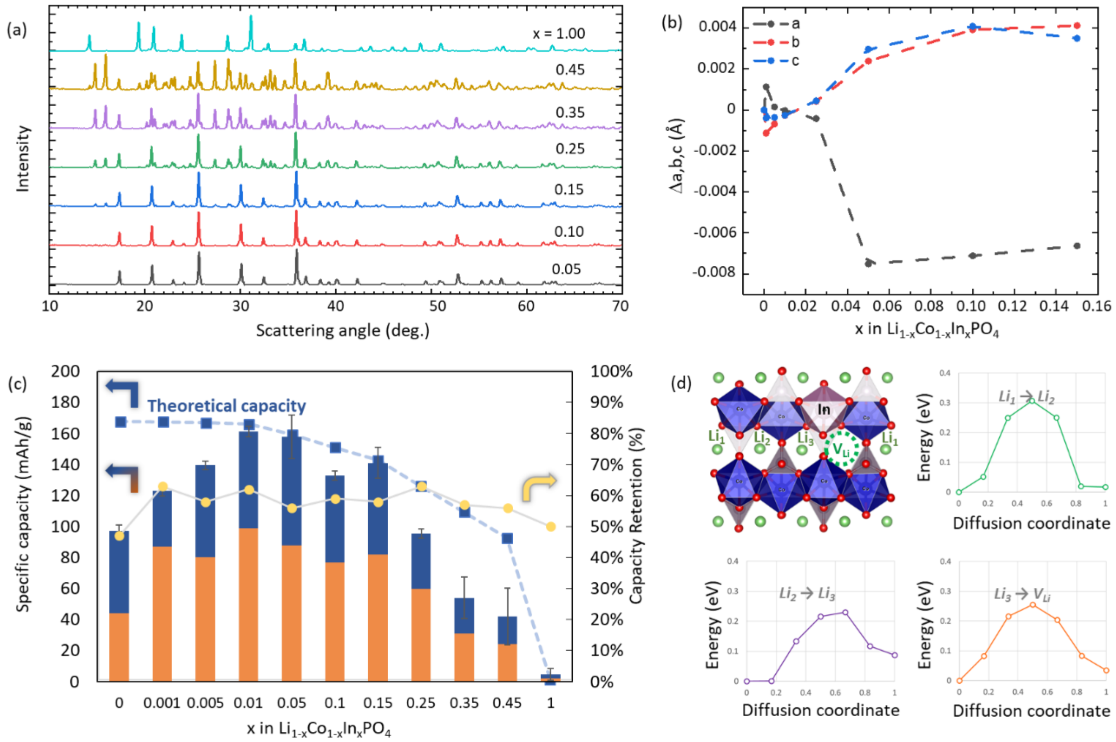

Figure 5.5 *Results for In-doped samples with varying In content. The XRD results in (a) yield the shifts in lattice parameters shown in (b). Phase pure materials are obtained below 10% In substitution. The resulting electrochemical data is shown in (c) along with the theoretical capacities assuming electrochemically inactive In. The blue and orange bars correspond to the 1*st *and 10*th *discharge specific capacities, respectively. The yellow dots correspond to the capacity retentions after 10 cycles. (d) Results of DFT calculations for the energy barriers of Li diffusion along the paths indicated in the structure, the position of the In atom and Li vacancy are also shown.*

that the source of the increase seen here will be discussed further below. It should be noted that other dopants were also studied at this stage of the current study but none performed as well at lower doping levels as at 10 %, except In (e.g. Re showed a diminished capacity of 110 mAh/g at 5%). Thus, our focus here will be on In-doping. Despite the above success, In-substituted samples consistently show a capacity retention of approximately 60 % over 10 cycles, regardless of In content. The sources of these effects were explored both using DFT calculations and conductivity measurements. Figures **5.5**e, and **S5.2**c,d show the result for the energy barrier from DFT for Li diffusion in a 12.5 % In substituted material, with details provided in SI notes **5.1**. This resulted in

***Table 5.1** Ionic and electronic conductivities measured on cold pressed pellets of various LCP samples. The electronic conductivity was determined using DC measurements in a Au/LCP/Au configuration as per ref. [37]. The ionic conductivities were extracted by fitting the EIS spectra with an equivalent circuit for a mixed conductor (the second conductor corresponding to the electronic conductivity, the extracted value from EIS matched that from DC measurements as expected). Typical patterns of each are shown in Figure **S5.8**. Carbon coated samples are denoted with @C.*

Sample	σ_i (S cm^{-1})	σ_e (S cm^{-1})
$LiCoPO_4$@C	6.9×10^{-7}	5.4×10^{-7}
$Li_{0.999}Co_{0.999}In_{0.001}PO_4$@C	5.2×10^{-7}	7.1×10^{-7}
$Li_{0.99}Co_{0.99}In_{0.01}PO_4$@C	4.1×10^{-7}	1.6×10^{-6}
$Li_{0.975}Co_{0.975}In_{0.025}PO_4$@C	8.1×10^{-7}	1.3×10^{-6}
$Li_{0.95}Co_{0.95}In_{0.05}PO_4$@C	7.5×10^{-7}	2.2×10^{-6}
$Li_{0.9}Co_{0.9}In_{0.1}PO_4$@C	7.7×10^{-7}	2.5×10^{-6}
$Li_{0.85}Co_{0.85}In_{0.15}PO_4$@C	7.2×10^{-7}	1.8×10^{-6}
$LiCoPO_4$	1.2×10^{-7}	4.2×10^{-8}
$Li_{0.9}Co_{0.9}In_{0.1}PO_4$	1.8×10^{-7}	5.5×10^{-8}

4 distinct activation energies, with 3 being smaller than in pure LCP (0.23 – 0.287 eV, vs 0.30 eV in pure LCP). This implies that In only lowers the barrier to Li diffusion near itself and that the 12.5% substitution used in the calculation is insufficient to create an entire diffusion path with lowered barriers. We therefore expect little to no improvement in the ionic diffusivity with In substitution, with the primary benefit being the creation of Li vacancies throughout the channels. Furthermore, the band structure shows no significant changes compared to the undoped such that we expect In-substituted LCP to continue to be electronically insulating (by contrast, the Mo-doped band structure shows defect bands that reduce the band gap as discussed in SI notes **5.2**). The results for the ionic conductivity of the non-carbon coated LCP samples (Table **5.1** based on data in Figure **S5.8**) did show a moderate improvement of about 50 %, consistent with the fact that

the largest barrier to Li diffusion remains 0.30 eV in the DFT calculations such that large gains are not made. Surprisingly though, the electronic conductivity of the carbon-coated samples significantly increased in the indium-substituted samples (by a factor of nearly 5 in the 10% sample, and a factor of 3 in the 1%). Given that the improved conductivities between 0.1 to 1% substitution correlate with the improved capacities in Figure **5.5**c, this strongly suggests that the primary benefit of indium is to improve the electronic conductivity of the carbon coated materials (the electronic conductivities in the uncoated materials do not improve significantly). Thus, we find that indium substitution slightly improves the ionic conductivity within the LCP particles and dramatically increases the electronic conductivity of the carbon-coated materials, giving rise to near theoretical capacities in the 1 – 5 % indium-substitution ranges and the reduced overpotential in Figure **5.4**a,e as compared to the undoped.

Next, the important limitation of poor extended cycling must now be addressed. This motivates the utilization of co-doping in this material: utilize one element to increase energy density (e.g. In) and a second to improve the extended cycling. Systematic co-doping was therefore performed on 5% In, 5% M samples made at 850 °C (the higher temperature being selected due to overall improvement in electrochemistry in the single-substituted samples and higher level of doping obtained based on XRD). The lattice parameter shifts for the In/M co-substituted LCP phases based on XRD data are shown in Figure **S5.9**, and the most common change seen is to expand the *a* lattice and contract *b, c* (the exact opposite of what was found in adding 5% In to the undoped as discussed above). While in the single dopant situation, it was possible to extract the fraction of dopant in the LCP structure, here it is not. There are too many possible compositions of the secondary phases which could contain either dopant or both. The CVs (Figure **S5.10**) show wide variations as was the case in the single-substitution case, and extracted battery performance

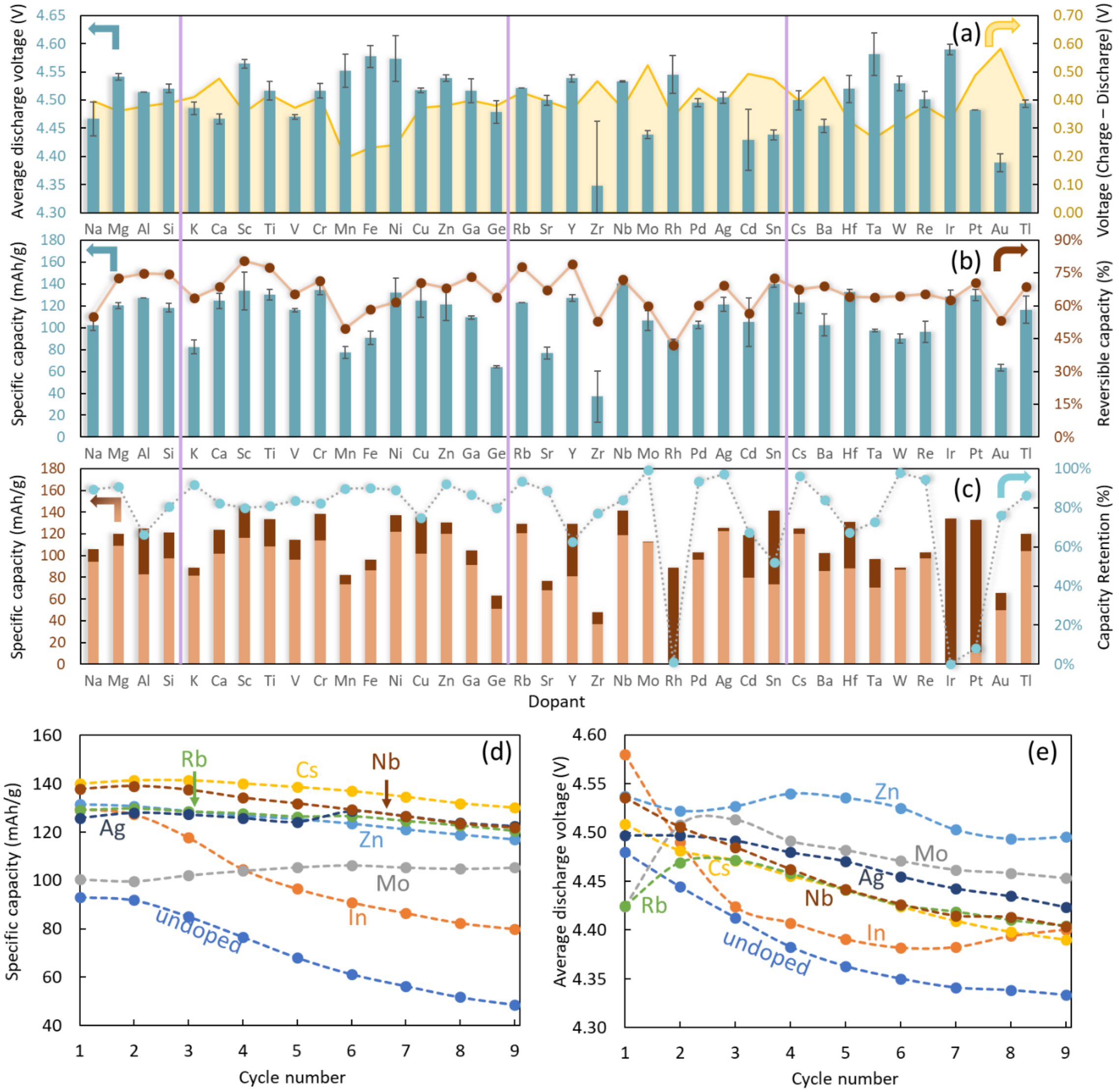

Figure 5.6 *Battery properties extracted for the* $Li_yCo_{0.9}In_{0.05}M_{0.05}PO_4$ *samples. The first cycle average voltages and capacities are shown in (a), (b), respectively. (c) shows capacity retention after 9 cycles, while (d-e) show the capacities and average voltages vs. cycle number for a selection of samples with a particularly high capacity retention. The blue and orange bars in (c) correspond to the 1st and 9th discharge specific capacities, respectively.*

metrics are shown in Figure **5.6**. In the co-substitution case, there is no dramatic improvement in capacities, however there are samples with greatly improved capacity retention. A number of samples retained more than 90 %, and Mo/In co-doped in fact retained 100 % (although with a more moderate capacity of 100 mAh/g). Figures **5.2** and **S5.11** show SEM images of In/Mo co-doped samples, with the morphology being dramatically impacted by the presence of Mo with massive 10-30 micron spherical particles making up the vast majority of the sample. Considering the size of particles, the capacities of 100 mAh/g are a testament to the improved transport properties in the doped samples (undoped particles of about 5-10 microns obtained a capacity of 5 mAh/g in ref.[35]). Given the large particles in the Mo/In co-doped samples, there is less surface area available for electrolyte oxidation in this sample as compared to the others shown in Figure **5.2** where a far greater number of smaller particles make up the electrode. The reduced surface area results in less electrolyte oxidation and this certainly contributes to the improved extended cycling obtained for Mo/In co-doping.

DFT calculations (detailed in SI notes **5.3**) were also performed for a set of dopants to determine the formation energy for Li/Co antisite defects to better understand why some dopants

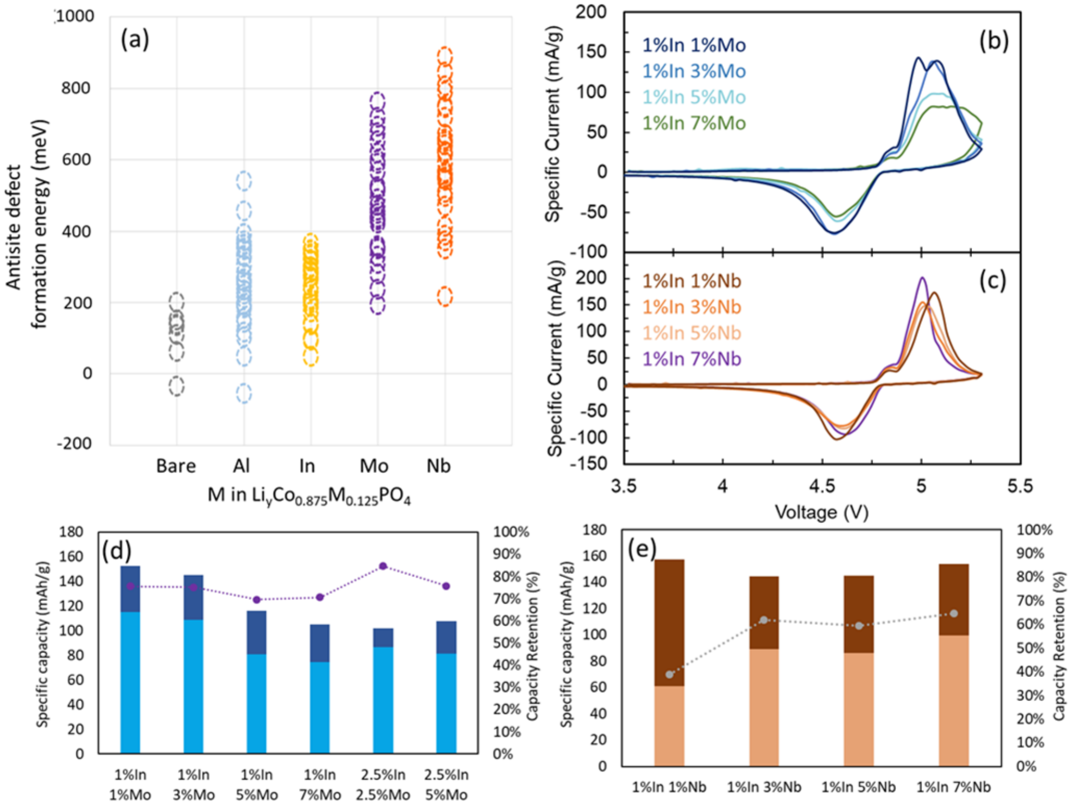

Figure 5.7 *Results of optimization of co-doping with indium. Results of DFT calculations (a) show which dopants are most effective in suppressing Li/Co antisite defects. The first cycles of CVs for various co-doping with either Mo (b) or Nb (c) are shown, while (d,e) show the corresponding capacity retentions after 10 cycles as dots. The dark blue and brown bars are the 1*st *discharge specific capacity while the light blue and brown bars are the 10*th *cycle discharge specific capacity.*

(e.g. Nb) improved the capacity retention, while others like Al did not. Such antisite defects are commonly correlated to poor extended cycling in LCP.[36] Figure **5.7**a shows the results for all possible Li/Co defects in the structures. The undoped and Al doped both show that some defects will form spontaneously (negative formation energy). While In-substitution results in defects requiring energy to form, the energy is small. We attribute the slight improvement in extended cycling in the In single dopant samples (60 % vs 45 % in undoped) to this change in formation energy. By contrast, other substituents such as Mo and Nb result in a dramatic increase in the formation energy. This explains why co-doping was so effective in further improving the extended cycling.

Seeing the dramatic improvement in extended cycling with co-doping, we explored more compositions of the In/Mo and In/Nb co-doped samples to see if the two key effects (improved capacity and extended cycling) could be optimized simultaneously. The best results were found to be for In/Mo as shown in Figure **5.7**d,e. For very moderate substitution levels (1% of each of In and Mo), capacities as high as 150 mAh/g were obtained along with a well improved retention of 75 % (compared to 60 % in In-single dopant, or 50 % in pure LCP), again under very harsh cycling conditions (CV up to 5.3 V). By contrast, In/Nb showed a retention that was not improved over the singly In-doped samples. We also confirm that the high performance for In/Mo co-doping is maintained when cycled under galvanostatic conditions in a coin cell. Figure **S5.18** and Table **S5.4** show that both 1%/1% and 5%/5% co-doped samples have first discharge capacities (150 and 80 mAh/g, respectively) in good agreement with the high-throughput CV work reported above (152 and 100 mAh/g, respectively). Similarly, the extended cycling is considerably better in the 5%/5% sample as compared to the 1%/1% sample (e.g. 98% vs 89% on the second cycle, and 85% vs 70% after 5 cycles), again consistent with the HT voltammetry. Though further work is needed to develop bulk synthesis of these materials and couple them to improved electrolytes, the results clearly indicate that the optimized co-doped materials show improved performance under galvanostatic conditions as well as cyclic voltammetry.

5.5 Conclusions

This work was focused on improving the performance of a very challenging high voltage cathode material for Li-ion batteries: $LiCoPO_4$ with a peak potential of about 4.8 V *vs*. Li. A total of 1300 samples were studied, with 263 distinct substituted samples with numerous duplicates to ensure reproducibility (e.g. the 10% In-doped samples had 11 duplicates and yielded a low standard error of about 3 mAh/g on an average capacity of 133 mAh/g). This work clearly demonstrates the extent to which the design of advanced battery cathodes can be accelerated with the use of high-throughput experimental screening to study the impact of composition and synthesis conditions on a wide variety of properties of importance for battery performance. Herein, certain electrochemically inactive dopants were found to dramatically improve the first cycle capacity by improving both ionic and electronic conductivity in carbon-coated materials. Co-doping was found to greatly improve the extended cycling by both preventing antisite defects and producing larger particles thereby minimizing the surface area per unit mass of cathode where electrolyte decomposition occurs at the very high potentials utilized here. The improvement from 95 mAh/g, 43 % retention in unsubstituted LCP to 150 mAh/g with 75 % retention with only 2% substitution of the cobalt with In/Mo is truly remarkable. This is especially noteworthy when one considers that all materials were cycled under the same harsh conditions of cyclic voltammetry up to 5.3 V (i.e. all samples spent 3 h above 5 V every cycle), such that improved extended cycling is truly significant. The dramatic improvement with In/Mo co-substitution was attributed to numerous factors: (i) improved Li diffusion with the addition of In, (ii) larger particles with the addition of

Mo, (iii) improved electronic conductivity in the carbon-coated material with the addition of In, and (iv) suppression of Li/Co antisite defects by the addition of both In and Mo. Given the wide variety of properties manipulated through the substitutions (morphology, defect suppression, lattice distortion to enable Li diffusion, nature of C-coating changing the electronic conductivity), high-throughput experiments are not only shown to be useful but in fact are necessary to design an optimum material. This work not only produces a novel state-of-the-art material (In/Mo co-doped LCP) despite decades of previous work on LCP, but also serves as a template for how to accelerate the design of cathodes for advanced batteries using high-throughput experimentation, complemented with traditional experimental and computational methods.

5.6 Acknowledgments

This work was primarily funded by the Samsung Advanced Institute of Technology and additionally funded by NSERC under the auspices of a discovery grant and the Canadian Foundation for Innovation.

5.7 Supporting information

Table S5.1 *Phase determination from XRD for samples made at 750 ℃ in air prior to carbon coating. %mol represents the molar fraction of each phase, while % substituted is the mount of dopant in LCP based on the phase fractions, and unidentified is the ratio of the height of the largest unidentified peak to that of the largest LCP peak.*

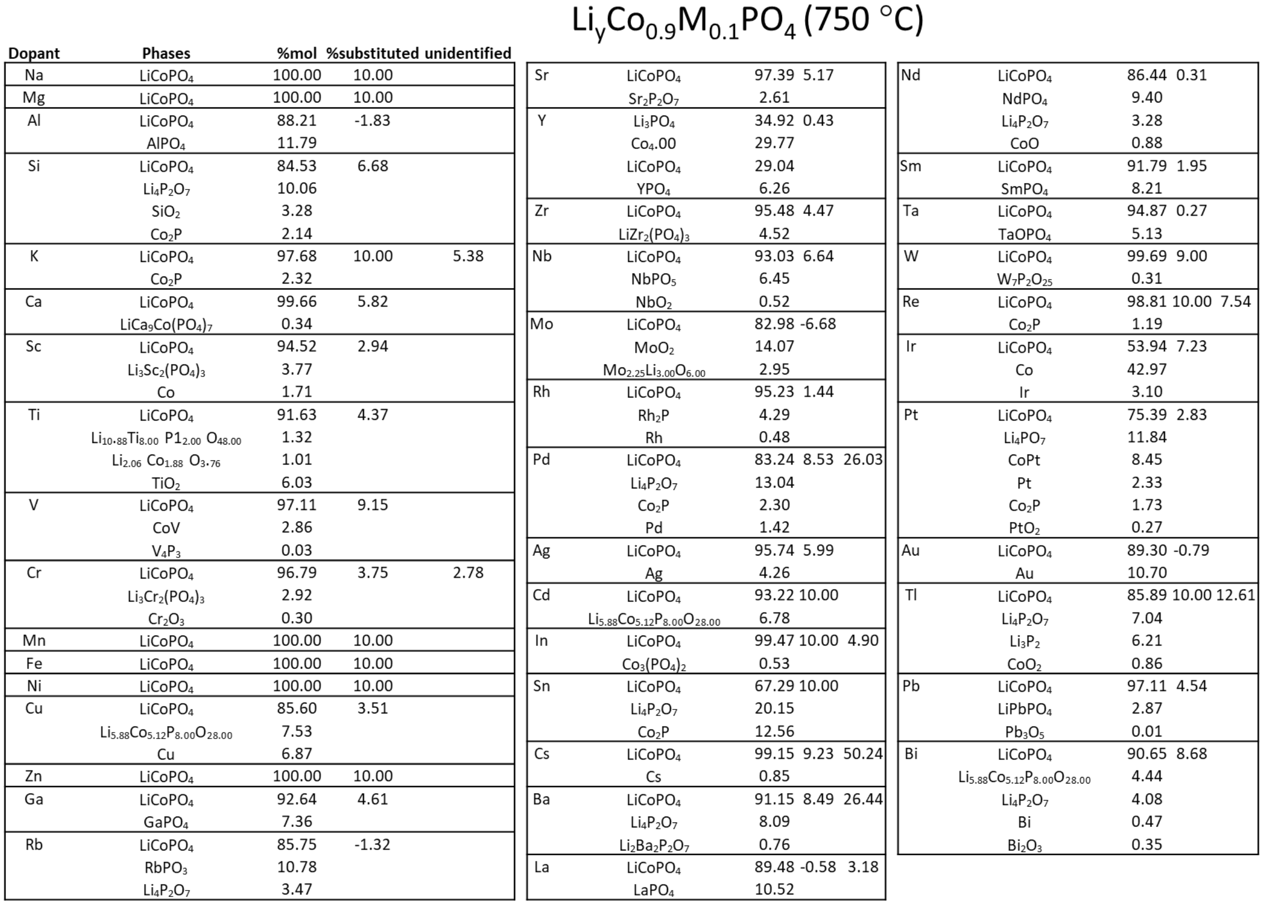

$Li_yCo_{0.9}M_{0.1}PO_4$ (750 °C)

Dopant	Phases	%mol	%substituted	unidentified
Na	$LiCoPO_4$	100.00	10.00	
Mg	$LiCoPO_4$	100.00	10.00	
Al	$LiCoPO_4$	88.21	-1.83	
	$AlPO_4$	11.79		
Si	$LiCoPO_4$	84.53	6.68	
	$Li_4P_2O_7$	10.06		
	SiO_2	3.28		
	Co_2P	2.14		
K	$LiCoPO_4$	97.68	10.00	5.38
	Co_2P	2.32		
Ca	$LiCoPO_4$	99.66	5.82	
	$LiCa_9Co(PO_4)_7$	0.34		
Sc	$LiCoPO_4$	94.52	2.94	
	$Li_3Sc_2(PO_4)_3$	3.77		
	Co	1.71		
Ti	$LiCoPO_4$	91.63	4.37	
	$Li_{10.88}Ti_{8.00}$ $P1_{2.00}$ $O_{48.00}$	1.32		
	$Li_{2.06}$ $Co_{1.88}$ $O_{3.76}$	1.01		
	TiO_2	6.03		
V	$LiCoPO_4$	97.11	9.15	
	CoV	2.86		
	V_4P_3	0.03		
Cr	$LiCoPO_4$	96.79	3.75	2.78
	$Li_3Cr_2(PO_4)_3$	2.92		
	Cr_2O_3	0.30		
Mn	$LiCoPO_4$	100.00	10.00	
Fe	$LiCoPO_4$	100.00	10.00	
Ni	$LiCoPO_4$	100.00	10.00	
Cu	$LiCoPO_4$	85.60	3.51	
	$Li_{5.88}Co_{5.12}P_{8.00}O_{28.00}$	7.53		
	Cu	6.87		
Zn	$LiCoPO_4$	100.00	10.00	
Ga	$LiCoPO_4$	92.64	4.61	
	$GaPO_4$	7.36		
Rb	$LiCoPO_4$	85.75	-1.32	
	$RbPO_3$	10.78		
	$Li_4P_2O_7$	3.47		
Sr	$LiCoPO_4$	97.39	5.17	
	$Sr_2P_2O_7$	2.61		
Y	Li_3PO_4	34.92	0.43	
	Co_4.00	29.77		
	$LiCoPO_4$	29.04		
	YPO_4	6.26		
Zr	$LiCoPO_4$	95.48	4.47	
	$LiZr_2(PO_4)_3$	4.52		
Nb	$LiCoPO_4$	93.03	6.64	
	$NbPO_5$	6.45		
	NbO_2	0.52		
Mo	$LiCoPO_4$	82.98	-6.68	
	MoO_2	14.07		
	$Mo_{2.25}Li_{3.00}O_{6.00}$	2.95		
Rh	$LiCoPO_4$	95.23	1.44	
	Rh_2P	4.29		
	Rh	0.48		
Pd	$LiCoPO_4$	83.24	8.53	26.03
	$Li_4P_2O_7$	13.04		
	Co_2P	2.30		
	Pd	1.42		
Ag	$LiCoPO_4$	95.74	5.99	
	Ag	4.26		
Cd	$LiCoPO_4$	93.22	10.00	
	$Li_{5.88}Co_{5.12}P_{8.00}O_{28.00}$	6.78		
In	$LiCoPO_4$	99.47	10.00	4.90
	$Co_3(PO_4)_2$	0.53		
Sn	$LiCoPO_4$	67.29	10.00	
	$Li_4P_2O_7$	20.15		
	Co_2P	12.56		
Cs	$LiCoPO_4$	99.15	9.23	50.24
	Cs	0.85		
Ba	$LiCoPO_4$	91.15	8.49	26.44
	$Li_4P_2O_7$	8.09		
	$Li_2Ba_2P_2O_7$	0.76		
La	$LiCoPO_4$	89.48	-0.58	3.18
	$LaPO_4$	10.52		
Nd	$LiCoPO_4$	86.44	0.31	
	$NdPO_4$	9.40		
	$Li_4P_2O_7$	3.28		
	CoO	0.88		
Sm	$LiCoPO_4$	91.79	1.95	
	$SmPO_4$	8.21		
Ta	$LiCoPO_4$	94.87	0.27	
	$TaOPO_4$	5.13		
W	$LiCoPO_4$	99.69	9.00	
	$W_7P_2O_{25}$	0.31		
Re	$LiCoPO_4$	98.81	10.00	7.54
	Co_2P	1.19		
Ir	$LiCoPO_4$	53.94	7.23	
	Co	42.97		
	Ir	3.10		
Pt	$LiCoPO_4$	75.39	2.83	
	Li_4PO_7	11.84		
	CoPt	8.45		
	Pt	2.33		
	Co_2P	1.73		
	PtO_2	0.27		
Au	$LiCoPO_4$	89.30	-0.79	
	Au	10.70		
Tl	$LiCoPO_4$	85.89	10.00	12.61
	$Li_4P_2O_7$	7.04		
	Li_3P_2	6.21		
	CoO_2	0.86		
Pb	$LiCoPO_4$	97.11	4.54	
	$LiPbPO_4$	2.87		
	Pb_3O_5	0.01		
Bi	$LiCoPO_4$	90.65	8.68	
	$Li_{5.88}Co_{5.12}P_{8.00}O_{28.00}$	4.44		
	$Li_4P_2O_7$	4.08		
	Bi	0.47		
	Bi_2O_3	0.35		

Table S5.2 *Phase determination from XRD for samples made at 850 ℃ in air prior to carbon coating. %mol represents the molar fraction of each phase, while % substituted is the amount of dopant in LCP based on the phase fractions, and unidentified is the ratio of the height of the largest unidentified peak to that of the largest LCP peak.*

$Li_yCo_{0.9}M_{0.1}PO_4$ (850 °C)

Dopant	Formula	%mol	%substituted	unidentified
Na	$LiCOPO_4$	93.94	10.00	
	Li_3PO_4	3.93		
	Co	2.13		
Mg	$LiCoPO_4$	100.00	10.00	
Al	$LiCoPO_4$	80.05	0.71	
	$AlPO_4$	8.61		
	Li_3PO_4	7.26		
	Co	4.07		
K	$LiCoPO_4$	87.40	10.00	7.05
	Li_3PO_4	12.60		
Ca	$LiCoPO_4$	98.63	8.78	
	$LiCa_9Co(PO_4)_7$	1.37		
Sc	$LiCoPO_4$	96.68	3.81	5.28
Sc	$Li_3Sc_2(PO)_3$	3.32		
Ti	$LiCoPO_4$	93.77	3.77	
	TiO_2	2.19		
	$LiTiPO_5$	4.04		
V	$LiCoPO_4$	100.00	10.00	3.67
Cr	$LiCoPO_4$	99.15	8.32	2.90
	Cr_2O_3	0.85		
Mn	$LiCoPO_4$	97.32	10.00	
	$Co_4.00$	2.68		
Fe	$LiCoPO_4$	100.00	10.00	2.36
Ni	$LiCoPO_4$	95.47	5.67	
	CoNiP	4.53		
Cu	$LiCoPO_4$	85.54	-0.95	
	Cu	11.76		
	$Li_{5.88}Co_{5.12}P_{8.00}O_{28.00}$	1.50		
	Co_2P	1.20		
Zn	$LiCoPO_4$	100.00	10.00	
Ga	$LiCoPO_4$	97.85	7.85	
	$GaPO_4$	2.15		
Rb	$LiCOPO_4$	90.31	1.89	
Rb	$RbPO_3$	8.08		
Rb	Co	1.61		
Sr	$LiCoPO_4$	100.00	10.00	
Y	$LiCoPO_4$	90.42	0.42	
	YPO_4	9.58		
Zr	$LiCoPO_4$	98.28	6.85	
	$LiZr_2(PO_4)_3$	1.72		
Nb	$LiCoPO_4$	98.12	8.19	
	$CoNb_2O_8$	1.88		
Mo	$LiCoPO_4$	93.25	-3.83	
	$Co_2Mo_3O_8$	4.89		
	MoO_3	1.86		
Rh	$LiCoPO_4$	95.39	5.39	56.17
	Rh	4.61		
Pd	$LiCoPO_4$	94.14	7.14	11.06
	Co_2P	2.66		
	Pd	1.93		
	CoO	1.27		
Ag	$LiCOPO_4$	92.36	2.33	
	Ag	7.64		
Cd	$LiCoPO_4$	100.00	10.00	6.28
In	$LiCoPO_4$	99.49	9.54	5.39
	Co_3O_4	0.27		
	In_2O_3	0.23		
Sn	$LiCoPO_4$	38.39	10.00	37.31
	Co_2P	36.90		
	Li_3PO_4	24.72		
Cs	$LiCoPO_4$	96.61	9.29	28.21
Cs	Co	2.68		
Cs	Cs	0.71		
Ba	$LiCoPO_4$	85.45	9.48	
	$LiCo_2P_3O_{10}$	7.91		
	$Co_3(PO_4)_2$	6.02		
	BaO	0.62		
La	$LiCoPO_4$	89.63	-0.37	5.51
	$LaPO_4$	10.37		
Nd	$LiCoPO_4$	90.06	0.06	
	$NdPO_4$	9.94		
Sm	$LiCoPO_4$	89.85	-0.15	
	$SmPO_4$	10.15		
Ta	$LiCoPO_4$	75.12	3.06	
	Li_3PO_4	19.28		
	$TaPO_5$	5.60		
W	$LiCoPO_4$	98.92	10.00	8.55
	Co_2P	1.08		
Re	$LiCoPO_4$	100.00	10.00	
Ir	$LiCoPO_4$	69.89	10.00	87.98
	Co_2P	30.11		
Pt	$LiCoPO_4$	91.79	1.79	
	Pt	8.21		
Au	$LiCoPO_4$	89.04	-0.96	11.69
	Au	10.96		
Tl	$LiCoPO_4$	96.04	10.00	33.92
	$LiCO_3O_4$	0.99		
	Co	2.96		
Pb	$LiCoPO_4$	97.14	8.12	12.13
	Pb	2.35		
	Pb_4O	0.51		
Bi	$LiCoPO_4$	99.20	9.10	5.87
	Bi	0.70		
	Bi_2O_3	0.10		

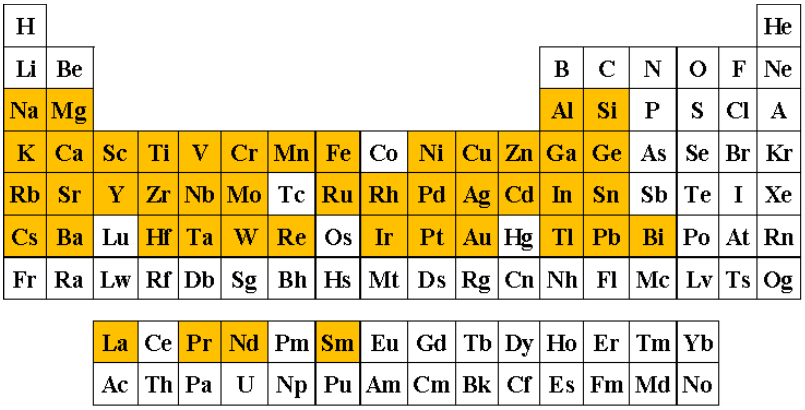

H																	He
Li	Be											B	C	N	O	F	Ne
Na	**Mg**											**Al**	**Si**	P	S	Cl	A
K	**Ca**	**Sc**	**Ti**	**V**	**Cr**	**Mn**	**Fe**	Co	**Ni**	**Cu**	**Zn**	**Ga**	**Ge**	As	Se	Br	Kr
Rb	**Sr**	**Y**	**Zr**	**Nb**	**Mo**	Tc	**Ru**	**Rh**	**Pd**	**Ag**	**Cd**	**In**	**Sn**	Sb	Te	I	Xe
Cs	**Ba**	Lu	**Hf**	**Ta**	**W**	**Re**	Os	**Ir**	**Pt**	**Au**	Hg	**Tl**	**Pb**	**Bi**	Po	At	Rn
Fr	Ra	Lw	Rf	Db	Sg	Bh	Hs	Mt	Ds	Rg	Cn	Nh	Fl	Mc	Lv	Ts	Og
		La	Ce	**Pr**	**Nd**	Pm	**Sm**	Eu	Gd	Tb	Dy	Ho	Er	Tm	Yb		
		Ac	Th	Pa	U	Np	Pu	Am	Cm	Bk	Cf	Es	Fm	Md	No		

Figure S5.1 *The periodic table with dopants utilized herein highlighted in orange. Li, Co, P and O are also present in all samples.*

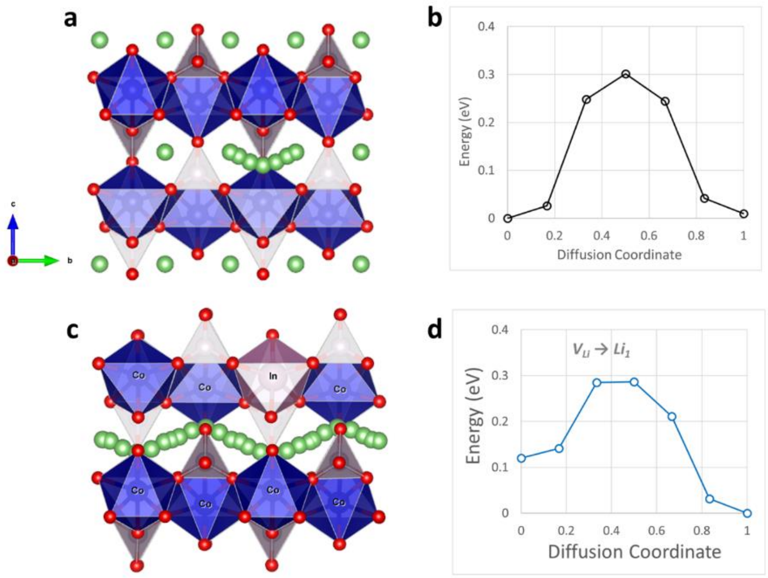

Figure S5.2 *Lithium diffusion barrier for bare LCP. (a) Li trajectories according to NEB calculations for bare LCP. Green, blue, gray and red spheres represent Li, Co, P and O atoms, respectively. (b) Calculated activation barriers for lithium diffusion along the b axis. (c) Li trajectory in the In-doped LCP. (d) Calculated activation barriers for lithium diffusion from site Li1 to VLi (other 3 barriers are including in Figure* ***5.5*** *in the main text).*

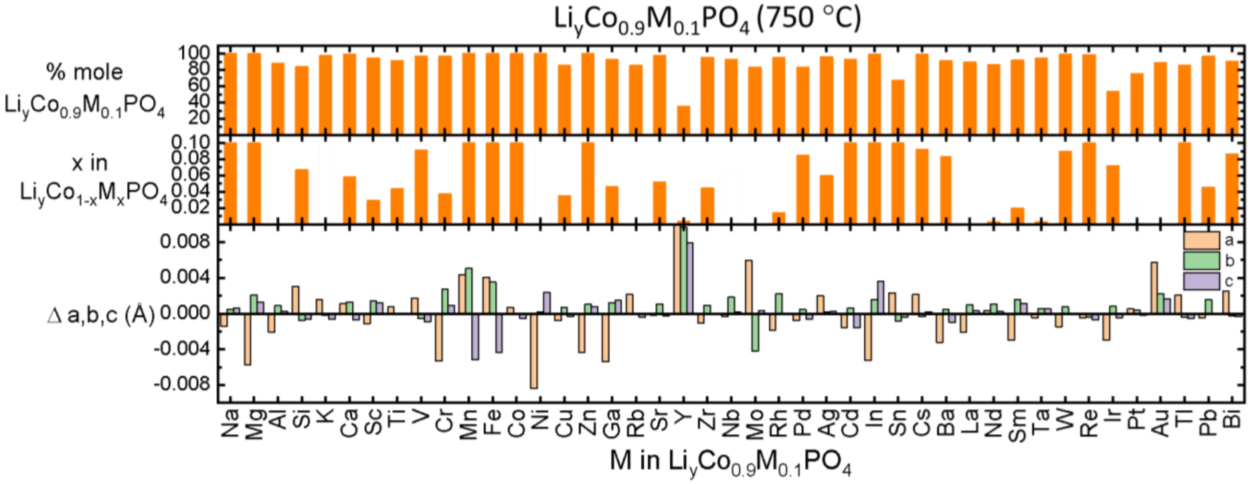

Figure S5.3 *Extracted parameters from Rietveld fitting of XRD patterns. % mole and x are obtained from Table* ***S5.1****, while Δa,b,c represent shifts in lattice parameters compared to those of the undoped LCP.*

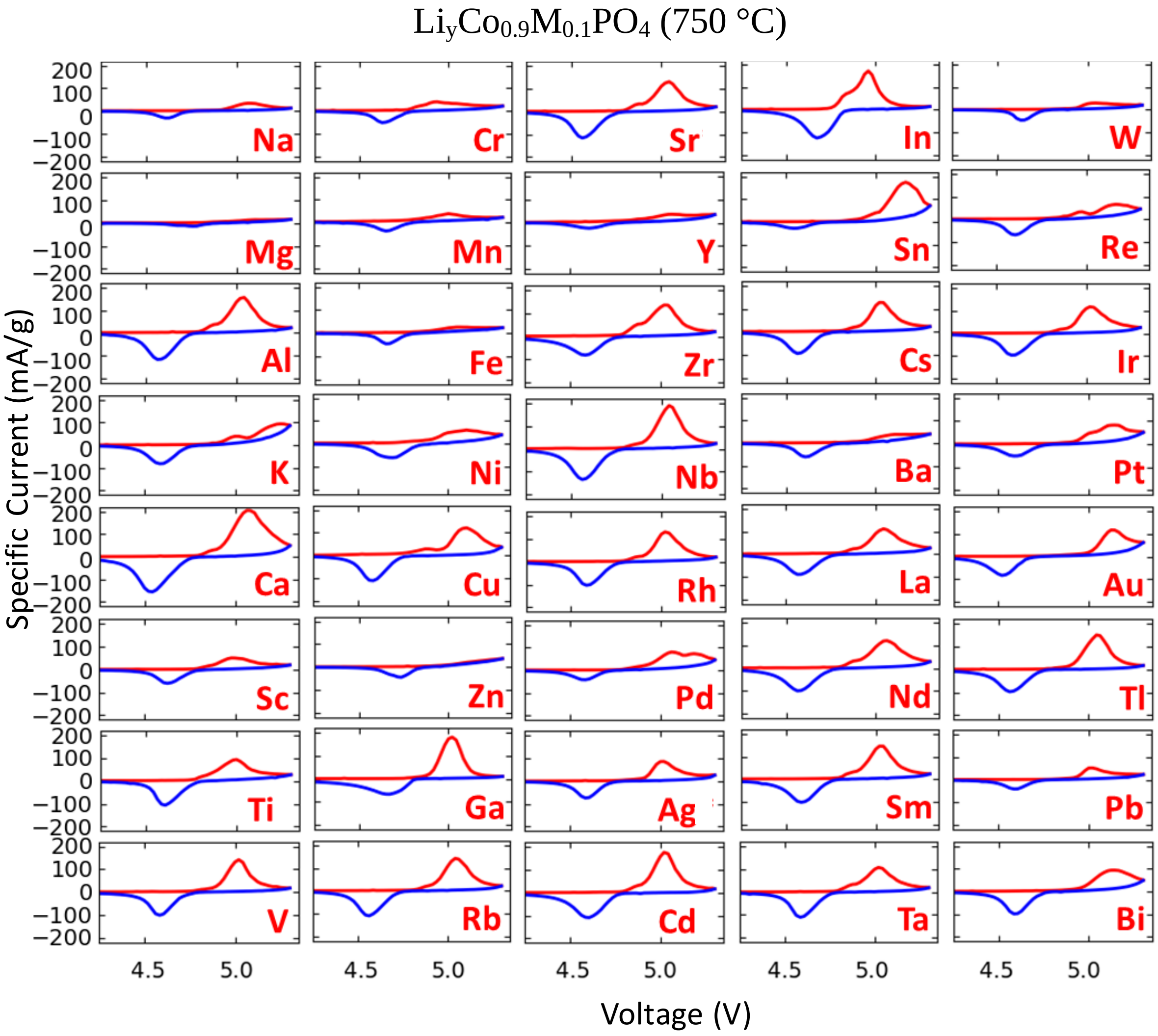
$Li_yCo_{0.9}M_{0.1}PO_4$ (750 °C)

Figure S5.4 *First cycle CVs for single dopant LCP samples prepared by heating to 750 °C prior to carbon coating. The extracted electrochemical properties are presented in Figure* ***S5.6****.*

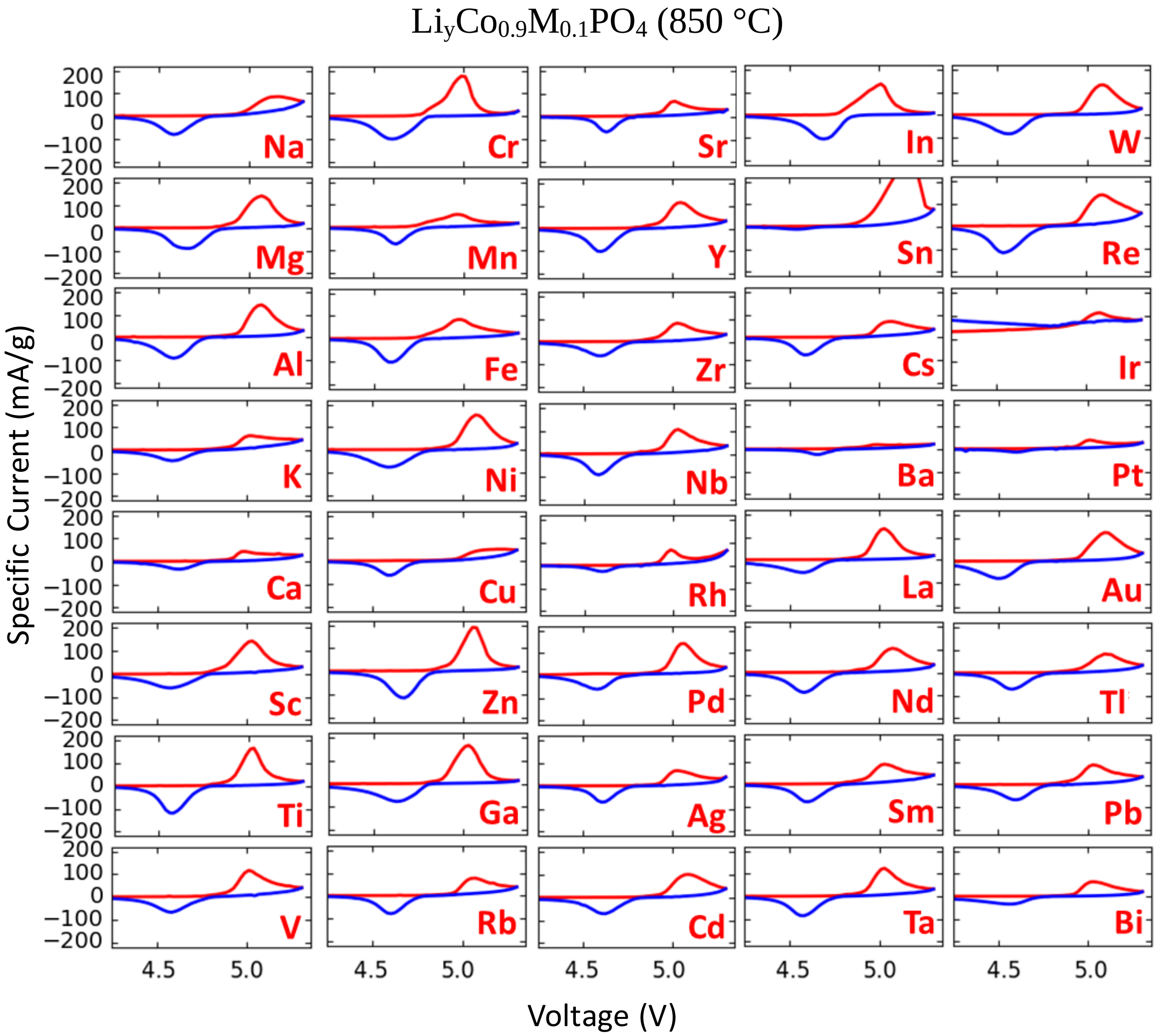

***Figure S5.5** First cycle CVs for single dopant LCP samples prepared by heating to 850 ℃ prior to carbon coating. The extracted electrochemical properties are presented in Figure **5.4i-k**.*

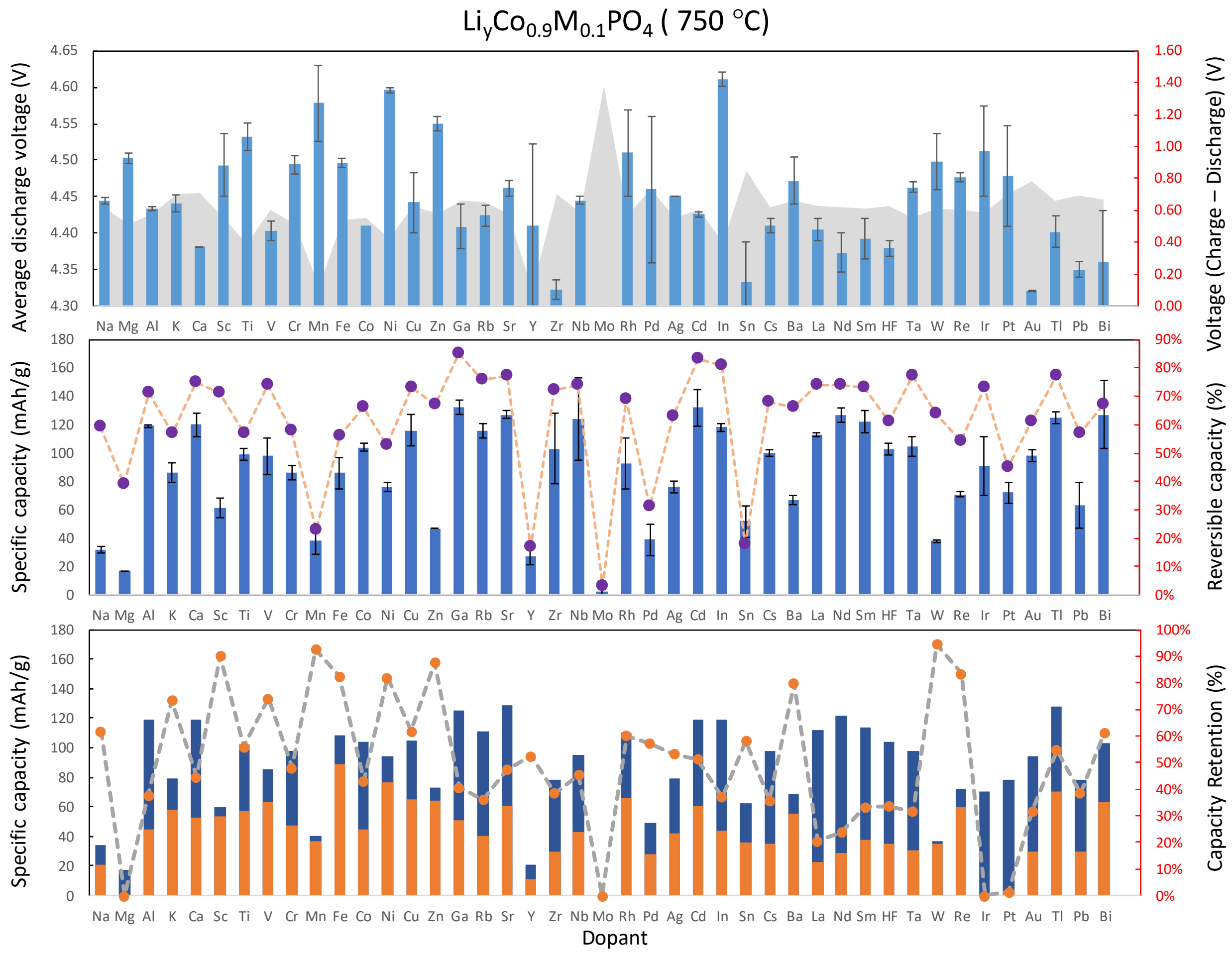

***Figure S5.6** Electrochemical properties extracted from the CVs of the single dopant LCP samples prepared at 750 ℃ prior to carbon coating (first cycle shown in Figure **S5.4**). The properties extracted for the first cycle. In the top panel, the gray shadow represents the overpotential, while the blue bars represent the average discharge voltage. The middle panel displays violet dots indicating the retention after 10 cycles, while the blue bars represent the discharge specific capacity. In the bottom panel, the orange dots correspond to the capacity retention after 10 cycles, and the blue and orange bars represent the discharge specific capacity for the 1st and 10th cycles, respectively.*

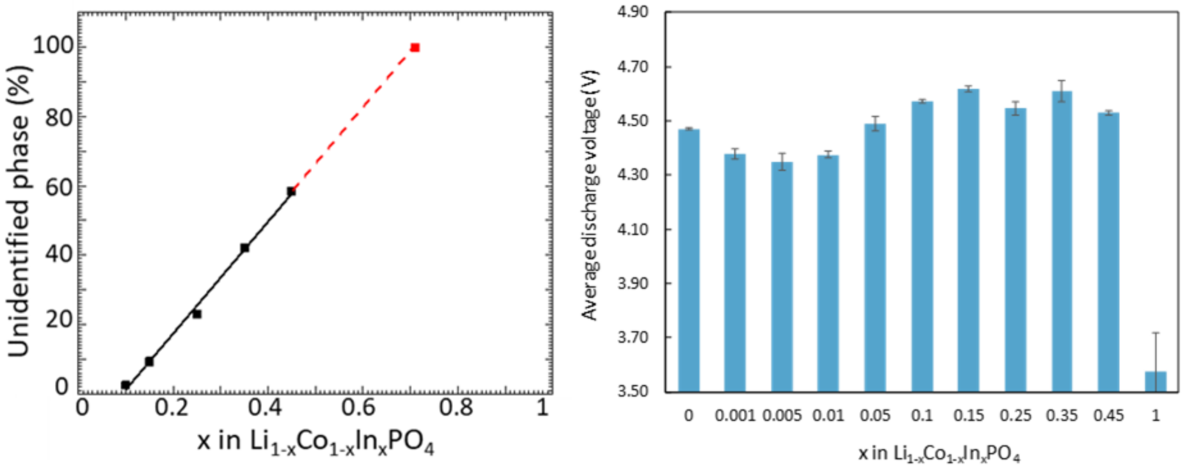

Figure S5.7 *Left: fraction of unidentified phase in In-doped LCP samples which is determined by calculating the ratio of the highest intensity XRD peaks of the LCP and the unidentified phase. The % extrapolates to zero at 9 % substitution. Right: average first cycle discharge voltage for the In-doped LCP samples with various doping levels.*

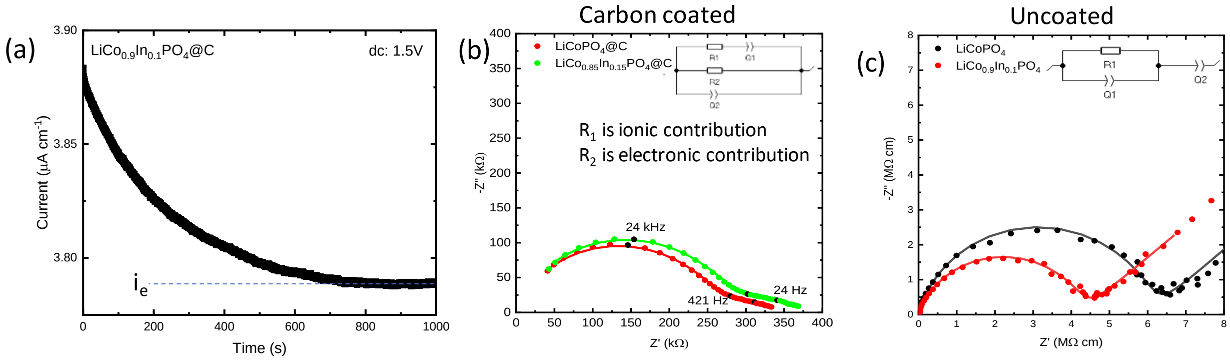

Figure S5.8*(a) DC conductivity measurement on the 10 % indium doped carbon-coated LCP sample indicating the current selected to calculate the electronic conductivity (i_e). (b) EIS spectra for two carbon coated LCP samples along with the equivalent circuit used to extract both electronic and ionic conductivities. (c) EIS spectra on two uncoated LCP samples along with the equivalent circuit used to extract the ionic conductivity. The electronic conductivities from DC measurements and the ionic conductivities from EIS are included in Table* ***5.1****. The electronic conductivities from EIS were always consistent with those from the DC measurements.*

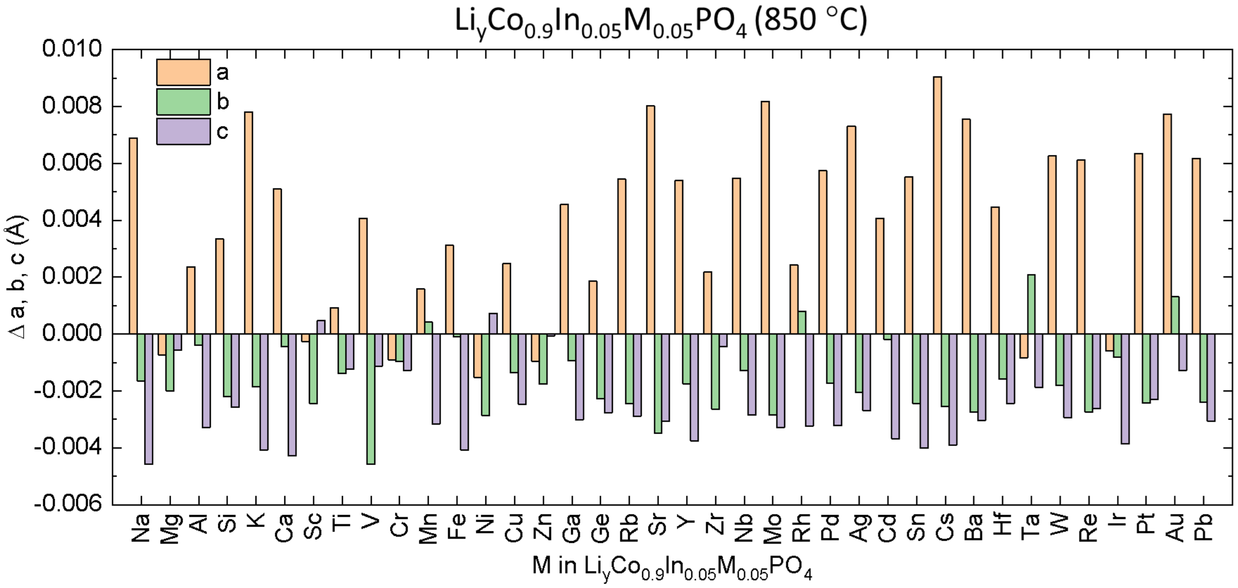

Figure S5.9 *Shifts in lattice parameters for the In/M co-doped samples with respect to the* $LiCo_{0.95}In_{0.05}PO_4$.

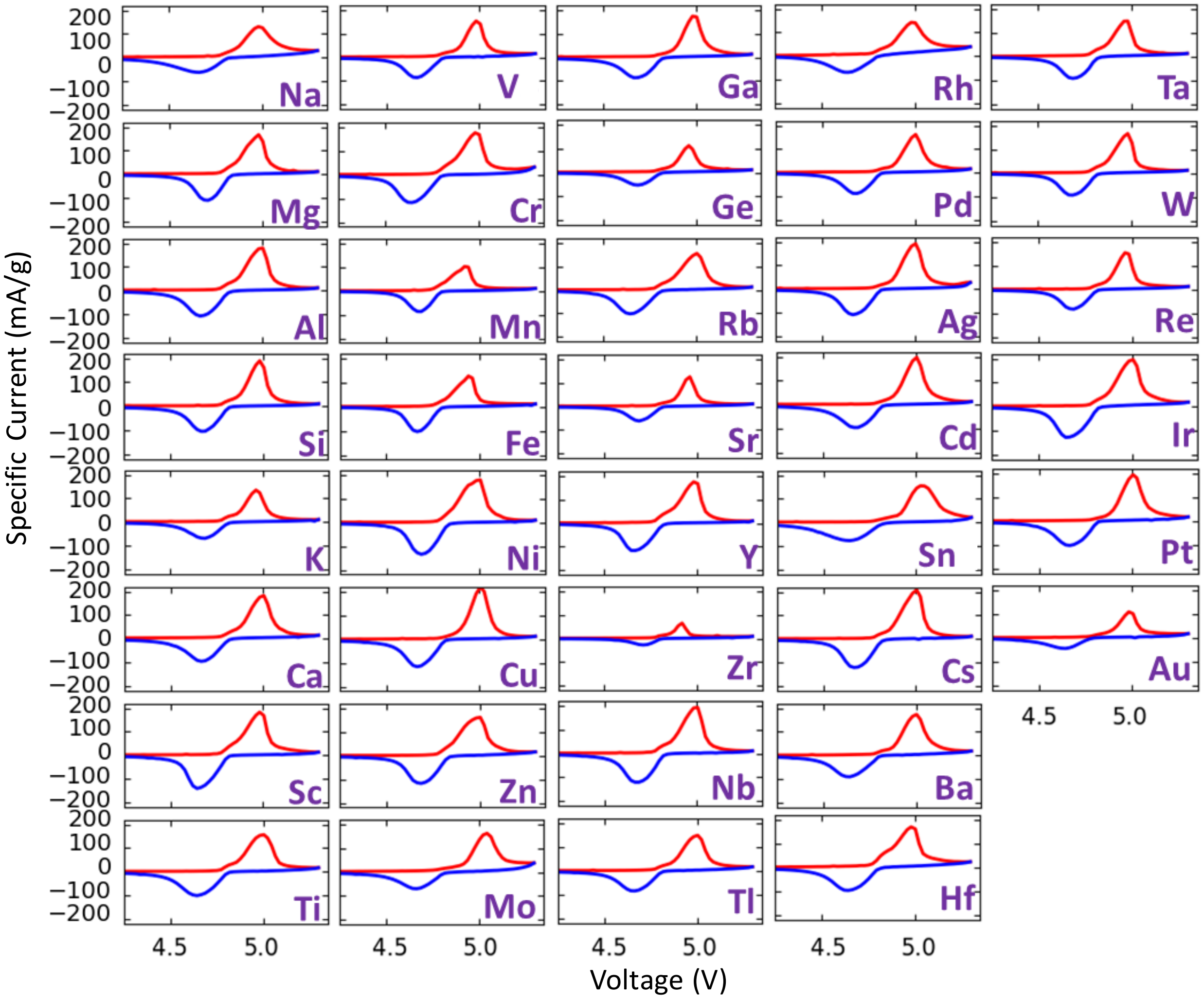

$Li_yCo_{0.9}In_{0.05}M_{0.05}PO_4$ (850 °C)

Figure S5.10 *First cycle CVs for the co-doped LCP samples with 5% In, and 5% M substituted for Co. All samples were synthesized at 850 ℃ in air prior to carbon coating. The extracted electrochemical properties are presented in* ***Figure 5.6a-c****.*

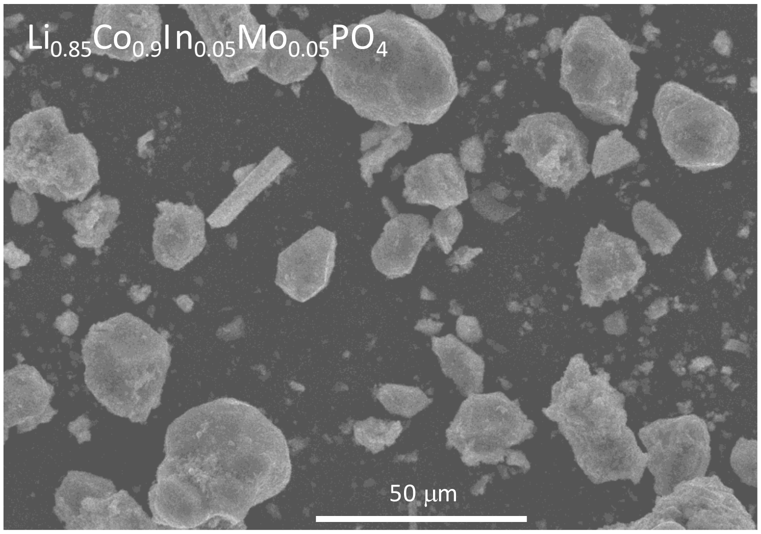

Figure S5.11 *SEM image of the In/Mo co-doped LCP sample showing the variability in the particle sizes.*

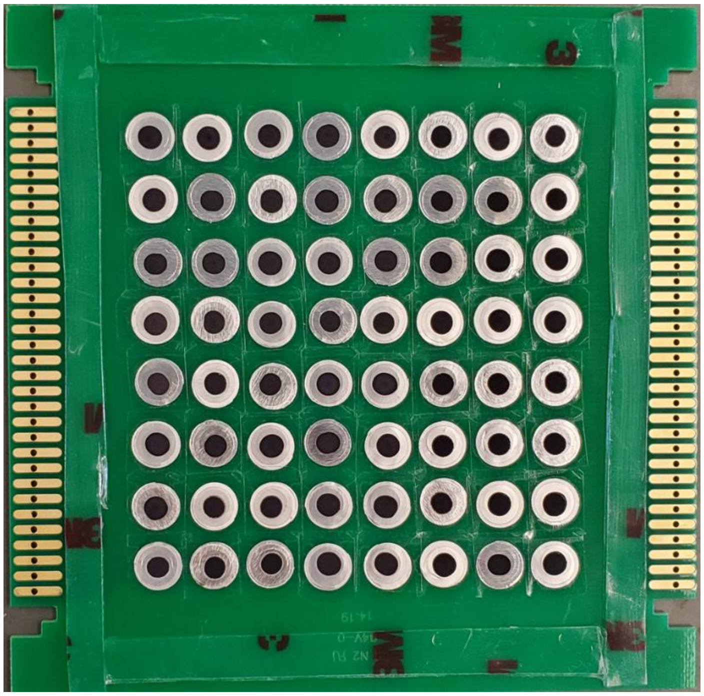

Figure S5.12 *Picture of the prepared electrodes on the printed circuit board with aluminum foil covering each contact.*

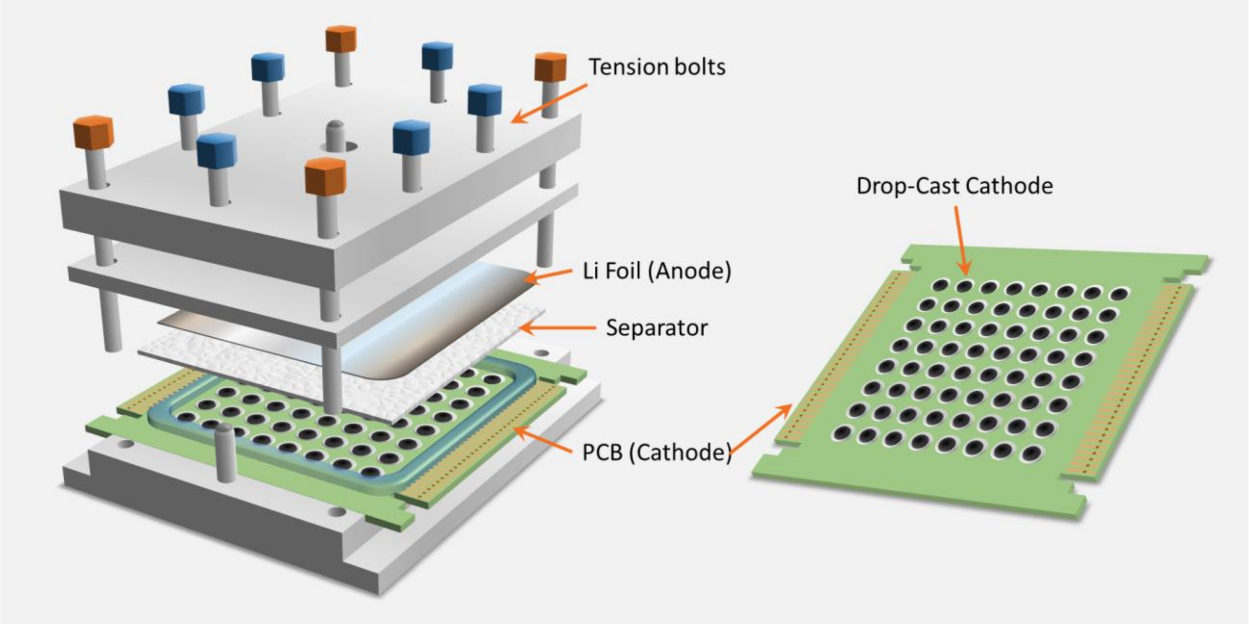

Figure S5.13 *Schematic of the combinatorial electrochemical cell used throughout. The printed circuit board (PCB) has 64 electrodes drop cast onto it, and the cell is assembled with a single lithium foil as counter/reference electrode.*

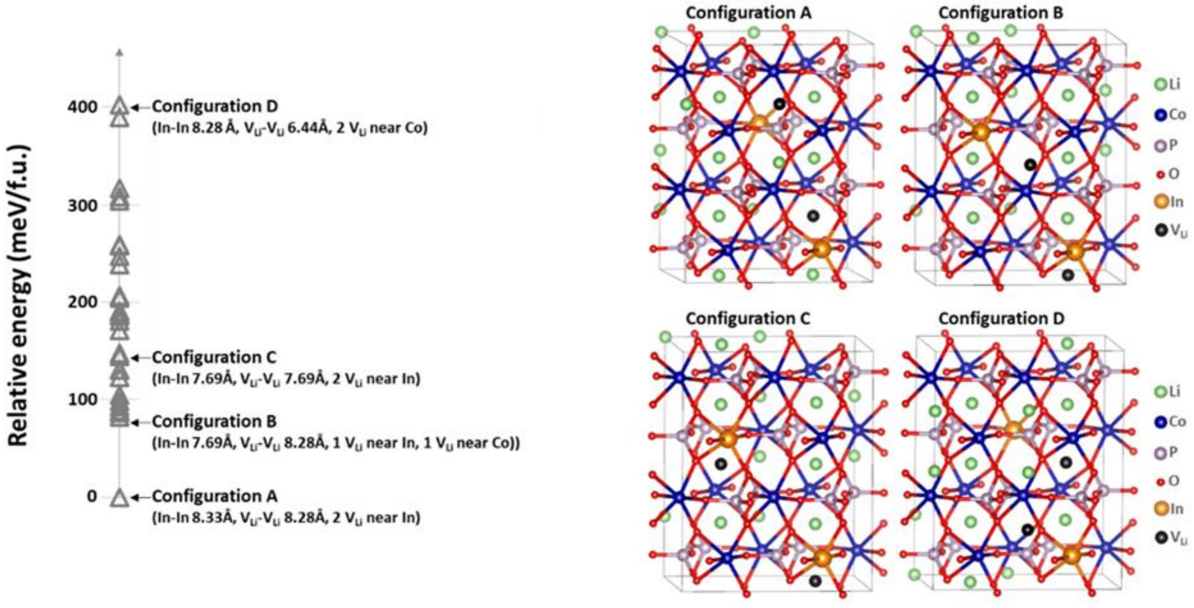

Figure S5.14 *Formation energies of 30 configurations for In-doped LCP ($Li_{14}Co_{14}In_2P_{16}O_{64}$).*

Additional notes:

SI notes 5.1 *Li-Ion Mobility of In-doped LCP*

The key advantage of replacing Co^{2+} with In^{3+} in LCP would be the generation of Li vacancies (V_{Li}). Theoretically, the initial structure of LCP (fully lithiated) does not have the V_{Li}. This means that it is difficult for Li ion to migrate, implying a low Li ion conductivity at the discharged state. On the other hand, for In-doped LCP, the V_{Li} can be created by the substitution of In^{3+} for Co^{2+} in LCP because the Li deficiency is required for the charge compensation. The Li^+/V_{Li} and Co^{2+}/In^{3+} configurations of the In-doped LCP creates many different local environment. Therefore, the formation energies of the In-doped LCP were calculated to explore the energetically favorable configurations for Li^+, V_{Li}, Co^{2+} and In^{3+}. In addition, Li ions must be able to pass through V_{Li} under the reasonable activation barrier to contribute to the Li ion conduction. Thus, the nudged elastic band (NEB) calculations were also performed to investigate the Li conduction pathway and diffusion barrier of the In-doped LCP.

The supercell of $Li_{14}Co_{14}In_2P_{16}O_{64}$ (12.5% In-doped LCP), which could imitate the experimentally-observed structure and composition (10% In-doped), was derived from $Li_{16}Co_{16}P_{16}O_{64}$ (LCP) by replacing two Co^{2+} by two In^{3+} in Co sites and two Li^+ by two V_{Li} in Li sites, resulting in various configurations of the Co^{2+}/In^{3+} and Li^+/V_{Li}. Except the symmetrically identical structures among all configurations, the formation energies for 30 configurations of the $Li_{14}Co_{14}In_2P_{16}O_{64}$ were calculated (Figure **S5.14**). The most stable structure (Configuration A) had three features; (1) the longest distance (8.33 Å) between two In^{3+} ions, (2) the longest distance (8.28 Å) between two V_{Li} (3) V_{Li} (octahedron) sharing the edge with the adjacent In-centered octahedron within the formula unit. Meanwhile, in the case of the shorter distance (7.69 Å) between two In^{3+} ions (Configuration B), its formation energy increased up to 82 meV, assuming that the formation energy of the most stable structure was 0 meV. When shortening the distances of both In^{3+} to In^{3+} (7.69 Å) and V_{Li} to V_{Li} (7.69 Å), its formation energy went up to 130 meV although two V_{Li} were located near In^{3+} (Configuration C). The instability of 402 meV much higher than the stable configuration was obtained at the shorter distance (6.44 Å) between two V_{Li} sharing the edge with the adjacent Co-octahedron despite the long distance (8.28 Å) between two In^{3+} ions (Configuration D). Based on the above calculation results, two In^{3+} dopants preferred to be away from each other as far as they can within a formula unit, whereas the two V_{Li} were highly likely to be formed right next to In^{3+} rather than Co^{2+}, as the distance of V_{Li} to V_{Li} was maximized. Thus, the electrostatic force is concluded to be the dominant factor in determining the location of the In^{3+} dopant and V_{Li} in the In-doped LCP structure. Given a difference of 82 meV between the lowest (Configuration A) and the second lowest (Configuration B) formation energy, Configuration A was selected for the further calculations.

Figures **5.5**e and **S5.2**c,d show the Li ion trajectories along the migration pathways in $Li_{14}Co_{14}In_2P_{16}O_{64}$ (Configuration A) and their activation energies. Li ions repeatedly can hop from *Li1* to *Li2*, *Li2* to *Li3*, *Li3* to V_{Li} and V_{Li} to *Li1* site in $Li_{14}Co_{14}In_2P_{16}O_{64}$ (Figure **5.5**e). The Li migration pathway of *Li1–Li2* was located away from the In^{3+} dopant, implying the little effect of In^{3+} on the Li diffusion. The activation barrier for *Li1–Li2* was 307 meV in the In-doped LCP (Figure **5.5**e). This is consistent with the activation barrier of 302 meV for the Li diffusion in the undoped LCP (Figure **S5.2**a,b). The high similarity between the barriers for *Li1–Li2* and undoped LCP might indicate that the In^{3+} dopant much less affected the ionic and electronic structure of the Co^{2+} and Li^+ which were farther from it. The Li diffusion from *Li2* (away from In) to *Li3* (next to In) site had a lower activation barrier of 230 meV than that for *Li1–Li2* (Figure **5.5**e). When the mobile Li ion is in the transition state along the migration path, it is close to a Co^{2+} ion, at which point the distance of Li^+–Co^{2+} was 2.63 Å and 2.73 Å for *Li1*–*Li2* and *Li2*–*Li3*, respectively. Therefore, the Li^+–Co^{2+} repulsion in the transition state for *Li2*–*Li3* would decrease with an increase of the Li^+–Co^{2+} distance. In addition, the tetrahedron at the transition state of *Li2*–*Li3* was 4.46 $Å^3$ slightly larger than 4.37 $Å^3$ of *Li1*–*Li2*, because the larger ionic radius of In^{3+} (80 pm) than Co^{2+} (74.5 pm) could provide the expanded diffusion pathway. This could be the main reason for the lower activation barrier of *Li2*–*Li3*, which is attributed to the In^{3+} dopant. Please note that the calculated activation energy did not go down to zero when the Li ion arrived at the *Li3* site through the *Li2*–*Li3* diffusion. This is because the Li vacancy formation is more energetically stable near In^{3+}, as mentioned earlier, especially when the V_{Li} site was occupied by a Li ion to calculate the *Li2*–*Li3* diffusion. The activation barrier from *Li3* (next to In) to V_{Li} (next to In) site was 255 meV (Figure **5.5**e). During the Li diffusion of *Li3*–V_{Li}, the Li ions passes between In^{3+} and Co^{2+}. The distance of Li^+–Co^{2+} in the transition state of *Li3*–V_{Li} was 2.64 Å, same as the undoped LCP. At the transition state of *Li3*–V_{Li}, i.e. in the middle between Co^{2+} and In^{3+}, the force for the longer distance of Li^+–Co^{2+} in the enlarged unit cell by In^{3+} can be compensated by the increased repulsion force of Li^+–In^{3+} (shorter distance of Li^+–Co^{2+}) due to the high oxidation state of In^{3+}. This compensation might result in the same distance of 2.64 Å in the transition state. However, the larger tetrahedron volume of the transition state for *Li3*–V_{Li} was maintained as seen in *Li2*–*Li3*, leading to the expanded diffusion pathway. Thus, the lower activation barrier was obtained compared with that of undoped LCP. The Li diffusion from V_{Li} (next to In) to *Li1* (away from In) site also showed a lower activation barrier of 287 meV than the undoped LCP. The distance of Li^+–Co^{2+} in the transition state was 2.71 Å, which was larger than 2.64 Å for the undoped LCP, implying a reduced repulsion in the transition state in the similar manner as the *Li2*–*Li3* diffusion. Please note that when the Li ion was occupying the V_{Li} site through the V_{Li}–*Li1* diffusion, the barrier was still 120 meV. This is because the Li vacancy formation is energetically preferred near the adjacent In^{3+}, meaning that it is unstable for Li ions to be accommodate in both V_{Li} and *Li3* site. Nevertheless, the lower activation barriers of the *Li2–Li3*, *Li3*–V_{Li} and V_{Li}–*Li1* pathway attributed to the introduction of the In^{3+} dopant enable the mobile Li ions to keep diffusing through the whole diffusion path along the b-axis.

Because Li mobility would be determined by the highest barrier along the pathway, the 307 meV (*Li1–Li2*) was considered as a barrier of the In-doped LCP, although Li ions could migrate faster around In^{3+}. Given 302 meV for the undoped LCP, the Li mobility of the In-doped LCP would not be much different from the undoped LCP. Usually, the ionic conductivity depends on the effective carrier concentration if the mobility does not change much. For the undoped LCP, theoretically there is no effective carrier in it, meaning that it is difficult for Li ions to hop due to no V_{Li} in LCP. However, in the case of the In-doped LCP, V_{Li} can be formed as much as the amount of In^{3+} dopant. In addition, by the above NEB calculations, we demonstrate that the V_{Li} is accessible and Li ion can pass through the V_{Li} with the low activation barrier. This is consistent with an improvement in experimentally-measured ionic conductivity of the In-doped LCP. Therefore, the main role of In^{3+} dopant would be the formation of V_{Li} and the reduction of the activation barrier around it. This improvement could result in a high capacity and low overpotential of In-doped LCP.

SI notes 5.2 *Band structure of Mo-doped LCP*

Previously, in ref. [S1], it has been reported that Mo-doped LCP is an electronic conductor based on DFT calculations. Figure **S5.15** shows the band structures obtained here for both undoped and Mo-doped (12.5 % substitution of Co with Mo) LCP. As was the case in ref. [S1], the addition of Mo creates defect bands in the gap. However, here, this serves to reduce the band gap from 4.36

eV in the undoped down to 1.73 eV in the Mo-doped rather than render the material conductive. Thus, Mo-doped LCP continues to be an insulator. The difference between the DFT calculations reported here and those in ref. [S1] are attributed to: (i) the composition here takes into account the Li vacancies introduced by doping supervalent Mo as discussed further in SI notes **5.3** below, and (ii) GGA+U is used for the calculations herein and this is well-known to improve the estimate of the band gap over the GGA method used in ref. [S1].

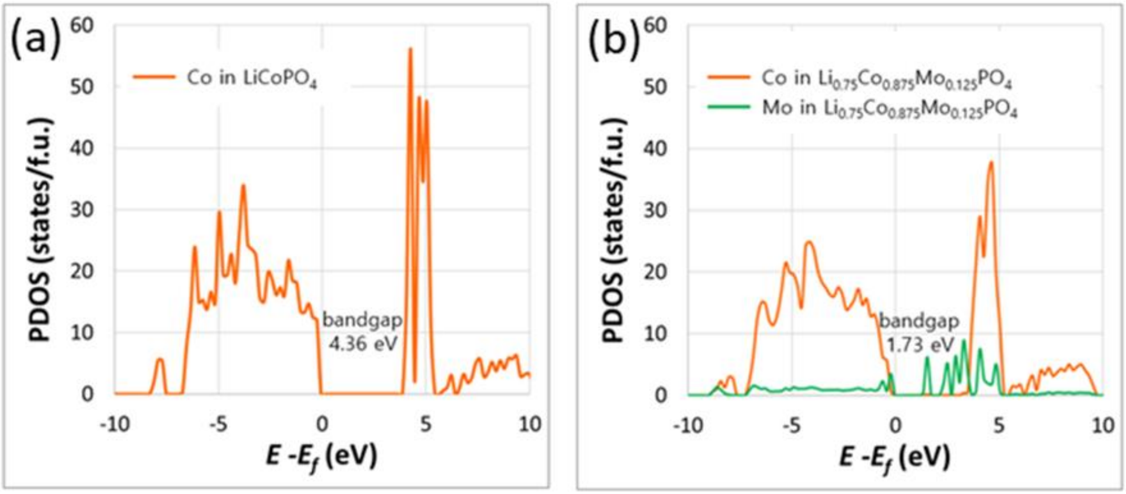

Figure S5.15 *Band structure calculated herein for both undoped LCP (a) and 12.5 % Mo-doped LCP (b).*

SI notes 5.3 *Antisite defect formation energy of M-doped LCP*

We found that In/Mo and In/Nb co-doped LCP showed enhanced cycle life compared to both In-doped and undoped LCP. The suppression of the antisite defect (Li-Co exchange) in the olivine structure has been considered as a good strategy to obtain better electrochemical performance, because the partial exchange between Li and Co can block the Li ion diffusion channels and cause a capacity fading of the LCP. Thus, the antisite defect formation energy (ADFE) was calculated to investigate the role of the Mo and Nb dopant in preventing the antisite defect. All oxidation states were attributed to be consistent with the XPS data (Figure **S5.16**). While In and Nb are clearly 3+ and 5+, respectively, Mo takes further analysis. The fitting of the Mo-doped spectrum was done in a manner consistent with ref. [S2]. Table **S5.3** shows the relative amounts of 4+ and 5+ for Mo. Given that the 4+ oxidation state is dominant (73.3 %), this is the oxidation state used to determine the composition for the DFT calculations for the Mo-doped LCP material below.

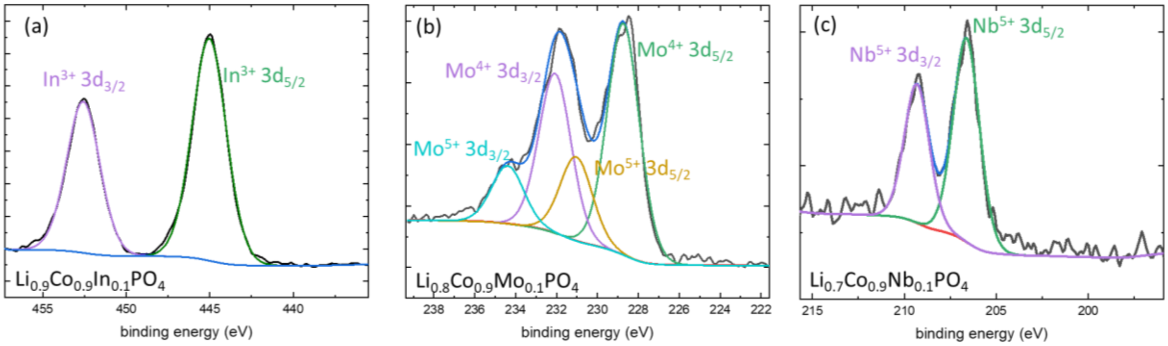

Figure S5.16 *XPS results for In, Mo and Nb in doped-LCP samples (compositions are indicated on each graph). Each pattern is fit effectively with the indicated oxidation states.*

Table S5.3 *Binding energies (BE) for Mo peaks in this study and from the literature. The atomic % is from the current study.*

	Peak BE (eV)	BE from literature (eV)	Atomic %
Mo^{4+}	228.7	228.8 (ref. [S3])	73.3
Mo^{5+}	231.0	231.1 (ref. [S4])	26.7

Figure 7a shows the ADFE of undoped, Al-doped ($Li_{14}Co_{14}Al_2P_{16}O_{64}$), In-doped ($Li_{14}Co_{14}In_2P_{16}O_{64}$), Mo-doped ($Li_{12}Co_{14}Mo_2P_{16}O_{64}$) and Nb-doped LCP ($Li_{10}Co_{14}Nb_2P_{16}O_{64}$). Except the symmetrically identical structures among all configurations of the Li-Co exchange, the ADFE for 30 configurations of M-doped LCP were calculated, while just 8 configurations for undoped LCP were calculated due to its high symmetry. The undoped and Al-doped LCP have the ADFE of -35 and -56 meV, respectively, indicating a spontaneous formation of the antisite defect which could shorten the cycle life. The slightly improved ADFE of 49 meV was found for the In-doped LCP. Nevertheless, the antisite defect seems to be unavoidable due to the still low ADFE. This is consistent with the experimental data where both the undoped and In-doped LCP had a poor capacity retention. When the Mo and Nb were doped into LCP, their ADFE increased to 193 and 216 meV. The higher ADFE can prevent the LCP structure from forming the antisite defect, implying an improved cyclability. For example, the In/Nb co-doped LCP experimentally proved to deliver 140 mAh/g with a capacity retention of 87% after 10 cycles, while the undoped one had 97 mAh/g with 45% retention at the 10th cycle. Therefore, the role of the Mo and Nb dopants is speculated to be the suppression of the antisite defect formation in M-doped olivine structure.

The M-doped LCP structure was scrutinized to better understand the reason for the high ADFE of Mo- and Nb-doped LCP in addition to the low ADFE of In- and Al-doped LCP. The volume difference between the Li- and Co-octahedron in the M-doped LCP structure seems roughly proportional to the ADFE (Figure **S5.17**a). The Nb-doped LCP showed the large volume difference of 0.71 Å^3 with the high ADFE of 216 meV while a small 0.11 Å^3 with low -35 meV was present for the undoped one. It would be reasonable to infer that the antisite defect can be easily formed if the Li- and Co-octahedron size are similar to each other, which means that the same size of the Li- and Co-octahedron might spend less energy to accommodate Li in Co site and Co in Li site owing to the reduced distortion and reduced stress after the exchange. This might be the main reason that the Mo- and Nb-doped LCP disfavor antisite defects due to the large volume differences between the Li- and Co-octahedron.

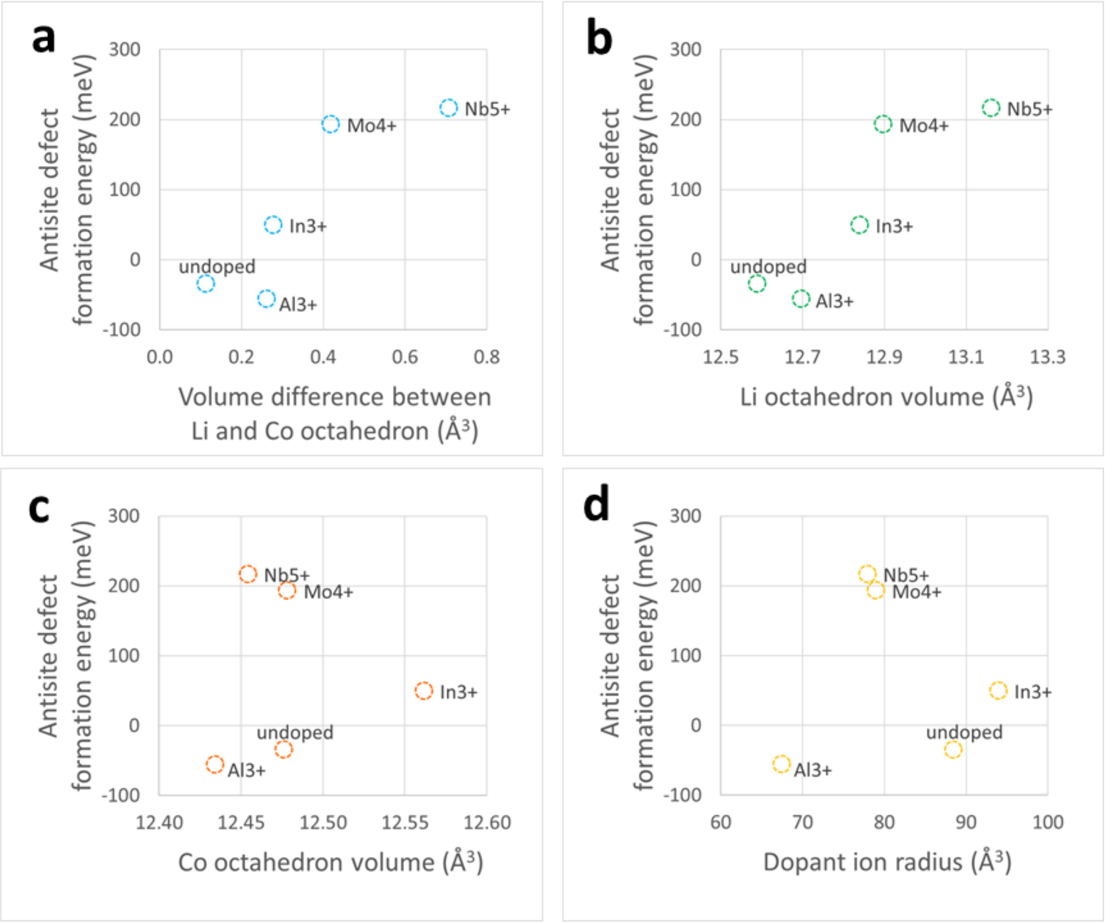

Figure S5.17 *ADFE for M-doped LCPs. Dependency of ADFE on the volume difference between Li and Co octahedra (a), on the average Li octahedral volume (b), on the average Co octahedral volume, and on the dopant ionic radius (d).*

The relationship between the ADFE and octahedron size was plotted to investigate which octahedron was dominant in making the volume difference between the Li- and Co-octahedron (Figure **S5.17**b,c). The Co-octahedron size was 12.48, 12.45 and 12.56 Å^3 for the undoped, Nb-doped and In-doped LCP, respectively (Figure **S5.17**c). This would be attributed to the dopant size (Figure **S5.17**d). Since the ionic radii of Co^{2+}, Nb^{5+} and In^{3+} are 88.5, 78 and 94 pm, respectively, the Co-octahedron of Nb-doped LCP became slightly smaller than the undoped one. Likewise, the In-doped case was somewhat larger. Please note that the difference in Co-octahedron size was as small as 0.03 Å^3 between the undoped and Nb-doped LCP. In contrast, the Li-octahedron size was significantly changed with varying dopants. The Li-octahedron size was 12.59, 13.16 and 12.84 Å^3 for the undoped, Nb-doped and In-doped LCP, respectively (Figure **S5.17**b). This might be related to the amount of V_{Li}. The V_{Li} would be generated for the charge compensation for the substitution of Nb^{5+} for Co^{2+} in LCP. At the V_{Li} site, when the positively charged Li ion disappeared in the center of the octahedron, because the repulsion between oxygen ions was not screened by Li ion, the V_{Li} octahedron volume can be increased, resulting in the larger volume of the edge-shared adjacent Li-octahedron. Because Nb^{5+} dopant required more V_{Li} than In^{3+}, the Li-octahedron of Nb-doped LCP became lager than the In-doped one. Although In^{3+} and Al^{3+} have the same oxidation state, indicating the same amount of V_{Li}, because the ionic radius of Al^{3+} (67.5 pm) is much smaller than In^{3+} (94 pm), the unit cell and Li-octahedron size of the Al-doped LCP become smaller than the In-doped one. Please note that the difference in Li-octahedron size between the undoped and Nb-doped LCP was as large as 0.57 Å^3, while that in Co-octahedron was just 0.03 Å^3. This means that the Li-octahedron volume is a dominant factor to decide the volume difference between the Li- and Co-octahedron.

In the previous reports, Kang *et al.*[S5] reported that the better cycling performance of the Fe-doped LCP could be explained by a larger ionic radius of Fe^{2+} (92 pm) than Co^{2+} (88.5 pm), which allowed a larger orbital splitting (t_{2g}-e_g separation) and stabilization of FeO_6. However, the good performance of our Nb-doped LCP would not be related to the orbital splitting of *d*-band due to the d^0 configuration of Nb^{5+}. In addition, in contrast with Fe^{2+}, the ionic radius of Nb^{5+} is 78 pm smaller than Co^{2+}. Moreover, according to the crystal field theory, the crystal field stabilization energies (CFSE, Δ_0) related to the orbital splitting is 0, 0, $-0.8\Delta_0$ and $-0.8\Delta_0$ for In^{3+} (d^{10}), Nb^{5+} (d^0), Mo^{4+} (d^2) and Co^{2+} (d^7), respectively, which means that In, Nb and Mo dopant cannot lead to a larger orbital splitting. Therefore, it is more reasonable to explain the improved cycle life of our Mo- and Nb-doped LCP by using the ADFE and the volume difference between the Li- and Co-octahedron, as described earlier, rather than the orbital splitting.

Galvanostatic cycling

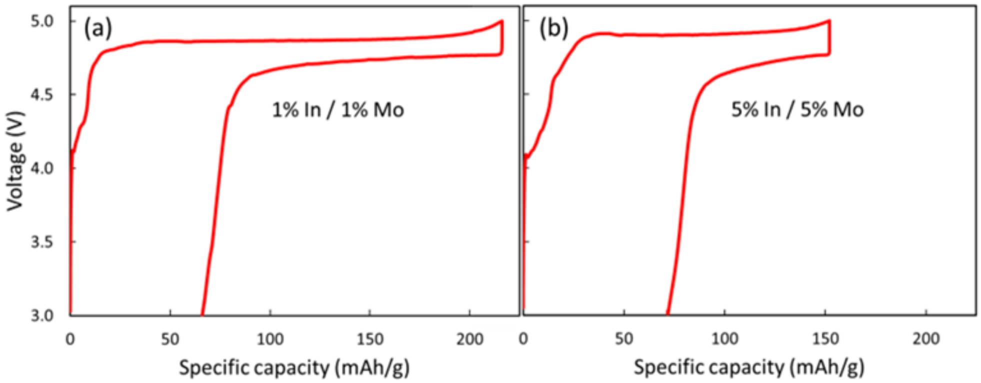

Figure S5.18 *First cycle of galvanostatic cycling obtained for LCP co-doped with 1% In / 1% Mo (a), and 5% In / 5 % Mo (b) at 10 mA/g in the voltage range 3.0 – 5.0 V. (active material loading of 2.4 mg/cm*^{2}*)*

Table S5.4 *Cycling data extracted from galvanostatic testing in coin cells for two samples co-doped with Mo and In.* Q_n *is the specific discharge capacity for the n*th *cycle.*

Sample	**Q_1 (mAh/g)**	**Q_2/Q_1 (%)**	**Q_3/Q_1 (%)**	**Q_4/Q_1 (%)**	**Q_5/Q_1 (%)**
1% In – 1% Mo	150.1	89	81	76	70
5% In – 5% Mo	80.3	98	93	88	85

SI References

(S1) Zhi-Ping, L., Yu-Jun, Z. & Yan-Ming, Z. Li- Site and Metal-Site Ion Doping in Phosphate-Olivine LiCoPO4 by First-Principles Calculation. *Chinese Phys. Lett.* **2009**, *26*, 038202.

(S2) Hu, W., Shi, Q., Chen, Z., Yin, H., Zhong, H., & Wang, P. Co2N/Co2Mo3O8 heterostructure as a highly active electrocatalyst for an alkaline hydrogen evolution reaction. *ACS applied materials & interfaces* **2021**, *13*, 8337.

(S3) DeVries, J. E., Yao, H. C., Baird, R. J., & Gandhi, H. S. Characterization of molybdenum-platinum catalysts supported on γ-alumina by X-ray photoelectron spectroscopy. *Journal of Catalysis* **1983**, *84*, 8.

(S4) McIntyre, N.S., Johnston, D.D.,Coatsworth, L.L., Davidson, R.D., & Brown, J.R. *Surface and Interface Analysis* **1990**, *15*, 265.

(S5) Kang, Y. M., Kim, Y. I., Oh, M. W., Yin, R. Z., Lee, Y., Han, D. W., ... & Ramanath, G. (2011). *Energy & Environmental Science* **2011**, *4*, 4978.

5.8 References

(1) Zhang, M.; Garcia-Araez, N.; Hector, A. L. Understanding and Development of Olivine $LiCoPO_4$ Cathode Materials for Lithium-Ion Batteries. *J. Mater. Chem. A* **2018**, *6* (30), 14483.

(2) Fan, X.; Wang, C. High-Voltage Liquid Electrolytes for Li Batteries: Progress and Perspectives. *Chemical Society Reviews* **2021**, *50* (18), 10486.

(3) Li, J.; Ma, Z.-F. Past and Present of $LiFePO_4$: From Fundamental Research to Industrial Applications. *Chem* **2019**, *5* (1), 3.

(4) Ludwig, J.; Marino, C.; Haering, D.; Stinner, C.; Gasteiger, H. A.; Nilges, T. Morphology-Controlled Microwave-Assisted Solvothermal Synthesis of High-Performance $LiCoPO_4$ as a High-Voltage Cathode Material for Li-Ion Batteries. *Journal of Power Sources* **2017**, *342*, 214.

(5) Li, H.; Wang, Y.; Yang, X.; Liu, L.; Chen, L.; Wei, J. Improved Electrochemical Performance of 5V $LiCoPO_4$ Cathode Materials via Yttrium Doping. *Solid State Ionics* **2014**, *255*, 84.

(6) Zhi-Ping, L.; Yu-Jun, Z.; Yan-Ming, Z. Li- Site and Metal-Site Ion Doping in Phosphate-Olivine $LiCoPO_4$ by First-Principles Calculation. *Chinese Phys. Lett.* **2009**, *26* (3), 038202.

(7) Cherkashinin, G.; Eilhardt, R.; Nappini, S.; Cococcioni, M.; Píš, I.; dal Zilio, S.; Bondino, F.; Marzari, N.; Magnano, E.; Alff, L. Energy Level Alignment at the Cobalt Phosphate/Electrolyte Interface: Intrinsic Stability vs Interfacial Chemical Reactions in 5 V Lithium Ion Batteries. *ACS Appl. Mater. Interfaces* **2022**, *14* (1), 543.

(8) Wolfenstine, J. Electrical Conductivity of Doped $LiCoPO_4$. *Journal of Power Sources* **2006**, *158* (2), 1431.

(9) Allen, J. L.; Allen, J. L.; Thompson, T.; Delp, S. A.; Wolfenstine, J.; Jow, T. R. Cr and Si Substituted-$LiCo_{0.9}Fe_{0.1}PO_4$: Structure, Full and Half Li-Ion Cell Performance. *Journal of Power Sources* **2016**, *327*, 229.

(10) Wang, Y.; Chen, J.; Qiu, J.; Yu, Z.; Ming, H.; Li, M.; Zhang, S.; Yang, Y. Cr-Substituted $LiCoPO_4$ Core with a Conductive Carbon Layer towards High-Voltage Lithium-Ion Batteries. *Journal of Solid State Chemistry* **2018**, *258*, 32.

(11) Li, H.; Wang, Y.; Yang, X.; Liu, L.; Chen, L.; Wei, J. Improved Electrochemical Performance of 5V $LiCoPO_4$ Cathode Materials via Yttrium Doping. *Solid State Ionics* **2014**, *255*, 84.

(12) Allen, J. L.; Thompson, T.; Sakamoto, J.; Becker, C. R.; Jow, T. R.; Wolfenstine, J. Transport Properties of $LiCoPO_4$ and Fe-Substituted $LiCoPO_4$. *Journal of Power Sources* **2014**, *254*, 204.

(13) Kreder, K. J.; Manthiram, A. Vanadium-Substituted $LiCoPO_4$ Core with a Monolithic $LiFePO_4$ Shell for High-Voltage Lithium-Ion Batteries. *ACS Energy Lett.* **2017**, *2* (1), 64.

(14) Fang, L.; Zhang, H.; Zhang, Y.; Liu, L.; Wang, Y. Design and Synthesis of Two-Dimensional Porous Fe-Doped $LiCoPO_4$ Nano-Plates as Improved Cathode for Lithium Ion Batteries. *Journal of Power Sources* **2016**, *312*, 101.

(15) Kishore, M. V. V. M. S.; Varadaraju, U. V. Influence of Isovalent Ion Substitution on the Electrochemical Performance of $LiCoPO_4$. *Materials Research Bulletin* **2005**, *40* (10), 1705.

(16) Dimesso, L.; Spanheimer, C.; Jaegermann, W. Influence of Isovalent Ions (Ca and Mg) on the Properties of $LiCo_{0.9}M_{0.1}PO_4$ Powders. *Journal of Power Sources* **2013**, *243*, 668.

(17) Karthickprabhu, S.; Hirankumar, G.; Maheswaran, A.; Daries Bella, R. S.; Sanjeeviraja, C. Structural and Electrical Studies on Zn^{2+} Doped $LiCoPO_4$. *Journal of Electrostatics* **2014**, *72* (3), 181.

(18) Shanmukaraj, D.; Murugan, R. Synthesis and Characterization of $LiNi_yCo_{1-y}PO_4$ (Y=0–1) Cathode Materials for Lithium Secondary Batteries. *Ionics* **2004**, *10* (1), 88.

(19) Fleischauer, M. D.; Hatchard, T. D.; Rockwell, G. P.; Topple, J. M.; Trussler, S.; Jericho, S. K.; Jericho, M. H.; Dahn, J. R. Design and Testing of a 64-Channel Combinatorial Electrochemical Cell. *J. Electrochem. Soc.* **2003**, *150* (11), A1465.

(20) Potts, K. P.; Grignon, E.; McCalla, E. Accelerated Screening of High-Energy Lithium-Ion Battery Cathodes. *ACS Appl. Energy Mater.* **2019**, *2* (12), 8388.

(21) Adhikari, T.; Hebert, A.; Adamič, M.; Yao, J.; Potts, K.; McCalla, E. Development of High-Throughput Methods for Sodium-Ion Battery Cathodes. *ACS Comb. Sci.* **2020**, *22* (6), 311.

(22) Jia, S.; Counsell, J.; Adamič, M.; Jonderian, A.; McCalla, E. High-Throughput Design of Na–Fe–Mn–O Cathodes for Na-Ion Batteries. *Journal of Materials Chemistry A* **2022**, *10* (1), 251.

(23) Perdew, J. P.; Burke, K.; Ernzerhof, M. Generalized Gradient Approximation Made Simple. *Phys. Rev. Lett.* **1996**, *77* (18), 3865–3868. https://doi.org/10.1103/PhysRevLett.77.3865.

(24) Kresse, G.; Furthmüller, J. Efficient Iterative Schemes for Ab Initio Total-Energy Calculations Using a Plane-Wave Basis Set. *Phys. Rev. B* **1996**, *54* (16), 11169.

(25) Dudarev, S. L.; Botton, G. A.; Savrasov, S. Y.; Humphreys, C. J.; Sutton, A. P. Electron-Energy-Loss Spectra and the Structural Stability of Nickel Oxide: An LSDA+U Study. *Phys. Rev. B* **1998**, *57* (3), 1505.

(26) Ping Ong, S.; L. Chevrier, V.; Hautier, G.; Jain, A.; Moore, C.; Kim, S.; Ma, X.; Ceder, G. Voltage, Stability and Diffusion Barrier Differences between Sodium-Ion and Lithium-Ion Intercalation Materials. *Energy & Environmental Science* **2011**, *4* (9), 3680.

(27) Ágoston, P.; Erhart, P.; Klein, A.; Albe, K. Geometry, Electronic Structure and Thermodynamic Stability of Intrinsic Point Defects in Indium Oxide. *J. Phys.: Condens. Matter* **2009**, *21* (45), 455801.

(28) Rellán-Piñeiro, M.; López, N. One Oxygen Vacancy, Two Charge States: Characterization of Reduced α-MoO_3(010) through Theoretical Methods. *J. Phys. Chem. Lett.* **2018**, *9* (10), 2568.

(29) Pasquier, D.; Yazyev, O. V. Charge Density Wave Phase, Mottness, and Ferromagnetism in Monolayer 1 T− $NbSe_2$. *Phys. Rev. B* **2018**, *98* (4), 045114.

(30) Gnewuch, S.; Rodriguez, E. E. Distinguishing the Intrinsic Antiferromagnetism in Polycrystalline $LiCoPO_4$ and $LiMnPO_4$ Olivines. *Inorg. Chem.* **2020**, *59* (9), 5883.

(31) Henkelman, G.; Jónsson, H. Improved Tangent Estimate in the Nudged Elastic Band Method for Finding Minimum Energy Paths and Saddle Points. *J. Chem. Phys.* **2000**, *113* (22), 9978.

(32) Henkelman, G.; Uberuaga, B. P.; Jónsson, H. A Climbing Image Nudged Elastic Band Method for Finding Saddle Points and Minimum Energy Paths. *J. Chem. Phys.* **2000**, *113* (22), 9901.

(33) McCalla, E.; Carey, G. H.; Dahn, J. R. Lithium Loss Mechanisms during Synthesis of Layered $L_{ix}Ni_{2-x}O_2$ for Lithium Ion Batteries. *Solid State Ionics* **2012**, *219*, 11.

(34) Lin, X.; Zhao, Y.; Liang, Z.; Yan, D.; Liu, X.; Wen, M.; Dong, Y.; Kuang, Q. Phase Relation of Li_2O–CoO–P_2O_5 Ternary System and Electrochemical Behaviors of Co-Base Polyphosphates within This System. *Journal of Alloys and Compounds* **2015**, *646*, 727.

(35) Wu, B.; Xu, H.; Mu, D.; Shi, L.; Jiang, B.; Gai, L.; Wang, L.; Liu, Q.; Ben, L.; Wu, F. Controlled Solvothermal Synthesis and Electrochemical Performance of $LiCoPO_4$ Submicron Single Crystals as a Cathode Material for Lithium Ion Batteries. *Journal of Power Sources* **2016**, *304*, 181.

(36) Wu, X.; Meledina, M.; Barthel, J.; Liu, Z.; Tempel, H.; Kungl, H.; Mayer, J.; Eichel, R.-A. Investigation of the Li–Co Antisite Exchange in Fe-Substituted $LiCoPO_4$ Cathode for High-Voltage Lithium Ion Batteries. *Energy Storage Materials* **2019**, *22*, 138.

Chapter 6

Discussion

6.1 Charge transport properties in solid electrolytes and cathode materials

The solid electrolyte must be a good ion conductor and electronic insulator. Therefore measuring the charge transport properties is essential for screening solid electrolytes. The total electrical conductivity is measured using EIS, while the electronic contribution is measured using chronoamperometry. We developed a cell to measure the electrical and electronic conductivity of 64 solid electrolyte pellets in high-throughput. Gold contacts are sputtered on both sides of solid electrolyte pellets using a custom mask after polishing the surface of the pellets to ensure good electrical contact during EIS measurements. Polishing the surface of the pellet helps to create a smooth, flat surface that allows for maximum contact between the pellet and the gold contacts, improving the accuracy and reliability of the EIS measurements. The EIS measurement is performed by a single-channel potentiostat connected to a multiplexer that switches between the channels of the cell. Assigning the arcs in a Nyquist plot to bulk and grain boundary resistances in the high-frequency and mid-frequency regions can be a critical part of analyzing EIS data. The assignment of the arcs can be based on their corresponding capacitance values. Using this EIS tool, we mapped the bulk and grain boundary conductivity of the perovskite region of the Li-La-Ti-O perovskite phase diagram. Some samples with a secondary phase had higher conductivity than the pure phase perovskites, showing the role that secondary phases can play in enhancing grain boundary conductivity. The cross-section SEM images and the relative densities measured by the Archimedes method showed consistently low porosity and high relative densities for samples in the perovskite mapped region, verifying that the conductivity trend observed is due to composition-structure rather than enhanced sintering. We checked the surface stability of the pellets in the air by performing XPS. A negligible amount of Li_2CO_3 forms when LLTO is in contact with air for a week to a month which did not affect the conductivity measurements.

The electronic conductivity is measured by applying a constant voltage to the tested solid electrolyte and measuring the current. The current response for a good solid electrolyte (pure ionic conductor) starts high due to the movement of all charge carriers decaying to a steady current (electronic current). The same combinatorial cell used for EIS measurement can be used for high-throughput electronic conductivity measurements. A constant voltage is applied across all pellets in parallel. The current passing through each channel is measured by measuring the potential drop across a resistor (connected in series with each channel) using a voltameter connected to a multiplexer that switches between channels.

We used these high throughput AC and DC measurement tools to study the effect of substitutions in LLTO solid electrolytes on their ionic and electronic conductivity. Most of the substitutions do not enhance bulk conductivity except for Nb. The higher bulk conductivity observed in Nb-substituted LLTO may be attributed to either an increased vacancy concentration resulting from the higher valency of Nb^{5+} compared to Ti^{4+}, or an increased bottleneck size due to the larger ionic radius of Nb^{5+} (0.064 nm) compared to Ti^{4+} (0.0605 nm). The electronic conductivity data show that some substitutions can introduce electronic conductivity for example Cr substitution. These ionic/electronic mixed conductors are good candidates for incorporation in composite cathodes. In future studies, it could be valuable to understand the mechanism behind this electronic conduction, whether due to the introduction of oxygen vacancies or a change in the band structure induced by the substituent.

Room temperature ionic conductivity is regulated by lithium mobility and lithium carrier concentration. Measuring the ionic conductivity at different temperatures and extracting the activation energy gives a hint of whether an improved ionic conductivity of the tested solid electrolyte is due to lower mobility or higher charge carrier concentration, or both. This guides in designing and optimizing solid electrolytes. The charge carrier concentration can be estimated from the chemical formula and structure of the material. In $Li_{3x}La_{2/3-x}\square_{1/3-2x}TiO_3$ (□ represents a lattice vacancy), the charge carrier concentration is proportional to the content of lithium (3x) and lattice vacancies (1/3-2x) per unit formula, as Li^+ ions migrate through the vacancy mechanism. The structure (change of lattice parameters, distortion) and the environment of the lithium cation along the diffusion path influence lithium mobility. The activation energy of the substituted LLTOs was extracted from the Arrhenius plot by measuring the electrical conductivity at 22 and 50 °C. We found that 15%Nb substitution enhances bulk and grain boundary conductivity. The lower bulk resistance of 15%Nb-LLTO compared to unsubstituted LLTO is partially due to the lower activation energy of bulk conduction that could be caused by a larger bottleneck size. The 15%Nb and 3% K substitutions in LLTO enhance grain boundary conduction but do not lower the activation energy of grain boundary lithium conduction. Therefore, the mechanism of enhancement could be due to a higher charge carrier concentration resulting from the reduction of charge density in the space-charge layer, which decreases the height of the Schottky barrier, increased ionic diffusion dimensionality in the bulk, and/or lower misorientation angles between neighboring grains that increase the charge carrier concentration at the grain boundary. Chapter 5 of our study involved improving the performance of $LiCoPO_4$ through substitution. To understand why specific substitutions led to better performance, we measured the electronic and ionic conductivities of the cathode. Our findings indicated that while the non-carbon coated LCP samples showed a moderate improvement of approximately 50% in their ionic conductivity, this improvement was not significant enough to overcome the largest barrier to Li diffusion, which remained at 0.30 eV in the DFT calculations. However, we observed a surprising increase in electronic conductivity in the carbon-coated samples with indium substitution, particularly with the 10% sample showing a nearly five-fold increase and the 1% sample showing a three-fold increase. The improved conductivities between 0.1% and 1% substitution correlated with the improved capacities, suggesting that the primary benefit of indium was to improve the electronic conductivity of the carbon-coated materials. Conversely, the electronic conductivities in the uncoated materials did not improve significantly.

These high throughput charge transport measurement tools can also be used to measure the ionic and electronic conductivity of composite cathodes. They can be utilized in optimizing the formulation of the composite cathodes for their better integration in an all-solid-state battery. This optimization could be conducted after screening all the essential properties of the solid electrolyte mentioned earlier and will be discussed next. Composite cathodes can be prepared through different methods, such as co-sintering, cold pressing with or without a binder, or the slurry method.[1] Many parameters can affect the performance of the composite cathode, from the ratio of the components to the mixing method used, for example ball milling. Optimizing the formulation of the composite cathode to have maximum ionic and electronic conductivity increases the chance of its integration into an all-solid-state battery.[2] While this guarantees a continuous electronic and ionic pathway, it does not ensure that the electronic additive and solid electrolyte wet the cathode active material and that the interfacial resistance is low.

6.2 ESW of solid electrolytes

In addition to having good transport properties, solid electrolytes should also be stable at the electrode potentials to which they are exposed during operation. The high electrochemical stability window allows the use of low-potential anodes and high-potential cathodes, maximizing cell voltage to give high energy density. The electrochemical stability window of electrolytes has often been measured using cyclic voltammetry (CV) with an inert electrode. To determine the ESW, an arbitrary current limit is typically chosen to define the start of electrolyte decomposition. The potential at which this current limit is reached is taken as the onset of electrolyte decomposition. Alternatively, the ESW can be determined by extrapolating the stable region of the cyclic voltammogram (i.e., the region where the current remains constant) and the current onset, then selecting the intercept of these two lines as the decomposition potential. The electrochemical stability window measured by this type of CV experiment depends on the electrode used and experimental parameters. This approach measures the kinetic ESW, which can be biased by sluggish electronic and ionic kinetics. Thus, measuring the electrochemical stability window of a solid electrolyte by attaching lithium metal on one side and sputtering gold on the other, followed by performing a CV overestimates the stability due to the limited electronic contact and ionic conductivity through the pellet. When the relatively small interface between the solid electrolyte and electrode decomposes, it produces a very low current that is hard to measure and passivation may occur due to limited electronic mobility. This method could be even more biased when the ionic conductivity of the solid electrolyte is low which adds on ionic overpotential that further overestimates the stability window. Therefore, preparing electrodes from the tested samples and cycling them using a good wetting and highly conductive electrolyte is essential to accurately measure the electrochemical stability window. Different conductive additives can be used in preparing the electrodes with test electrolyte as the active materials for the electrochemical stability window test. The choice of the conductive additive can change the electrochemical stability window because it can act as a catalyst. In the composite cathode of all-solid-state batteries and Li-ion batteries, carbon black is used as the additive. Therefore, using carbon black as an additive in the electrochemical stability window test can further reveal how the test solid electrolyte will interact with carbon black during cycling in an all-solid-state battery.

If a specific solid electrolyte shows high ionic conductivity, low electronic conductivity and a wide electrochemical stability window, it is important to measure the electrochemical stability with anode/cathode active materials as a composite electrode. This is because the electrode active materials can act as a catalyst and shift the electrochemical stability window of the solid electrolyte. Due to the reasons mentioned above, we are utilizing the composite electrode method in our high-throughput system for screening the ESW. This method involves the use of carbon black as the conductive additive with a liquid electrolyte to ensure good wettability and ionic conductivity. The drawback of using a liquid electrolyte is that the stability window tested is limited by the electrochemical stability window of the liquid electrolyte. We identified the stability limit by the potential where the current of the tested sample was first higher than that of an identical electrode without any active material. We used carbonate-based electrolyte for these tests, but ionic liquids with wider electrochemical stability windows can be used occasionally to confirm wide stability windows. When we measured the oxidative stability using an ionic liquid, we got similar stability potential limits as with the carbonate.

The effect of substitutions in LLTO on its cathodic and anodic stability potentials was explored by preparing two batches of electrodes via mixing with carbon black, one batch for sweeping to low potential on Ni current collector and the other high potential on Al current collector. CVs of some substituted samples had reversible redox peaks. We can easily identify a reversible process from the CVs where peaks appear in both sweep directions. Samples showing reversible redox are not suitable as solid electrolytes without significant reduction in stability window but they can be electrode materials.

On the other hand, suppose a process is irreversible and the Faradaic current did not show again on the second cycle. In this case, it means a passivating layer is formed, which can potentially kinetically extend the electrochemical stability window. The nature of this passivating layer dictates the electrode-electrolyte interfacial resistance. This passivating layer is likely an electronic insulator because the degradation did not propagate, but it needs to be a good ionic conductor or very thin to ensure low electrode/electrolyte interfacial resistance. Substitutions in LLTO, lowers the reductive stability limit by around 0.3 V vs. Li/Li^+ (Mg) but do not make it stable against lithium. Improvement of reductive stability by as low as 0.1 V vs Li/Li^+ in LLTO is beneficial because it allows the usage of $Li_4Ti_5O_{12}$, a high-potential anode.

6.3 Stability of SEs against lithium metal anode

The stability of the lithium metal/solid-state electrolyte interface is assessed by attaching a lithium metal electrode to the electrolyte and observing the evolution of the interfacial impedance over time using EIS. The reductive stability of the lithium lanthanum zirconate (LLZO) solid electrolyte was evaluated using cyclic voltammetry and was found to exhibit high reductive stability (0 V vs, Li/Li^+). Therefore next the stability against lithium metal was also explored. The interfacial resistance between LLZO and lithium metal increases a little, then remains constant, indicating the formation of a passivating layer that is an electronic insulator and an ionic conductor or very thin. In contrast, when LLTO comes in contact with lithium metal, the resistance decreases continuously, indicating the formation of an electronically conductive interphase.

6.4 Composition-structure relationships in LLTO and effect of substitutions

Structural analysis of solid electrolytes is important to understand the composition-structure-property relationship. Our high-throughput XRD setup has high sensitivity as it uses a Mo source and the measurement is done in transmission mode, allowing the detection of trace amounts of phases. It is always helpful to start exploring a specific solid electrolyte system by sampling compositions around the solid electrolyte known composition. Thus mapping the phase diagram can help to identify small amounts of secondary phases found in the samples and determine the existence of solid solutions. We used the high-throughput XRD to explore the Li-La-Ti-O pseudoternary phase diagram and focused on the perovskite region. We mapped the phase diagram using 192 samples, with 64 more densely sampled around the perovskite region.

Most solid-state synthesis methods require high temperatures (~1350°C) and sacrificial powder, but we managed to control Li loss in our mg-scale sample by using the sol-gel method, which lowers the sintering temperatures. During the calcination, an amorphous phase forms, which crystallizes and densifies upon sintering. Relative densities of >92% were achieved without sacrificial powder at 1200°C. These samples exhibited conductivity comparable to those synthesized by others using the solid-state method at 1350°C. It is important to note that samples can become contaminated with Al from alumina substrate at these high sintering temperatures, which can lead to unintentional substitution. We measured Al content in our samples using ICP and found a very small amount of Al, lower than the threshold that affects crystal structure and properties. Lithium and lanthanum share the same crystallographic site. La tends to order at low lithium contents, forming a double perovskite with La-rich and poor alternating layers, and the phase becomes orthorhombic. On the other hand, less ordering is observed at high lithium contents, and the phase becomes tetragonal. Quenched samples have no A-site ordering, but there is a distortion, and the phase becomes pseudocubic. The amount of ordering is known from the intensity of the low-angle superlattice diffractions.

The phase stability diagram was constructed by performing the Rietveld refinement on each sample and quantifying the phase contents. The lever rule was used to confirm the positions of some end members. The lever rule from the two-phase region, one of which is LLTO, extrapolates to the composition of pure LLTO, but the sample with that composition contains a higher content secondary phases. Thereby we concluded that LLTO is a metastable phase, and secondary phases are required to stabilize it. The samples cooled naturally from 1200 °C did not show a pure solid solution perovskite along the composition line. Instead, we found a region with a high content of LLTO. We prepared quenched samples to ensure the equilibrium product is locked and not converted during slow cooling. We also found a region of high LLTO content in the quenched samples, and surprisingly the highest LLTO content was lower than in the slow-cooled samples. To ensure the thermodynamic product was reached, we heated the samples for a longer time, 12 hours instead of 6 hours, but the LLTO content did not increase. When we carefully checked the XRD patterns of LLTO reported to be single phase in the literature, we consistently found secondary phases that are overlooked such as $Li_2Ti_3O_7$, Li_2TiO_3, TiO_2, and $Li_4Ti_5O_{12}$. In one report, although the XRD patterns collected for the samples showed a pure phase of LLTO, the High-Angle Annular Dark-Field Scanning Transmission Electron Microscopy (HAADF-STEM) image and EDS mapping results revealed the presence of a second phase that was epitaxially located inside the grain of LLTO.[3] In another similar instance, a sample with an almost pure XRD pattern was observed to have a second phase by Scanning Electron Microscopy (SEM) using a backscatter electron detector.[4] A study found that the secondary phase is located at the triple junction using Transmission Electron Microscopy (TEM).[5] There has therefore already been substantial corroboration of our finding that LLTO is in fact metastable.

In contrast, our subsequent study revealed that the perovskite structure can be stabilized through substitution, and pure perovskite can be achieved by incorporating various elements as stabilizers. We used bond valence mismatch as a predictor and calculated its values at La and Ti sites to predict the optimal site for substituents in the structure. The site with the lowest BVM is the most likely location for the substituent. Our findings indicate that both A and B site substitutions can effectively stabilize the pure phase.

6.5 Improvement of $LiCoPO_4$ performance by substitutions

We have successfully optimized the performance of LLTO solid electrolyte by carefully selecting synthesis conditions, optimizing composition, and performing substitutions. One of the key advantages of using LLTO solid electrolyte is its ability to support high-potential cathodes like $LiCoPO_4$. To ensure their optimal performance in all-solid-state batteries, we have used similar methodologies to enhance the properties of $LiCoPO_4$ cathodes by optimizing synthesis conditions and introducing substituents. Olivine cathodes with the $LiMPO_4$ formula have been extensively studied. Although $LiFePO_4$ in particular exhibits a moderate energy density compared to nickel-containing layered oxides, it has still been successfully commercialized due to several factors. Firstly, it contains iron, an abundant material that helps reduce costs. Secondly, $LiFePO_4$-based cells have a long lifespan because their operating potential is below the oxidative stability window of the carbonate-based liquid electrolyte. Thirdly, it offers excellent thermal stability. Alternatively $LiMnPO_4$ has a higher voltage (4.1 V vs. Li/Li^+) than $LiFePO_4$ (3.45 V vs. Li/Li^+), providing a 20% higher energy density of 701 Wh/kg. On the other hand, $LiCoPO_4$ has a superior theoretical energy density of 800 Wh/kg with a 4.8 V (vs. Li/Li^+) operating potential.[6] We were drawn to this specific cathode not only for its high energy density but also for its low volume expansion of only 2% during charge/discharge, which results in less stress being applied to the solid electrolyte in all-solid-state batteries. Despite these advantages, olivine cathodes suffer from intrinsic low electronic and ionic conductivity. These issues are addressed in $LiFePO_4$ by nanosizing to shorten the lithium diffusion path and carbon coating to increase electronic conductivity. These approaches have been successful in commercializing $LiFePO_4$-based batteries due to the low potentials such that the electrolyte is stable. However, the same approach with $LiCoPO_4$ can lead to drastic reductions in cell performance because at the high operating potential of LCP accelerated electrolyte decomposition occurs at the larger surface area.

The synthesis and coating of the pristine LCP were optimized before investigating the effect of substitution. The substitutions at the Co-site were conducted at two heat treatment temperatures 750°C and 850°C. Although pristine LCP made at 750°C had a higher discharge capacity than the one made at 850°C due to smaller particle size, more substituents were incorporated into LCP at 850°C due to higher diffusion. We systematically studied the effect of substitution on performance, starting with single substitutions and moving to co-substitutions. The performance of the materials was investigated by preparing electrodes and cycling them against lithium metal by cyclic voltammetry in a combinatorial cell. In this test, the cell stays at high potentials for a longer time than in galvanostatic cycling thereby accelerating the electrolyte consumption which allows us to see high contrast in capacity retention within only 10 cycles. Multiple single substitutions at the Co-site in LCP improved its performance. In particular, 10%In decreases the overpotential and increases the first discharge capacity. The measured charge transport properties indicate that indium substitution increases the electronic conductivity of the carbon-coated LCP. The complementary computational simulation revealed that 10% In substitution does not change the band structure of LCP to introduce electronic conductivity. In future studies, we will explore the mechanism underlying the enhanced electronic conductivity in carbon-coated In-LCP by analyzing the oxidation states of the cations at the surface and in bulk, providing us with valuable insights.

We prepared samples with a gradient of substitution content because the 10% In substituted LCP contained a tiny amount of unidentified phase. 1% to 5% In substitutions delivered capacities matching the theoretical, keeping in mind that In^{3+} is electrochemically inactive. Moreover, by introducing Mo, as co-substituent with In tunes the morphology producing micron-sized particles. These larger particles exhibit higher capacity retention due to their lower surface area, which reduces their reactivity with the electrolyte. In the computational studies, we also found Mo substitution reduces the formation of Li/Co antisite defects compared to the pristine material, which has a negative antisite formation energy. Formation of such antisite defects during cycling is commonly correlated to poor extended cycling in LCP as they blook 1D Li diffusion channels. For very moderate substitution levels (1% of each of In and Mo), capacities as high as 150 mAh/g can be obtained with improved retention of 75% (compared to 60% in 10%In-LCP or 50% in unsubtituted LCP). We have emphasized the importance of tuning multiple properties to enhance performance, which can be achieved through substitutions that tune the structure, transport properties, and morphology of the particles. Our findings imply that a small amount of co-substitution, specifically 1%In and 1%Mo for Co in LCP, can significantly improve the performance of the cathode by tuning its properties and morphology.

The overall performance of solid-state batteries can be enhanced by improving the properties of the solid electrolyte and cathode active material. Transport properties are one of the key properties needed in both. The solid electrolyte must have high ionic conductivity and be an electronic insulator to ensure the low internal resistance of the cell, while the cathode must have good ionic and electronic conductivity to lower overpotential and improve the practical discharge capacity. Moreover, the solid electrolyte should have a wide electrochemical stability window to allow the use of low/high potential cathode increasing energy density and the cathode should have low antistite defects to ensure long capacity retention. These charge transport and electrochemical properties were enhanced in LLTO solid electrolyte and LCP cathode by optimizing synthesis conditions, selecting composition, and performing substitutions using high throughput accelerated screening methodologies. Our findings here not only provide state-of-the-art materials but also provide a guide for developing materials with other chemistries.

6.6 References

(1) Al-Salih, H.; Houache, M. S. E.; Baranova, E. A.; Abu-Lebdeh, Y. Composite Cathodes for Solid-State Lithium Batteries: "Catholytes" the Underrated Giants. *Advanced Energy and Sustainability Research* **2022**, *3* (8), 2200032.

(2) Falco, M.; Ferrari, S.; Appetecchi, G. B.; Gerbaldi, C. Managing Transport Properties in Composite Electrodes/Electrolytes for All-Solid-State Lithium-Based Batteries. *Molecular Systems Design & Engineering* **2019**, *4* (4), 850.

(3) Li, F.; Li, J.; Zhu, F.; Liu, T.; Xu, B.; Kim, T.-H.; Kramer, M. J.; Ma, C.; Zhou, L.; Nan, C.-W. Atomically Intimate Contact Between Solid Electrolytes and Electrodes for Li Batteries. *Matter* **2019**, *1* (4), 1001.

(4) Braun, P.; Uhlmann, C.; Weber, A.; Störmer, H.; Gerthsen, D.; Ivers-Tiffée, E. Separation of the Bulk and Grain Boundary Contributions to the Total Conductivity of Solid Lithium-Ion Conducting Electrolytes. *Journal of Electroceramics* **2017**, *38* (2), 157.

(5) Chung, H.-T.; Cheong, D.-S. The Microscopic Features of $(Li_{0.5}La_{0.5})TiO_3$. *Solid State Ionics* **1999**, *120* (1), 197.

(6) Tolganbek, N.; Yerkinbekova, Y.; Kalybekkyzy, S.; Bakenov, Z.; Mentbayeva, A. Current State of High Voltage Olivine Structured $LiMPO_4$ Cathode Materials for Energy Storage Applications: A Review. *Journal of Alloys and Compounds* **2021**, *882*, 160774.

Chapter 7

Conclusions and Future Work

7.1 Conclusions

We have developed a high throughput suite to accelerate the discovery and optimization of solid electrolytes. The tools in this suite allow for screening a wide range of material compositions to uncover promising candidates that may have been missed using traditional experimentation, where samples are tested one composition at a time. Our suite includes methodologies for synthesizing and screening the essential properties required to evaluate the potential of solid electrolytes in batches of 64 samples. These properties include ionic/electronic conductivity, the activation energy of lithium diffusion, and the electrochemical stability window. The optimized workflow enables fast testing of these properties in high throughput within 1-2 weeks, making our suite an efficient solution for electrolyte development. Although high-throughput screening is crucial, additional tests are necessary to thoroughly investigate the most promising candidates and further explore their properties. Therefore, the stability against lithium test is included in this suite but is conducted only on selected promising samples.

We have validated our suite using two reference materials with contrasting properties (LLTO and tetragonal LLZO). The results demonstrate excellent reproducibility and agreement with the literature, showcasing the precision and accuracy of our tools. Our systematic method enables us to evaluate the performance of solid electrolytes under identical synthesis and test conditions, providing insights into the relationship between material structure, composition, and properties guiding us in developing better solid electrolytes.

We investigated the effect of composition within the Li-La-Ti-O pseudoternary phase diagram and partial substitutions in the LLTO solid electrolyte system on its performance using the high-throughput suite developed. LLTO has promising high bulk conductivity and oxidative stability but suffers from low grain boundary conductivity and reductive instability. Over 576 samples in the Li-La-Ti-O pseudoternary phase diagram were synthesized and characterized using XRD. From the structural analysis at various sintering temperatures and periods, complemented by the lever rule, we found that perovskite LLTO is a metastable phase that stabilizes by the presence of a secondary phase such as TiO_2. Our study reveals that much of the LLTO growth occurs during slow cooling. This new instance of stabilization of metastable LLTO is of interest to both materials science and solid electrolyte engineering. By performing 50 single partial substitutions at 5 different substitution levels, we found that the perovskite phase can be stabilized by partial substitutions, resulting in a single-phase perovskite. To predict the site of substitution, we used bond valence mismatch.

We discovered that secondary phases play a significant role in reducing grain boundary resistance. Therefore, choosing the correct composition and synthesis conditions can improve total ionic conductivity without additional sintering steps, additives, or sacrificial powder beds. While some substitutions did not affect bulk conductivity, others decreased it, possibly due to low charge carrier concentration, hindered lithium diffusion paths, or reduced bottleneck size. We observed a minor enhancement of bulk conductivity in LLTO substituted with K. The substituent in pure perovskites dramatically impacted grain boundary conductivities. However, secondary phases introduced via substitution could also improve grain boundary conductivity (e.g. LLTO substituted with Na). We found that Cr, Mn, Rh, and Cd substitutions increase the electronic conductivity of

LLTO, making it a viable option for use as an electrolyte in composite electrodes for all-solid-state batteries.

Most substitutions in LLTO did not shift the high potential stability limit, except for Cr, which had a reversible peak in its CV, making it a potential cathode. Conversely, substitutions such as Mg lowered the low potential stability limit, allowing lithium titanate anode to be used. Our findings provide insights into the impact of synthesis conditions, composition, and substitutions on the structure and performance of LLTO solid electrolytes. We screened over 226 substitutions to identify potential candidates for the first epitaxial battery, which is an ideal use for this electrolyte with poor grain boundary conductivities. This study also provides a guide for improving the performance of LLTO through partial substitutions for energy storage applications, demonstrating the potential of this approach and identifying the limits to how far each property can be tuned. Overall, our study contributes to a better understanding of LLTO solid electrolytes.

After witnessing the success of the high-throughput approach and partial substitutions in optimizing LLTO solid electrolyte, we became interested in applying a similar methodology to improve the performance of the high-voltage $LiCoPO_4$ cathode, knowing that LLTO is compatible with high-potential cathodes. We successfully improved the performance of LCP by investigating the impact of partial single and co-substitution at the Co-site and synthesis conditions on a wide variety of properties necessary for battery performance. 1300 samples were studied, including 263 distinct substituted sample compositions with numerous duplicates to ensure reproducibility. The study demonstrates the usefulness and necessity of high-throughput experimental screening to design an optimum material. Specifically, Indium partial substitution (1-5%) improved the first cycle capacity and lowered the overpotential by improving ionic and electronic conductivity in carbon-coated materials. Additionally, the Co-substitution of In with either Mo or Nb prevented

Li/Co antisite defects and improved extended cycling. Mo also produced larger particles, thereby minimizing the surface area of the cathode where electrolyte decomposition occurs at high potentials. Remarkably, only 1% In/1% Mo partial co-substitution of Co showed a dramatic performance improvement. The capacity increased from 95 mAh/g, 43% retention in unsubstituted LCP to 150 mAh/g with 75% retention in the substituted material. This improvement is attributed to various factors, including larger particles, improved electronic conductivity in carbon-coated material, and suppression of Li/Co antisite defects. The study produced a novel state-of-the-art material and can serve as a template for accelerating the design of cathodes for advanced batteries using high-throughput experimentation, along with traditional experimental and computational methods.

7.2 Future work by chapter

7.2.1 Chapter 2

The suite we have developed for screening solid electrolytes represents a significant advance in developing solid-state lithium batteries. However, there is still scope for further research and development in this area. There is potential for expanding the suite to include additional properties. While the suite we have developed covers the essential properties required in solid electrolytes for their integration into solid-state batteries, other properties are also important but not currently covered by the suite. For example, physical properties such as density, mechanical strength, deformability, and interface compatibility with the cathode (optimization of composite cathode formulation) could also be crucial for solid-state battery performance. Including these properties in the suite would offer a more comprehensive approach to screening solid electrolytes. The suite we have developed focuses on screening solid electrolytes, but many other components of a solid-state battery could also benefit from high-throughput screening. For instance, the same suite could be used to screen the ionic and electronic conductivity of cathode and anode materials.

Finally, the integration of machine learning approaches could improve screening efficiency. As the suite generates large amounts of data, there is potential in using machine learning algorithms to analyze this data and identify patterns that could help improve screening efficiency. Integrating machine learning approaches into the suite could speed up the screening process and potentially identify new solid electrolyte compositions. Overall, the suite we have developed represents an important contribution to the field of solid-state lithium batteries. However, there is still significant room for improvement in automating the process and screening additional properties.

7.2.2 Chapter 3

In our study, we found that secondary phases such as TiO_2 can play a role in reducing grain boundary resistance. Analyzing the microstructure of the LLTO sample that had the highest conductivity with secondary phases using electron backscatter diffraction (EBSD) could help us understand how the secondary phases interact at the grain boundaries to affect ionic conductivity. This could help improve our engineering of grain boundary conductivity. In the future, we could also explore the effect of grain size and orientation on ionic conductivity by testing different sintering conditions, such as temperature, time, and atmosphere in the same composition where phase fraction is optimum.

7.2.3 Chapter 4

Future work could involve preparing an all-solid-state epitaxial battery that uses Cr-LLTO as the cathode and investigating the effect of higher Cr content on the capacity and performance of

Cr-LLTO. The specific mechanisms responsible for the observed effects of partial substitutions on the properties of LLTO could also be explored. For example, how does Mn substitution convert LLTO into an ionic and electronic mixed conductor? To investigate whether oxygen vacancies are the underlying mechanism of this conversion, we could use a combination of experimental and computational techniques to explore their presence and quantify them. The choice of techniques will depend on the concentration of oxygen vacancies. We could start by performing conductivity or Hall measurements under various oxygen partial pressures and temperatures by assuming a low concentration of oxygen vacancies (ppm) that cannot be determined by analyzing the oxidation state of the elements from which oxygen vacancy content can be calculated from chemical neutrality. Depending on the results we obtain from the previous measurements, if the concentration of the oxygen vacancy is higher it can be determined from the oxidation state and environment of the elements in the material by using XPS, electron energy loss spectroscopy (EELS), and X-ray absorption spectroscopy (XAS).[1] These experimental observations could be used to construct the band structure through computational calculation, which can provide further insights into the mechanism behind electronic conductivity. Additionally, the single substitutions study could be expanded to co-substitutions to achieve further improvements by combining properties. For example, can Fe and Cr co-substitution yield a highly conductive cathode?

7.2.4 Chapter 5

Although we attempted to understand the mechanism underlying the better performance of 1%In and 1%Mo co-subsituted LCP by conducting complementary experiments (transport properties) and a computational study, further insight could be gained by exploring the distribution of elements within the particles (homogeneous, phase separated, gradient, or core-shell). This could be accomplished by cutting the particles with a focused ion beam (FIB) and conducting elemental mapping of their cross-sections using EDS.[2] Additionally, the oxidation states of the elements in bulk and on the surface could be identified by XAS and XPS, respectively. Finally, we could investigate the performance of co-substituted $LiCoPO_4$ in all-solid-state batteries using the LLTO solid electrolyte we developed in Chapters 3 and 4. Given concerns around the sustainability of Co in $LiCoPO_4$, future work could involve investigating other olivine cathode materials, such as $LiMnPO_4$. While $LiMnPO_4$ has a lower theoretical capacity than $LiCoPO_4$, it has several advantages, including a lower cost, improved thermal stability, and reduced toxicity. Challenges associated with this material include increasing its electronic conductivity (which is currently below 10^{-9} S cm^{-1}, lower than that of $LiCoPO_4$) and addressing the Jahn-Teller anisotropic lattice distortion in MnPO4. This distortion leads to strain at the interface between the $LiMnPO_4$ (discharge state) and $MnPO_4$ (charge state) phases.[3] For high energy density demanding applications, we could turn to $LiNiPO_4$. Its theoretical energy density is higher than $LiCoPO_4$ because of its higher operating voltage of 5.1V vs. Li/Li^+.[4] The first challenge before starting to work on this system will be finding a liquid electrolyte that is stable at such high voltages. Using an ionic liquid could be one choice which is more expensive than carbonate liquid electrolyte increasing the cost of the study.

The single and double substitution data set can be used to train machine learning models using matrices such as capacity, overpotential, and capacity retention. By leveraging the relationships between different elements and their effect on the electrochemical performance of the material, the machine learning algorithms can predict the optimal combination of three co-substituted elements, which can then guide the further enhancement of LCP performance by triple co-substitution.

Our research has made significant contributions to the field of solid electrolytes and cathode materials for lithium batteries. One of our key achievements is the development of high-throughput screening tools that allow for the measurement of ionic and electronic conductivity, as well as the determination of the electrochemical stability window. Through our investigations, we have made a crucial discovery regarding the metastable nature of LLTO, highlighting the importance of a secondary phase for stabilization. Additionally, we have demonstrated the essential role of secondary phases in enhancing grain boundary conductivity. We have found that 100% perovskite can be stabilized by substitutions leading to minor improvements in bulk conductivity and moderate enhancements in grain boundary conductivity. Moreover, we showed the possibility of tuning ESW by substitutions. Our work has also focused on improving the performance of $LiCoPO_4$ cathodes through high-throughput substitutions and gaining a deeper understanding of the underlying mechanisms behind their enhanced performance. We have observed that substitutions not only improve transport properties but also allow for control over particle size. Overall, our research has significantly advanced the understanding and development of solid electrolytes and cathode materials within the field of battery technology.

7.3 References

(1) Gunkel, F.; Christensen, D. V.; Chen, Y. Z.; Pryds, N. Oxygen Vacancies: The (In)Visible Friend of Oxide Electronics. *Applied Physics Letters* **2020**, *116* (12), 120505.

(2) Sui, T.; Song, B.; Dluhos, J.; Lu, L.; Korsunsky, A. M. Nanoscale Chemical Mapping of Li-Ion Battery Cathode Material by FIB-SEM and TOF-SIMS Multi-Modal Microscopy. *Nano Energy* **2015**, *17*, 254.

(3) Wani, T. A.; Suresh, G. A Comprehensive Review of $LiMnPO_4$ Based Cathode Materials for Lithium-Ion Batteries: Current Strategies to Improve Its Performance. *Journal of Energy Storage* **2021**, *44*, 103307.

(4) Rommel, S. M.; Schall, N.; Brünig, C.; Weihrich, R. Challenges in the Synthesis of High Voltage Electrode Materials for Lithium-Ion Batteries: A Review on $LiNiPO_4$. *Monatshefte für Chemie - Chemical Monthly* **2014**, *145* (3), 385.